GEORG-AUGUST-UNIVERSITÄT
GÖTTINGEN

Fakultät für
Physik

Master's Thesis

# Myontrigger für Suchen nach Supersymmetrie in Multileptonischen Endzuständen mit dem ATLAS Detektor

# Muon triggers for Searches for Supersymmetry in Multi-Lepton Final States with the ATLAS Detector

prepared by

**Jannik Hofestädt**

from München

at the II. Physikalischen Institut

**Thesis number:** II.Physik-UniGö-MSc-2012/05

**Thesis Period:** 15th October 2011 until 14th April 2012

**First Referee:** Prof. Dr. Arnulf Quadt

**Second Referee:** Dr. Carsten Hensel

# Abstract

In this thesis, the efficiencies and rates of single and di-muon triggers at the ATLAS detector at the Large Hadron Collider are studied. It is shown that the di-muon trigger efficiencies can be factorised into the single muon trigger efficiencies, under the condition that the muon candidates are separated by a sufficiently large angle. The systematic uncertainties introduced by this factorisation are less than 1 %. The statistical uncertainties are reduced considerably with respect to the direct measurement of di-muon trigger efficiencies.
A cost-benefit analysis of various muon trigger strategies is performed. The different triggers are evaluated in the context of a benchmark search for Supersymmetry in a tri-lepton final state and their applicability to high interaction rates. A combination of a single muon trigger with high transverse momentum threshold and a di-muon trigger with lower transverse momentum threshold is found to be an adequate trigger strategy.



# Zusammenfassung

In dieser Arbeit werden die Effizienzen und Raten von Einzel-Myon- und Di-Myon-Triggern am ATLAS Detektor am Large Hadron Collider studiert. Es wird gezeigt, dass die Di-Myon-Triggereffizienzen sich in die Einzel-Myon-Triggereffizienzen faktorisieren lassen unter der Annahme, dass die Myon-Kandidaten durch einen ausreichend großen Winkelabstand separiert sind. Die systematischen Unsicherheiten, die durch diese Faktorisierung entstehen, sind kleiner als 1 %. Die statistischen Unsicherheiten werden im Vergleich zur direkten Messung der Di-Myon-Triggereffizienzen deutlich reduziert.
Es wird eine Kosten-Nutzen-Analyse von verschiedenen Myon-Triggerstrategien durchgeführt. Die unterschiedlichen Myon-Trigger werden im Kontext einer Benchmarksuche nach Supersymmetrie mit drei Leptonen im Endzustand und im Hinblick auf ihre Anwendbarkeit bei hohen Interaktionsraten bewertet. Eine Kombination aus einem Einzel-Myon-Trigger mit einer hohen Transversal-Impuls Schwelle und einem Di-Myon-Trigger mit einer niedrigeren Transversal-Impuls Schwelle hat sich als eine adäquate Triggerstrategie herausgestellt.

# Contents

# 1. Introduction

Elementary particles physics provides insights into the workings of nature at the most fundamental level. Our knowledge about the behaviour of the fundamental constituents of matter on tiny length scales and at high energies is described by the Standard Model of elementary particle physics. This theoretical framework is very successful in the description of the physics of elementary particles using symmetries. Symmetries play an important role in all fields of physics, since they facilitate the description of nature considerably. According to Noether's[1] theorem, any continuous symmetry of a physical system is related to a conserved quantity [1].

Despite its success, the Standard Model of elementary particle physics has shortcomings, some of which can be resolved by introducing an additional symmetry, called Supersymmetry. As a consequence of this additional symmetry, new elementary particles are predicted. So far, none of these particles has been observed. It is believed that, if Supersymmetry is realised in nature, hints for its existence will be seen at the Large Hadron Collider (LHC) at CERN. This collider accelerates protons to high energies that have never been reached under laboratory conditions before, and brings them to collision. The LHC operates since the end of 2008.

The proton-proton collisions at the LHC take place at very high rates, leading to data rates that cannot be handled by current storage elements. Only a small fraction of the collisions can be recorded by the detectors at the LHC: ATLAS, CMS, ALICE and LHCb. Hence, sophisticated trigger systems were devised to select interesting collisions.

The ATLAS trigger system has an extensive menu of triggers, selecting collisions

[1] Emmy Noether (* 1882, † 1935) formulated this fundamental theorem of theoretical physics in Göttingen in 1915 and published it in 1918.

based on various signatures. A promising opportunity for the discovery of Supersymmetry is offered by proton-proton collisions producing muons. Muons give a unique signature in the detector, which can be used to trigger on. Several muon triggers are implemented and are working well under the current experimental conditions. However, to be prepared for even higher collision rates in the future it is necessary to adjust the triggers. Therefore, extensive studies of different trigger strategies have to be carried out.

This thesis focuses on various muon trigger strategies at the ATLAS detector. For this purpose, the most important properties of muon triggers are discussed, in particular their rates and efficiencies. Since only collisions selected by the trigger are recorded, while all others are discarded, the precise knowledge of the trigger efficiency is of particular importance. Therefore, the efficiencies of single muon and di-muon triggers are studied in detail. These triggers select collisions with at least one or two muons according to certain criteria. In addition, the benefit of these and of further muon triggers for a benchmark search for Supersymmetry is evaluated.

This thesis is organised as follows: In Chapter 2, the Standard Model of particle physics and its supersymmetric extension are summarised. The LHC and the ATLAS detector, in particular its trigger system, is described in Chapter 3. The basic concepts of triggers at collider experiments are explained in Chapter 4. Emphasis is put on the trigger rates and trigger efficiencies at the ATLAS experiment using single muon triggers as an example. In Chapter 5, the efficiencies of di-muon triggers are studied, in particular whether they can be modelled from single muon trigger efficiencies. In Chapter 6, a cost-benefit analysis of various muon triggers is performed. For this purpose, the impact of different muon trigger strategies on a benchmark search for Supersymmetry in a tri-lepton final state is examined. Chapter 7 concludes the results and gives an outlook.

# 2. Theory

In this chapter, the Standard Model of elementary particle physics is introduced. Its major shortcomings and solutions to those shortcomings provided by the supersymmetric extension of the Standard Model are discussed. The basic ideas of Supersymmetry are introduced. Additionally, the phenomenology of Supersymmetry at hadron colliders is discussed.

## 2.1. The Standard Model of Elementary Particle Physics

The Standard Model of elementary particle physics (SM) [2–8] is a set of quantum field theories that describe elementary particles and their interactions. It has been developed over many years, and its current form is most successful in describing almost all experimental results in the field of high energy physics [9–11]. In the following, the SM is briefly introduced. This overview is based on [12–14].
In the SM, two types of elementary particles are distinguished, namely *bosons* with integer spin and *fermions* with half-integer spin. The latter are the building blocks of matter, while the former mediate forces. The three fundamental forces described by the SM are the electromagnetic force, strong force and weak force.
Within the SM, there are two groups of elementary fermions: quarks and leptons. Both have spin 1/2. Six flavours of quarks are known to exist, which bear the names up $u$, down $d$, charm $c$, strange $s$, top $t$, and bottom $b$ and are organised in three generations. Each generation consists of an up-type quark with electric charge $+2/3$ ($u$, $c$, $t$) and a down-type quark with electric charge $-1/3$ ($d$, $s$, $b$) in units of the electron charge magnitude $e$. The six leptons in the SM are also grouped into three generations, each with one charged ($-1\,e$) and one neutral par-

ticle. The charged leptons are the electron $e$, muon $\mu$, and tau $\tau$. Every charged lepton is associated with its neutral partner, the electron neutrino $\nu_e$, muon neutrino $\nu_\mu$, and tau neutrino $\nu_\tau$, respectively. The particle content of the SM is summarised in Table 2.1. Additionally, the masses and the electric charges of the particles are given. For each of the twelve fermions, there exists an antiparticle partner, which has reserved quantum numbers. The fields corresponding to the fermionic particles are divided into left-handed (subscript $L$) and right-handed states (subscript $R$). Only the left-handed states take part in the weak interaction. They form doublets of the weak isospin (charge of the $SU(2)$ group, see below), while the right-handed states are singlets.
The bosons are the mediators of the three fundamental forces described by the SM:

- the electromagnetic force mediated by the massless neutral photon $\gamma$,
- the weak force mediated by the heavy charged $W^\pm$ and the neutral $Z^0$ bosons,
- the strong force mediated by the eight massless neutral gluons $g$.

All of these bosons have spin one and arise from gauge symmetries, therefore they are called gauge bosons. The electromagnetic and the weak force can be described by a unified theory [2–4]. Mathematically, the unification is described by an $SU(2) \times U(1)$ gauge group. The corresponding gauge bosons are the $B^0$ boson of weak hypercharge from U(1) and the three $W$ bosons ($W^+$, $W^0$, $W^-$) of weak isospin from SU(2), respectively. In order to obtain gauge symmetry, all of these bosons are massless, which is inconsistent with experimental observations (cf. Table 2.1). However, the SM predicts that by spontaneous breaking of the electroweak symmetry, caused by the Higgs mechanism [5, 15, 16], the $B^0$ and $W^0$ field mix to form the physical fields $\gamma$ and $Z^0$. Additionally, the $W^\pm$ and $Z^0$ bosons acquire masses and a neutral scalar boson, the so-called Higgs boson $H$, is predicted by theory. However, it has not been discovered so far [1]. Its discovery and the determination of its properties is one of the main goals of currents particle physics experiments at the Large Hadron Collider (see Section 3.1).

[1] At the time of writing the Higgs boson had not been discovered and most of the mass range up to 600 GeV is excluded. However, an excess of events in the mass range around 125 GeV has been observed by ATLAS, CMS, DØ, and CDF [17–19].

| | Particle | El. Charge [$e$] | Mass [MeV] |
|---|---|---|---|
| Leptons: | electron neutrino ($\nu_e$) | 0 | $< 2 \cdot 10^{-6}$ |
| | electron ($e$) | $-1$ | 0.511 |
| | muon neutrino ($\nu_\mu$) | 0 | $< 2 \cdot 10^{-6}$ |
| | muon ($\mu$) | $-1$ | 105.7 |
| | tau neutrino ($\nu_\tau$) | 0 | $< 2 \cdot 10^{-6}$ |
| | tau ($\tau$) | $-1$ | $1776.82 \pm 0.16$ |
| Quarks: | up quark ($u$) | $+2/3$ | $1.7 - 3.3$ |
| | down quark ($d$) | $-1/3$ | $4.1 - 5.8$ |
| | charm quark ($c$) | $+2/3$ | $1270^{+70}_{-90}$ |
| | strange quark ($s$) | $-1/3$ | $101^{+29}_{-21}$ |
| | top quark ($t$) | $+2/3$ | $172000 \pm 16000$ |
| | bottom quark ($b$) | $-1/3$ | $4190^{+180}_{-60}$ |
| Bosons: | photon ($\gamma$) | 0 | 0 |
| | gluon ($g$) | 0 | 0 |
| | $W$ boson ($W^\pm$) | $\pm 1$ | $80399 \pm 23$ |
| | $Z$ boson ($Z^0$) | 0 | $91187.6 \pm 2.1$ |

***Table 2.1.:*** The elementary fermions and bosons of the Standard Model of elementary particle physics with their masses and electric charges in terms of the electron charge magnitude $e$. The masses are taken from [14]. For the neutrinos, upper limits on the mass from tritium decay are given [20]. The uncertainties of the electron and muon mass are negligible.

The strong force is described by Quantum Chromodynamics (QCD), which is the gauge theory of the $SU(3)$ gauge group [6–8]. The corresponding quantum number is called colour charge. Only quarks and gluons carry colour charge. The gluons can interact among themselves, in contrast to photons [2]. This self-interaction leads to *asymptotic freedom* and *confinement* of the quarks. The former means that the strong interaction gets weaker at short distances and the latter describes the fact that all observed bound states of quarks are colourless. Due to the confinement, isolated free quarks combine with spontaneously created quark-antiquark pairs to so-called hadrons.

[2] Mathematically, this self-interaction originates from the fact that U(1) is abelian, while SU(3) is not.

Besides the $SU(3) \times SU(2) \times U(1)$ gauge symmetry, the SM obeys the global Poincaré symmetry [3], which gives all relativistic quantum field theories their mathematical structure. Gravitation, the fourth fundamental force, is not part of the SM. Due to the weakness of gravity at scales where quantum effects become visible, gravity does not play a key role for elementary particle physics.

Mathematically, the SM can be derived from a Lagrangian density $\mathcal{L}$ following the Lagrangian formalism and using Noether's theorem [1], which connects continuous symmetries of a physical system to physical conserved quantities. The most general SM Lagrangian depends on 19 parameters, whose numerical values have to be determined by measurements. The free parameters of the SM are the masses of the fermions (generated by Yukawa couplings of the fermion fields to the Higgs field), the gauge couplings, different mixing angles, a CP-violating [4] phase and the Higgs quadratic coupling and self-interaction strength.

### 2.1.1. Shortcomings of the Standard Model

The SM is an extremely successful theoretical framework, which has predicted experimental results very precisely over the last decades. Nevertheless, there are several indications which suggest that the SM needs to be extended. In the following, some of the most unsatisfactory aspects of the SM are discussed.

**The Hierarchy Problem of the Higgs Mass** In the SM, the Higgs mass $m_H$ receives corrections, e.g. from fermionic loops, which are given by

$$\Delta {m_H}^2 \;=\; -\frac{|\lambda_f|^2}{8\pi^2}\Lambda_{UV}^2 + ... \tag{2.1}$$

where $\lambda_f$ is the Yukawa coupling, and $\Lambda_{UV}$ is called ultraviolet cutoff parameter and determines the scale up to which the SM is assumed to be valid. A natural choice for $\Lambda_{UV}$ would be at the order of the Planck scale [5] [22], which is the scale at which quantum gravitational effects become relevant. Thus, these contribu-

[3] The Poincaré group is the physical symmetry underlying special relativity and consists of translations, rotations and Lorentz boosts. A detailed description can be found in [21].
[4] Violation of the combination of charge conjugation (C) and parity (P) symmetry.
[5] The Planck scale is defined by the Planck mass $m_{\mathrm{P}} \approx 1.22 \cdot 10^{19}\,\mathrm{GeV}$, at which the Compton wavelength and the Schwarzschild radius become equal.

tions are quadratically divergent, but a Higgs mass of about 100 GeV is strongly favored from electroweak precision data [9–11]. This discrepancy is called hierarchy problem [23–26]. The phenomenologically required low Higgs mass can be retained by adjusting the parameters of the SM. This fine-tuning is in principle not excluded, but is considered to be very unlikely and therefore "unnatural".

**Unification of the Forces** In the past, different forces have been unified into a single more fundamental force, e.g. the electric and magnetic forces were unified in the 19th century by Maxwell's theory of electromagnetism [27] and in the 1970s, the electromagnetic and the weak forces were unified in the electroweak model [2–4]. It is expected that in a similar sense, the electroweak force can be unified with the strong force, such that all three forces are different manifestations of a single fundamental force [28]. This grand unification is mostly expected to happen at energies at the order of $10^{16}$ GeV. If the measured SM gauge couplings are extrapolated [6] to higher energies such a grand unification of the couplings does not appear, as illustrated in Figure 2.1 (left).
At energies of the order of the Planck scale, gravity might be included and unified with the other forces. This unification cannot be provided by the SM, as it does not even include a quantum theory of gravity.

**Dark Matter** Dark matter (DM) is a currently undetermined form of matter which neither emits nor scatters electromagnetic radiation, and therefore cannot be directly observed with telescopes. However, the existence of DM can be proven indirectly by its gravitational effects on visible matter.
Today, from a number of cosmological observations, like the cosmic microwave background radiation, it has been found that the energy content of the universe presently consists of about 5% ordinary baryonic matter as it is described by the SM, about 23% is DM, and the remaining 72% are attributed to dark energy [29]. Although the existence of DM is well-established, its fundamental make-up is not known. Any candidate for DM particles must only interact via the weak force (if at all) or via gravity. Additionally, in order to explain the large scale structure of the universe, DM has to be cold, i.e. non-relativistic. The most commonly assumed candidates for Cold Dark Matter (CDM) are weakly interacting massive particles

[6] Due to higher order processes, the coupling strength depends on the energy scale.

(WIMP). In the SM, neutrinos are the only stable particles which exclusively interact weakly, but they are relativistic and hence cannot be considered as CDM. To summarise, the SM does not offer an explanation for 95% of our universe.

## 2.2. Supersymmetry

A possible extension of the SM is Supersymmetry (SUSY) [30–38]. It can solve a number of shortcomings of the SM outlined above, without making predictions which are inconsistent with existing experimental observations. In the following, the general idea of SUSY is introduced briefly. A more detailed description can be found in [22, 39, 40].
Supersymmetry is a generalisation of the Poincaré symmetry and transforms fermions into bosons, and vice versa. For the generators $Q$ of SUSY transformations it holds

$$Q \mid \text{Boson}\rangle \sim \mid \text{Fermion}\rangle \qquad Q \mid \text{Fermion}\rangle \sim \mid \text{Boson}\rangle. \tag{2.2}$$

It turns out that the complex generators $Q$ and $Q^\dagger$ transform like anticommuting spinors and carry a spin of 1/2. According to the Haag-Łopuszański-Sohnius extension [41] of the Coleman-Mandula theorem [42], the forms for such extensions of the Poincaré symmetry in an interacting quantum field theory are highly restricted. The only possible symmetries of a consistent 4-dimensional quantum field theory are the Poincaré symmetry, gauge symmetries and Supersymmetry, making SUSY unique in this sense [43].

The simplest supersymmetric extension of the Poincaré algebra is the Super-Poincaré algebra (also called SUSY algebra). In component form, the SUSY algebra is given by the following commutation and anti-commutation relations:

$$\begin{aligned} \left\{Q_a, Q_b^\dagger\right\} &= (\sigma^\mu)_{ab} P_\mu \\ \{Q_a, Q_b\} = \left\{Q_a^\dagger, Q_b^\dagger\right\} &= 0 \\ [Q_a, P_\mu] = \left[Q_a^\dagger, P_\mu\right] &= 0 \end{aligned} \tag{2.3}$$

$P_\mu$ is the $\mu$-th component, $\mu \in \{0, \ldots, 3\}$, of the generator of space-time translations, $\sigma^\mu$ are the Pauli matrices and the indices $a$ and $b$ denote there components in the Weyl spinor representation. The irreducible representations of the SUSY algebra are called supermultiplets. Each supermultiplet contains fermionic and bosonic states, which are commonly known as superpartners of each other.
It is not possible to combine only SM particles into supermultiplets, because superpartners must have the same quantum numbers [7]. Thus, new supersymmetric particles have to be introduced. The simplest possible supersymmetric extension of the SM with minimal particle content is the "Minimal Supersymmetric Standard Model" and is introduced in chapter 2.2.2.

### 2.2.1. Supersymmetric Solutions of the SM Shortcomings

Supersymmetry provides natural solutions to some of the problems of the SM outlined in Section 2.1.1. The solutions for the hierarchy problem and the unification of the forces are briefly discussed below. Additionally, SUSY provides a natural candidate for DM [44, 45], which is explained in Section 2.2.6.

**SUSY Solution for the Hierarchy Problem** For every fermionic contribution to the loop corrections of the Higgs mass, a bosonic counterpart arises due to the additional superpartners of the SM particles. This counterparts have the opposite signs due to the different spin statistics (Bose-Einstein and Fermi-Dirac). This leads to a cancellation of the quadratic divergences [46–51]. Thus it is not necessary to fine-tune the parameters of the SM.

**SUSY Solution for the Unification of the Forces** By introducing the superpartners of the SM particles, the energy dependence of the gauge couplings is modified such that the extrapolated gauge couplings in the MSSM can meet within the uncertainties at an energy of about $10^{16}$ GeV [52–55]. The energy at which this unification (Grand Unified Theory, GUT) takes place is called GUT scale. This is illustrated in Figure 2.1 (right).

[7] The SUSY generators $Q$, $Q^\dagger$ commute with the generators of the gauge transformations resulting in the same quantum numbers

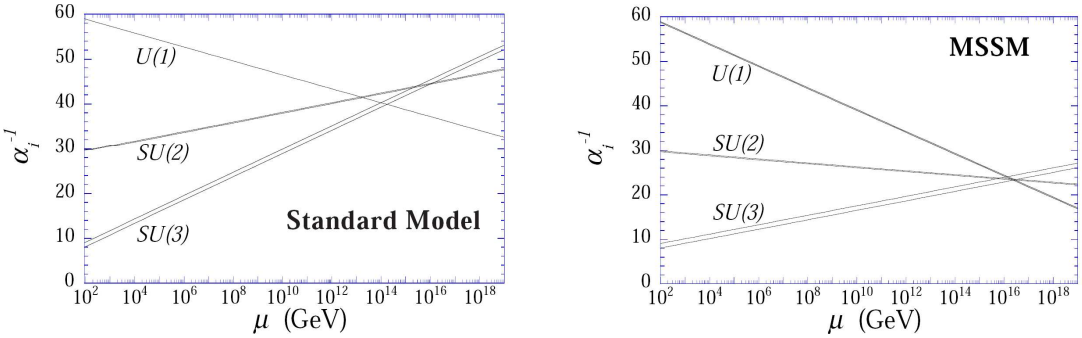


***Figure 2.1.:*** Comparison of the extrapolation of the gauge couplings, as assumed in the SM (left) and the MSSM (right). The inverse of the coupling strength $\alpha_i^{-1}$ is shown, where $\alpha_i$ is the gauge coupling of the groups $U(1)$, $SU(2)$, $SU(3)$ for $i = 1, 2, 3$, respectively, as a function of the logarithm of the energy scale $\mu$. Taken from [56].

### 2.2.2. The Minimal Supersymmetric Standard Model

The minimal extension to the SM that realises SUSY is the Minimal Supersymmetric Standard Model (MSSM). Table 2.2 shows the field content of the MSSM [14]. Each SM particle is accompanied by its superpartner, conventionally denoted by a tilde ($\tilde{}$) above the corresponding SM symbol. The superpartners of the SM fermions are called scalar fermions (sfermions), whereas the superpartners of the gauge and Higgs bosons are called gauginos and higgsinos, respectively. Unlike in the SM, the Higgs sector in supersymmetric models needs to be extended. To give masses to up-type and down-type quarks, two independent Higgs doublets [8] are needed [39].

The MSSM Lagrangian density can be constructed from the SM Lagrangian density by requiring that the Lagrangian density fulfills the SUSY algebra in Equation 2.3, is Lorentz invariant, renormalisable and gauge invariant under $SU(3) \times SU(2) \times U(1)$. Additionally, all allowed supersymmetric interactions which do not violate either lepton number ($L$) or baryon number ($B$) conservation are added [46, 57–60]. Without the latter requirement, the proton would not be stable, which is in conflict with observations [14].

For this purpose, a new multiplicative quantum number is introduced. The so-

[8] The two MSSM-Higgs doublets have eight real degrees of freedom, resulting in five Higgs bosons, three neutral ($h, H, A$) and two charged ($H^+, H^-$), after the electroweak symmetry breaking.

called $R$-parity, $P_R$, is defined by

$$P_R \;=\; (-1)^{3(B-L)+2S} \tag{2.4}$$

where $S$ is the spin. By this definition, the SM particles and the Higgs bosons have even $R$-parity ($P_R = 1$), while all SUSY particles have odd $R$-parity ($P_R = -1$). The conservation of the $R$-parity prevents the proton decay and leads to characteristic SUSY signatures, discussed in Section 2.2.6.

Like in the SM, supersymmetric particles with the same quantum numbers can mix. As a consequence, the gauge and mass eigenstates of these particles are not the same. The charged higgsinos ($\tilde{H}_u^+$ and $\tilde{H}_d^-$) and charged winos ($\tilde{W}^\pm$) combine to form the mass eigenstates $\tilde{\chi}_{1,2}^\pm$, called charginos. Similarly, the neutral higgsinos ($\tilde{H}_u^0$ and $\tilde{H}_d^0$), the neutral wino ($\tilde{W}^0$) and the bino ($\tilde{B}^0$) mix to form the mass eigenstates $\tilde{\chi}_{1...,4}^0$, called neutralinos. These mass eigenstates are sorted according to their mass, i.e. $m_{\tilde{\chi}_1^0} < ... < m_{\tilde{\chi}_4^0}$ and $m_{\tilde{\chi}_1^\pm} < m_{\tilde{\chi}_2^\pm}$. Gluinos are the only neutral coloured SUSY particles and therefore do not mix. In the sfermion sector, a mixing between the two superpartners of the left- and right-handed fermions, $\tilde{f}_L$ and $\tilde{f}_R$, occurs.

| Name | Spin 0 | Spin 1/2 | Spin 1 |
|---|---|---|---|
| Squarks, Quarks | $(\tilde{u}\ \tilde{d})_L$ | $(u\ d)_L$ | |
| | $\tilde{u}_R$ | $u_R$ | |
| | $\tilde{d}_R$ | $d_R$ | |
| Sleptons, Leptons | $(\tilde{\nu}\ \tilde{e}^-)_L$ | $(\nu\ e^-)_L$ | |
| | $\tilde{e}_R^-$ | $e_R$ | |
| Higgs, Higgsinos | $(H_d^0\ H_d^-)$ | $(\tilde{H}_d^0\ \tilde{H}_d^-)$ | |
| | $(H_u^+\ H_u^0)$ | $(\tilde{H}_u^+\ \tilde{H}_u^0)$ | |
| Gluinos, Gluon | | $\tilde{g}$ | $g$ |
| Winos, $W$ bosons | | $\tilde{W}^\pm \quad \tilde{W}^0$ | $W^\pm \quad W^0$ |
| Bino, $B$ boson | | $\tilde{B}^0$ | $B^0$ |

***Table 2.2.:*** Field content of the MSSM. The SM superpartners are denoted with a tilde. For (s)quarks and (s)leptons only the first generation is shown. Note that the sfermion indices ($L$ an $R$) do not indicate the chirality of the SUSY particles, but their SM superpartners. Taken from [22].

### 2.2.3. Supersymmetry Breaking

According to the SUSY algebra in Equation 2.3, the generator of space-time translations $P$ commutes with the SUSY generators $Q$ and $Q^\dagger$. The same holds for the invariant mass operator $M^2 = P_\mu P^\mu$. Thus, superpartners have the same mass as their SM counterparts. However, no selectron with a mass of $m_{\tilde{e}} = m_e = 0.511\,\text{MeV}$ or any other supersymmetric particle has been observed so far. Therefore, some form of breaking of Supersymmetry is inevitable in order to bring the sparticle masses up to a not yet excluded range (of the order of 100 GeV).
In order not to reintroduce a hierarchy problem, the breaking needs to be "soft". The attribute "soft" means that the breaking only appears via terms that maintain the cancellation of quadratical divergences in the loop corrections of the Higgs mass (cf. Section 2.1.1 and 2.2.1). The effective Lagrangian density of the MSSM can be written in the form

$$\mathcal{L} \;=\; \mathcal{L}_{\text{SUSY}} + \mathcal{L}_{\text{soft}} \tag{2.5}$$

where $\mathcal{L}_{\text{SUSY}}$ is the unbroken SUSY Lagrangian density containing only terms which preserve SUSY invariance and $\mathcal{L}_{\text{soft}}$ contains the soft SUSY breaking terms. Different supersymmetric models assume different breaking terms. However, for all softly broken SUSY models, the leading term of the loop corrections of the Higgs mass depends only logarithmically on the ultraviolet cutoff parameter $\Lambda_{UV}$ and is of the form

$$\Delta m_H^2 \;=\; m_{\text{soft}}^2 \left[ \frac{\lambda}{16\pi^2} \ln\left(\Lambda_{UV}/m_{\text{soft}}\right) \right] \tag{2.6}$$

where $m_{\text{soft}}$ is the mass scale associated to the SUSY breaking and $\lambda$ stands exemplarily for various dimensionless couplings. In most viable supersymmetric models, $m_{\text{soft}}$ around 100 GeV to 1 TeV is strongly favoured [61]. The masses of at least the lightest SUSY particles should be of the same order.
Although the constraints on the SUSY breaking are rather strict, 105 additional free parameters are needed in the most general form of the MSSM. Only one of these additional parameters with respect to the SM is needed in the SUSY-conserving part on the MSSM, the Higgs mass parameter $\mu$. The amount of new parameters introduced by the SUSY breaking makes the unconstrained MSSM

quite flexible, but also makes it rather difficult to interpret experimental results. Thus, simplified models within the MSSM are constructed by imposing certain assumptions, which enforce phenomenological constraints, resulting in a significant reduction of the number of free parameters.

There are two ways to reduce the amount of a priori unknown parameters. The first approach is to assume a specific SUSY breaking scenario. One of the most widely investigated such models is mSUGRA (minimal SUperGRAavity) [62], described in Section 2.2.4. An alternative approach is to impose a set of theoretically and experimentally well-motivated constraints on the MSSM, without making any assumption about a specific SUSY breaking mechanism. One such model is the phenomenological MSSM (pMSSM) [63, 64], where the number of free parameters is reduced to 19 parameters at the electroweak scale, which completely describe all aspects of the relevant SUSY phenomenology at present collider experiments, like the LHC (see Section 3.1). The studies performed in this thesis are based on the pMSSM, which is discussed in more detail in Section 2.2.5.

### 2.2.4. The mSUGRA Model

In the mSUGRA model, the actual SUSY breaking takes place in a hidden sector and is mediated to the visible SUSY sector via gravity. It is highly predictive and only four input parameters and a sign are needed to determine the SUSY phenomenology that is relevant for searches. These parameters are: a common scalar (i.e. sfermion and Higgs boson) mass $m_0$ at the GUT scale; a common gaugino mass $m_{1/2}$ at the GUT scale; a common trilinear sfermion-sfermion-Higgs coupling $A_0$ at the GUT scale; the ratio of the vacuum expectation values of the two neutral Higgs fields $\tan(\beta) = \langle H_u^0 \rangle \,/\, \langle H_d^0 \rangle$; the sign of the Higgs mass parameter $\mu$.

### 2.2.5. Phenomenological MSSM

The pMSSM imposes the following set of requirements onto the general $R$-parity conserving MSSM: (*i*) no new CP-violating source beyond those in the usual CKM matrix [65, 66], (*ii*) minimal flavour violation at the TeV scale [67], (*iii*) negligible trilinear couplings as well as degenerate masses for the first and sec-

ond sfermions generations, and (*iv*) the lightest neutralino is assumed to be the *Lightest Supersymmetric Particle* (LSP) and a stable thermal WIMP. With these conditions, the remaining 19 free parameters are: three gaugino masses $M_{i=1-3}$; three Higgs(ino) sector parameters $\mu$, $M_A$ and $\tan(\beta)$ (same as for mSUGRA); two left-handed and four right-handed squark masses (degenerate first and second generation); two left-handed and two right-handed slepton masses (degenerate first and second generation); three trilinear couplings of the third generation $A_t$, $A_b$ and $A_\tau$.

For the studies performed in this thesis, the production of supersymmetric particles is dominated by direct production of electroweak gauginos (charginos and neutralinos). The specific composition of these gauginos is determined by the parameters $M_1$ (only for neutralinos), $M_2$ and $\mu$, and slightly by $\tan(\beta)$. In general, the phenomenology is very sensitive to the underlying neutralino/chargino structure. This is in contrast to models like mSUGRA, where the parameters are confined at the electroweak scale to a narrow slice of the ($M_1$, $M_2$, $\mu$) parameter space, typically $2M_1 \approx M_2 > \mu$. Hence, these models result in a somewhat static picture of the possible electroweak gaugino phenomenology [68]. The parameters strongly affect the (pair) production cross-sections and determine the branching patterns.

The pMSSM parameter space assumed for the studies performed in Section 6 are described in more detail in Section 6.4.1.

### 2.2.6. SUSY Phenomenology at Hadron Colliders

This section gives a short summary of SUSY phenomenology at hadron colliders, especially at proton-proton colliders, like the LHC (see Section 3.1).

Protons are bound states of three valence quarks ($uud$) and sea quarks held together by gluons. Therefore, in proton-proton collisions, the protons do not interact as a whole with each other, but their partons. These carry only a fraction of the momentum of the proton [69]. The probability of finding a parton (gluon, valence quark, or sea quark) with a given momentum fraction of the proton's momentum is described by the parton distribution functions (PDFs). For each individual collision, the momentum of interacting partons is unknown. However, due to momentum conservation the vectorial sum of the transverse momenta of all produced particles is zeros. For this reason, transverse quantities, like the

transverse momentum $p_T$ or energy $E_T$, are often utilised at hadron colliders. If particles escape undetected, the vectorial sum of all transverse momenta of all observed particles does not vanish. Its absolute value is called *missing transverse energy* $E_T^{miss}$.

Depending on the assumed SUSY model, a variety of different SUSY signatures are possible. However, all $R$-parity conserving models have in common that (*i*) SUSY particles can only be produced in pairs, (*ii*) all SUSY particles decay into an odd number of SUSY particles and an arbitrary number of SM particles, and (*iii*) the LSP is stable. In most models the LSP is the lightest neutralino, which only interacts weakly and gravitationally, and is therefore a good candidate for DM (cf. Section 2.1.1). Moreover, it escapes undetected from the detector resulting in $E_T^{miss}$. Hence, searches for SUSY often combine large $E_T^{miss}$ with model-depend signatures.

The dominant SUSY production channel at the LHC depends on the masses of the SUSY particles. The coloured SUSY particles (quarks and gluinos) have significantly higher production cross-sections (via the strong force) than non-coloured SUSY particles of equal mass such as electroweak gauginos and sleptons. In SUSY models where the gluinos and squarks are sufficiently heavier than electroweak gauginos and sleptons, the first sign of SUSY at the LHC may show up in the production of electroweak gauginos and sleptons via the weak force. The phenomenology of these models is very sensitive to the underlying chargino/neutralino composition. Exemplarily, the production of a $\tilde{\chi}_1^{\pm}\tilde{\chi}_2^0$ pair and two possible decay channels into a tri-lepton final state are depicted in Figure 2.2. Other decay modes into quarks are also possible. These quarks can be detected as a spray of collimated hadrons, called jets. In general, the observable signals for SUSY are $E_T^{miss}$ + $n$ leptons + $m$ jets, where either $n$ or $m$ may be zero.

Promising signatures for searches for SUSY depend on the assumed supersymmetric model. For the model assumed in the studies performed in this thesis (see Section 6), a tri-lepton final state with $E_T^{miss}$ is a promising SUSY signature.

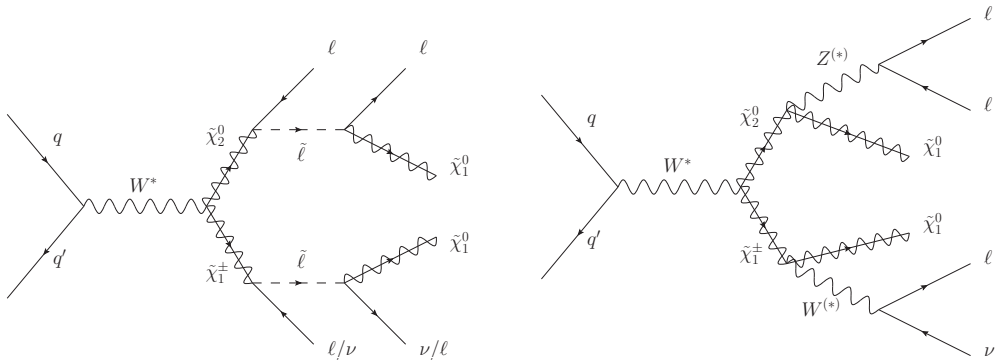


(a) with intermediate slepton (b) without intermediate slepton

***Figure 2.2.:*** Feynman diagrams for the production of a $\tilde{\chi}_1^\pm\tilde{\chi}_2^0$ pair via a virtual $W^\pm$ and two possible decay modes with three leptons ($\ell$), one neutrino ($\nu$) and two neutralinos ($\tilde{\chi}_2^0$) in the final state: (a) with intermediate sleptons and (b) without. The $\nu$ and the two $\tilde{\chi}_1^0$ result in $E_T^{miss}$, leading to tri-lepton signature with $E_T^{miss}$.

# 3. The LHC and the ATLAS Experiment

This chapter deals with the technical details of the Large Hadron Collider (LHC) and the ATLAS (A Toroidal LHC Apparatus) experiment. The ATLAS detector is one of the multi-purpose detectors located at the LHC. After a general overview of the ATLAS detector, the subsystems and their properties are described. The ATLAS muon system and the ATLAS trigger, especially the muon trigger system are explained in more detail.

## 3.1. Large Hadron Collider

The LHC [70–73] is a hadron-hadron circular collider, located at the European Organization for Nuclear Research (CERN) near Geneva, Switzerland. It is designed as a proton accelerator, which can accelerate heavy ions (lead nuclei) as well. It was built in the former accelerator tunnel of the Large Electron-Positron Collider (LEP). The LHC tunnel with a circumference of 27 km is situated about 100 m underground.

The LHC machine is designed to accelerate protons to energies up to 7 TeV. This is achieved with the help of a chain of different pre-accelerators, schematically shown in Figure 3.1. The protons in the LHC are accelerated using radio frequency cavities and bent along the beam pipe using superconducting dipole magnets, providing a nominal magnetic field of 8.33 T. The magnets operate at a nominal temperature of 1.9 K, cooled down by superfluid helium.

The two LHC proton beams are brought to collision with centre-of-mass energies $\sqrt{s}$ up to 14 TeV. Around the interaction points (IPs), different detectors are installed to record these collisions. Each proton beam consists of 2808 bunches

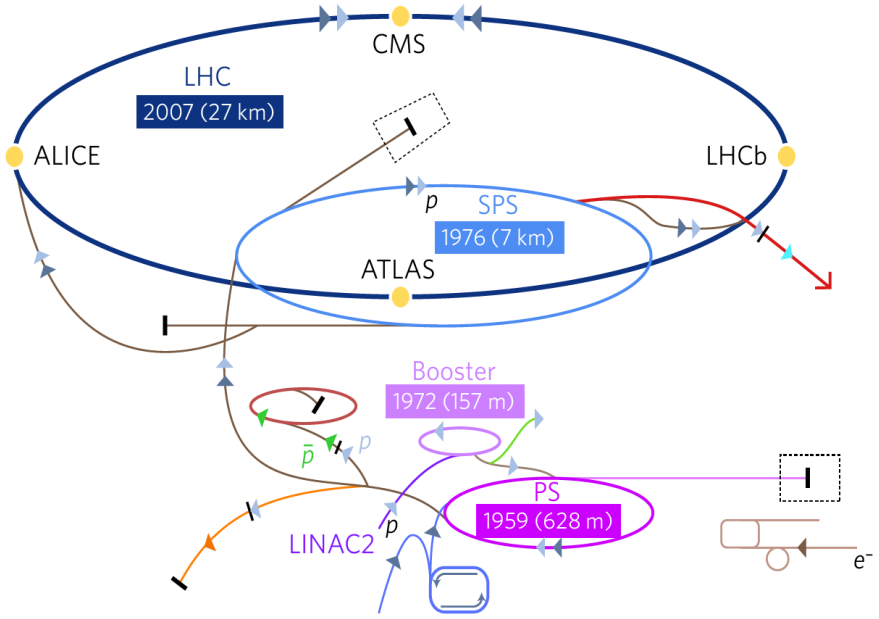


***Figure 3.1.:*** Schematic view of the LHC with its four main experiments: ALICE, ATLAS, CMS and LHCb (see Section 3.1.2). In addition, the preaccelerators Linear accelerator (Linac2), Proton Synchrotron Booster (Booster), Proton Synchrotron (PS) and Super Proton Synchrotron (SPS) are shown. Taken from [74].

at full intensity, which contain about $10^{11}$ protons each. A bunch crossing can occur every 25 ns, giving a maximum bunch crossing rate (BCR) of 40 MHz. In this configuration, the LHC is designed for an instantaneous luminosity of $L = 10^{34}\,\mathrm{cm}^{-2}\,\mathrm{s}^{-1}$. The instantaneous luminosity is a quantity that characterises the particle beams, and relates the cross-section $\sigma$ of a given process to its corresponding interaction rate $\mathrm{d}N/\mathrm{d}t$:

$$\frac{\mathrm{d}N}{\mathrm{d}t} = \sigma \cdot L. \tag{3.1}$$

In physics, a cross-section is a measure of the probability of a given process to occur [13, 14]. It is usually given in barn [b] defined as $10^{-28}\,\mathrm{m}^2$. The cross-section of a specific process can be calculated from the Feynman rules and the available phase space [13] and is in general energy-dependent. The total inelastic proton-proton cross-section expected for 14 TeV is of the order of 100 mb resulting in about 23 proton-proton interactions on average for each bunch crossing at design luminosity [75]. Thus, the overall interaction rate is in the GHz regime.
A common measure for the amount of data collected over a certain time interval

is specified in terms of integrated luminosity:

$$L_{\text{int}} = \int L \, \mathrm{d}t. \tag{3.2}$$

### 3.1.1. Timeline of LHC and Future Plans

The first proton beams were successfully circulated in the main ring of the LHC on 10th September 2008 [76], but a few days later the machine was severely damaged due to a magnet quench incident [77]. After one year of repairs and consolidating, the proton beams circulated again on 20th November 2009 [78] and three days later the first proton-proton collisions were recorded at $\sqrt{s} = 900\,\text{GeV}$ [79]. On 30th March 2010, the first collisions at $\sqrt{s} = 7\,\text{TeV}$ took place [80]. Until the end of 2011, the LHC delivered in total more than $5\,\text{fb}^{-1}$ at $\sqrt{s} = 7\,\text{TeV}$ to its multi-purpose detectors ATLAS and CMS each. The delivered and recorded integrated luminosity for ATLAS in 2011 as a function of time is shown in Figure 3.2.

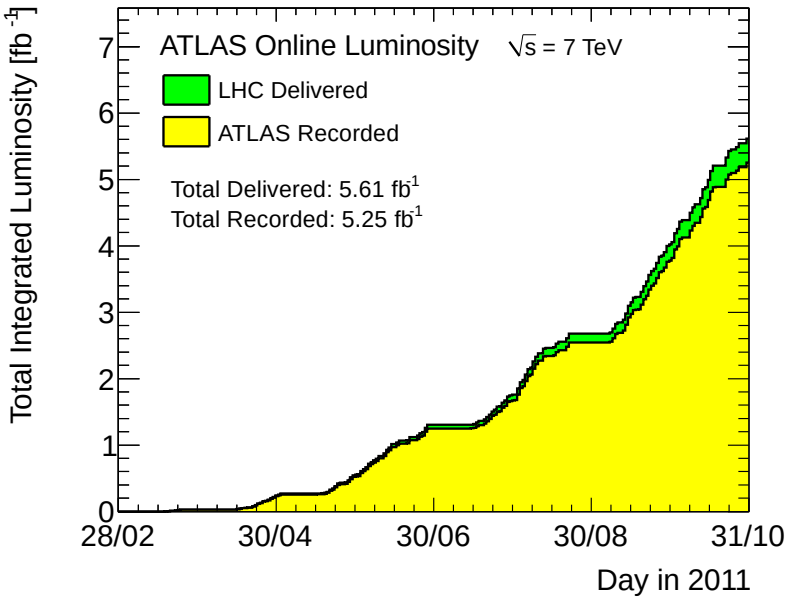


***Figure 3.2.:*** Cumulative luminosity versus time in 2011 delivered to (green), and recorded by ATLAS (yellow) during stable beams. Taken from [81]

After the winter shutdown 2011/2012, the LHC will operate at $\sqrt{s} = 8\,\text{TeV}$ until the end of 2012. Then, a technical stop of 20 months is scheduled for upgrades to enable the LHC to operate at its design centre-of-mass energy of $\sqrt{s} = 14\,\text{TeV}$

[82].

### 3.1.2. Detectors at the LHC

Besides the ATLAS detector, which is described in detail in Section 3.2, there are 3 further large-scale detectors (ALICE, CMS and LHCb) and three smaller ones (LHCf, MoEDAL and TOTEM) hosted at the LHC. These experiments and their scientific goals are briefly summarised in the following.

**Compact Muon Solenoid (CMS)**
The CMS detector [83] is a multi-purpose detector with a typical onion-like layout. The innermost layer is a silicon-based tracker, surrounded by a scintillating crystal electromagnetic calorimeter and a sampling calorimeter for hadrons. The tracker and the calorimeters are compact enough to fit inside a solenoid magnet. This magnet generates a powerful magnetic field of 3.8 T. The return yoke of the magnet is interspersed with muon detectors.
The CMS experiment shares the same scientific goals as the ATLAS experiment (see Section 3.2). This allows to do cross-checks of the results of the respective other detector.

**A Large Ion Collider Experiment (ALICE)**
The ALICE detector [84] is specifically designed to study heavy ion collisions, in which a quark-gluon plasma is expected to be created. In this plasma the quarks and gluons are nearly free and not confined. This state is supposed to have existed shortly after the Big Bang.

**Large Hadron Collider beauty (LHCb)**
The LHCb detector [85] is a single arm forward spectrometer and is specialised on $b$-physics. It measures CP-violation in the decays of $b$-hadrons. The results are supposed to shed light on the matter-antimatter asymmetry in the Universe.

**Large Hadron Collider forward (LHCf)**
The LHCf experiment [86] consists of two special-purpose detectors, which are located at a distance of 140 m on either side of the interaction point where ATLAS is situated. These detectors are intended to measure the energy of neutral

pions produced by inelastic proton-proton scattering. The results are supposed to understand the origin of ultra-high-energy cosmic rays.

**Monopole and Exotics Detector At the LHC (MoEDAL)**
The MoEDAL detector [87] is an array of plastic nuclear track detectors, located at the same IP as LHCb. Its primary goal is to directly search for highly ionizing stable massive particles such as magnetic monopoles and other hypothetical particles predicted by different theories beyond the SM.

**TOTal Elastic and diffractive cross section Measurement (TOTEM)**
The TOTEM experiment [88] measures the total proton-proton cross-section, as well as the cross-section of elastic scattering and diffractive processes. All LHC detectors are using TOTEM's measurements to calibrate their luminosity monitors.

## 3.2. The ATLAS Detector

In the following, the ATLAS detector and its subsystems are described. Emphasis is put on the purpose of each subsystem with respect to its contribution to the identification of particles and the measurement of their properties. The description of the ATLAS detector is based on [75, 89, 90].
The trigger system is explained in detail in Section 3.3.

### 3.2.1. Overview

The overall ATLAS detector layout is shown in Figure 3.3. The ATLAS detector is roughly 44 m in length and 25 m in height/width and its weight is approximately 7000 t. It has a forward-backward symmetric cylindrical geometry and consists of a barrel part and endcaps on each side covering nearly $4\pi$ in solid angle. Due to its onion-like layout it is possible to distinguish between different particle types using the complementary information of the several subsystems. The typical signatures of electrons, photons, charged and neutral hadrons as well as muons in the ATLAS detector are illustrated and explained in Figure 3.4.

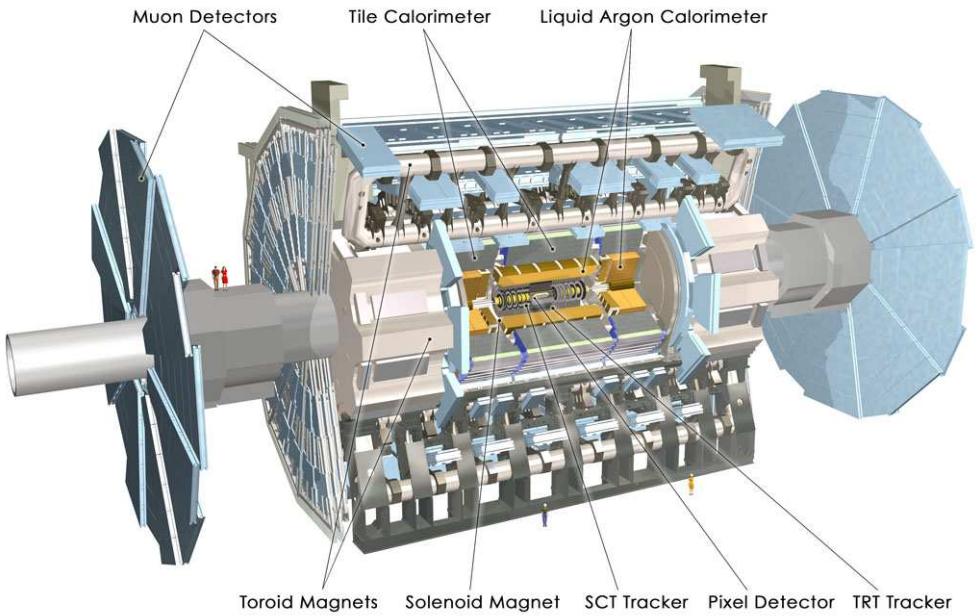


***Figure 3.3.:*** The ATLAS detector with its subsystems as explained in the text (computer-generated cut-away view). Taken from [91].

Closest to the interaction point, at the centre of the detector, is the Inner Detector, which accurately measures the tracks of charged particles. It is immersed in a solenoid magnetic field, in order to allow for momentum measurements of the particles from the curvature of their tracks. The solenoid magnet is surrounded by the calorimeter system composed of the electromagnetic calorimeters and the hadronic calorimeters, which measure the energy of particles stopped in them. Finally, the outermost part of the detector forms the muon system, which consists of a toroidal magnet system and muon chambers. The latter perform additional measurements of muons penetrating all other layers of the detector.
In Table 3.1, an overview of the performance goals with respect to the design of the ATLAS detector components is given. In order to be able to describe in more detail the detector subsystems, first the ATLAS coordinate system is introduced, which is used throughout this thesis.
The right-handed ATLAS coordinate frame has its origin at the centre of the detector, the nominal interaction point. The $z$-axis is defined by the beam pipe and the positive $x$-axis is pointing to the centre of the LHC ring, while the $y$-axis points upwards. The side of the ATLAS detector with positive $z$ is the A-side and the other side is the C-side.

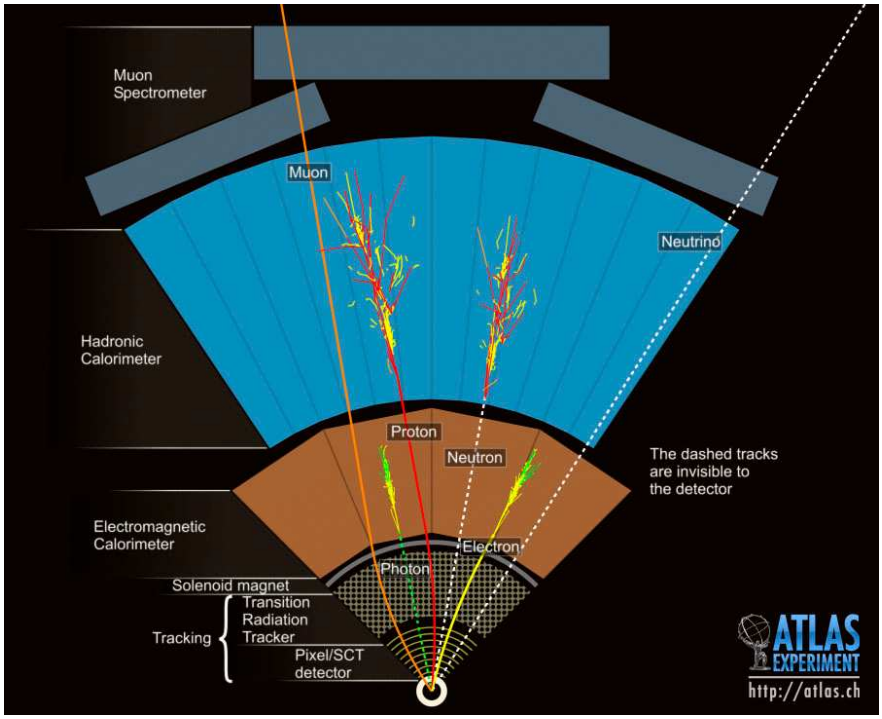


***Figure 3.4.:*** Typical signatures of an electron, a photon, a proton, and a neutron (as representatives for charged and neutral hadrons) as well as a muon in the ATLAS detector. Taken from [91].
The electron leaves a track in the Inner Detector (ID) and creates an electromagnetic shower in the electromagnetic calorimeter. Such showers without an associated track can originate from photons (and neutral pions, not shown in the figure). Similarly, charged hadrons can be identified by showers in the hadronic calorimeters with an associated ID track, while neutral hadrons deposit most of their energy in the hadronic calorimeter. Exemplarily, this is shown for protons and neutrons. Muons are the only visible particles which reach the muon chambers at the outermost part of the detector. As illustrated, muons can also be seen by the ID, such that for a precise muon reconstruction the information from the ID and the muon system can be combined. Additionally, a neutrino is depicted escaping the detector without any detector response.

| Detector component | Resolution goal |
|---|---|
| Tracking (Inner Detector) | $\sigma(p_T)/p_T = 0.05\,\% \, p_T \oplus 1\,\%$ |
| EM calorimetry | $\sigma(E)/E = 10\,\%/\sqrt{E} \oplus 0.7\,\%$ |
| Hadronic calorimetry (jets) | |
| barrel and endcaps | $\sigma(E)/E = 50\,\%/\sqrt{E} \oplus 3\,\%$ |
| forward | $\sigma(E)/E = 100\,\%/\sqrt{E} \oplus 10\,\%$ |
| Muon sprectrometer | $\sigma(p_T)/p_T = 10\,\%$ at $p_T = 1\,\text{TeV}$ |

***Table 3.1.:*** Resolution goals of the ATLAS detector components. Energy $E$ and transverse momentum $p_T$ are given in GeV and $\oplus$ stands for the quadratic sum, $a \oplus b = \sqrt{a^2 + b^2}$. The numbers are taken from [89] and may differ from the resolution actually achieved.

Due to the geometry of the ATLAS detector spherical coordinates are often used to describe positions and momenta. The azimuthal angle $\phi$ is measured around the $z$-axis, the polar angle $\vartheta$ is defined with respect to the $z$-axis and the distance from the origin is given by $r$. Instead of $\vartheta$, the pseudorapidity $\eta$ is commonly used. It is defined as

$$\eta = -\ln\left(\tan\left(\frac{\vartheta}{2}\right)\right) \tag{3.3}$$

and is the ultrarelativistic limit of the rapidity

$$y = \frac{1}{2}\ln\left[\frac{E + p_z}{E - p_z}\right]. \tag{3.4}$$

Geometric distances are often expressed in terms of

$$\Delta R = \sqrt{(\Delta\eta)^2 + (\Delta\phi)^2}. \tag{3.5}$$

### 3.2.2. Inner Detector

The Inner Detector (ID) is the innermost detector surrounding the beam pipe and consists of three independent and complementary tracking systems. Its purpose is to accurately measure the tracks of charged particles. Charged particles can be detected by ionisation when passing through a medium, or by the production of photons as Cherenkov radiation, scintillation or transition radiation. From the measured tracks, the direction of motion of the particles and in combination with the magnet system (see Section 3.2.5), their momenta can be determined. Ad-

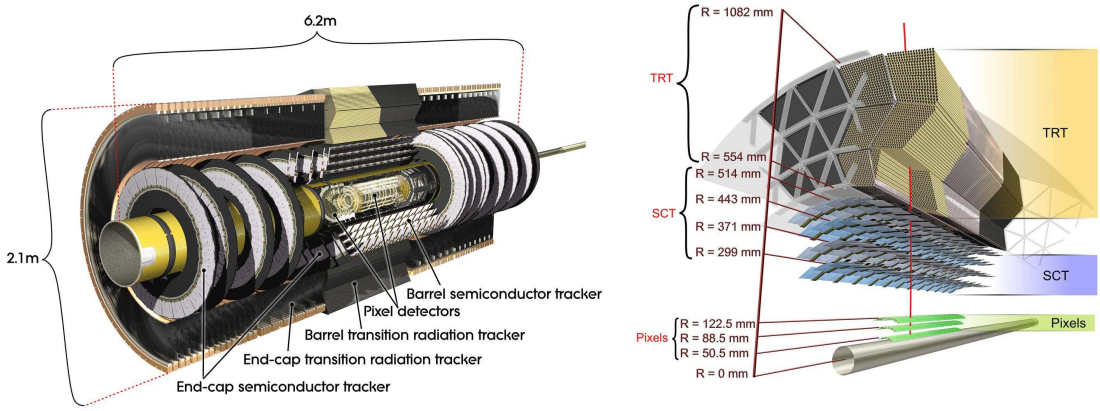


***Figure 3.5.:*** The ATLAS Inner Detector consisting of the Pixel Detector, the Silicon Microstrip Tracker and the Transition Radiation Tracker (left). Additionally, the relative distances to the beam pipe of each detector component are shown (right). Taken from [91].

ditionally, if the tracks are measured with adequate accuracy, the vertices, the positions where the particles originate from, can be determined.

The innermost component is the Silicon Pixel Detector, surrounded by the Silicon Microstrip Tracker (SCT) and followed by the Transition Radiation Tracker (TRT), as shown in Figure 3.5. The Pixel Detector SCT cover the region $|\eta| < 2.5$, while the TRT covers only $|\eta| < 2.0$. In the barrel region, the detector components are arranged in concentric cylinders around the beam axis, while in the endcap region they are arranged in disks perpendicular to the beam axis.

The Pixel Detector has the highest granularity, needed for the vertex detection. It consists of three layers in the barrel and in the endcaps, with a minimal pixel sensor size of $50\,\mu\text{m} \times 400\,\mu\text{m}$ in $r$-$\phi \times z$. The intrinsic accuracies in the barrel (endcaps) are $10\,\mu\text{m}$ in $r$-$\phi$ and $115\,\mu\text{m}$ in $z$ ($r$). In total, 80.4 million pixels are installed and connected to the readout electronics via bump bonding techniques, leading to the same number of readout channels.

The SCT consists of four coaxial cylindrical double layers in the barrel and nine disks in each endcap. These are arranged such that a straight track with $|\eta| < 2.5$ crosses at least four modules, giving four space-point measurements with two hits each. Each silicon microstrip detector has 780 strips with a mean pitch of $80\,\mu\text{m}$. In the barrel, the set of strips of each double layer are rotated by (40 mrad) against each other, where one set of strips is parallel to the beam axis, allowing

to do stereo measurements of both coordinates. In the endcaps, the detectors are constructed in a similar way, but with one set of strips being aligned radially. The intrinsic accuracies in the barrel (endcaps) are 17 $\mu$m in $r$-$\phi$ and 580 $\mu$m in $z$ ($r$). In total, the SCT has 6.3 million readout channels.
The TRT is a combination of a transition radiation detector and a straw tracker. It is made of gaseous straw tubes with 4 mm in diameter, filled with an ionisable gas, $Xe/CO_2/O_2$. Typically, 36 hits per track are expected, providing an intrinsic accuracy of 130 $\mu$m in $r$-$\phi$. In combination with the other parts of the ID, a robust pattern recognition and high momentum resolution is achieved. The straw hits contribute significantly because the lower spatial resolution is compensated by a large number of hits and the long lever arm. Additionally, the TRT detects transition radiation, photons created in a radiator between the straws providing electron identification capability.

### 3.2.3. Calorimeters

The ATLAS calorimeter system is shown in Figure 3.6. It consists of an electromagnetic calorimeter (ECal) and different hadronic calorimeters (HCal) and covers the region up to $|\eta| < 4.9$. All ATLAS calorimeters are sampling calorimeters using different materials. The innermost calorimeter in the barrel as well as in the endcaps is the liquid argon electromagnetic calorimeter (LAr ECal), which is designed to detect electromagnetically interacting particles, in particular electrons and photons, and measure their energy deposition. In the barrel, the LAr ECal is surrounded by the Tile calorimeter (TileCal) using scintillating tiles as active component, while in the endcaps the hadronic endcap calorimeter (HEC) and the forward calorimeter (FCal) are installed, both using Ar as active material. In analogy to the ECal, the HCal detects and measures the energy of hadronic jets, which are initiated by quarks or gluons.
From the energy depositions in the calorimeters, conclusions about the energy of the initial particles can be drawn. The underlying physics processes are bremsstrahlung and $e^+e^-$-pair production, but also ionisation and Compton scattering at lower energies [14, 92]. In general, the relative energy resolution of the calorimeters can be parametrised in three terms with different scaling behaviour

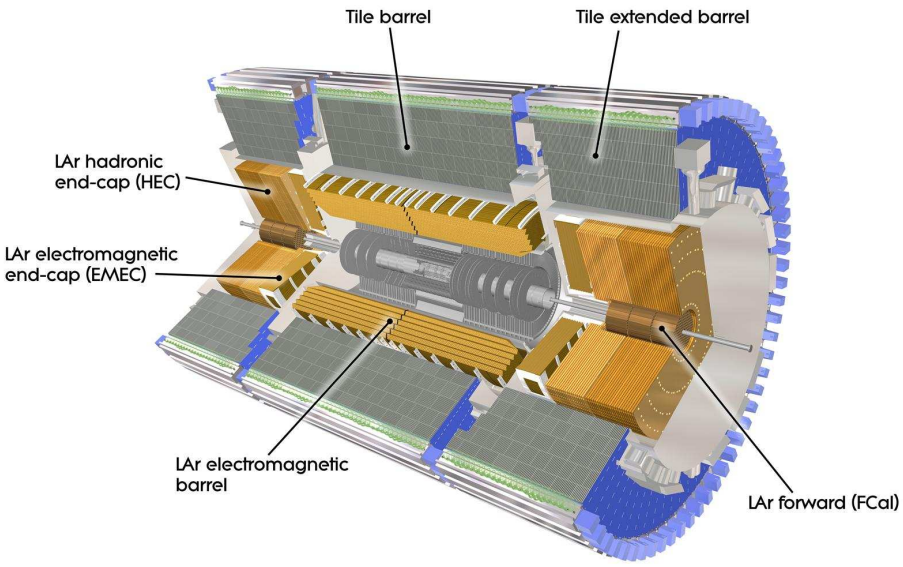


***Figure 3.6.:*** The ATLAS calorimeters consisting of the barrel and endcap electromagnetic calorimeter, the Tile calorimeter, the hadronic endcap calorimeter and the forward calorimeter. Taken from [91].

with respect to the energy $E$

$$\frac{\sigma(E)}{E} = \frac{a}{\sqrt{E}} \oplus \frac{b}{E} \oplus c, \tag{3.6}$$

where $\oplus$ stands for the quadratic sum, $x \oplus y = \sqrt{x^2 + y^2}$. The parameter $a$ describes the intrinsic stochastic fluctuations in the number of particles produced in the shower process, the parameter $b$ describes the noise and parameter $c$ incorporates different systematic uncertainties, e.g. detector non-uniformities, incomplete shower containment or calibration uncertainties.

In order to ensure a good energy measurement as well as to prevent the particles from reaching the muon system (*punch-through*), the calorimeters have to provide a good containment for the electromagnetic and hadronic showers. Hence, the thickness of the ECal is $\geq$ 22 radiation lengths[1] ($X_0$) in the barrel and $\geq 24\, X_0$ in the endcaps. For the HCal, the thickness amounts to 9.7 interaction

[1]The radiation length $X_0$ is defined as the characteristic length after which the energy of an high-energetic electron is reduced by a factor of $1/e$ due to Bremsstrahlung, or 7/9 of the mean free path for $e^+e^-$-pair production of high-energetic photons, respectively.

lengths[2] ($\lambda$) in the barrel and about $10\,\lambda$ in the endcaps. Together with the large $\eta$-coverage, this thickness ensures a good $E_T^{miss}$ measurement, which, amongst others, is important for SUSY searches.
The LAr ECal, situated next to the solenoid magnet, consists of accordion-shaped Kapton electrodes and lead absorber plates and uses LAr as active medium. Electromagnetically interacting particles create showers when passing through the detector, which ionise the LAr. The latter is measured and the energy of the initial particle can be calculated. Like the ID, the ECAL is divided into a barrel part and two endcap parts. In the barrel, the region up to $|\eta| < 1.475$ is covered and in the endcaps, particles in the range $1.375 < |\eta| < 3.2$ can be measured. The highest granularity of the ECal is in the same $\eta$ region that is covered by the ID, to provide a precise measurement of the electron and photon energy.
The TileCal is placed directly outside the ECal and uses steel as absorber and scintillating tiles as active material. It covers the region up to $|\eta| < 1.7$ and has a slight overlap with the HEC, which covers the range $1.5 < |\eta| < 3.2$. The HEC uses copper plates interleaved with LAr as active material.
The FCal covers the region closest to the beam pipe with $3.1 < |\eta| < 4.9$ and consists of three modules in each endcap. The first is made of copper and LAr as active material and is optimised for electromagnetic measurements, while the other two are made of Tungsten and LAr as active material to measure predominantly hadronic interactions.
In total, all calorimeter systems have roughly $1.9 \cdot 10^5$ readout channels. There are two different readout paths: One with coarse granularity for the Level 1 trigger (see Section 3.3.1) and the other with full granularity used by the High-Level Trigger and the offline reconstruction.

### 3.2.4. Muon Spectrometer

The ATLAS muon spectrometer (MS) is designed to detect muons, which pass through all other detector components depositing only a small amount of energy. Muons produced at the LHC are in the GeV-TeV regime, thus, they are minimum ionizing particles (MIP) [14, 92]. All other detectable SM particles are stopped in the calorimeters, except for accidental punch-through. Besides the muon identifi-

[2] Nuclear interaction length is the mean path length required to reduce the numbers of relativistic charged hadrons by the factor $1/e$ as they pass through matter.

cation, the muon momentum and charge is determined by measuring its trajectory bent by the magnetic field (see Section 3.2.5) in tracking chambers. Additionally, the muon spectrometer is also designed to trigger on muons utilizing specialised trigger chambers. For these purposes, four different detector technologies are employed. Monitored Drift Tubes (MDTs) and Cathode Strip Chambers (CSCs) are used for precision spatial measurements. The triggering is done by Resistive Plate Chambers (RPCs) and Thin Gap Chambers (TGCs), because they have a good time resolution. As can be seen in Figure 3.7, they are organised in three concentric cylindrical layers in the barrel at approximately 5, 7.5 and 10 m from the IP and in large wheels, perpendicular to the beam pipe, in the endcap region at distances of 7.4, 10.8, 14 and 21.5 m from the IP.

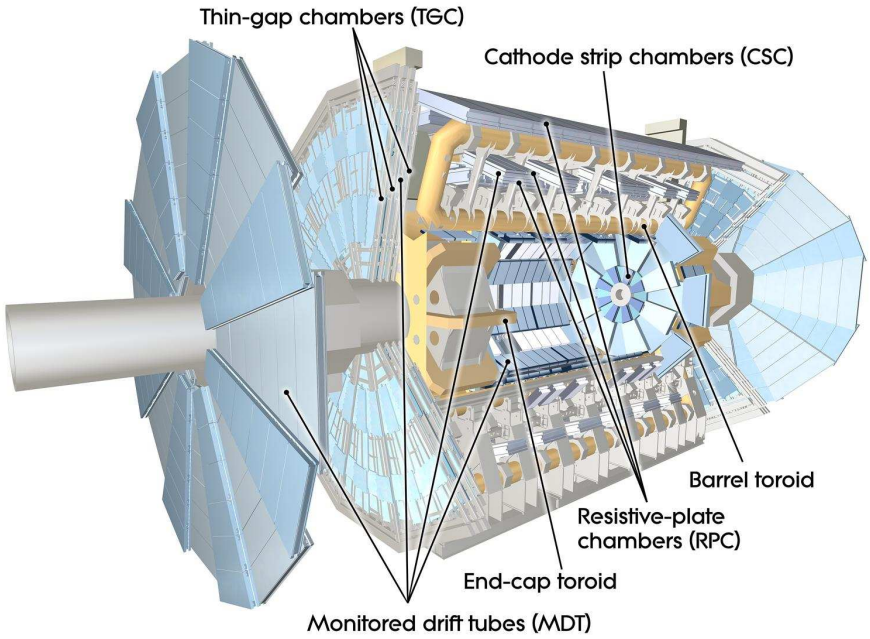


***Figure 3.7.:*** The ATLAS muon system consisting of the Monitored Drift Tubes, the Cathode Strip Chambers, the Resistive Plate Chambers and the Thin Gap Chambers. Taken from [91].

The driving performance goal for the muon spectrometer is a standalone transverse momentum resolution of approximately 10% for a 1 TeV muon, which translates into a resolution of 50 $\mu$m for the sagitta of the track. To achieve this high spatial resolution, three layers (stations) of MDTs are installed in the barrel and endcaps, covering $|\eta| < 2.7$ (2.0 for the innermost station). The MDTs consist

of three to eight layers of pressurised drift tubes per chamber and achieve an average resolution of about 80 $\mu$m per tube, or about 35 $\mu$m per chamber. In the innermost layer station of the forward region $2.0 < |\eta| < 2.7$, the MDTs are complemented by the CSCs, which have a higher rate capability needed so close to the beam pipe. The CSCs are multiwire proportional chambers, with cathodes segmented into strips in the direction orthogonal to the wires. From the induced charge distribution, the coordinates in the bending ($r$-$z$) plane and transverse plane can be measured with 40 $\mu$m and 5 mm resolution, respectively. Additionally, a good time resolution of 7 ns is achieved.

To achieve the sagitta resolution quoted above, the locations of the MDT wires and the CSC strips has to be known very precisely. For this purpose, an optical alignment system monitors the positions of the MDT chambers relative to each other. Track-based alignment algorithms are used in addition to determine the global position and to improve the sagitta accuracy.

The trigger chambers are used to differentiate between muons from different bunch crossings (the bunch crossing interval of 25 ns sets the required timing resolution). The trigger chambers have a time resolution of 1.5-4 ns (at cost of spatial resolution). The RPCs are installed in the barrel, covering a range of $|\eta| < 1.05$, and the TGCs in the endcap region covering $1.05 < |\eta| < 2.7$ (2.4 for triggering). They are also used to measure the muon coordinate in the direction orthogonal to that determined by the precision chambers. The RPCs are gaseous parallel electrode-plate detectors, while the TGCs are multiwire proportional chambers.

The nominal spatial and time resolutions of the different muon chamber technologies are compared in Table 3.2.

| Resolution | MDT | CSC | RPC | TGC |
|---|---|---|---|---|
| $z/r[\mu\text{m}]$ | $35(z)$ | $40(r)$ | $10^4(z)$ | $(2\text{-}6) \cdot 10^3(r)$ |
| $\phi$[mm] | - | 5 | 10 | 3-7 |
| $t$ [ns] | - | 7 | 1.5 | 4 |

***Table 3.2.:*** Comparison of spatial ($z$, $r$ and $\phi$) and time ($t$) resolution of the muon spectrometer technologies. The numbers are taken from [89] and may differ from the resolution actually achieved.

The continuous $\eta$ coverage of the muon chambers has a gap at $\eta \approx 0$ to allow for cables and service outlets for the inner detector systems. Additional gaps in acceptance occur due to the detector feet and cables. In these regions the detector is blind to muons.

### 3.2.5. Magnet System

The trajectories of charged particles are bent if a magnetic field perpendicular to their direction of motion is present. The curvature of the tracks then depends on the strength of the magnetic field and on the particle's momenta. Thus, in the presence of a known magnetic field $B$, the momentum $p$ of a particle (with charge $q$ in terms of the electron charge magnitude $e$) can be measured via

$$p = 0.3 \frac{\text{GeV}}{\text{Tm}} \cdot qBr, \tag{3.7}$$

where $r$ is the bending radius of the particle's trajectory, determined from the sagitta of the track. The momentum resolution $\sigma_p$ for a track measured at $N$ equidistant points over a length $L$ with a spatial hit resolution of $\sigma_x$ is given by the Glueckstern formula [93]

$$\frac{\sigma_p}{p} = \frac{\sigma_x p}{0.3BL^2} \sqrt{\frac{720}{N+4}}. \tag{3.8}$$

Hence, besides a good spatial resolution and preferably large lever arm, a strong magnetic field is needed for high precision momentum measurements. In the ATLAS detector, this is achieved by two magnets. The solenoid magnet provides an axial magnetic field of 2 T for the ID. It is located between the ID and the LAr ECal. For the muon chambers, a system of three toroidal magnets each consisting of eight superconducting air-core coils provides the magnetic field. The field strength varies from 0.15 to 2.5 T in the barrel, and from 0.2 to 3.5 T in the endcap region, depending on $r$ and $\phi$. The light and open structure of the toroidal magnets is needed to minimise multiple scattering effects, which are unwanted because they deteriorate the determination of the initial direction of motion of the muon and also its momentum resolution.

The transverse momentum resolution of the ID and MS can be parametrised as

$$\frac{\sigma(p_T)}{p_T} = \frac{a^{MS}}{p_T} \oplus b \oplus c \cdot p_T, \tag{3.9}$$

where the parameter $a^{MS}$ describes the uncertainties for muons due to energy loss in the calorimeter material (only relevant for the MS momentum measurement), the parameter $b$ is related to multiple scattering and $c$ parametrises the intrinsic resolution (cf. Equation 3.8) [94].

## 3.3. The ATLAS Trigger and Data Acquisition System

At the LHC design luminosity, the proton-proton interaction rate is in the GHz regime corresponding to a data rate in the order of 1 PByte/s (due to the high resolution of the detector components and the large amount of readout channels). Current storage systems can only handle data rates of about 300 MByte/s. Additionally, only a small fraction of the collisions are useful for physics analyses. Hence, the ATLAS trigger system was designed to reduce the initial data rate by several orders of magnitude to manageable output rates of $\mathcal{O}(200\,\text{Hz})$. Figure 3.8 shows the expected cross-sections and event rates for several processes (SM and beyond) at the LHC at design luminosity and centre-of-mass energy. For comparison, the maximum output rate of the trigger is also shown. For example, the predicted Higgs/SUSY production lies in the mHz regime, while the well-understood $W^{\pm}/Z^0$ boson production lies in the kHz regime. These differences in the rate make the selection of "interesting" events, which may originate from rare, barely understood SM or non-SM processes, a crucial task. In general, events with one or more high $p_T$ leptons and/or jets are interesting.

In order to decide during data-taking (in the following called "online") which events should be retained for physics studies, ATLAS uses a three-level trigger system, where each trigger level refines the decision of its predecessor [96–98]. A general overview of the ATLAS trigger system and the Data Acquisition (DAQ) System is shown in Figure 3.9 and is described in the following, with a focus on the muon trigger system.

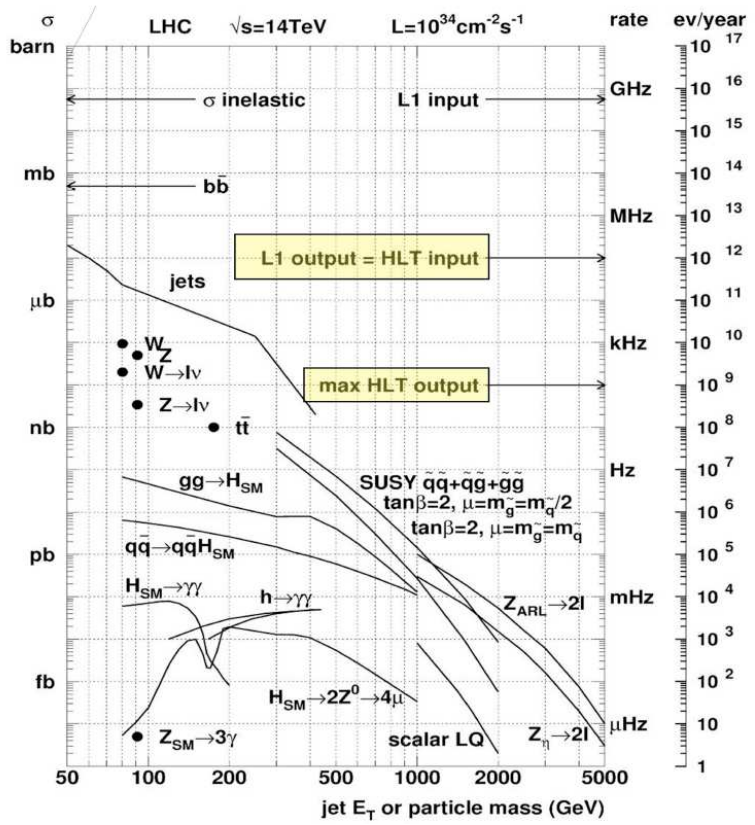


***Figure 3.8.:*** The expected cross-sections and event rates for several processes (SM and beyond) at the LHC at design luminosity and centre-of-mass energy. Taken from [95].
The total interaction rate corresponds to the input of the first level (L1) of the ATLAS trigger system. In addition, the output rate of L1 which is the input rate for the ATLAS High-Level-Trigger (HLT) is indicated as well as the maximum output rate of the HLT, which is the final output rate of the ATLAS trigger system.

### 3.3.1. Level 1 Trigger

The Level 1 (L1) trigger performs the initial event selection based on the information from the calorimeters and the muon trigger detectors. It is completely implemented in hardware, using custom electronics and algorithms, and is integrated into the particular detector components. It works highly parallelised to cope with the fast online event selection.
In the muon trigger chambers (RPC and TGC, see Section 3.2.4), low-$p_T$ ($<$ 10 GeV) and high-$p_T$ muons ($\geq$ 10 GeV) are identified by finding hit coincidences between the different detector layers. Low-$p_T$ muons exhibit smaller bending radii,

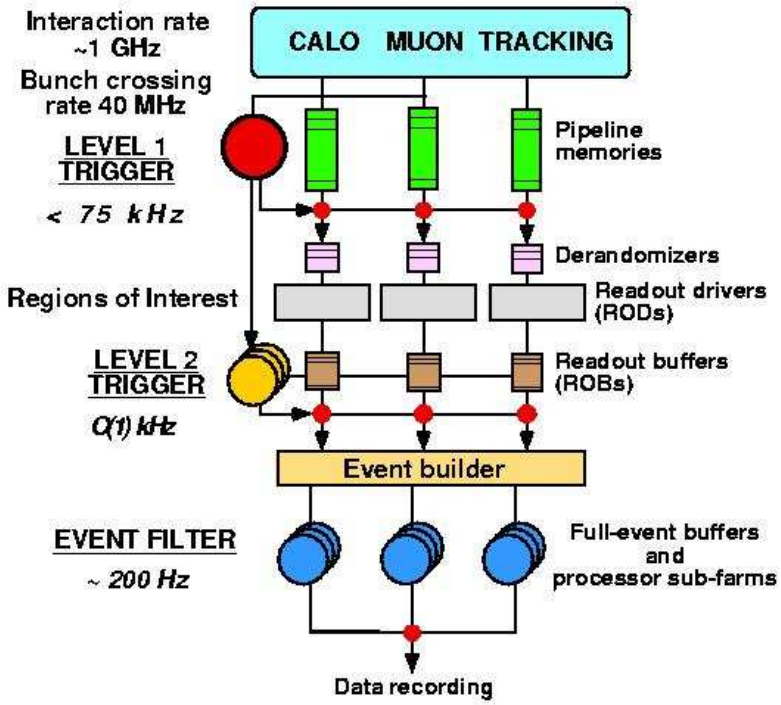


***Figure 3.9.:*** Schematic diagram of the ATLAS trigger and data acquisition system. The three different stages of triggering and the most important components are shown. In addition, on the left-hand side the respective output rates of each trigger level are given. Taken from [99].

thus, they are detected in two detector stations relatively close to each other. In the barrel, the consecutive RPC1 and RPC2 stations[3], while in the endcaps TGC2 and TGC3 are used. This is shown in Figure 3.10. In contrast, the tracks of high-$p_T$ muons are almost straight. Therefore, for high-$p_T$ muons, additional coincidences with the third muon trigger station (RPC3 and TGC1, respectively) are required. Six $p_T$ thresholds can be configured using look-up tables for the size of the coincidence windows, giving an estimate for the momentum. The procedure is described in more detail in [96].

The calorimeter trigger system is designed to identify high-$p_T$ electrons, photons, jets, and large amount of total $E_T$ and $E_T^{miss}$. It uses low resolution information from the calorimeters.

[3]The numbers behind the chamber type, RPC and TGC, denote the station.

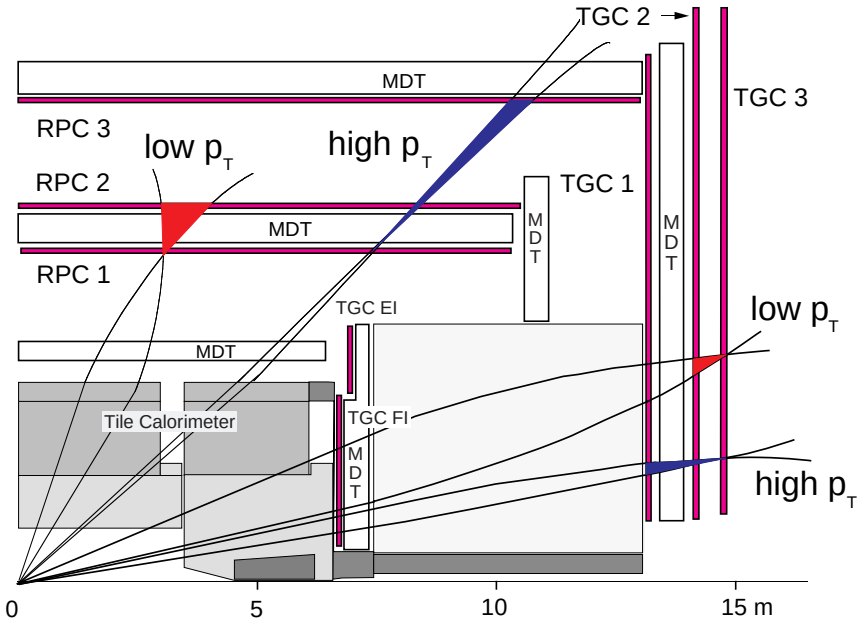


***Figure 3.10.:*** Layout of the ATLAS muon trigger chambers (cross-section in the bending plane, $r$-$z$ plane). Additionally, typical low- and high-$p_T$ muon tracks and the corresponding coincidence windows in the different stations in the barrel (RPC1-3) and in the endcaps (TGC1-3) are shown. Taken from [75].

The L1 trigger decision is computed by the Central Trigger Processor (CTP) with a maximum latency of 2.5 $\mu$s. During this time, the detector data is kept in pipeline memories. Upon an accept signal from the CTP, the data is transferred to the detector specific Read-Out-Buffers (ROBs), where it is kept until it is requested by the other trigger levels. In addition, the L1 trigger defines Regions of Interest (RoIs), which include geometrical coordinates ($\eta$ and $\phi$) and the passed $p_T$-threshold of the object candidates (muons, electrons, tau-leptons and jets). This information is passed on to the next trigger level for further investigations. The designed output rate of L1 is 75 kHz.

### 3.3.2. High-Level Trigger

The Level 2 (L2) trigger and the Event Filter (EF) together constitute the High-Level Trigger (HLT). They are completely software-based and run on dedicated computer farms.

The L2 trigger is seeded by the RoIs defined by the L1 trigger, but can use the full-granularity information from all detector components in the RoIs, including

the ID, the full-granularity calorimeter and the precision muon chamber information. With an increased processing latency of $\mathcal{O}(40\,\text{ms})$, the L2 trigger allows for more complex algorithms being applied to the data received from the ROBs with respect to L1. However, the algorithms to conduct the L2 trigger decision still have to be kept simple and fast. To minimise the average time spent for the computation of the trigger decision, the trigger steering is designed to reject events as early as possible. Additionally, the seeded reconstruction based on RoIs reduces the amount of data which has to be transmitted to about 2 % of the full data of the event. The L2 trigger reduces the event rate to about 3 kHz.
The EF has access to the complete event data with full granularity from all detector systems, collected from the ROBs. Therefore, an event reconstruction using similar algorithms as in the case of offline reconstruction is performed, accessing also calibration and alignment information from databases. In addition, more complex algorithms, such as vertex reconstruction and track fitting, are performed. These reconstructed objects have to fulfill predefined criteria that are more complex than for the L1 trigger. By this, the event rate is reduced to roughly 200 Hz, with an average latency of the order of seconds. Events which pass the EF are stored and can be analyzed offline.

### 3.3.3. Trigger Implementation and Terminology

The information used by the CTP to conduct the L1 trigger decision is given in terms of multiplicities of candidates for physics objects (like muons or electrons), called trigger elements, together with the passed $p_T$-threshold. The given multiplicities are compared with multiplicity requirements/conditions using look-up tables. Examples for such conditions are:

**MU10**: Muon on L1 with $p_T > 10\,\text{GeV}$,
**J20**: Jet on L1 with $E_T > 20\,\text{GeV}$.

Each trigger condition leads to a value "yes" or "no", which can be combined (logical `AND`) to more complex trigger items. The latter represent the signatures the L1 trigger decision is based on, e.g. a muon with $p_T > 10\,\text{GeV}$ `AND` an electron with $p_T > 15\,\text{GeV}$. The final L1 trigger decision is the logical `OR` of all defined trigger items. The trigger decisions of all trigger items are sent to the HLT.
In each of the HLT stages (L2 and EF), feature extraction and hypothesis algo-

rithms are executed. The former perform the time-consuming unpacking of the data and the trigger object reconstruction, while the latter conduct the trigger decision based on selection criteria applied to the reconstructed trigger objects. For muon triggers, these selection criteria comprise: track quality, isolation and measured $p_T$. The step-by-step execution of the different trigger algorithms is called *trigger chain*, consisting of different intermediate trigger signatures, similar to trigger items on L1. The successive trigger algorithms refine the intermediate trigger signatures in the course of a trigger chain. Examples for these trigger signatures are:

**mu18**: Muon on L2/EF with $p_T > 18\,\text{GeV}$,
**j50**: Jet on L2/EF with $E_T > 50\,\text{GeV}$.

Different trigger chains are defined to select various physics signatures, e.g. "at least one electron with 22 GeV" or "at least two muons with at least 10 GeV". These trigger chains bear the name EF_e22 and EF_2mu10. The general notation of trigger chains is

(Trigger Level)_(Multiplicity if > 1)(Trigger Type)(Threshold Value)_(Postfix)

where the trigger type is an abbreviation (in uppercase letters for L1 and lowercase letters for L2 and EF) stating the type of the trigger, e.g. MU/mu for muons. The threshold value is normally given in GeV and the postfix specifies additional trigger features, e.g. "loose" or "tight" for variants of the same trigger chain.
The value of the threshold given in the name of a trigger chain is the nominal threshold and the actual trigger thresholds can be slightly different. For muon triggers, the $p_T$-thresholds are $\eta$-dependent and a few hundred MeV below the nominal threshold. The exact thresholds for the muon triggers studied in this thesis are summarised in Appendix B.
Often the terms "trigger" and "trigger chain" are used interchangeably, as in this thesis. Trigger chains which select events based on signatures with more than one reconstructed object are call *multi-object* triggers. Trigger chains which select events based on signatures with only one reconstructed object are call *single-object* triggers[4]. As an example, a particular di-muon trigger chain is shown in Figure 3.11. An extensive menu of trigger chains run in parallel.

[4]Single-object triggers can also select events with more than one reconstructed object, but their decision is based on the reconstructed objects individually.

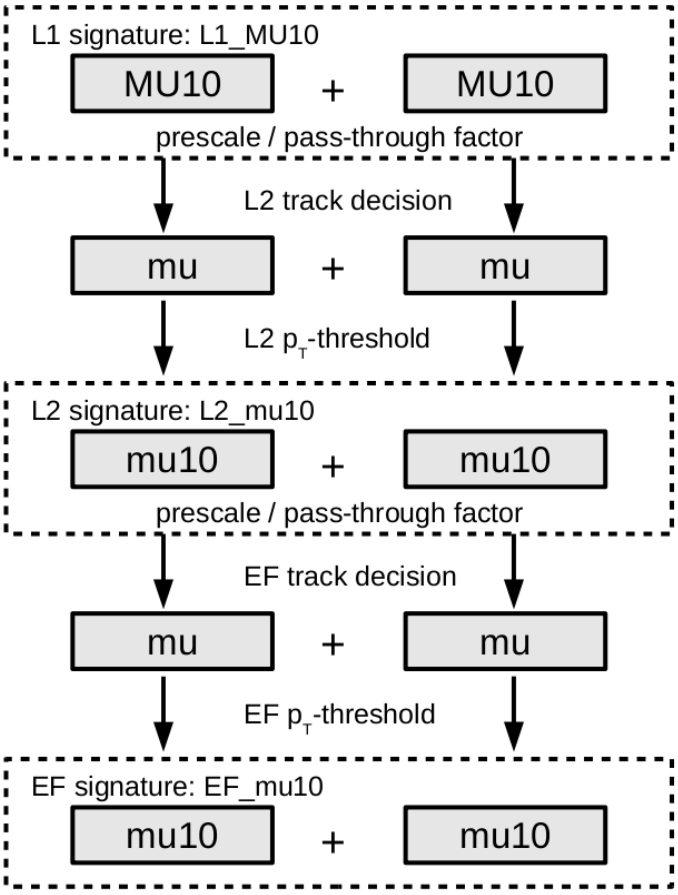


***Figure 3.11.:*** Schematic block diagram of the EF_2mu10 trigger chain. At L1 the trigger chain requires the trigger item "L1_2MU10" (consisting of two "MU10" trigger elements). On each trigger level a decision is made based on the tracks and the estimated $p_T$, leading to the trigger signatures L2_2mu10 and EF_2mu10, respectively. The track and $p_T$-threshold requirements are applied to both trigger elements (the "+" indicates a logical `AND`). If one of the intermediate trigger signatures did not fulfill the requirements of the trigger chain, e.g. one muon object candidate misses the $p_T$-threshold, the trigger chain would stop and the event would not be accepted by the trigger.

Trigger chains can be modified by *prescale* or *pass-through* factors. A prescale factor of $N$ means that on average only one out of $N$ events in which the trigger would have fired is accepted. This is achieved by holding back each event passing the L1 trigger with a probability of $(N-1)/N$ without running the corresponding L2/EF trigger chain. A pass-through factor of $N$ means that on average one of $N$ events is passed to the next trigger level regardless of the actual trigger decision. Prescale and pass-through factors can be applied at every trigger level. Prescale factors are used to adjust the rate of a particular trigger, while pass-through fac-

tors can be used to obtain samples of rejected events, which would have been lost otherwise. In contrast to the trigger chains and their $p_T$ thresholds, the prescales can be changed during-data taking.
A trigger chain can be run in *rerun mode*. This means that the trigger decision at EF (L2) is conducted regardless of the trigger decisions (and prescales) of the previous levels if the event is accepted by another trigger on EF (L2). The rerun mode allows to study the trigger decisions of prescaled trigger chains.
Since the conditions of the detector and the configuration of the trigger are not constant over time, this information is saved in the ATLAS Conditions Database (COOL) database [97]. Additionally, the instantaneous luminosity measured with dedicated forward detectors [5] and the trigger counts for every trigger chain are also stored. The trigger counts are the number of events accepted by a trigger chain in a certain interval of time. This information can be used offline in data analyses. For example, from stored detector information "Good Runs Lists" (GRLs) can be created [100]. These lists define which data was recorded under good and stable conditions and can therefore be used for physics analyses.
ATLAS uses an inclusive streaming model. This means that every event which has been accepted by one or more EF triggers is written to the data streams associated to the triggers. There are four streams for storing events for physics analysis, called `Egamma` (for photon and electron triggers), `Muons` (for muon triggers), `JetTauEtmiss` (for jet, tau-lepton and $E_T^{miss}$ triggers) and `MinBias` (for minimum-bias and random triggers, which are not discussed in this thesis).
The total trigger rate on EF level is limited by the maximum bandwidth that the storage elements can handle. Each of the streams mentioned above is assigned a certain fraction of the maximum trigger rate. This assigned fraction can be changed dynamically by setting prescales.

[5] There are groups of special detectors, situated relatively far away from the IP at very high pseudorapidities. These detectors bear the names LUCID, ZDC and ALFA and are located $\pm 17\,\mathrm{m}$, $\pm 140\,\mathrm{m}$ and $\pm 240\,\mathrm{m}$ away from the IP. Their purpose is the online measurement of the instantaneous luminosity.

# 4. Trigger Rates and Efficiencies

In this chapter, the basic concepts of triggers at collider experiments are explained. After a short general overview of triggers, emphasis is put on the trigger rates and trigger efficiencies. Both quantities are needed for the studies presented in Sections 5 and 6.

## 4.1. Trigger Concepts at High Energy Physics Collider Experiments

In general, triggers at high energy physics collider experiments have the primary goal to reduce the immense data rate, while selecting potentially interesting events for storage and further analysis from a large amount of data. This has been motivated in Section 3.3 for the ATLAS Trigger System, which reduces the event rate of the ATLAS detector by several orders of magnitude.
Ideally, a trigger rejects all uninteresting events while it keeps the interesting ones at a high efficiency during data taking. For this task, trigger systems at high energy physics collider experiments usually comprise different more or less independent triggers running in parallel, for instance triggers for muons, jets or $E_T^{miss}$. A well-designed trigger system is required to have the following properties (in no particular order):

- Robustness: In order to ensure a reliable and stable operation, technical problems in one part of the trigger system should not lead to a crash of the whole trigger system or parts of it.

- Speed: To meet the time constraints for the online decision making, the trigger has to take decisions quickly.

- Simplicity: Defining the triggers in such a way that their decisions are easy to comprehend simplifies the commissioning and maintenance of the trigger system.

- Inclusiveness: In general, the data taken with a trigger should be suitable for a variety of analyses, and not only for one specific analysis. To achieve this, the selection criteria which a trigger applies online to the data should be rather general. Additionally, this strategy helps to avoid missing unexpected but interesting events.

- Redundancy: Redundancy is important with respect to online data taking as well as offline data analysis. During data taking, it may be necessary to disable a particular trigger because it causes problems, e.g. due to a misconfiguration, or it just exceeds a certain output rate. For trigger studies, it is important that a particular class of events is not only recorded by one specific trigger. At least a small fraction of events that a trigger is intended to select should always be recorded by additional triggers. This redundancy allows for cross-checks and can be exploited for trigger efficiency measurements (see Section 4.3.2). Normally, the total output rate of the trigger system is not increased substantially by this redundancy.

- Efficiency: A trigger should efficiently select the events that it is intended to select from the bulk of events because the events that were not triggered events are not recored. Therefore, the more efficient a trigger is, the more significant results can be deduced from the same amount of (input) data.

Most of the listed properties are difficult to quantify. In general, the performance of a trigger is quantified in terms of its output rate and its efficiency. In this context, the trigger efficiency is defined as the fraction of triggered events that the trigger is intended to select (see Section 4.3). Usually, more efficient triggers come along with higher rates and vice versa. In the extreme cases, a trigger would accept every event (maximal rate and 100 % efficiency) or no event (zero rate and 0 % efficiency). Therefore, a trigger has to be optimised by finding the best working point as a compromise between a reasonable rate and efficiency. This is discussed in Section 6 for different muon triggers using the example of a search for SUSY.

The maximal allowed trigger rates are mainly defined by experimental constraints, while they do not directly affect the physics analyses. On the contrary, the trigger efficiencies and in particular their uncertainties have a direct impact on most measurements. For example, discoveries of new particles as well as measurements of cross-sections and particle properties can only be correct with a precise knowledge of the trigger decisions. Hence, the determination and the application of trigger efficiencies and their uncertainties is a crucial task.
In the context of trigger efficiency measurements, two types of errors have to be considered:

- Type I errors: rejecting events that should have been accepted (*(in)efficiency*)
- Type II errors: accepting events that should have been rejected (*fake efficiency*)

This thesis focuses on muon triggers at the ATLAS detector, for which the muon fake efficiency is rather small due to the clean signal of muons in the detector (cf. Section 3.2). Therefore, the fake efficiency is not considered in this thesis. Nevertheless, there are methods to determine the fake efficiency, e.g. discussed in [101].
In the following, trigger rates and efficiencies are discussed in more detail using the example of muon triggers.

## 4.2. Trigger Rates

The maximum data rate of the Trigger and Data-Acquisition System defines the limit for the maximum output rate of the ATLAS Trigger System (cf. Section 3.3). Each trigger chain is assigned a fraction of this maximum rate, which determines the composition of the total recorded sample.

The trigger rates presented in this thesis are based on the information stored in the COOL database (cf. Section 3.3.3), which holds, among others, information about the trigger counts and luminosity that was measured online. The package `TrigCostPython` [102] is used to read out the information from the COOL database.
The data taken with the ATLAS detector is subdivided into data-taking *periods*,

each spanning a certain interval of time. Usually, a new data taking period indicates that there has been a major change with respect to the preceding period with non-negligible impact on the detector performance. The periods consist of one or more physics *runs*. A physics run usually starts after the protons have been accelerated to their nominal energy and the beams are stable and ends several hours later when the beams are dumped. The smallest blocks of data are the so-called luminosity blocks (LBs) with a nominal length of one minute (for 2011 data-taking), into which each run is subdivided. Over the time of one LB the data-taking conditions are assumed to be stable. The conditions of the trigger are also stable during one LB because changes of the trigger configuration, e.g. of prescales, can only be made at the beginning of every new LB. Every LB usually contains several thousands of *events*, which is the data from all proton-proton collisions of the same bunch crossing.

Since this thesis focuses on muon triggers, the trigger rates of the EF_mu18 trigger are shown exemplarily in the following. This trigger is a single muon trigger with a $p_T$-threshold of roughly 18 GeV at EF/L2 and 10 GeV at L1. The exact configuration of all muon triggers used in this thesis is summarised in Appendix B. Until the end of July 2011, the EF_mu18 trigger was the lowest unprescaled [1] single muon trigger. Hence, it has the highest rate among the muon triggers.

An example of a trigger rate is given in Figure 4.1, where the output rate of the EF_mu18 trigger as a function of time and luminosity is shown for one run. This shown run is chosen because it is rather long such that an adequate range of time and integrated luminosity is covered. Every point in the plot corresponds to the rate in one LB, i.e. averaged over one LB. The effect of applying a GRL (cf. Section 3.3.3) can also be seen.

The rate as a function of time decreases exponentially after stable beam and detector conditions have been achieved until the beams are dumped. Some of the LBs of this run have also been masked by the applied GRL, because the detector conditions in these LBs do not fulfill the predefined requirements. The GRL used throughout this thesis is provided by the ATLAS SUSY Working Group [103] and can be found in Appendix D. In this appendix, additional information about the different data-taking periods is given, too.

The rate as a function of luminosity shows a linear behaviour over the range cov-

[1] The term 'lowest unprescaled trigger' means the trigger with the lowest $p_T$-threshold which is unprescaled.

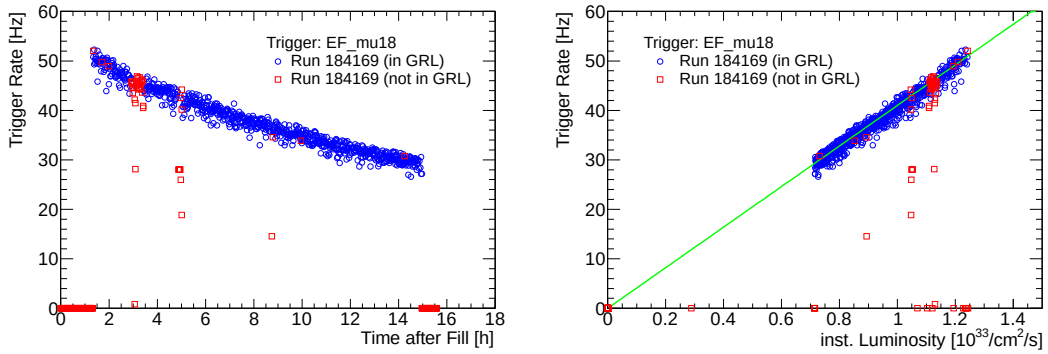


(a) as a function of time (b) as a function of inst. luminosity

***Figure 4.1.:*** Output rate of the EF_mu18 trigger for run 184169 from period 2011H as a function of time (a) and instantaneous luminosity (b). Luminosity blocks which have been masked by the GRL are indicated as red squares, while the "good" luminosity blocks are shown as blue circles. The trigger rate depends approximately linearly on the instantaneous luminosity, indicated by the green line.

ered by this run, about 0.7-1.3 $\cdot 10^{33}\,\mathrm{Hz/cm^2}$, as indicated by the green line. In fact, this behaviour is observed in a larger luminosity interval, as can be seen in Figure 4.2, which allows for extrapolation to higher luminosities. A direct proportionality between the single muon trigger rates and the luminosity is expected, because the centre-of-mass energy and, therefore, the cross-sections for processes resulting in muons in the detector, are constant. Hence, the luminosity is proportional to the number of interactions taking place in a given period of time. The probability that two interactions at the same bunch crossing produce muons, which can issue the trigger, is negligible, resulting in this linearity. This linearity is for example not the case for $E_T^{miss}$ trigger due to pile-up [104] leading to non-linear dependencies.

For period 2011K, the maximum EF_mu18 trigger rate was roughly 80 Hz, which is about one-third to half of the maximum allowed EF output rate (cf. Section 3.3). A similar fraction was assigned to the lowest unprescaled single electron trigger. Therefore, the output rate of the trigger system reached its bandwidth limit, such that the EF_mu18 trigger was prescaled if needed [2] (above roughly $2 \cdot 10^{33}\,\mathrm{Hz/cm^2}$). In that case, another single muon trigger was the lowest unprescaled trigger, namely EF_mu18_medium with a higher $p_T$-threshold on L1

[2] In period 2011J, the EF_mu18 trigger was prescaled the first time due to bandwidth limitations.

than EF_mu18 (see Appendix B for trigger configuration). For higher instantaneous luminosities, the EF_mu18_medium trigger will also reach the bandwidth limitations.
The running conditions are not the same in all periods, leading to a deviation in the slope of the muon trigger rates as a function of luminosity. This can clearly be seen in the kink between period 2011E and 2011F, presumably caused by a shorter bunch spacing (from 75 ns to 50 ns) ramping up the rates at L1 due to out-of-time pile-up.

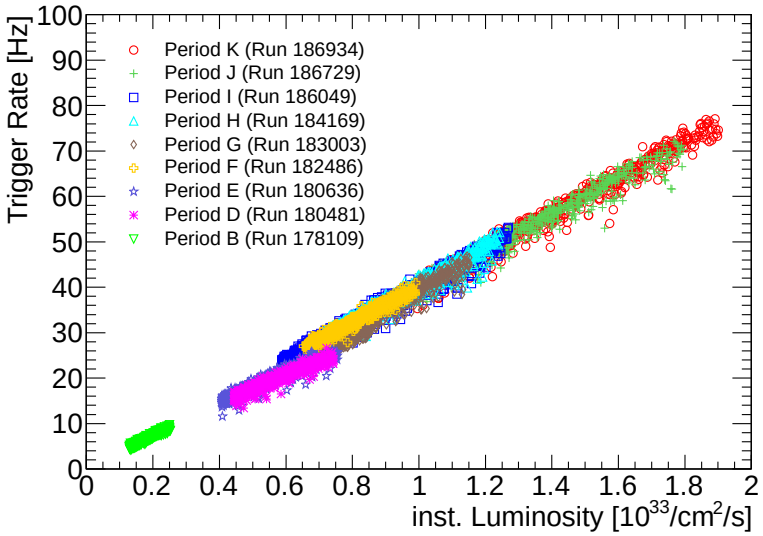


***Figure 4.2.:*** Output rate of the EF_mu18 trigger for different periods in 2011 as a function of instantaneous luminosity. For each period, one particular run is chosen exemplary. In period 2011J and 2011K the EF_mu18 trigger was partly prescaled. To increase the covered instantaneous luminosity range, the rate for the unprescaled luminosity blocks is also shown. The kink between period 2011E and 2011F is commented in the text.

## 4.3. Trigger Efficiencies

Precise knowledge of the efficiency of a trigger and its uncertainties is of particular importance for every analysis which evaluates data filtered by a trigger. Generally speaking, the efficiency of a trigger is the probability that the trigger accepts an event it is intended to accept. It depends on the detector hardware and its software implementation, and has to be determined for every trigger chain individually.

Additionally, it depends on the event properties themselves.
In general, trigger efficiencies can be defined in a variety of different ways, e.g. *event efficiency* or *object efficiency*. The former is the probability of an event issuing the trigger, while the latter is the probability that a certain object, like a muon, issues the trigger. For triggers which are evaluating event variables, like $E_T^{miss}$, this differentiation does not make sense. For events with only one object of interest these two efficiencies are naturally the same, while for events with more than one object of interest not. However, for the latter, the event efficiency can often be approximated by an appropriate combination of the efficiencies of the involved objects. If the object efficiencies are independent from the rest of the event, this approximation is exact. This assumption holds for many cases, such that the approximation works well, e.g. in events with exactly one muon and one electron, which emerge under sufficiently different angles, such that their signatures in the detector do not overlap. If the trigger efficiency $\epsilon_{\text{obj.}}$ of an object is described by sets of parameters $\vec{\alpha}$, the event trigger efficiency $\epsilon_{\text{ev.}}$ for an event with $n$ objects, for which independent object trigger probabilities are assumed, is given by

$$\epsilon_{\text{ev.}}(\vec{\alpha}_1, \ldots, \vec{\alpha}_n) = 1 - \prod_{i=1}^{n} \left(1 - \epsilon_{\text{obj.}}(\vec{\alpha}_i)\right). \tag{4.1}$$

In the following, the term efficiency always refers to object efficiency, if not stated otherwise, and only efficiencies of the full trigger chain (L1, L2 and EF) are considered. Additionally, the trigger efficiencies are defined with respect to offline reconstructed objects, called *offline* objects, in order to decouple the trigger efficiency from the reconstruction efficiency and the geometric acceptance. Hence, the trigger efficiencies can be estimated by the ratio of the number of offline objects that have passed the trigger, $N_{\text{obj.}}^{\text{offline\&triggered}}$, and the total number of offline objects, $N_{\text{obj.}}^{\text{offline}}$:

$$\hat{\epsilon} = \frac{N_{\text{obj.}}^{\text{offline\&triggered}}}{N_{\text{obj.}}^{\text{offline}}} \xrightarrow{N_{\text{obj.}}^{\text{offline}} \to \infty} \epsilon. \tag{4.2}$$

For infinite statistics this estimator $\hat{\epsilon}$ is equal to the true trigger efficiency $\epsilon$. To be able to determine object-wise trigger efficiencies, a matching between the objects reconstructed online by the trigger system, which are called *online* objects, and the respective offline reconstructed objects has to be performed. From the properties of a trigger object, it can be inferred whether this object has issued

the trigger or not. The matching is explained in more detail in Section 4.3.4
The trigger efficiencies are usually parameterised in the relevant offline object variables. A variable is considered to be *relevant* if the trigger efficiency is not sufficiently flat in this variable (taking the dependencies of other relevant variables into account). Usually, a certain trigger is developed to take its decision based on a certain variable. The corresponding offline reference variable is always relevant, like the transverse momentum $p_T$ for the muon triggers. The typical behaviour of trigger efficiencies as a function of their offline reference variable is discussed in detail in Section 4.3.1. In addition, trigger efficiencies often depend on further variables, like the object direction (often given in $\eta$ and $\phi$, cf. Section 3.2.1). The muon trigger efficiencies as functions of their relevant variables are presented in Section 4.3.4. The methods to reliably measure these efficiencies are summarised in Section 4.3.2 and the statistical interpretation of the trigger efficiencies is discussed in Section 4.3.3. The application of trigger efficiencies in physics analyses is discussed in Section 4.3.5. Finally, conditional trigger efficiencies for different muon trigger chains are discussed in Section 4.3.6.

### 4.3.1. Turn-On Curve

The plot of the trigger efficiency as a function of the offline reference variable is often referred to as the *turn-on curve* of that trigger. Ideally, the trigger response resembles a Heaviside function, i.e. below the threshold of the trigger, no object would pass the trigger (efficiency 0 %), while every object above would be accepted (efficiency 100 %). This is the case if the measured online quantity, determined by the trigger, equals the offline reconstructed quantity. However, in general, the online measurement has a worse resolution leading to a smearing of the step function. If a Gaussian error with constant width is assumed for the online measurement, the trigger efficiency as a function of the offline reference is described by a Gaussian error function. However, the resolution of the online measurement usually changes as a function of the offline variable, such that the trigger efficiency deviates from a pure Gaussian error function. This is demonstrated in Figure 4.3 (left), assuming different resolutions of the online measurement, as e.g. the muon momentum resolution has constant, linear, and quadratic contributions (cf. Equation 3.9). If the resolution depends on the offline variable, the turn-on curve is asymmetric.

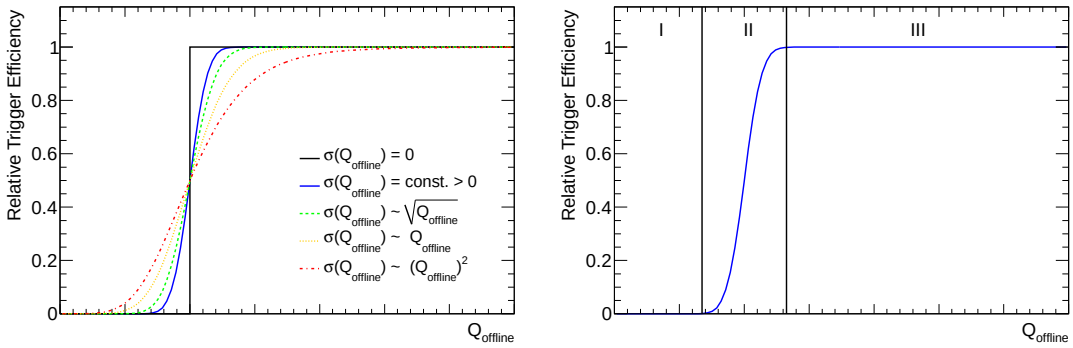


***Figure 4.3.:*** Schematic behaviour of a typical trigger turn-on curve. Left: the relative trigger efficiencies (fraction of the maximum efficiencies) as a function of the offline quantity $Q_{offline}$ for different assumed resolutions $\sigma(Q_{offline})$ of the online measurement with respect to the offline reconstruction. The coefficients for the different resolutions are adjusted, such that the curves do not overlap. Right: trigger turn-on curve resembling a Gaussian error function ($\sigma(Q_{offline}) = \text{const.}$) with region of minimum efficiency (I), turn-on region (II), and plateau region (III).

Three different regions can be identified: region of minimum efficiency, turn-on region, and plateau region. These regions are illustrated Figure 4.3 (right). Depending on the form of the actual trigger efficiency, different definitions for the turn-on region are in use. For muon triggers, the turn-on is very steep such that the trigger efficiency saturates a few GeV above the $p_T$-threshold. The saturation value can be considerable below one (see Section 4.3.4).

### 4.3.2. Methods to Measure Trigger Efficiencies

In the following, an overview of methods for the determination of trigger efficiencies is given. One possibility is to use simulated *Monte Carlo* (MC) pseudo data, where the produced particles, their detector response, and the trigger decisions are simulated. From these MC samples the trigger efficiencies can be determined by direct counting, referred to as *Monte Carlo Counting* method. This method relies on the correctness of the trigger simulation. Therefore, techniques which measure the trigger efficiencies on data are necessary in order to be independent from the correctness of the trigger simulation. These methods are commonly known as *data-driven* techniques.
A counting method on all stored events like for MC pseudo data is not applicable,

because only the events that issued a trigger are stored. In contrast to MC pseudo data, the events that have not been seen by any trigger are not available. Therefore, the trigger efficiency measurement would be biased. The general concept to measure trigger efficiencies on data is to obtain a sample that is biased only to a minimum extend (ideally unbiased). On these samples the trigger efficiencies can be measured by counting, as defined in Equation 4.2.
A sample that is biased only to a minimum extend is obtained by decoupling the event selection from the determination of the trigger efficiencies. Three methods commonly used to achieve this decoupling are explained below. These methods have been discussed in literature, e.g. [105, 106].

- *Tag & Probe* method: This method exploits the fact that for a given two-body decay with kinematic constraints between both decay products, from the observation of one of the decay products, the presence of the other particle can be inferred. In such events one of the particles, which definitively triggered the event, can be used to *tag* the event, while the other particle is the *probe* used to perform the actual trigger efficiency measurement. This method is often used to determine muon or electron trigger efficiencies in decays of $Z^0$ bosons (sometimes also $J/\psi$ or $\Upsilon$ mesons). To obtain a well-defined sample of such decays, a selection cut on the invariant mass of the reconstructed pair of particles is used.

- *Orthogonal Trigger* method: This method exploits the fact that sometimes there are triggers which are, in the ideal case, completely independent of the trigger under study. The orthogonality is often only approximate. For example, the muon trigger decision should in principle be independent from the calorimeter based triggers, like triggers for electrons or jets. Using a *minimum-bias* or *random* trigger to obtain an unbiased sample is a special case of the Orthogonal Trigger method.

- *Bootstrapping* method: This method exploits the fact that the bias introduced by a non-orthogonal trigger as sample trigger can be corrected under certain conditions. The turn-on curve of the sample trigger has to be known to perform the bias correction using Bayes' theorem [107]. This method is not used in this thesis. More details about the application of this method can be found in [104].

In this thesis, the Tag & Probe method and the Orthogonal Trigger method are used to select large samples to measure muon trigger efficiencies. It is known that each of the methods can introduce small biases, therefore it is desirable to measure the trigger efficiencies with more than one method and perform cross-checks to get an estimate for the bias.
The invariant mass requirement in the Tag & Probe method incorporates the probe into the event selection, which can introduce a bias. Additionally, this method assumes that the trigger decisions of the two objects are uncorrelated and thus the trigger efficiency for the probe is independent from the presence of a second object of the same type in the event. Therefore, the Tag & Probe method is essentially only a special case of the Orthogonal Trigger method, with the additional property that fake muons are reduced due to selecting only muons from a certain physics process. The latter allows for comparisons with MC simulations. This is not possible for the Orthogonal Trigger method, because only well-understood processes can be simulated and the composition of the sample collected using orthogonal triggers has to be known.
In general, the trigger efficiency averaged over a certain range of the relevant variables depends on the distribution of these variables in the selected sample and therefore on the method used to obtain the sample. Additionally, the trigger efficiencies can only be determined within the kinematics covered by a given sample. In particular, with the Tag & Probe method using $Z^0 \to \mu\mu$, only muon trigger efficiencies within the covered muon kinematics can be measured. In a similar sense, the Orthogonal Trigger method depends on the employed orthogonal trigger. Different orthogonal triggers select different event topologies.
Very little or no bias is assumed to be introduced by the minimum-bias or random triggers. However, for most studies, these triggers yield too low statics, since most of the events recorded by this type of triggers do not contain signatures that can issue the target trigger (cf. Figure 3.8).

### 4.3.3. Statistical Interpretation of Trigger Efficiency Measurements

While Equation 4.2 gives an estimate for the absolute trigger efficiency with respect to reconstruction, it does not provide a measure for the uncertainty of that quantity. To estimate the statistical uncertainties, a probability density function

for the trigger efficiencies can be derived by modelling the trigger decisions as Bernoulli processes and applying Bayes theorem [107]. This Bayesian approach accounts for the asymmetry of the underlying Binomial distribution the trigger efficiency calculation is based on and is discussed in more detail in Appendix A. Essentially, the probability distribution function for the trigger efficiencies is given by

$$p\left(\varepsilon\right) = A\left(N_{\text{reco}}, N_{\text{reco}}^{\text{triggered}}\right) \cdot \varepsilon^{N_{\text{reco}}^{triggered}} \cdot \left(1-\varepsilon\right)^{N_{\text{reco}} - N_{\text{reco}}^{\text{triggered}}}, \tag{4.3}$$

where $A$ is a normalization factor. An estimator for the absolute efficiency $\hat{\epsilon}$ and asymmetric uncertainties, $\hat{\sigma}^{\text{high}}$ and $\hat{\sigma}^{\text{low}}$, of the efficiency can be defined as:

$$\hat{\varepsilon} = \text{mode}\left(p\left(\varepsilon\right)\right) \tag{4.4}$$

$$\int_{\hat{\varepsilon}-\hat{\sigma}^{\text{low}}}^{\hat{\varepsilon}+\hat{\sigma}^{\text{high}}} p\left(\varepsilon\right) d\varepsilon = 0.6827 \text{ (equivalent to } 1\sigma \text{ region of a Gaussian)}, \tag{4.5}$$

where the sum $\hat{\sigma}^{\text{high}} + \hat{\sigma}^{\text{low}}$ is minimal. The estimator for the absolute efficiency as defined in Equation 4.4 gives the same result as the naive approach in Equation 4.2, which a posteriori justifies the choice of this definition.
For some applications of trigger efficiencies, a symmetric uncertainty is desirable. For sufficiently large statistics, the uncertainty can be approximated by a Gaussian with a standard deviation equal to the Binomial uncertainty. The latter can be estimated form the estimated efficiency $\hat{\varepsilon}$ and number of offline reconstructed objects $N_{\text{reco}}$:

$$\hat{\sigma}_{\text{binomial}} = \sqrt{\frac{\hat{\varepsilon}(1-\hat{\varepsilon})}{N_{\text{reco}}}}. \tag{4.6}$$

This simplified uncertainty model has some major deficiencies, discussed in Appendix A.
In the following, the given uncertainties are the statistical uncertainties estimated from the Bayesian approach (leading to asymmetric uncertainties), if not stated otherwise.

### 4.3.4. Muon Trigger Efficiency Measurements

The muon trigger efficiency measurements shown below were performed using ATLAS software provided by the `ATHENA` framework [3] [109] (release 17.3.1). The used data format is the so-called DPD (derived physics data, [110]), which contains reconstructed objects. Trigger information is read out using the `TrigDecisionTool` [111].

Physics analyses usually select events and reconstructed objects according to some quality criteria [4], for instance track and muon reconstruction quality or the status of certain subdetectors. For trigger efficiency measurements the same selection criteria should be applied as for the physics analysis the efficiencies are used for. The selection criteria used for the trigger efficiency measurements in this thesis are summarised below together with the definition for the matching between online and offline reconstructed objects. Additionally, the implementation of the Tag & Probe method and the Orthogonal Trigger method used for the presented trigger efficiencies is described. Finally, results of EF_mu18 trigger efficiency measurements are presented and the parametrisation of the trigger efficiencies is discussed. Additionally, the different methods to measure the trigger efficiencies are compared.

#### Event Preselection

Events from periods 2011B and 2011D to 2011I, corresponding to $1.47\,\mathrm{fb}^{-1}$, are selected using an appropriate GRL to ensure a good data quality. The integrated luminosity of each individual period is summarised in Appendix D, where the GRL is also quoted. Additionally, at least one primary vertex with more than four associated tracks in the event is required.

#### Muon Object Selection

Muons are reconstructed using the STACO algorithms [112], which combine Inner Detector and Muon Spectrometer track information to form muon candidate objects. Only *combined muon* candidates [113] are used in the following, because these are the candidates the muon trigger is intended to select.

[3] `ATHENA` is the control framework used by the ATLAS collaboration and is a concrete implementation of an underlying architecture, called `GAUDI` [108].

[4] In general, these event and object selection criteria match the recommendations, from the different ATLAS performance groups.

These muon candidates are required to satisfy some quality criteria, which match the ATLAS Muon Combined Performance Group (MCP) recommendations [114], summarised as follows:

- "loose" quality criteria, documented in [115],
- pseudorapidity $|\eta| < 2.4$,
- the associated inner detector tracks must satisfy a set of quality cuts:
  - at least one b-layer hit, if expected,
  - at least 1 Pixel detector and at least 6 SCT hits,
  - less than 3 holes in the Pixel detector and SCT,
  - TRT requirements (where $n := n_{TRT}^{hits} = +n_{TRT}^{outliers}$):
    if $|\eta| < 1.9$, require $n > 5$ and $n_{TRT}^{outliers} < 0.9 \cdot n$;
    if $|\eta| > 1.9$ and $n > 5$ require $n_{TRT}^{outliers} < 0.9 \cdot n$.

To reject muons from cosmic radiation, the muons are required to originate from the interaction region by limiting the distance of closest approach to the vertex in longitudinal (along the $z$-axis) and transverse direction to be smaller than 1.0 mm and 0.2 mm, respectively.
Physics processes of interest usually produce isolated leptons. In the following, *isolated muons* are muons satisfying the criteria above and in addition the sum of transverse momentum of all tracks with $p_T > 1\,\text{GeV}$ within $\Delta R \leq 0.2$ around the muon track (excluding the muon candidate itself) is required to be smaller than 1.8 GeV. This is a definition common to many physics analyses at ATLAS, e.g. [116].

**Matching of Offline and Online Muons**

For the matching between offline and online muons, the geometrical distance in the $\eta - \phi$ space with the usual metric $\Delta R = \sqrt{(\Delta\eta)^2 + (\Delta\phi)^2}$ is used. In the following, an offline muon is regarded to match an EF online muon if the distance in terms of $\Delta R$ is smaller than 0.15. This distances have been chosen to account for differences in the algorithms the EF trigger and offline reconstruction employ. The triggers under study are EF triggers, which are seeded by L2 and L1. Therefore, with this matching procedure, the efficiencies of the full trigger

chain is measured.
Figure 4.4 (left) shows the distribution of $\Delta R$ between the offline muon and the closest online muon for all $Z^0 \to \mu\mu$ events selected by the Tag & Probe method procedure described below. Additionally, the distribution of the $\Delta R$ between the tag and the probe muon in these events is shown in Figure 4.4 (right). No ambiguities in the matching process occur, because the muons in $Z^0 \to \mu\mu$ events are mainly back-to-back (explaining the peak in distribution at $\Delta R(\mu^{\text{tag}}, \mu^{\text{probe}}) \approx \pi$).

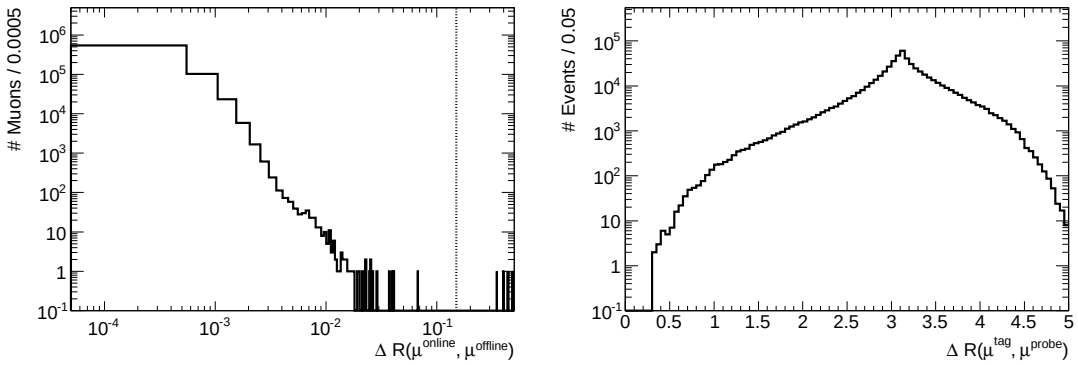


***Figure 4.4.:*** Distribution of the $\Delta R$ between (left) the offline muons and the closest online muon in all $Z^0 \to \mu\mu$ events selected by the Tag & Probe and (right) between the tag and the probe muon in these events.

To avoid ambiguities in the matching procedure in events selected by the Orthogonal Trigger method, offline muons which have a distance in terms of $\Delta R$ smaller than 2 times the maximum matching distance ($\Delta R < 0.3$) are both discarded. This restriction is a negligible loss of acceptance for the trigger efficiency measurement, but avoids mismatchings at small $\Delta R$ and takes the organisation of the ATLAS Muon Trigger System in RoIs into account, which have size of about 0.1 in terms of $\Delta R$.

**Implementation of the Tag & Probe Method using $Z^0 \to \mu\mu$ Decays**
In order to measure the muon trigger efficiencies using the Tag & Probe method (cf. Section 4.3.2), a well-defined $Z^0 \to \mu\mu$ sample is selected. For this purpose, exactly two muons with opposite charge and $|M_{\mu\mu} - M_Z| \leq 10\,\text{GeV}$, where $M_{\mu\mu}$ is the invariant mass of the two muons and $M_Z$ is the mass of the $Z^0$ boson, are required. Additionally, the tag muon has to be isolated and is required to have

a trigger match, such that the muon trigger efficiency can be measured from the probe muon. To enhance the statistics, each of the muons is regarded once as the tag and once as the probe.

**Implementation of the Orthogonal Trigger Method**

As mentioned in Section 4.3.2, muon trigger efficiencies can be measured in samples obtained by calorimeter based triggers. These triggers are jet and electron triggers, but also $E_T^{miss}$ triggers. For the latter, only energy depositions in the calorimeters are used and no muon trigger information. Thus, $E_T^{miss}$ are very efficient to obtain a muon enriched sample, because high-energetic muons result in $E_T^{miss}$ for the trigger. Additionally, hadronic tau and $b$-jet triggers are used. By the combination (logical `OR`) of different orthogonal triggers, the statistics is enhanced. Double counting of events which are stored in the `Egamma` and `JetTauEtmiss` stream is avoided by vetoing events from the `JetTauEtmiss` stream selected by an egamma trigger. The trigger efficiencies presented in the following distinguish between different types of orthogonal trigger (jet, egamma and $E_T^{miss}$) to show that the trigger efficiencies determined on samples obtained with different orthogonal triggers are compatible.

**Results of EF_mu18 Trigger Efficiency Measurements**

Figure 4.5 shows the trigger efficiencies for isolated muons as a function of muon $p_T$ and direction, described by $\eta$ and $\phi$, where for the latter two only muons in the $p_T$ plateau (cf. Section 4.3.1) are considered. Due to the finite statistics available for the trigger efficiency measurement, an appropriate binning [5] in these muon properties has to be chosen. The binning has been optimised for the available statistics. This optimization is discussed in Section 4.3.5.

The presented plots are projections of the trigger efficiencies onto one of the muon properties, where the dependencies on other properties has been integrated out. Since different technologies are used to trigger on muons in the endcaps and in the barrel (cf. Section 3.2.4 and 3.2.4), the trigger efficiencies are shown separately for these parts of the detector. Due to the good $p_T$ resolution of the muon triggers the turn-on in Figure 4.5 (a) and (b) is very steep. Therefore, in many analyses, the plateaus of muon trigger efficiencies are assumed to start 2 GeV above the

[5] The term "binning" means a discretisation of the real-valued muon properties, e.g. $p_T$, $\eta$, $\phi$.

nominal $p_T$-threshold, e.g. 20 GeV for the EF_mu18 trigger. This definition of the plateau is used throughout this thesis. The value of the plateau efficiency in the barrel ($\approx 76\,\%$) is lower than in the endcaps ($\approx 88\,\%$), due to the different trigger technologies and due to a larger fraction of dead regions (with respect to the trigger) in the barrel.
These inefficient regions can be identified in Figure 4.6, where the trigger efficiencies are shown for a fine-grained binning, i.e. a binning a smaller bin size, as a function of the muon $\eta$ and $\phi$ for isolated muons in the plateau. The feet of the ATLAS detector ($-2 < \phi < -1$ in the barrel region) and regions where cables and electronics are located can clearly be seen. The latter lead to a periodic behaviour in muon $\phi$ seen in Figure 4.5 (c) and (d), which is more pronounced in the barrel region. The projection onto the muon $\eta$ in Figure 4.5 (e) shows that in the endcaps, the trigger efficiencies are mostly flat, while this is not the case in the barrel, where the efficiencies are very inhomogeneous.
Finally, the trigger efficiencies as a function of the distance in terms of $\Delta R$ to the next muon in the event are shown in Figure 4.7. For $\Delta R < 0.3 = 2 \cdot R_{\text{matching}}$, an unambiguous matching is chosen by additional requirements: an offline muon is regarded to match an EF online muon if, in addition to $\Delta R < 0.15$ there is

- no other online muon which is closer in terms of $\Delta R$ to the same offline muon,
- no other offline muon which is closer in terms of $\Delta R$ to the best matching online muon.

Due to the topologies of two muons originating from a $Z^0$ decay, only the Orthogonal Trigger method can be used to study these dependencies (cf. Figure 4.4). The plot shows that the cut on a minimal distance of two times $\Delta R_{\text{matching}}$ is justified.

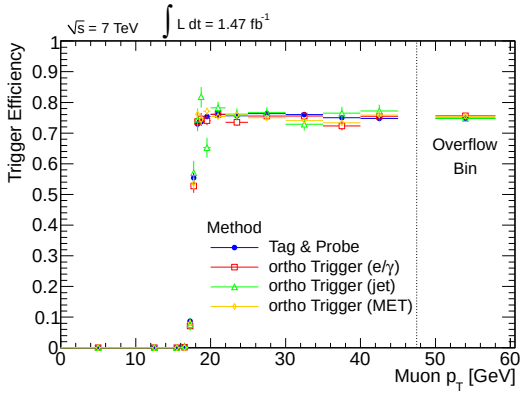


(a) trigger efficiencies vs. $p_T$ in the barrel

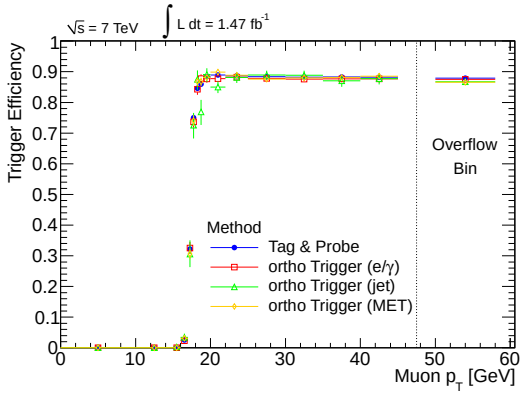


(b) trigger efficiencies vs. $p_T$ in the endcaps

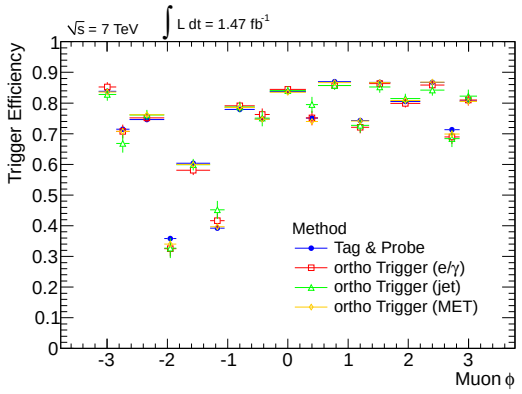


(c) trigger efficiencies vs. $\phi$ in the barrel

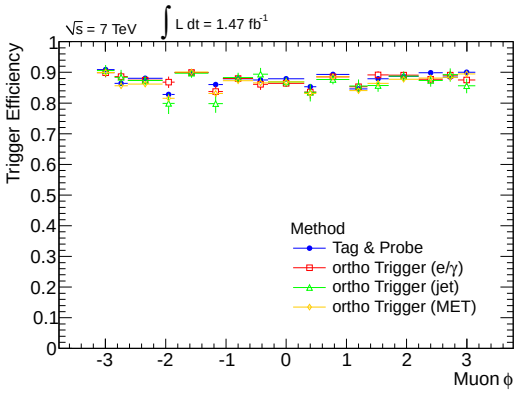


(d) trigger efficiencies vs. $\phi$ in the endcaps

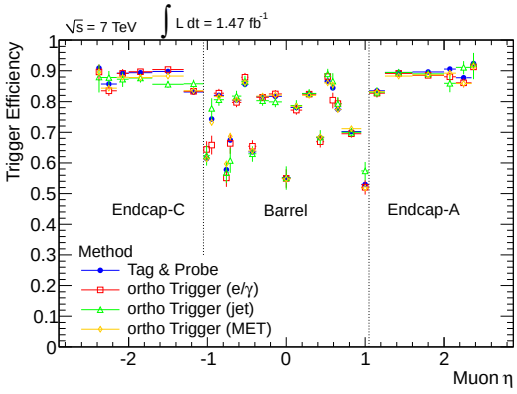


(e) trigger efficiencies vs. $\eta$

***Figure 4.5.:*** EF_mu18 trigger efficiencies for combined, isolated muons measured with the Tag & Probe and Orthogonal Trigger method (three different types of orthogonal triggers are distinguished: egamma, jet and $E_T^{miss}$ triggers) as a function of the muon $p_T$ (a, b), $\phi$ (c, d) and $\eta$ (e) in the barrel ($|\eta| < 1.05$) and the endcaps ($1.05 < |\eta| < 2.4$). For c, d, and e, the muons are required to be in the plateau ($p_T > 20\,\text{GeV}$). The error bars represent the statistical uncertainty only.

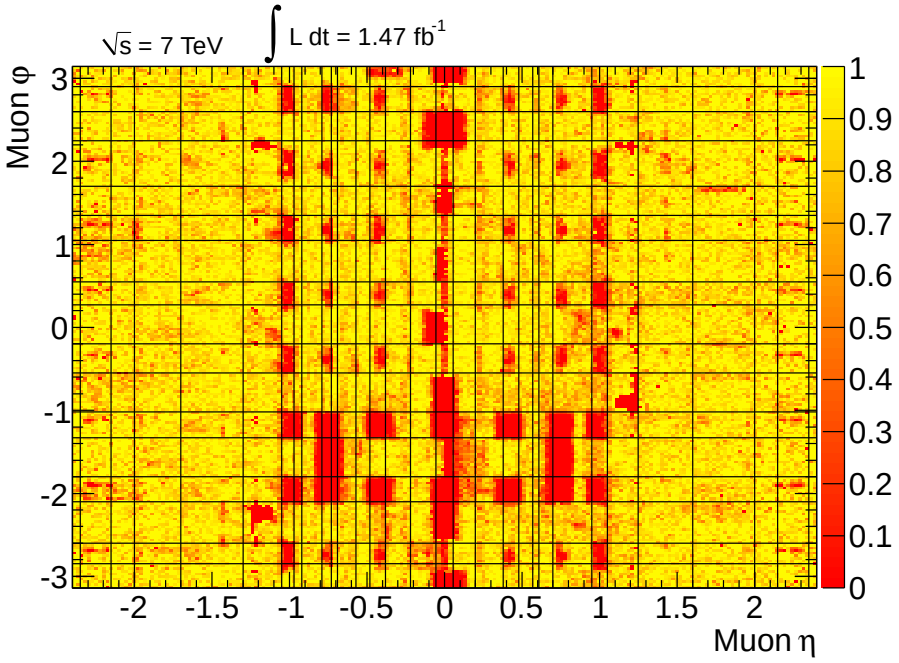


***Figure 4.6.:*** EF_mu18 trigger efficiencies measured with the Orthogonal Trigger method (combination of all orthogonal triggers listed in Appendix E) as a function of the muon $\eta$ and $\phi$, for combined, isolated muons in the plateau ($p_T > 20\,\text{GeV}$). The color in each bin corresponds to the trigger efficiencies measured for that bin, as defined in the legend on the right-hand side. Additionally, the binning chosen in the other plots is indicated by the black lines. The inhomogeneities are described in the text.

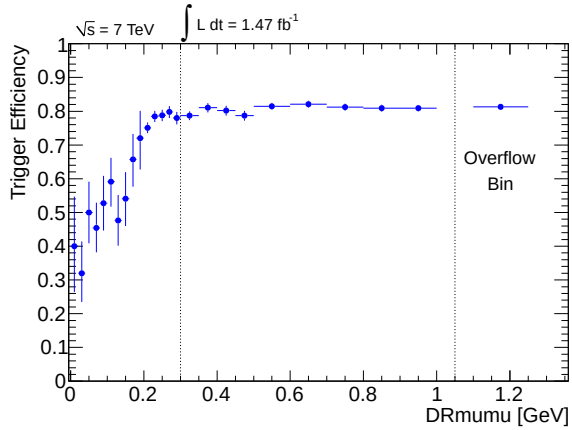


***Figure 4.7.:*** EF_mu18 trigger efficiencies measured with the Orthogonal Trigger method (combination of all orthogonal triggers listed in Appendix E) as a function of $\Delta R$ to the next muon, for combined, isolated muons in the plateau ($p_T > 20\,\text{GeV}$). The matching between online and offline muons for offline muons which are closer than two times $\Delta R_{\text{matching}}$ (indicated by the dotted line at $\Delta R = 0.3$) is described in the text. The error bars represent the statistical uncertainty only.

### Discussion of the Relevant Muon Properties

Figure 4.5 and Figure 4.6 show that the trigger efficiencies are not flat in at least muon $p_T$, $\eta$ and $\phi$. Thus, at least these muon properties are relevant and the trigger efficiencies have to be parametrised in at least these variables. It has been shown [117] that these three variables are sufficient to get reasonable results in the application of trigger efficiencies in physics analyses following a trigger reweighting approach (see Section 4.3.5). In [117] this has been done by comparing event yields from the trigger simulation and trigger reweighting in MC samples with different physics content. However, the distribution of other muon properties, for instance properties describing the quality of the muon candidates or the distance of closest approach to the vertex in longitudinal $z_0$ and transverse $d_0$ direction, is rather similar for most physics processes of interest. Therefore, the muon trigger efficiencies in some of these properties have been studied, but no significant dependency was found. Exemplarily, the trigger efficiencies as a function of $z_0$ is shown in Figure 4.8 for two $\eta$-$\phi$ ranges, for which the trigger efficiencies are rather flat such that correlations between $z_0$ and $\eta/\phi$ do not contribute. For the muon trigger efficiencies, no significant dependency on $z_0$ is observed. With increasing statistics further refined studies can be done.

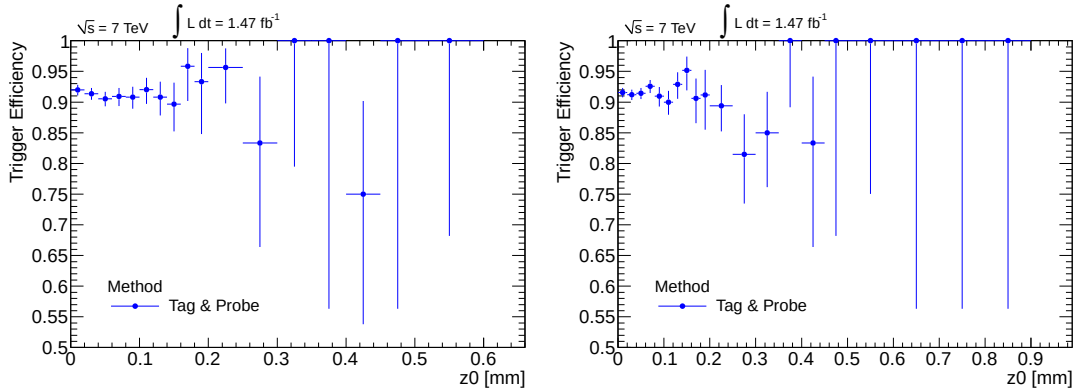


(a) for $-0.69 < \eta < 0.48$ (in barrel) (b) for $-1.7 < \eta < 0.3$ (in endcaps)

***Figure 4.8.:*** EF_mu18 trigger efficiencies measured with the Tag & Probe as a function of the distance of closest approach to the vertex in longitudinal direction for combined, isolated muons, which are in the plateau ($p_T > 20\,\text{GeV}$) and in a certain $\eta$-$\phi$ range in the barrel (a) and in the endcaps (b). For both plots the muons are required to be in $0.55 < \phi < 1.05$. The error bars represent the statistical uncertainty only.

For muon triggers with different algorithms, additional dependencies are possible, e.g. muon triggers with additional online isolation criteria depend on muon isolation properties.
To summarise, within the available statistics, the muon $p_T$, $\eta$ and $\phi$ are a good choice for the parametrisation of the efficiencies of the muon triggers studied in this and Chapter 5.

### Comparison of Muon Trigger Efficiencies Obtained with Different Methods

In principle, the trigger efficiencies should be independent of the method which is used to measure them. The only difference between the methods is the way the samples from which the trigger efficiencies are determined are obtained. Furthermore, the trigger is not sensitive to the origin of the muon, but only to its properties. Therefore, muons with the same properties but from different physics processes have the same trigger efficiencies. However, due to the finite binning and differences in the trigger probability within a single bin in conjunction with the different distributions of the muon properties in the sample the trigger efficiencies are measured from, slightly different trigger efficiencies for different methods are expected. Therefore, the different methods can be used to obtain a measure for the uncertainty introduced due to the chosen binning. This uncertainty is estimated in the following from the difference of the trigger efficiencies determined with the Tag & Probe method and the Orthogonal Trigger method (with a combination of all orthogonal triggers listed in Appendix E).
A comparison of the efficiencies projected on one of the binning dimensions is not sufficient, because the other dimensions are integrated out. Therefore, a bin-by-bin comparison is more appropriate. To enhance the statistics in each bin, a binning only in $\eta$ and $\phi$ is chosen, since the trigger efficiencies are sufficiently flat in $p_T$ in the plateau. Consequently, trigger efficiency maps as shown in Figure 4.6 are obtained for both methods. The distribution of the absolute difference between corresponding bins is shown in Figure 4.9 (a), separately for the barrel and endcaps. In addition, the distribution of the pulls is shown in Figure 4.9 (b). The pull $\delta_i$ of a bin $i$ is defined as:

$$\delta_i = \frac{\hat{\epsilon}^i_{\mathrm{T\&P}} - \hat{\epsilon}^i_{\mathrm{ortho}}}{\hat{\sigma}_{stat.}}, \tag{4.7}$$

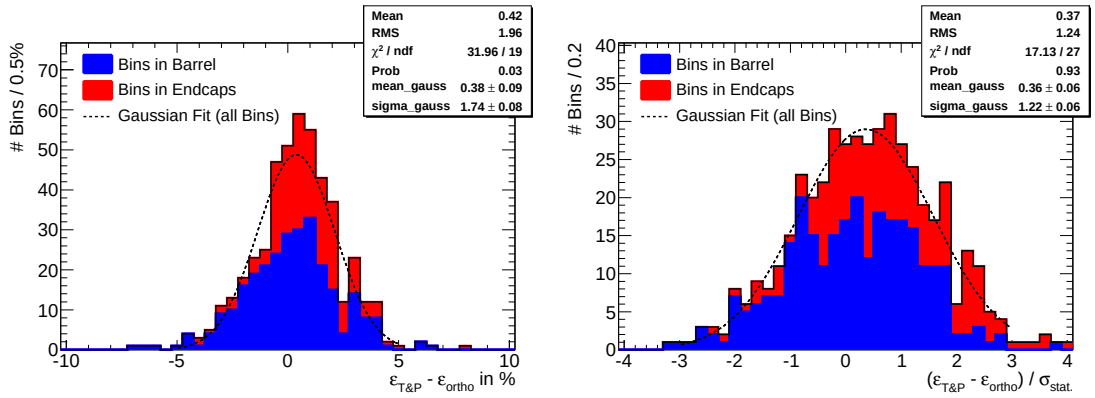


(a) distribution of the absolute difference

(b) distribution of the pulls

***Figure 4.9.:*** Comparison of the trigger efficiencies determined by the Tag & Probe method and the Orthogonal Trigger method on a bin-by-bin basis as explained in the text. Shown is the stacked distribution of the absolute difference (a) and the pulls (b), where bins in the barrel (blue) and endcaps (red) are differentiated. The total distribution (barrel and endcaps) is fitted with a Gaussian.

where $\hat{\epsilon}^i_{\mathrm{T\&P}}$ and $\hat{\epsilon}^i_{ortho}$ are the estimators for the trigger efficiencies in bin $i$ determined by the Tag & Probe and the Orthogonal Trigger method, respectively, and $\hat{\sigma}_{stat.}$ is a combined statistical uncertainty. The two measured efficiencies can be assumed to be uncorrelated, because selected $Z^0 \to \mu\mu$ events rarely [6] ($\mathcal{O}(1\,\%)$) issue one of the orthogonal triggers due to the high thresholds of the orthogonal triggers. Additionally, in most bins, the trigger efficiencies can be determined based on more than 500 selected muons, such that a Gaussian approximation for each of the trigger efficiency measurements (explained in more detail in Appendix A) as well as for the combined uncertainty is reasonable:

$$\hat{\sigma}_{stat.} = \sqrt{\hat{\sigma}^2_{\mathrm{T\&P}} + \hat{\sigma}^2_{\mathrm{ortho}}}, \tag{4.8}$$

where the symmetric Binomial uncertainties from Equation 4.6 are used for the uncertainties from the two efficiency measurements.

On average, the binned trigger efficiencies determined with the Tag & Probe method are slightly higher ($\approx 0.4\,\%$) than the efficiencies determined with the Orthogonal Trigger method. Due to the larger bins in the endcaps, this effect is more visible in the endcaps than in the barrel. The distribution of the pulls

[6] For the studied take-taking periods, roughly 1 % of the selected $Z^0 \to \mu\mu$ issued also one of the chosen orthogonal triggers (see Appendix E).

shows that this difference is in the order of roughly $0.3 - 0.4$ times the statistical uncertainty. The width of the pull distribution is slightly larger than 1 ( a width of 1 is the expectation for statistical fluctuations only). Since the employed methods measure the trigger efficiencies from different samples, additional deviations are expected due to the finite binning. In conjunction with the statistical fluctuations, this leads to a wider Gaussian than a standard Gaussian.

### 4.3.5. Application of Trigger Efficiencies in Physics Analyses

In many physics analyses performed with the ATLAS detector, MC pseudo data is used to estimate either a signal or a background contribution if data-driven techniques are not applicable, e.g. due to low statistics. The simulation of the detector, which includes the simulation of the trigger, is not perfect. To account for the trigger efficiencies in the calculation of event yields, two different approaches are common, namely the *scale factor approach* and the *reweighting approach*. These approaches are discussed in detail in [117] and are briefly summarised in the following.

In the scale factor (SF) approach, the detector simulation is used and the trigger efficiencies derived from the simulation are corrected by scale factors such that the actual trigger efficiencies measured from data are reflected by the corrected MC trigger efficiencies.

In the reweighting approach, the MC events, regardless of the simulated trigger decisions, are weighted according to the actual trigger efficiencies measured on data.

The scale factor approach has a few shortcomings. Some of them are outlined in the following. Firstly, events which are discarded by the simulated trigger are completely neglected in the analyses. For muon triggers, the efficiencies can differ by more than 20 % from one (cf. Section 4.3.4), which means that a considerable amount of computing time spent for the generation and simulation of these events is wasted. Secondly, the correct treatment of correlations between uncertainties of different SFs is complicated. Usually, the uncertainties are treated as 100 % correlated, although that is not necessarily true, if the SFs are determined in more than one bin. Another shortcoming of the SF approach is that it is not appropriate in analyses with more than one lepton in the final state. Depending

on the trigger, a large number of binning dimensions for the SFs is needed to take the correlations between the leptons into account. For a single object trigger, this is elaborated in [117].
The reweighting approach does not suffer from the same shortcomings, because all simulated events are taken into account, the correlations between the uncertainties of the trigger efficiencies can easily be taken into account and the calculation of event weights for events with an arbitrary number of objects is straightforward. If the object efficiencies of a trigger designed for objects of the same type are independent, the event weight can be factorised properly into the object efficiencies. For a single muon trigger the event weight is then given by Equation 4.1. For a di-muon trigger this independence is shown in Section 5 and the event weights can be calculated by a similar formula (see Section 5.2).
It is crucial that the objects that enter the calculation of the event weights are well defined. Therefore, the same event and object selection criteria are applied to data and MC. With regard to the trigger, this means that on data only events are taken into account where at least one of the objects in the plateau issued the trigger (trigger matching, cf. Section 4.3.4), while on MC only selected objects in the plateau are used for the calculation of the event weights.
The major challenge for the trigger reweighting approach is to find an approximate binning for the trigger efficiencies, such that all dependencies are implemented in a reasonable way. In the following, the binning chosen in Section 4.3.4 is motivated.

**Binning Optimization**

The binning has to be optimised in terms of granularity, that means that it has be neither too fine nor too coarse. The former ensures that each bin has enough statistics to calculate the trigger efficiency with a reasonable statistical uncertainty and the latter ensures that the inhomogeneities in the trigger performance are properly taken into account.
Since the trigger efficiencies as a function of $p_T$ are sufficiently flat in the plateau, only one large bin is used for the binning in $p_T$. This allows for a fine-grained binning in muon $\eta$ and $\phi$, where the trigger efficiencies are more inhomogeneous. The main strategy is to combine regions in the detector where the trigger probability is roughly flat. Consequently, the measured trigger efficiency within a single bin

is then independent from the sample (and its distributions) used for the trigger efficiency measurement. This strategy has been pursued to find an appropriate binning, as indicated in Figure 4.6. The chosen binning ensures that the fluctuations for a more fine-grained binning are close to the statistical uncertainties and in most bins less than 5 %.

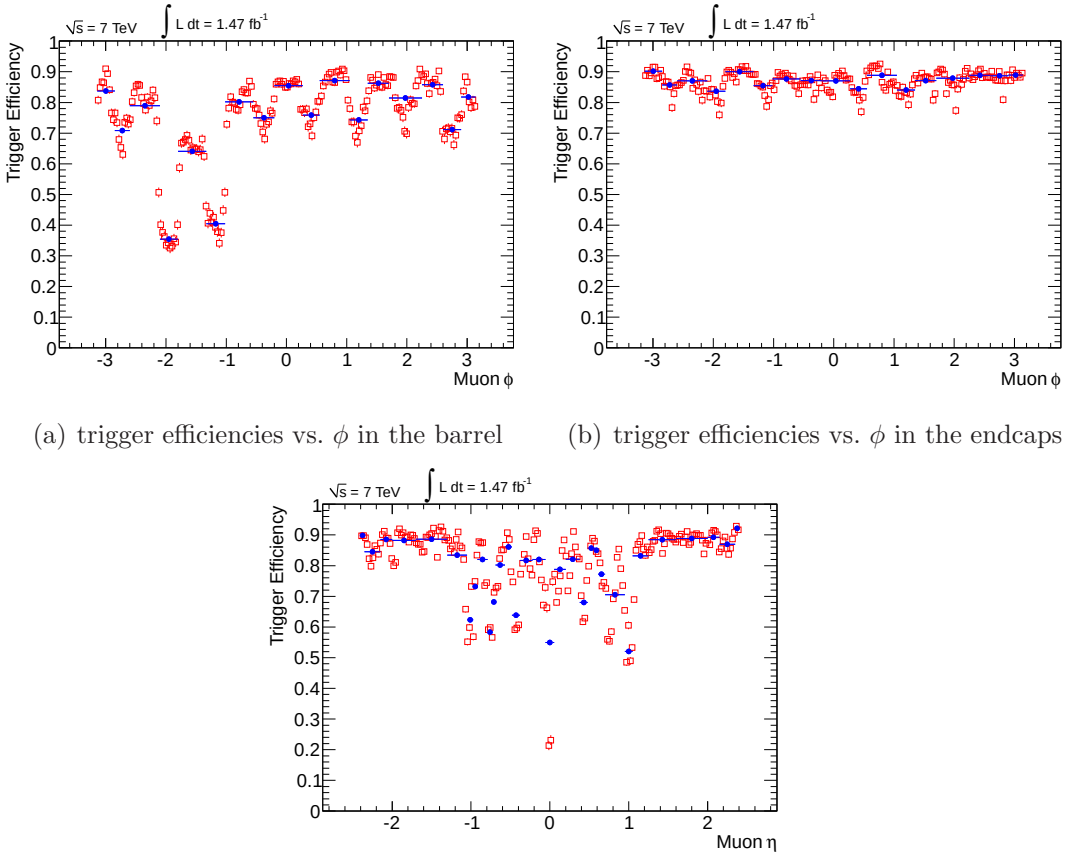


(a) trigger efficiencies vs. $\phi$ in the barrel

(b) trigger efficiencies vs. $\phi$ in the endcaps

(c) trigger efficiencies vs. $\eta$

***Figure 4.10.:*** EF_mu18 trigger efficiencies measured with the Orthogonal Trigger method (combination of all orthogonal triggers listed in Appendix E) for different binnings as a function of the muon $\phi$ (a, b) and $\eta$ (c) in the barrel ($|\eta| < 1.05$) and the endcaps ($1.05 < |\eta| < 2.4$), for isolated muons and in the plateau ($p_T > 20\,\text{GeV}$). The blue markers show the trigger efficiencies for the optimised binning and the red markers for a more fine-grained binning. The error bars represent the statistical uncertainty only.

Figure 4.10 shows the EF_mu18 trigger efficiencies as a function of muon $\eta$ and $\phi$ for the chosen binning and for a more fine-grained binning. The oscillating behaviour in $\phi$, caused by the dead regions of the muon detector (feet of the ATLAS

detector, cables, and electronics, cf. Figure 4.6), is covered by the optimized binning. In muon $\eta$, a few bins in the endcaps are sufficient to model this behaviour, while in the barrel it seems hard to find a binning fulfilling both the requirements mentions above. However, if the additional binning dimension in muon $\phi$ is taken into account, the differences can be partly resolved (cf. Figure 4.6).
With increasing statistics, the binning can be refined and the modelling of the inhomogeneities improves. The presented binning is used in Section 4.3.4 and throughout the thesis, if not stated otherwise.

### 4.3.6. Conditional Trigger Efficiencies

In many physics analyses performed with the ATLAS detector, a combination of different triggers is applied to enhance the statistics. If the trigger efficiencies are not independent from each other, the correlation between the trigger efficiencies has to be taken into account. For example, in analyses with more than one muon in the final state, a single and a di-muon trigger with a lower $p_T$-threshold than the single muon trigger can be combined by a logical `OR` of these triggers. For the combination, the probability that the di-muon trigger issues under the condition that the single muon trigger does not is needed. The di-muon trigger efficiencies can be factorised into single muon trigger efficiencies. This is shown in Section 5. Therefore, for combining exemplary the EF_mu18 (single muon trigger) and EF_2mu10_loose (di-muon trigger) triggers, the conditional probability $p$(EF_mu10_loose|!EF_mu18) is needed. Although the EF_mu10_loose trigger chain is prescaled, its decision may be recovered via the rerun mode (cf. Section 3.3.3), such that the trigger efficiencies can be determined in the same way as for EF_mu18. At L2 and EF level both triggers employ the same trigger algorithms, but different $p_T$-thresholds are required (cf. Appendix B). However, at L1 the trigger L1_MU0 and L1_MU10 with 0 GeV and 10 GeV $p_T$-thresholds, respectively, have different hit coincidence requirements. L1_MU10 requires additional hit coincidences with respect to L1_MU0 (cf. Section 3.3.1). Thus, it can happen that muons in the plateau of both triggers issue EF_mu10_loose but not EF_mu18, due to failing the additional hit coincidence requirements. This happens more often in the endcaps than in the barrel, as shown in Figure 4.11.

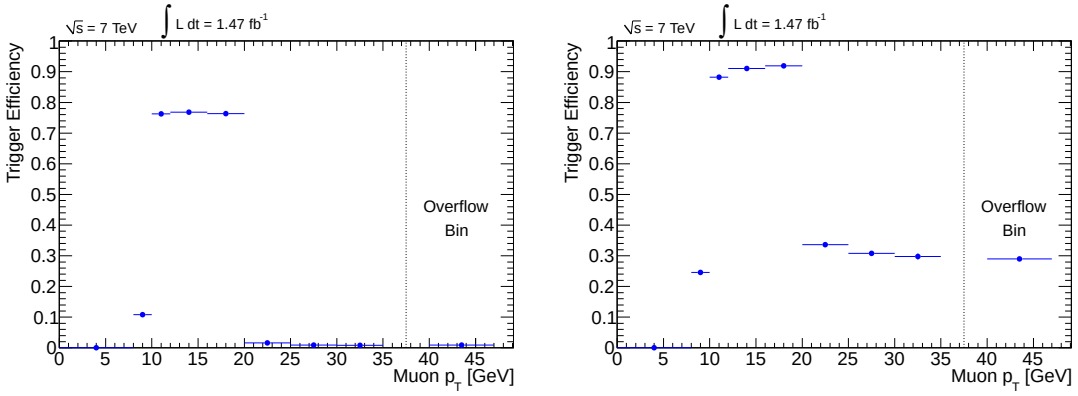


(a) barrel (b) endcaps

***Figure 4.11.:*** Conditional trigger efficiencies $p$(EF_mu10_loose|!EF_mu18) measured with the Orthogonal Trigger method as a function of muon $p_T$ in the barrel ($|\eta| < 1.05$) and the endcaps ($1.05 < |\eta| < 2.4$) for isolated muons.

# 5. Di-Muon Trigger Efficiency Studies

The instantaneous luminosity delivered to the ATLAS detector steadily increased during 2011 and will increase further in 2012. Until now, many analyses with leptons in the final state employed the lowest unprescaled single lepton triggers. However, the single lepton triggers in their present configuration have reached the maximum assigned bandwidth consumption, as discussed in Section 4.2 for single muon triggers. To reduce the output rate of lepton triggers, different modifications are possible. These possibilities and their implication for a search for new physics [1] are:

- Introducing prescales: This reduces the rate by the prescale factor $N$, but only $1/N$ of the signal events are recorded.
- Higher $p_T$-thresholds: The higher the $p_T$-thresholds are, the lower the trigger rates, but the trigger acceptance to the signal is reduced.
- Stricter online selection criteria: For example, an additional isolation criterion at L2/EF reduces the rate. Depending on the implementation, the trigger efficiency dependencies can become very complex. This has to be studied separately for each analysis and is beyond the scope of this thesis.
- Multi-lepton triggers: By requiring additional leptons (above a given $p_T$-threshold), the rate is reduced dramatically, even if the $p_T$-thresholds for each of the leptons are lowered. Of course, these triggers are only appropriate for analyses with more than one lepton in the final state.

[1] The term "new physics" means physics processes not described by the SM.

For muon triggers, the impact of a higher $p_T$-threshold or an additional muon on the trigger rates can be seen in Figure 5.1. The rates of the EF_mu22 (single muon trigger with nominal 22 GeV $p_T$-threshold), EF_2mu10_loose (di-muon trigger with nominal 10 GeV $p_T$-threshold for each muon) and EF_mu18 (single muon trigger with nominal 18 GeV $p_T$-threshold) as reference are shown for the same run as in Figure 4.1. In Appendix B the configuration of these triggers is summarised. The EF_2mu10_loose trigger rate is only 2-3 Hz and hence more than a magnitude smaller than the EF_mu18 trigger rate, although the $p_T$-thresholds for the muons are lowered: from 18 GeV to 10 GeV at L2/EF and from 10 GeV to 0 GeV at L1 . This rate reduction is caused by two facts: firstly, events with two or more muons with sufficient $p_T$ are much rarer than single muon events and, secondly, the trigger probability for di-muon triggers is lower than for single muon triggers, since two instead of only one muon candidate have to be found by the trigger. Certainly, this lower trigger probability is also the main drawback of di-muon triggers. Similar statements hold for other multi-lepton triggers.

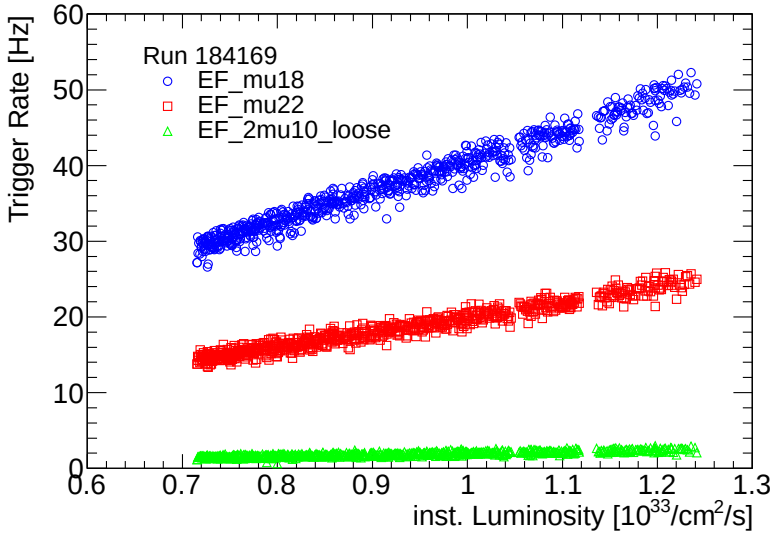


***Figure 5.1.:*** Output rate of the EF_mu22 and EF_2mu10_loose trigger for the same run as in Figure 4.1 (run 184169 from period 2011H) as a function of instantaneous luminosity. Additionally, the EF_mu18 output rate is shown as reference.

The actual choice of the trigger strategy is analysis-specific. For lepton-rich analyses, like the SUSY search presented in Section 6, multi-lepton triggers are an appropriate way to expand the trigger acceptance to signal regions with lower

transverse momenta by increasing the total rate only slightly. However, to apply multi-lepton triggers, their trigger efficiencies have to be known. In the following, trigger efficiencies of di-muon triggers are investigated. The study of any other multi-lepton trigger could be done in a similar way, but for the sake of simplicity, in this thesis only di-muon triggers are considered.

As for single muon triggers, di-muon trigger efficiencies have to be parameterised and binned in the relevant di-muon variables. These are $p_T$, $\eta$ and $\phi$ for both muons, which doubles number of binning dimensions (exponential increase of the number of bins). Additionally, correlations between the muons can be taken into account.
That means that, for the direct measurement of the di-muon trigger efficiencies, less events (due to the smaller rates) are available, while a larger number of binning dimensions is necessary, than in the case of single muon triggers. Thus, the di-muon efficiencies cannot be measured directly with an accuracy as precise as the single muon efficiencies. To reduce the number of binning dimensions and to profit from the accuracy of the single muon trigger efficiencies, the trigger logic of the di-muon triggers can be exploited, such that the di-muon trigger efficiencies can be modelled from the single muon trigger efficiencies.
In the following, the hypothesis is studied, if the di-muon trigger efficiencies can be factorised into the single muon trigger efficiencies of the muons involved and how large the systematic uncertainties introduced by this factorisation are. The factorisation is described in Section 5.1. The application of the factorised di-muon trigger efficiencies in the reweighting approach is discussed in Section 5.2. The factorisation hypothesis is tested on MC simulated pseudo data and actual data in Section 5.3. Finally, a conclusion is drawn in Section 5.4.

## 5.1. Factorising Di-Muon Trigger Efficiencies

As motivated above, it is desirable to model the di-muon trigger efficiencies from single muon trigger efficiencies, especially for the reweighting approach, which becomes applicable due to this modelling (see Section 5.2).
In principle, the algorithms for di- and single muon triggers are similar, with the main exception that the di-muon triggers require at least two online muons

with sufficient transverse momenta instead of only one. This is implemented in the di-muon trigger algorithms by a logical `AND` of two single muon triggers (cf. Section 3.3.3).
However, a priori it is unclear that the trigger decision of one of the muons is independent from the existence of another muon. Therefore, the interference of the muons has to be taken into account. Hence, for an event with two muons the efficiency $\epsilon_{\mathrm{di,2muons}}$ for a di-muon trigger with symmetric $p_T$-thresholds (same thresholds for both muons on each trigger level) is given by

$$\epsilon_{\mathrm{di,2muons}} = \epsilon_{\mathrm{si,1}} \cdot \epsilon_{\mathrm{si,2}} + corr(\mu_{\mathrm{si,1}}, \mu_{\mathrm{si,2}}), \tag{5.1}$$

where $\epsilon_{\mathrm{si,j}}$ is the single muon trigger efficiency for the $j$-th muon and the $corr(\mu_{\mathrm{si,1}}, \mu_{\mathrm{si,2}})$ term describes the interference between the muons.
For a di-muon trigger with asymmetric $p_T$-thresholds, e.g. one muon with at least 15 GeV and the other with at least 10 GeV, conditional probabilities have to be considered due to permutability of the muons. For the sake of simplicity, in the following only di-muon triggers with symmetric $p_T$-thresholds are considered.
The possible interference between the muons precludes the factorisation into the single muon trigger efficiencies. However, it is often assumed that the trigger decision of one of the muons is in principle independent from the trigger decision of the other muon. That means a vanishing interference term $corr(\mu_{\mathrm{si,1}}, \mu_{\mathrm{si,2}})$. In the following, this assumption is tested under the condition that the muons are separated by a sufficiently large angle, such that their detector signatures do not overlap. Collinear muons are excluded in the trigger matching (cf. Section 4.3.4).
The estimator for the factorised di-muon trigger efficiency in a event with two muons is given by

$$\hat{\varepsilon}_{\mathrm{di,2muons}} = \hat{\varepsilon}_{\mathrm{si,1}} \cdot \hat{\varepsilon}_{\mathrm{si,2}}, \tag{5.2}$$

where $\hat{\varepsilon}_{\mathrm{si,j}}$ is the estimator for the efficiency of the $j$-th muon of the corresponding single muon trigger (same algorithms and $p_T$-thresholds on each trigger level).
The uncertainties of the product of the single muon trigger efficiencies is estimated by

$$\hat{\sigma}_{\mathrm{di,2muon}} = \sqrt{\left(\hat{\varepsilon}_{si,1} \cdot \hat{\sigma}_{si,2}\right)^2 + \left(\hat{\varepsilon}_{si,2} \cdot \hat{\sigma}_{si,1}\right)^2}, \tag{5.3}$$

where $\hat{\sigma}_{si,j}$ are the estimators for Binomial uncertainty from Equation 4.6 of the single muon trigger efficiency of the $j$-th muon. The single muon trigger efficiencies can be determined with sufficient statistics such that the Gaussian approximations for the uncertainties of the single muon trigger efficiencies itself as well as of their product is reasonable.

## 5.2. Application of Factorised Di-Muon Trigger Efficiencies

In the reweighting approach (cf. Section 4.3.5), the simulated MC events are weighted with the probability to trigger the event, determined from the trigger efficiencies measured on data. In the case of di-muon triggers this becomes much easier if the di-muon trigger efficiencies are factorised into single muon trigger efficiencies, like in Equation 5.2 for events with two muons, because then the probability depends only on the single muon trigger efficiencies and not on the correlations between the muons. The latter would cause an exponential increase of bins for the trigger efficiency measurements.
The modelled efficiency $\epsilon_{\mathrm{di}}$ of the di-muon trigger to select a particular event with $N \geq 2$ muons is given by the logical `OR` that two or more muons in the event have passed the hypothesis of the corresponding single muon trigger:

$$\epsilon_{\mathrm{di}} \overset{5.2}{=} 1 - \prod_{i=1}^{N}(1 - \varepsilon_{\mathrm{si,i}}) - \sum_{i=1}^{N} \varepsilon_{\mathrm{si,i}} \prod_{\substack{j=1 \\ j\neq i}}^{N}(1 - \varepsilon_{\mathrm{si,j}}), \tag{5.4}$$

where $\varepsilon_{si,k}$ is the single muon trigger efficiency for the $k$-th muon.

## 5.3. Testing the Factorising Hypothesis

In this section, different tests for the factorising hypothesis are presented. The lowest unprescaled di-muon trigger with symmetric $p_T$-thresholds in 2011 was EF_2mu10_loose. This trigger chain requires at least two muons with a minimum $p_T$ of about 10 GeV on EF/L2 level and is seeded[2] from L1_2MU0. The corre-

[2] In 2011 EF_2mu10_loose was seeded by L1_2MU0 until period 2011K and from period 2011L onwards by L1_2MU4.

sponding single muon trigger is EF_mu10_loose, which has the same $p_T$-thresholds on every trigger level. The exact configuration of these triggers can be found in Appendix B. In the following, these two trigger chains are used to test the factorising hypothesis.
Since the statistics of di-muon events on data is limited, the hypothesis is at first tested on MC events, where the simulated trigger decisions are used. The trigger efficiencies determined from simulations cannot be compared to data, but can be compared among each other. The event and muon object selection is the same as outlined in Section 4.3.4 as well as the measurement of the single muon trigger efficiencies.
In Section 5.3.1 the direct measurement of di-muon trigger efficiencies on data and MC is described. A selection of the performed tests of the factorising hypothesis for simulated data is presented in Section 5.3.2 and Section 5.3.3 and for the actual data in Section 5.3.4. Finally, a conclusion is drawn in Section 5.4.

### 5.3.1. Measuring Di-Muon Trigger Efficiencies

To measure the di-muon trigger efficiencies a Tag & Probe method, is not applicable. Therefore, the Orthogonal Trigger method (cf. Section 4.3.2 and 4.3.4) has to be applied to measure the di-muon trigger efficiencies directly. To keep the determination of the di-muon trigger efficiencies as simple as possible without loosing too much statistics, only events with exactly 2 offline reconstructed muons are considered.
As noted before, additionally, the offline reconstructed muons are required to have no other offline reconstructed muon in their vicinity [3] ($\Delta R < 2 \cdot \Delta R_{\text{matching}} = 0.3$, cf. Section 4.3.4). The di-muon event is regarded to be triggered if both offline muons have matching online muons (associated to EF_2mu10_loose) according to the matching definition in Section 4.3.4.
On simulated MC events, the single and di-muon trigger efficiencies are determined with the Monte Carlo Counting method (cf. Section 4.3.2).

[3] For collinear muons (small distances in terms of $\Delta R$), e.g. from decays of boosted $J/\psi$, specialised triggers are implemented. General di-muon triggers have not been developed for these collinear muons, but rather for muon-rich analyses, where the muons are typically non-collinear. Therefore, the exclusion of collinear muons is a negligible loss of acceptance for these muon-rich analyses, but avoids mismatchings at small $\Delta R$.

### 5.3.2. Comparison of Factorised and Directly Measured Di-Muon Trigger Efficiencies on Monte Carlo

In the following, a comparison between the directly measured di-muon trigger efficiencies in events with two muons and the product of the corresponding single muon trigger efficiencies, both measured on MC events, is performed. This is done on a bin-by-bin basis, similar to the comparison of the single muon trigger efficiencies determined with different methods (cf. Section4.3.4). The di-muon trigger efficiencies are measured in the same binning as the single muon trigger efficiencies for each of the two muons. For this purpose, the optimised binning (cf. Section 4.3.5) is used. For every di-muon trigger efficiency bin, the directly measured di-muon trigger efficiency is compared with the product of the single muon trigger efficiencies corresponding to the di-muon trigger efficiency bin.
The comparison is performed only for combined, isolated muons which are in the $p_T$ plateau ($p_T > 12\,\text{GeV}$ for the EF_mu10_loose trigger), because usually these muons are used in physics analyses. The single and di-muon trigger efficiencies are measured on a $Z^0 \to \mu\mu$ MC sample [4]. Using a $Z^0 \to \mu\mu$ MC sample has assets and drawbacks.
The muons from the $Z^0$ decays are back-to-back in the majority of cases (cf. Figure 4.4). This means that, if the properties of one muon are fixed, only a very limited part of the possible phase space (all possible directions) of the second muon is covered by $Z^0 \to \mu\mu$ events, due to the kinematic correlations. Therefore, the di-muon trigger efficiencies can only be measured accurately for a small area of the possible two muon phase space. The restriction to these event topologies is of course a disadvantage. However, due to this correlation, the phase space regions corresponding to muons which reflect this event topology are highly populated. Hence, a fine-grained binning can be used for the trigger efficiency measurement in these regions.
Of course, the single muon trigger efficiency measurement does not suffer from this correlation. Due to the correlation of the muons, the distribution within a single di-muon trigger efficiency bin can differ from the distributions in the corresponding single muon trigger efficiency bins. This is discussed in more detail below. Therefore, the trigger efficiencies within a single bin should be preferably flat, otherwise systematic discrepancies are introduced. The latter are minimised

[4] The MC samples used in this section are summarised in Appendix D.

by choosing the optimised binning (cf. Section 4.3.5).
MC samples with other physics content ($WW$ and $t\bar{t}$) and two isolated muons in the final state have also been tested. These MC samples do not have the correlation drawback, but the di-muon trigger efficiencies can not be determined in an appropriate binning with enough statistics due to the "missing" correlation. Thus, in the following, only results for the $Z^0 \to \mu\mu$ MC sample are shown. This issue of limited statistics for an appropriate binning of the di-muon trigger efficiencies shows the importance of the factorisation of the di-muon trigger efficiencies.
The single muon trigger efficiencies are determined on 20 % of the $Z^0 \to \mu\mu$ MC sample and the rest of the sample is used for the di-muon trigger efficiency measurement. The distribution of the absolute difference between the directly measured di-muon trigger efficiencies and the product of the corresponding single muon trigger efficiencies is shown in Figure 5.2. Only di-muon trigger efficiency bins with a minimum of 30 di-muon events, $N_{\mathrm{di}}$, are considered and the distribution is shown separately for bins with different statistics ($30 \leq N^{\mathrm{di}}_{\mathrm{trials}} < 50$, $50 \leq N^{\mathrm{di}}_{\mathrm{trials}} < 100$ and $N^{\mathrm{di}}_{\mathrm{trials}} > 100$).
A comparison based on the pulls (similar to Equation 4.7) is not appropriate, because the di-muon trigger efficiency bins do not have enough statistics that a Gaussian approximation is justified.
Simulations have shown that the expected mean of the distribution of the pulls differs systematically from zero if the statistics is not sufficient due to the underlying asymmetric Binomial distribution. On the contrary, the mean of the distribution of the absolute differences is expected to be zero, independent of the statistics. The expected mean of both distributions for two different numbers of di-muon events is shown in Figure 5.3.
Consequently, the deviations of the mean of the absolute difference distribution from zero in Figure 5.2 can be accounted for by systematic discrepancies due to the factorisation in conjunction with the chosen binning. In all three bin, categories the systematic discrepancies are roughly 0.2 %.

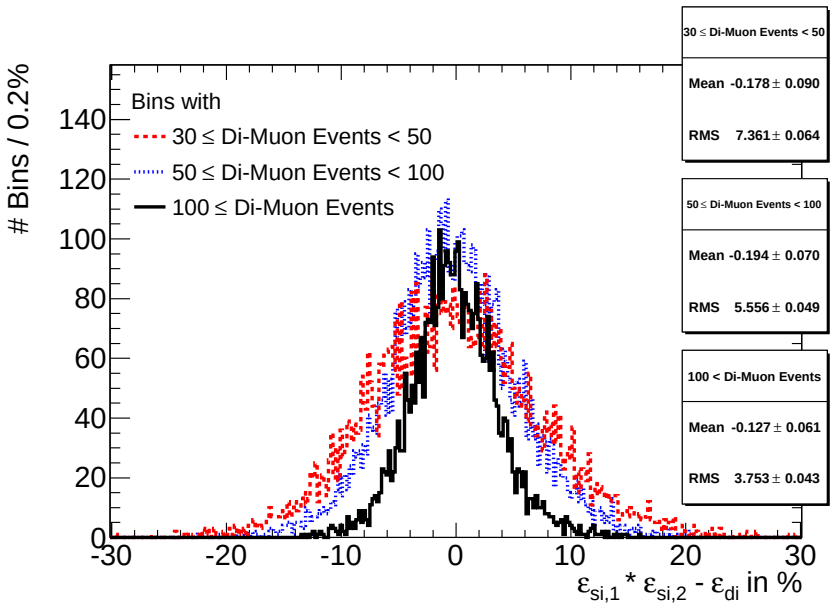


***Figure 5.2.:*** Distribution of the absolute difference in % between the directly measured EF_2mu10_loose trigger efficiencies and the product of the EF_mu10_loose trigger efficiencies, both determined with the Monte Carlo Counting method on a $Z^0 \rightarrow \mu\mu$ MC sample. The efficiencies are compared on a bin-by-bin basis. The distributions for di-muon trigger efficiency bins with different di-muon event statistics is shown separately. The higher the available statistics, the smaller are the statistical uncertainties and the narrower are the distribution of the difference.

In order to check if the observed deviation of the di-muon trigger efficiencies from the product of the corresponding single muon trigger efficiencies is larger than expected from statistical fluctuations only, the fraction of bins where the difference lies in the 1- and 2-$\sigma$ intervals of the measurements can be considered. This fraction is given in Table 5.1 for the three bin categories. The observed differences are slightly larger than expected. A possible explanation are the different muon distributions within a single bin of the single and di-muon trigger efficiencies in conjunction with the finite binning. The different distributions can be inferred from Figure 5.4 showing exemplarily the distribution of the high-$p_T$ muon in $\eta$ and $\phi$ for bins with $N^{\text{di}}_{\text{trials}} > 30$, where the low-$p_T$ muon direction is fixed in a certain $\eta$-$\phi$ range. Only bins corresponding to muons with opposite directions fulfill the minimum statistics requirement. While the distributions of the muons for the single muon trigger efficiency measurements are rather flat, the distribution of the muons for the di-muon trigger efficiency measurements reflect the back-to-back topology. Hence, the distributions in the bins is also different and

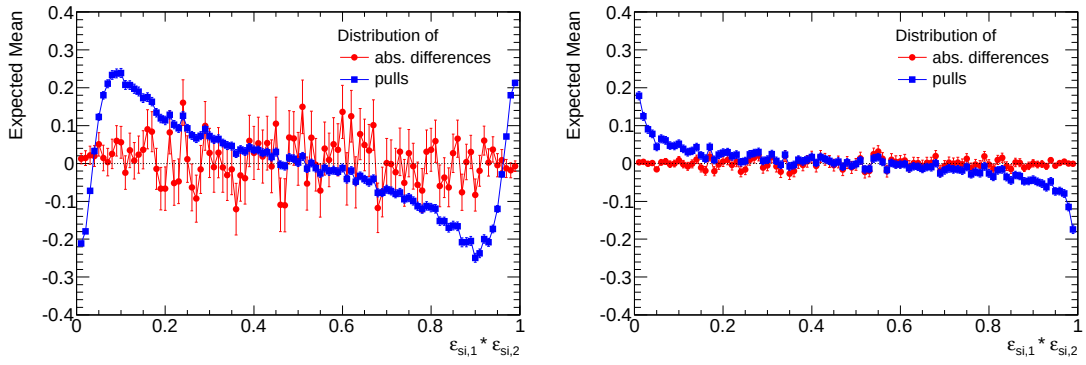


(a) $N^{\text{di}}_{\text{trials}} = 50$ (b) $N^{\text{di}}_{\text{trials}} = 1000$

***Figure 5.3.:*** Expected mean of the distribution of the absolute difference (red circle marker) between the product of the single muon trigger efficiencies $\epsilon_{\text{si},1} \cdot \epsilon_{\text{si},2}$ and the simulated di-muon trigger efficiency measurement (drawn from a Binomial distribution) for different numbers of di-muon events $N^{\text{di}}_{\text{trials}}$ as a function of the assumed product of the single muon trigger efficiencies. Additionally, the mean of a pull distribution (blue square marker) is shown, where the pulls are defined similarly as in Equation 4.7.
The systematic discrepancy of the expected mean of the pull distribution increases if $\epsilon_{\text{si},1} \cdot \epsilon_{\text{si},2}$ approaches 0 or 1, because the underlying Binomial distribution becomes more asymmetric. The reversing behaviour at $\epsilon_{\text{si},1} \cdot \epsilon_{\text{si},2}$ close to 0 and 1 is also an artifact of the asymmetric Binomial distribution and occurs if it becomes possible that zero or all events are triggered. Therefore, this reversing behaviour is not visible in the right plot due to the higher statistics and the chosen sampling.

small variations in the trigger efficiencies within a single efficiency bin lead to discrepancies between the measured di-muon trigger efficiencies and the product of the single muon trigger efficiencies exceeding the statistical fluctuations.

| Bins | $1\,\sigma$-Interval (expected: 68.27 %) | $2\,\sigma$-Interval (expected: 95.45 %) |
|---|---|---|
| $30 \leq N_{\text{di}} < 50$ | $65.3^{+0.7}_{-0.6}$ | $94.1^{+0.3}_{-0.3}$ |
| $50 \leq N_{\text{di}} < 100$ | $65.8^{+0.7}_{-0.6}$ | $93.8^{+0.4}_{-0.3}$ |
| $N_{\text{di}} > 100$ | $63.4^{+0.9}_{-0.8}$ | $92.7^{+0.5}_{-0.5}$ |

***Table 5.1.:*** Fraction of bins in which the difference between EF_2mu10_loose trigger efficiency and the product of the EF_mu10_loose trigger efficiencies lies in the 1- and 2-$\sigma$ uncertainty intervals of the measurements. Bins with different di-muon event statistics are distinguished.

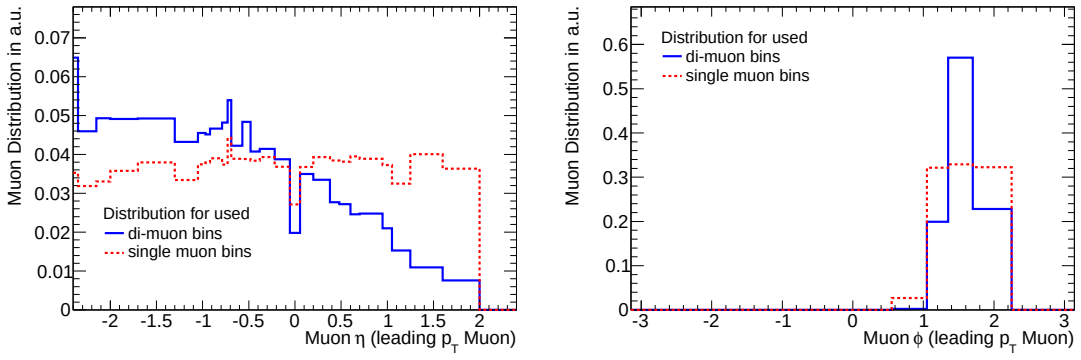


(a) as a function of muon $\eta$ (b) as a function of muon $\phi$

***Figure 5.4.:*** Distribution of the muons used to measure the single and di-muon trigger efficiencies as a function of (a) $\eta$ and (b) $\phi$ for the high-$p_T$ muon, where for the low-$p_T$ muon $-1.7 < \eta < -1.3$ and $-1.8 < \phi < -1.33$ is required. The binning is the same as used for the comparison in Figure 5.2.

### 5.3.3. Comparison of Event Yields from Factorisation and Trigger Simulation on Monte Carlo

The test of the factorisation hypothesis presented in the previous section suffers from the limited statistics and the amount of bins needed for the di-muon trigger efficiencies. To overcome this issue of the direct measurement of di-muon trigger efficiencies, the event yields from the di-muon trigger simulation and the event yields from reweighting (cf. Section 4.3.5) the MC events according to their probability to issue the di-muon trigger, given by Equation 5.4, are compared. The single muon trigger efficiencies for the factorisation of the di-muon trigger efficiencies are determined on a MC $Z \to \mu\mu$ sample and then applied to other MC samples with different physics processes ($Z \to \mu\mu$, $WW$ $WZ$, $ZZ$ and $t\bar{t}$). A list of all used MC samples is summarised in Appendix D.

For single muon triggers it has been shown that the reweighting approach gives reliable estimates for the event yields [117]. In the following, it is tested if the same holds for the di-muon triggers and their factorisation. For this purpose, a similar procedure as in [117] is used. The procedure and the arising uncertainties are summarised briefly in the following. Then the results are presented.

**Procedure**

First, the single muon trigger efficiencies are determined on the MC $Z \to \mu\mu$ sample. Then events with two/three/four combined, isolated muons in $p_T$ plateau are selected. The expected number of the selected events passing the di-muon trigger is calculated by reweighting the events according to their probability to be seen by the di-muon trigger using Equation 5.4. In addition, the number of selected events passing the di-muon trigger simulation, where at least two offline muons match different online muons, is counted. These two numbers are called *event yields*. Finally, the comparison between both numbers shows if the event yields from the di-muon trigger simulation can be reproduced by reweighting the events according to the factorisation hypothesis.

**Uncertainty of Event Yields from Reweighting**

The uncertainties from the single muon trigger efficiency measurements eventually result in uncertainties of the event yields. The statistical uncertainties associated to different bins are uncorrelated, while the uncertainties for muons with the same properties, which end up in the same efficiency bin, are completely correlated. This has to be taken into account for the estimation of the uncertainties of event yields from reweighting. A linear addition of the uncertainties of the event weights for each event overestimates (full correlation) the total statistical uncertainty, while adding them in quadrature underestimates (no correlation) the total statistical uncertainty of the event yields. To take the correlations approximately into account the same approach as described in [117] is chosen.

The event weights $W_{\text{sisi}}$ are given by the probability that the event is selected by the di-muon trigger, cf. Equation 5.4. The total event yield $Y$ is calculated by

$$Y = \sum_{i=1}^{N} W_{\text{sisi}}, \tag{5.5}$$

where the sum is over all selected events $N$. To estimate the uncertainty $\hat{\sigma}_Y$ of the total event yield, a histogram with the same binning as for the single muon trigger efficiencies is used. For each selected event the contribution from each of the muons in the event is added to the content of the bins in the additional histogram corresponding to the properties of the muons. The contribution $\Delta W_{\text{sisi}}^{\text{cont}}$

of the $k$-th muon is given by

$$\Delta W_{\mathrm{sisi}}^{\mathrm{cont}} = \frac{\partial W_{\mathrm{sisi}}}{\partial \varepsilon_{\mathrm{si,k}}} \cdot \hat{\sigma}_{\varepsilon_{\mathrm{si,k}}}|_{\varepsilon_k = \hat{\varepsilon}_k}, \tag{5.6}$$

where $\hat{\sigma}_{\varepsilon_{si,k}}$ is the estimated uncertainty of the single muon trigger efficiency $\varepsilon_{si,k}$ as given in Equation 4.6. For completeness, the partial derivative with respect to the single muon trigger efficiency $\varepsilon_{si,k}$ is given by

$$\frac{\partial W_{\mathrm{sisi}}}{\partial \varepsilon_{\mathrm{si,k}}} = \sum_{\substack{i=1 \\ i \neq k}}^{N} \varepsilon_{\mathrm{si,i}} \prod_{\substack{j=1 \\ j \neq i, j \neq k}}^{N} (1 - \varepsilon_{\mathrm{si,j}}). \tag{5.7}$$

After all events are processed the contents of all bins in the additional histogram are added in quadrature. The procedure described above corresponds to a first order approximation of the covariance of the different event weights.

**Uncertainty of event yields from trigger simulation**

The number of events passing the di-muon trigger simulation is not expected to be perfectly equal to the sum of event weights obtained from the reweighting procedure even if the event weights were exactly known, because the total number of events passing the di-muon trigger simulation is distributed according to a Binomial distribution. The Binomial uncertainty $\sigma_{N_{\mathrm{di}}}$ of this distribution is estimated by

$$\hat{\sigma}_{N_{\mathrm{di}}} = \sqrt{N \cdot p \cdot (1-p)} = \sqrt{N \cdot \left( \frac{Y}{N} - \frac{Y^2}{N^2} \right)}, \tag{5.8}$$

where $N$ is the number of selected events before the trigger decision, $Y$ the event yield from the reweighting given by Equation 5.5. The ratio $p = Y/N$ gives the fraction of events passing the simulated di-muon trigger expected from the reweighting.

**Results**

At first, the reweighting procedure for the di-muon trigger is tested on the same MC $Z \to \mu\mu$ sample the single muon trigger efficiencies are determined from. This keeps the systematic uncertainties introduced by different muon distributions in conjunction with the finite binning at a minimum. Besides testing the factori-

sation hypothesis, this allows for a test of the uncertainty estimation described above. For this purpose, the distribution of the significance of the difference between the event yields from the di-muon trigger simulation and the reweighting procedure is examined.
The single muon trigger efficiencies are estimated on 20% of the MC $Z \to \mu\mu$ sample, containing roughly $1.5 \cdot 10^6$ isolated, combined muons in the $p_T$ plateau passing the selection criteria for the single muon trigger efficiency measurement. The remaining MC sample is split into 1000 subsamples such that each subsample contains roughly $N = 2000$ events with exactly 2 muons, which are isolated, combined and in the $p_T$ plateau. Roughly $W = 1300$ of these events pass the simulated EF_2mu10_loose trigger with two matching online muons. For the single muon trigger efficiencies the optimised binning (cf. Section 4.3.5) is used.
For each subsample the two event yields described above are compared. For this purpose, the significance of the difference, called pull $S_{\text{yield}}$, is defined as

$$S_{\text{yield}} = \frac{\left(\sum_{k=1}^{N} W_{\text{sisi}}\right) - N_{di}}{\sigma_{\text{yield}}}, \tag{5.9}$$

where $\sigma_{yield}$ is the uncertainty of the difference between both event yields, estimated by

$$\hat{\sigma}^2_{\text{yield}} \;=\; \left(\hat{\sigma}_Y\right)^2 + \left(\hat{\sigma}_{N_{\text{di}}}\right)^2 . \tag{5.10}$$

The distribution of the pulls $S_{\text{yield}}$ and a Gaussian fit is shown in Figure 5.5. The reweighting procedure slightly underestimates the event yield. The width of the distribution is slightly narrower than expected from statistical fluctuations only (standard Gaussian with zero mean and unity width), indicating that the estimated uncertainties are slightly overestimated. Nevertheless, the estimated uncertainties seem reasonable.
For the complete sample (sum of all 1000 subsamples), the reweighting procedure expects $W_{\text{total}} = (1,330.9 \pm 1.1) \cdot 10^3$ selected events passing the di-muon trigger, while $N_{\text{di,total}} = (1,336.7 \pm 0.7) \cdot 10^3$ actually issued the simulated di-muon trigger. Due to the large statistics for the total sample the uncertainty of the reweighting procedure dominates, while for the smaller subsamples the Binomial uncertainty of the di-muon trigger simulation dominates.

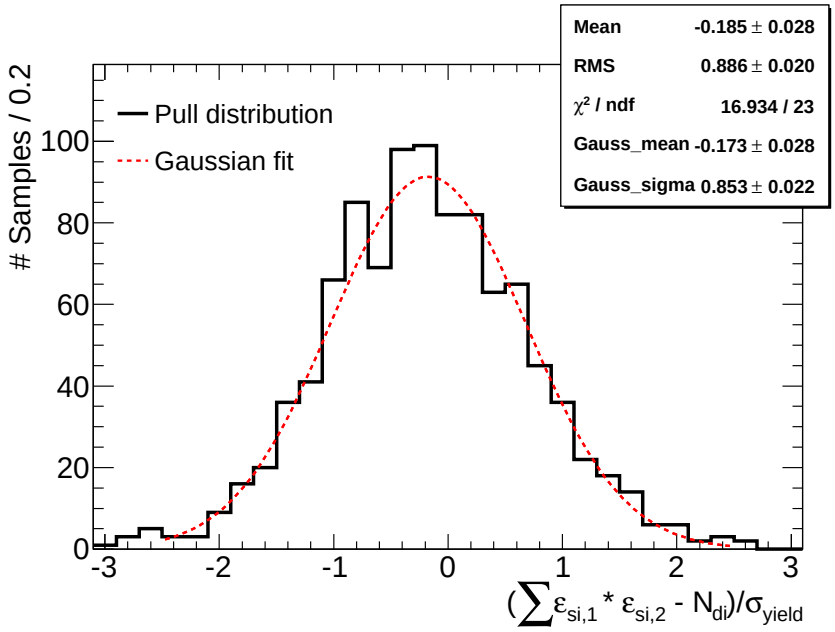


***Figure 5.5.:*** Distribution of the pulls $S_{\text{yield}}$, as defined in Equation 5.9, for 1000 $Z \to \mu\mu$ MC subsample. The distribution is fitted with a Gaussian in the range of [-2.5,2.5].

In a next step, the factorisation hypothesis is tested by reweighting MC samples containing other physics processes with single muon trigger efficiencies determined on the $Z \to \mu\mu$ MC sample. The procedure is the same as before, but the full $Z \to \mu\mu$ MC sample is used for the single muon trigger efficiency measurements. In Table 5.2, the outcome for different MC samples and different muon multiplicities is summarised. The observed agreement between the event yields is good. For most MC samples the relative difference is less than 1 %, but slightly larger than expected from statistical fluctuations only ($|S_{\text{yield}}|$ larger than expected).
In addition to the total event yield, the distributions of the event yields in the relevant muon properties ($p_T$, $\eta$ and $\phi$) is examined in Figure 5.6. A bin-by-bin comparison in a binning with 200 equidistant bins in each relevant muon property is shown exemplarily for the MC $WW$ sample. The uncertainty in each bin is estimated as for the total event yield. Since the binning chosen for the plots (200 equidistant bins) differs from the binning used in the reweighting procedure (optimized binning, cf. Section 4.3.5), the event yield from neighbouring bins can be correlated. However, the uncertainties arising from this correlation is rather small, because the combined uncertainties are dominated by the uncertainties

| Sample | $n_{\text{Muons}}$ | Reweighting | Simulation | Rel. Diff. [%] | $S_{\text{yield}}$ |
|---|---|---|---|---|---|
| $WW$ | 2 | $39794.2 \pm 12.3$ | $39592 \pm 116.5$ | 0.51 | 1.73 |
| $WZ$ | 2 | $43360.4 \pm 13.8$ | $43331 \pm 123.2$ | 0.07 | 0.24 |
| $WZ$ | 3 | $5525.3 \pm 0.8$ | $5530 \pm 23.1$ | $-0.08$ | $-0.20$ |
| $ZZ$ | 2 | $32187.6 \pm 10.3$ | $32079 \pm 106.2$ | 0.34 | 1.02 |
| $ZZ$ | 3 | $823.1 \pm 0.2$ | $817 \pm 8.7$ | 0.74 | 0.71 |
| $ZZ$ | 4 | $602.6 \pm 0.1$ | $597 \pm 4.2$ | 0.93 | 1.37 |
| $t\bar{t}$ | 2 | $117642.8 \pm 41.0$ | $117337 \pm 208.7$ | 0.26 | 1.44 |
| $t\bar{t}$ | 3 | $568.1 \pm 0.2$ | $577 \pm 8.0$ | $-1.56$ | $-1.12$ |

***Table 5.2.:*** Outcome of the comparison between the event yields from the di-muon trigger simulation and the reweighting procedure according to the factorisation hypothesis using various MC samples containing different physics processes and requiring different muon multiplicities in the final state.
The uncertainties of the reweighting procedure and the simulation are explained in the text, as well as the significance $S_{\text{yield}}$ of the difference between both event yields. The relative difference (Rel. Diff.) between both event yields is given in %.

arising from the trigger simulation. Therefore, these uncertainties are neglected. The distributions of the event yields in the relevant muon properties from the reweighting procedure and the di-muon trigger simulation show a good agreement within the estimated uncertainties. However, in the barrel, larger differences accumulate, but this is expected due to the more pronounced inhomogeneities of the trigger performance (cf. Figure 4.6) in this part of the detector. This discrepancies become smaller if a more fine-grained binning for the single muon trigger efficiencies used in the reweighting procedure is chosen. For such a fine-grained binning, where each bin of the optimised binning for the single muon trigger efficiencies is divided in a few smaller bins, the distribution of the event yields is shown in Figure 5.6 (d).

In summary, a good agreement is observed between the event yields from applying the reweighting approach using the factorisation hypothesis for the di-muon trigger and the trigger simulation. The estimated uncertainties seem reasonable, though slightly overestimated. Additionally, it can be deduced that the single muon trigger efficiencies determined on MC can be used to model the decision of the di-muon trigger on other MC samples with different physics content.

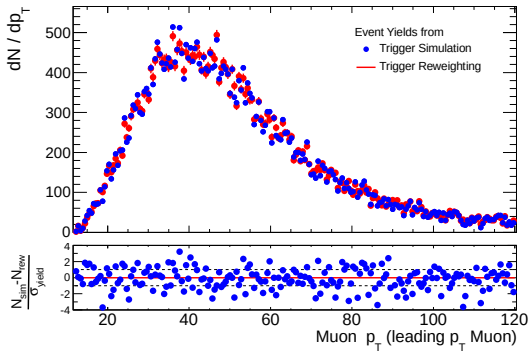


(a) event yields vs. muon $p_T$

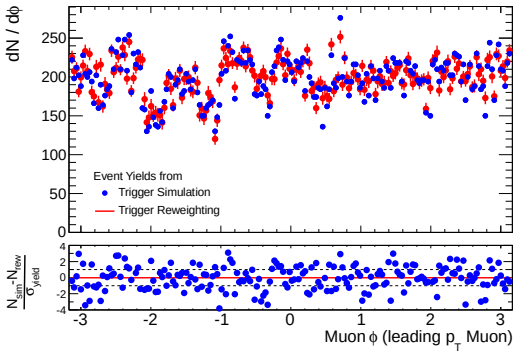


(b) event yields vs. muon $\phi$

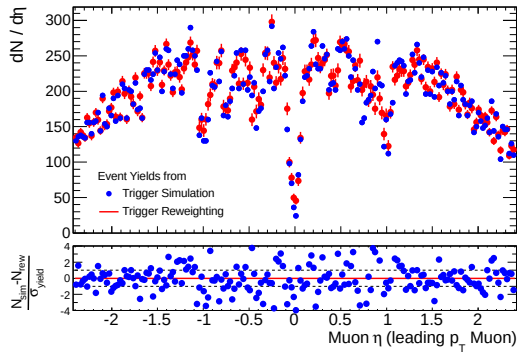


(c) event yields vs. muon $\eta$

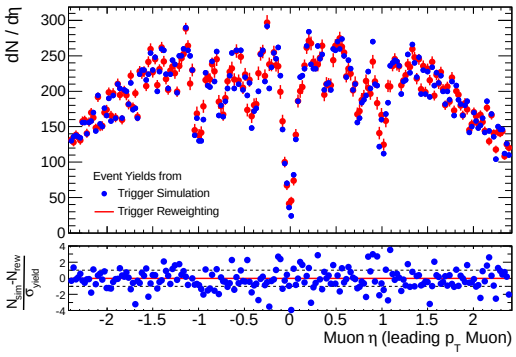


(d) event yields vs. muon $\eta$ (finer efficiency binning)

***Figure 5.6.:*** Distributions for the event yields from the reweighting procedure and the di-muon trigger simulation as function of (a) $p_T$, (b) $\eta$ and (c) $\phi$ of the leading muon in 200 equidistant bins. The single muon trigger efficiencies for the reweighting procedure according to the factorisation hypothesis are determined in the optimised binning (cf. Section 4.3.5). Additionally, the distributions as function of muon $\eta$, where the event yields from the reweighting procedure are determined with a more fine-grained binning for the single muon trigger efficiencies, is shown in (d).

### 5.3.4. Comparison of Factorised and Directly Measured Di-Muon Trigger Efficiencies on Data

In the previous sections, it has been shown that the factorisation hypothesis for the di-muon trigger holds for simulated trigger decisions. In the following, the factorisation hypothesis is tested for trigger efficiencies measured on data.
The single and di-muon trigger efficiencies are measured on data from the periods 2011B and 2011D to 2011K, corresponding to $2.28\,\mathrm{fb}^{-1}$. The data from period 2011L onwards is not used, because from then on the EF_2mu10_loose and EF_mu10_loose trigger chains were seeded by L1_2MU4 and L1_MU4, respectively. Systematic uncertainties arising from merging the trigger efficiencies from these different trigger configurations are avoided.
In the considered data sample, roughly 15000 di-events issued the EF_2mu10_loose trigger and in addition one of the orthogonal triggers. As reference, roughly 500000 events issued the EF_mu10_loose trigger and an additional orthogonal trigger. To be statistically independent, the single muon trigger efficiencies are measured only on events, which are not used for the di-muon trigger efficiency measurements. These are events containing one and three or more muons.
The factorisation hypothesis is first tested by comparing the projections of the trigger efficiencies onto one of the binning dimensions. In a next test, a bin-by-bin comparison similar to the one presented in Section 5.3.2 is performed. However, due to the limited statistics a coarse-grained binning for the trigger efficiency measurement is used.

#### Comparison of Transverse Momentum Turn-On Curves

The di-muon trigger efficiencies are binned in $p_T$ of both muons, while the single muon trigger efficiencies depend only on $p_T$ of one muon. Thus, the di-muon trigger efficiencies are compared with the products of the single muon trigger efficiencies as a function of $p_T$ of the low-$p_T$ muon, while the high-$p_T$ is required to be in the plateau (high-$p_T$ muon: $p_T > 12\,\mathrm{GeV}$). This comparison is shown for isolated, combined muons in Figure 5.7. Since the muon $\eta$ and $\phi$ distributions are different in events selected to measure the single and di-muon trigger efficiencies in conjunction with the trigger inhomogeneities, the $p_T$ turn-on curves are compared separately for both muons in the barrel region and for both muons in the endcap region. This keeps the impact of different muon $\eta$ distributions small,

while keeping sufficient statistics. The turn-on curves of the EF_2mu10 trigger efficiencies and the products of the EF_mu10_loose trigger efficiencies show a good agreement.

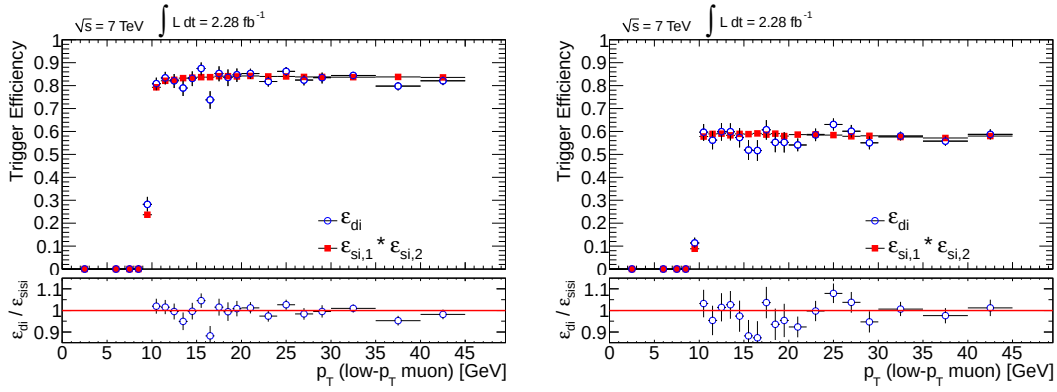


(a) barrel (b) endcaps

***Figure 5.7.:*** Trigger efficiencies of the EF_2mu10_loose trigger ($\varepsilon_{\mathrm{di}}$, blue circles) as a function of $p_T$ of the low-$p_T$ muon, while the high-$p_T$ muon is required to be in the plateau ($p_T > 12\,\mathrm{GeV}$), compared with the products of the EF_mu10_loose trigger efficiencies ($\varepsilon_{\mathrm{si}}$, red squares) for two isolated, combined muons in the barrel region (a) and in the endcap region (b). The trigger efficiencies are measured in 2011 ATLAS collisions data (period 2011B and 2011D to 2011K). The error bars represent the statistical uncertainty only.

### Comparison on a Bin-By-Bin Basis

In the following, the di-muon trigger efficiencies and the product of the single muon trigger efficiencies measured on data are compared on a bin-by-bin basis, similar to the comparison presented in Section 5.3.2. The binning has to be chosen coarser-grained as before in order to determine the di-muon trigger efficiencies with an appropriate statistical uncertainty. The chosen binning has for each of the muons 5 bins in $\phi$, 9 bins in $\eta$ (3 bins for each endcap and the barrel) and 1 bin for the whole $p_T$ plateau.

The distribution of the absolute difference between the directly measured di-muon trigger efficiencies and the product of the corresponding single muon trigger efficiencies is shown in Figure 5.2. Only di-muon trigger efficiency bins with a minimum of 10 di-muon events are considered. The mean is roughly zero, however, a significant larger discrepancy as in Section 5.3.2 is observed. A possible explanation for this discrepancy is the coarser-grained binning, such that the in-

homogeneities in the muon trigger performance are not as well covered as for the optimised binning. In conjunction with differences in the muon distributions of the samples used for the single and di-muon trigger efficiency measurements systematic deviation are possible. Thus, the trigger efficiencies measured on data are not incompatible with the factorisation hypothesis, but suffer from low statistics.

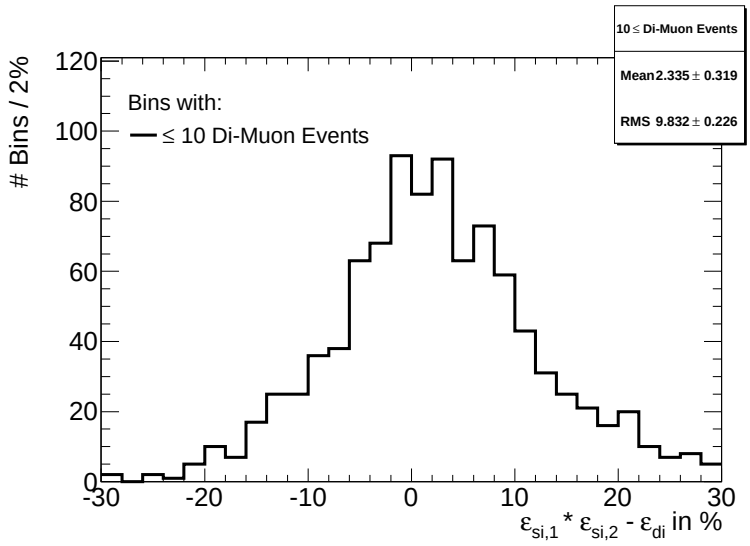


***Figure 5.8.:*** Comparison of the directly measured EF_2mu10_loose trigger efficiencies and the product of the EF_mu10_loose trigger efficiencies, both determined with the Orthogonal Trigger method from 2011 ATLAS collisions data (period 2011B, 2011D to 2011K), on a bin-by-bin basis. Only di-muon trigger efficiency bins with at least 10 di-muon events are used.

## 5.4. Conclusion

The performed tests for the factorisation hypothesis show that the di-muon trigger efficiencies can be modelled from the single muon trigger efficiencies for muons which are non-collinear. The systematic uncertainties introduced due to this modelling are at the order of 1 % or even less if enough statistics are available for a binning covering the trigger inhomogeneities adequately. This systematic uncertainty is of the same order of magnitude as the systematic uncertainty for the trigger efficiency measurements introduced by the method used to obtain the samples from which the efficiencies are measured (cf. Section 4.3.4). Therefore, all presented tests are compatible with the factorisation hypothesis. A previous version of this study has been summarised in an ATLAS internal note [118].

# 6. Application of Muon Triggers in a Search for Supersymmetry

In the previous chapters (cf. Section 4 and 5), the output rates and efficiencies of single muon and di-muon triggers as well as their application in physics analysis is discussed. In this chapter, a cost-benefit analysis of different single and multi-muon triggers is performed.
The cost of triggers is measured in terms of their output rate and their benefit is quantified with regard to the expected significance of a benchmark discovery channel for Supersymmetry. For this purpose, a search for Supersymmetry with three leptons and $E_T^{miss}$ in the final state, similar to the analysis presented in [119], is chosen.

## 6.1. Studied Muon Triggers

In the past, most analyses at ATLAS with at least one lepton in the final state have been performed on a dataset collected using unprescaled single lepton triggers with the least restrictions for a given maximum trigger rate. As discussed in Section 4.2 using single muon triggers as an example, these lowest unprescaled triggers reach the assigned bandwidth consumption (cf. Section 3.3) if the instantaneous luminosity is increased. Therefore, other muon trigger strategies that comply with the limitations also for higher instantaneous luminosities have to be studied.
The muon triggers discussed in this chapter are various single and multi-muon

triggers. As a reference, the single muon trigger EF_mu18, which was unprescaled in the first half of 2011 data-taking, is used throughout this chapter. The output rate of this reference trigger is taken to be the maximum allowed rate. The other studied single muon triggers triggers are chosen, such that they differ from the reference trigger in exactly one trigger requirement ($p_T$-threshold, isolation criteria). For the multi-muon triggers lower $p_T$-threshold than the reference trigger for each of the muons are chosen. In addition to actually implemented triggers also triggers, which are not implemented, are studied. The latter triggers are referred to as *virtual* triggers in the following and are denoted by a star ($^*$). All triggers studied in this chapter are outlined below.

- EF_mu18: reference single muon trigger with a $p_T$-threshold of 18 GeV.
- EF_mu22: a single muon trigger with a higher threshold (22 GeV) than the reference trigger.
- EF_mu15: a single muon trigger with a lower threshold (15 GeV) than the reference trigger. This trigger has to be prescaled such that its output rate is below the maximum allowed rate (defined by the reference trigger, see Section 6.2).
- EF_mu18i$^*$: a single muon trigger with the same threshold as the reference trigger, but an additional isolation requirement. This trigger is not implemented, but its rate and efficiency can be inferred from EF_mu15i (15 GeV threshold and isolation requirement), which is implemented.
- EF_mu16c22f$^*$: a single muon trigger with an $\eta$ dependent threshold, 16 GeV is the central region and up to 22 GeV in the forward region. This trigger is not implemented. The thresholds are chosen such that it has a similar output rate as the reference trigger (see Section 6.2). Its efficiency can be inferred from EF_mu15.
- EF_mu22c16f$^*$: a single muon trigger similar to EF_mu16c22f, but with a threshold of 22 GeV is the central region and 16 GeV in the forward region.
- EF_2mu10_loose: di-muon trigger with a threshold of 10 GeV for each of the two muons.

- EF_3mu6: tri-muon trigger with a threshold of 6 GeV for each of the three muons.

The stated $p_T$-thresholds are the nominal thresholds. The exact $p_T$ thresholds ($\eta$ dependent and usually slightly below the nominal thresholds) and the begin of the trigger efficiency plateaus are summarised for all studied triggers in Appendix B. Besides these triggers, the combination (logical `OR`) of single and multi-muon triggers is studied, using the example of combining EF_mu22 and EF_2mu10_loose as well as EF_mu18i and EF_2mu10_loose.

## 6.2. Output Rates of Studied Muon Triggers

In the presented cost-benefit analysis, the output rates of the muon triggers are used to quantify the costs of the triggers. For the implemented triggers the rate can be measured from data, as explained in Section 4.2, while for the virtual triggers the output rate has to be estimated. For this purpose, the output rates of other triggers of the same type, but with a lower threshold, can be used. This is discussed in detail below.

All studied muon triggers employ the same reconstruction algorithms on EF/L2 (besides additional criteria: isolation, muon multiplicity), but test the online reconstructed muons for other threshold hypotheses. Therefore, the trigger decision on EF/L2 can be emulated from the online measured $p_T$ of a trigger with a lower threshold. Due to the good muon $p_T$ resolution on L2 [120, 121], it is generally sufficient to apply this online $p_T$ requirement only on EF level. For emulating the L1 trigger decision, the situation is different due to the coincidence requirements (cf. Section 3.3.1). However, in this thesis, the output rates are always estimated from trigger chains with the same L1 thresholds, such that an online $p_T$ requirement on EF level is sufficient.

To apply online $p_T$ requirements, the trigger rates saved in the COOL database (cf. Section 3.3.3) are not sufficient, because no information about the measured online muons are saved. Hence, these studies are performed on DPDs, where the trigger decisions and the measured muon properties are read out using the `TrigDecisionTool`, like in Section 4.3.4.

The estimator for the output rate described above can be tested by predicting the rate of a trigger for which the actual trigger rate can also be measured directly. For

example, the output rate of the EF_mu22 trigger can be predicted from EF_mu18 with the corresponding EF level $p_T$ requirements ($\eta$ dependent and slightly below 22 GeV, see Appendix B). This is illustrated in Figure 6.1, where the rate of the EF_mu18 trigger is shown as a function of the highest measured muon $p_T$ on EF level averaged over the same run (run 184169) as in Section 4.2. Since the run, over which the trigger rates are averaged, contains sufficient statistics, the statistical uncertainties for the estimates rates are negligible. Therefore, no uncertainties for the rates are given in the following.
The estimated EF_mu22 output rate is 18.9 Hz, which is roughly the same rate as the actual measured rate of 18.4 Hz. The small difference is caused by the approximations, e.g. neglected L2 trigger decisions. Similarly, the output rate of the virtual EF_mu18i trigger can be estimated from the EF_mu15i trigger decisions, also shown in Figure 6.1. Requiring the highest online muon $p_T$ above the same thresholds as the EF_mu18 trigger gives an estimated EF_mu18i output rate of 9.8 Hz.

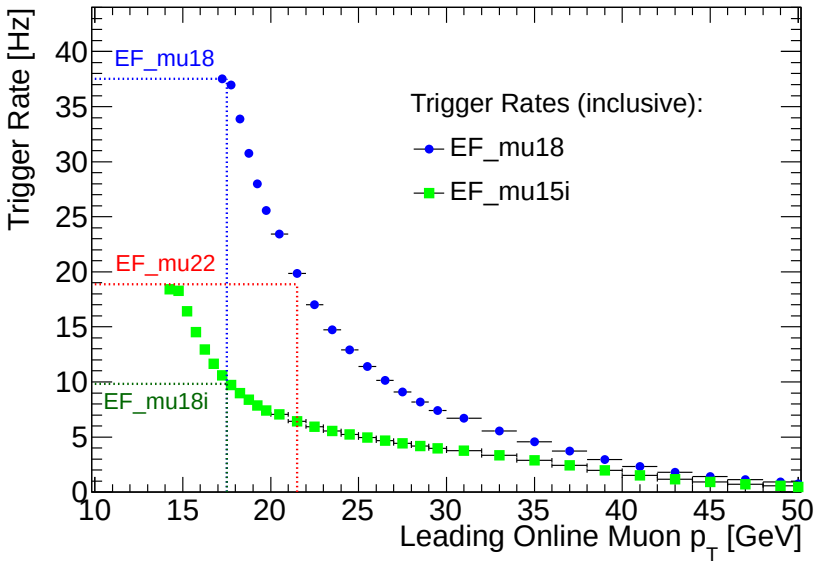


***Figure 6.1.:*** Inclusive output rates of the EF_mu18 and EF_mu15i trigger averaged over all events in run 184169 as a function of the highest measured $p_T$ on EF level. Events with a certain measured highest online $p_T$ contribute to the output rates below this online $p_T$ value.

For prescaled triggers, the expected average output rate $R_{\text{ps corrected}}$ without any

prescale can be estimated from the output rate of the prescaled triggers and the prescale factor $\mathrm{ps}_i$, which is saved for each luminosity block in the COOL database, by

$$R_{\mathrm{ps\,corrected}} = \frac{\sum_i N_i \cdot \mathrm{ps}_i}{\sum_i \mathrm{LB}_i^{\mathrm{length}}}, \tag{6.1}$$

where $N_i$ is the number of triggered events in the $i$-th luminosity block and $\mathrm{LB}_i^{\mathrm{length}}$ is its duration. The uncertainty $\sigma_{\mathrm{ps\,corrected}}$ of this prescale corrected output rate increases for higher prescale factors and is estimated by

$$\hat{\sigma}_{\mathrm{ps\,corrected}} = \frac{\sqrt{\sum_i N_i \cdot (\mathrm{ps}_i)^2}}{\sum_i \mathrm{LB}_i^{\mathrm{length}}}, \tag{6.2}$$

where it is assumed that the observed number of events follows a Poisson distribution. Figure 6.2 shows the output rate of the prescaled EF_mu15 trigger and the expected output rate without any prescales averaged over the same run as before. For comparison, the EF_mu18 output rate is also shown.

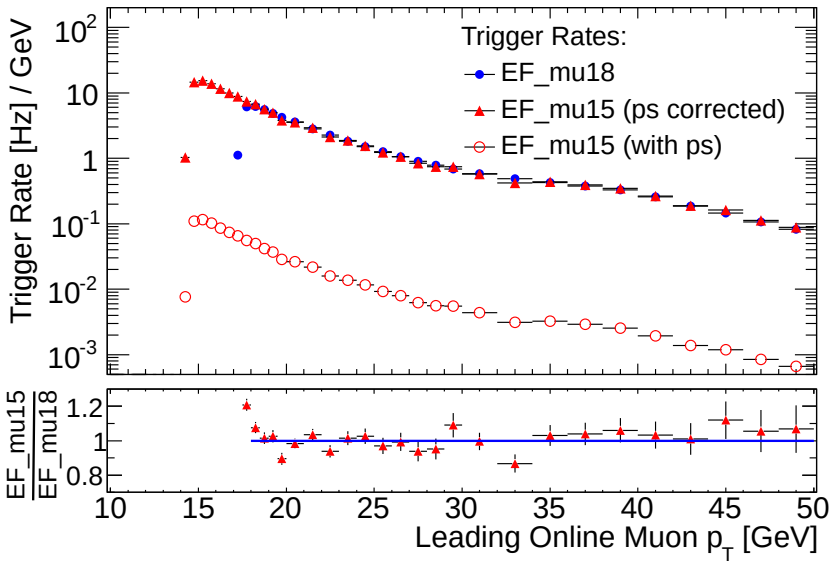


***Figure 6.2.:*** Average output rates of the EF_mu18 and the prescaled (ps) EF_mu15 trigger in run 184169 as a function of the highest measured $p_T$ on EF level. Additionally, the expected output rate of the EF_mu15 trigger without any prescale is shown, estimated as described in the text. The prescale factor for EF_mu15 varies between 101 and 197 in this run. Each event contributes only to the output rate of the bin containing the highest measured online muon $p_T$ in this event.

In contrast to Figure 6.1, each event contributes only to the output rate of the bin containing the highest measured online muon $p_T$, such that the rates of different bins are statistically independent. Above 18 GeV, the expected output rate of the EF_mu15 trigger (prescale corrected) is consistent within the statistical uncertainties [1] with the measured output rate of the (unprescaled) EF_mu18 trigger. A comparison of the expected total output rate of the EF_mu15 trigger (75.4 Hz) and the measured output rate of the EF_mu18 (37.5 Hz) shows that a prescale factor of 2.01 is needed for the EF_mu15 trigger, such that the EF_mu15 trigger obeys the maximum rate limit (EF_mu18 output rate). By taking the direction of the online measured muons into account, the expected output rate for a muon triggers that are active only in a certain region of the detector can be predicted. The decomposition of the prescale corrected output rate of the EF_mu15 trigger into the expected output rate for exclusively the barrel region or endcaps region is illustrated in Figure 6.3.

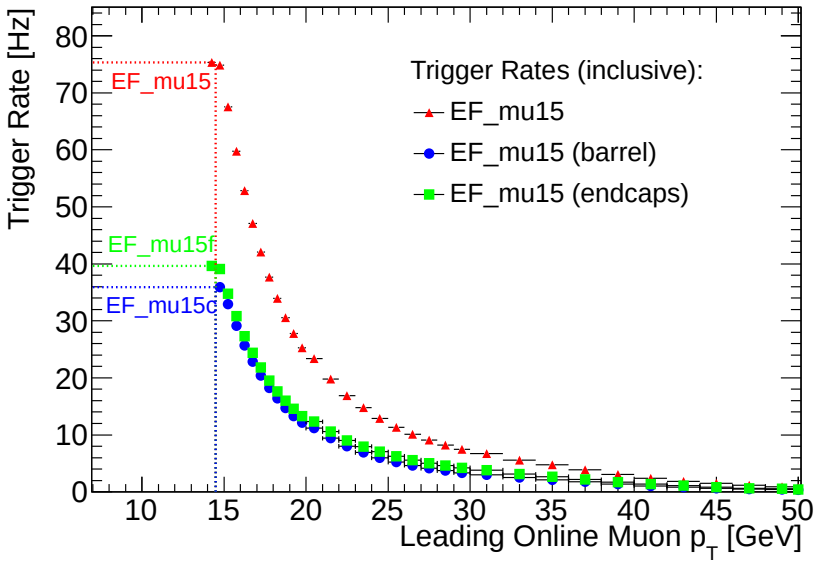


***Figure 6.3.:*** Average inclusive output rates of the prescale corrected EF_mu15 trigger in run 184169 as a function of the highest measured $p_T$ on EF level. Additionally, the expected output rate is decomposed into the contributions from the barrel ($|\eta| < 1.05$) and endcaps region ($1.05 < |\eta| < 2.4$). Event with more than one muon can contribute to the output rate of all triggers shown.

[1] The events used for the estimation of the EF_mu15 trigger rate are also used for the estimation of the EF_mu18 trigger rate. Therefore, both estimated rates are correlated. However, due to the high prescale factors for the EF_mu15 trigger (101 up to 197), the correlation is small.

The sum of both output rates (35.9 Hz in barrel, 39.6 Hz in endcaps) is slightly higher than the rate of the EF_mu15 trigger (75.4 Hz) due to events for which the trigger finds a muon candidate in the barrel and in the endcaps.
Similarly, output rates of triggers with $\eta$ dependent thresholds can be predicted or these triggers can be constructed such that a given output rate is not exceeded, respectively. The $\eta$ dependent thresholds for the virtual triggers EF_mu16c22f and EF_mu22c16f are chosen such that they are nominal 16 GeV (22 GeV) in the central region and up (down) to 22 GeV (16 GeV) in the forward region and that the total output rate is below the maximum allowed output rate (defined by the reference trigger). The exact thresholds can be found in Appendix B. The output rates of all studied triggers are summarised in Table 6.1. Additionally, the ratio of the EF output rate of a trigger $T$ with respect to the EF output rate of the reference trigger is given:

$$r^T = \frac{\text{rate}^T}{\text{rate}^{\text{ref.}}}. \tag{6.3}$$

| Trigger | EF Rate | $r^T$ | Comment |
|---|---|---|---|
| EF_mu18 | 37.5 Hz | 1.00 | reference trigger |
| EF_mu22 | 18.4 Hz | 0.49 | |
| EF_mu18i* | 9.8 Hz | 0.26 | predicted from EF_mu15i |
| EF_mu15ps* | 37.5 Hz | 1.00 | prescale factor of 2.01 |
| EF_mu16c22f* | 37.1 Hz | 0.99 | $\eta$ dependent threshold |
| EF_mu22c16f* | 37.2 Hz | 0.99 | $\eta$ dependent threshold |
| EF_2mu10_loose | 1.9 Hz | 0.05 | di-muon trigger |
| EF_3mu6 | 0.1 Hz | $< 0.01$ | tri-muon trigger |
| EF_mu22 OR EF_2mu10_loose | 19.7 Hz | 0.52 | overlap taken into account |
| EF_mu18i* OR EF_2mu10_loose | 11.3 Hz | 0.30 | overlap taken into account |

***Table 6.1.:*** EF output rates of different muon triggers averaged over run 184169. Additionally, the relative output rate $r^T$ with respect to the reference trigger is given. For virtual triggers, labeled by a star (*), the rate is estimated from output rates of other triggers. The exact trigger configurations are summarised in Appendix B. For the combination of single and di-muon triggers, the overlap between both triggers is taken into account. The statistical uncertainties of the trigger rates are negligible, besides for the tri-muon trigger due to its very small rate. However, the absolute uncertainty of the ratio $r^T$ is negligible. Therefore, the uncertainties of all rates are omitted.

## 6.3. Expected Significance of a Discovery

Particle physics experiments often search for processes that have been predicted but not yet observed, such as the production of supersymmetric particles. The statistical significance of an observed signal can be quantified by means of a $p$-value or its equivalent Gaussian significance. Usually the sensitivity of an experiment is characterised by the expected (e.g. median) significance with which the background-only hypothesis can be rejected for an assumed signal model.
The $p$-value gives the probability, under the assumption of the hypothesis in question, of obtaining data of equal or greater incompatibility with the predictions of the hypothesis. Often the $p$-value is converted into the *significance*, defined as the number of standard deviations $Z$ at which a Gaussian random variable of zero mean has an upper-tail probability equal to the $p$-value [122].
The expected significance of a discovery can be calculated from the number of expected signal and background events, $S$ and $B$, respectively, based on likelihood-based statistical tests, as described in [123]. For sufficiently large MC datasets to determine the expected background and signal events, it can be shown using Wilks' theorem [124] that the median expected significance for Poisson distributed numbers of events is given by

$$\mathrm{med}[Z_W] = \sqrt{2 \cdot [(S+B)\ln(1+S/B) - S]}. \tag{6.4}$$

No systematical uncertainties are included in this significance.
In the limit $S \ll B$, Equation 6.4 gives the widely used formula for Poisson distributed data

$$\mathrm{med}[Z_W] \xrightarrow{S/B \to 0} \frac{S}{\sqrt{B}}. \tag{6.5}$$

In the following, the benefit of a muon trigger is quantified in terms of the amount of data needed to achieve the same median expected significance, given by Equation 6.4, as the reference trigger. For constant beam and detector conditions, the number of expected signal and background events scales linearly with the integrated luminosity. Hence, for $f$ times more integrated luminosity, the median expected significance is

$$\mathrm{med}[Z_W^f] = \mathrm{med}[Z_W(f \cdot S, f \cdot B)] = \sqrt{f} \cdot \mathrm{med}[Z_W(S,B)], \tag{6.6}$$

where med$[Z_W(S,B)]$ is the median expected significance for the number of expected signal and background events, $S$ and $B$, for a reference integrated luminosity. Or put another way, a factor of $f^T$ more integrated luminosity is needed for a trigger $T$ with an expected significance of med$[Z_W^T]$ to give the same expected significance med$[Z_W^{\text{ref.}\cdot}]$ as a reference trigger for a reference integrated luminosity:

$$f^T = \left(\frac{\text{med}[Z_W^{\text{ref.}\cdot}]}{\text{med}[Z_W^{\text{T}\cdot}]}\right)^2, \tag{6.7}$$

where med$[Z_W^T]$ and med$[Z_W^{\text{ref.}\cdot}]$ are calculated for the same integrated luminosity. Note that the factor $f^T$ does not depend on the initially chosen reference integrated luminosity.

## 6.4. Search for Supersymmetry

In order to quantify the benefit of muon triggers using the expected significance, a benchmark analysis has to be chosen. Since single, di- and tri-muon triggers are examined, the search has to have the potential to study all of these triggers. Therefore, a search for Supersymmetry with three leptons and $E_T^{miss}$ in the final state is performed, which is based on [119]. Here, leptons only comprise electrons and muons ($\ell = e, \mu$), including those from $\tau$ decays.

Previous SUSY motivated searches in the tri-lepton final state have been performed at LEP [125], Tevatron[126–129] and LHC [130–132]. The combination of the four LEP experiments yielded a lower chargino mass limit of 103.5 GeV valid for the MSSM [133]. At ATLAS, similar searches have also been performed in a two and four lepton final states [68, 116, 134].

At the LHC, a three lepton signature may arise from decay chains of squarks and gluinos via electroweak gauginos or sleptons, if the squark and gluino masses are within the reach of the LHC. Events with high lepton multiplicity may also originate from the direct production of electroweak gauginos, as depicted in Figure 2.2. The latter type of events can give the first sign of SUSY at the LHC, if SUSY is realised in nature with squarks and gluinos significantly heavier than the electroweak gauginos.

In several SUSY models where the breaking mechanism is explicitly given, like mSUGRA (cf. Section 2.2.4), the mass difference between coloured and non-

coloured sparticles is not large enough to allow for much lighter electroweak gauginos than squarks and gluinos. In the more general framework of the pMSSM (cf. Section 2.2.5), this is perfectly possible. In this thesis, a particular subspace of the pMSSM parameter space is assumed, where a considerable amount of tri-lepton events is produced via the direct production of electroweak gauginos. The assumed SUSY scenario is discussed in Section 6.4.1.
The performed search is designed to discriminate events containing charginos and neutralinos from events due to SM processes. The background from SM processes is estimated from MC only. In Section 6.4.2, the main SM background sources are explained. Since the signal as well as the background are estimated from MC and the expected significance, which is based on the expected signal and background, is of interest for the quantification of the muon triggers' benefit, the expectations from MC are not compared with data. However, the MC expectations are corrected for several aspects which are not well-modelled in MC. The event reconstruction and preselection as well as the applied corrections are outlined in Section 6.4.3. The tri-lepton signal region is defined in Section 6.4.4. The results for the reference trigger (EF_mu18) are discussed in Section 6.4.5. For the other studied muon triggers the expected significance is presented and discussed in Section 6.4.6.

### 6.4.1. Supersymmetry Scenarios

The assumed SUSY scenario is the pMSSM (cf. Section 2.2.5) with heavy gluinos and squarks (above energies accessible at the LHC). The chargino and neutralino sector are dominated by the parameters $M_1$, $M_2$ and $\mu$, and slightly by $\tan(\beta)$. For the parameter grids used in the following the parameters $M_1$, $M_2$ and $\mu$ are varied, while the other parameters are fixed at the electroweak scale.
The mass of the CP-odd Higgs ($m_A$) is set to 500 GeV at the electroweak scale and the stau trilinear coupling $A_\tau$ to zero. The right-handed slepton ($\tilde{e}_R$, $\tilde{\mu}_R$) masses are degenerate and their value is inserted midway between the masses of the two lightest neutralinos. All other mass parameters (for squarks, gluinos and left-handed sleptons) are set to 2 TeV. Maximum mixing in the stop sector is imposed in order to increase the lightest Higgs mass above the LEP direct limit [135] and $\tan(\beta)$ is set to 6 in order to provide a large branching ratio into sleptons of the first and second generation.

Three values of $M_1$ (100 GeV, 140 GeV, 250 GeV) are considered, and for each of these $M_1$ values a two-dimensional grid in $M_2 \times \mu$ is scanned, with 7 values (100 GeV, 110 GeV, 120 GeV, 140 GeV, 160 GeV, 180 GeV, 250 GeV) each, totaling 147 parameter sets. In the following, a set of parameters ($M_1$, $M_2$, $\mu$) is referred to as "grid point".
Some of the grid points are already excluded [68, 119]. However, this signal grid provides a lot of events with multi-muon final state needed for the quantification of the muon triggers' benefit, which is of interest in this thesis.

**Relevant Phenomenology of the Parameter Space Covered by the Signal Grid**

The phenomenology of the different grid points is very sensitive to the underlying chargino/neutralino structure. The parameters $M_1$, $M_2$ and $\mu$ strongly impact the production cross-sections and determine the branching patterns. A detailed discussion of the phenomenology of the grids can be found in [68, 119]. The most relevant phenomenology is summarised below. Additionally, in Appendix C, the bino/wino/higgsino composition of the neutralinos and charginos, their masses and the relevant branching ratios as well as the relative importance of the relevant subprocesses are shown.
For most grid points, the dominant electroweak gaugino production channels are $\tilde{\chi}_1^0\tilde{\chi}_2^0$, $\tilde{\chi}_1^\pm\tilde{\chi}_1^\mp$ and $\tilde{\chi}_1^\pm\tilde{\chi}_2^0$. The latter pair can decay into a tri-lepton final state, $\tilde{\chi}_1^\pm\tilde{\chi}_2^0 \to (\ell^\pm\nu\tilde{\chi}_1^0)(\ell^-\ell^+\tilde{\chi}_1^0)$.
The default decay of $\tilde{\chi}_1^\pm$ is into $\tilde{\chi}_1^0 W^{(*)}$, where the $W^{(*)}$ decays into $e\nu_e$, $\mu\nu_\mu$, $\tau\nu_\tau$ or $qq'$. Since the sleptons in the signal grid are right-handed, the charginos do not couple to selectrons and smuons. However, the Yukawa coupling to staus is non-vanishing, if the chargino has a higgsino content. The decay into staus, if kinematically allowed, dominates over default decays via virtual $W$ bosons. This is mostly notable in the low $M_1$ grid. If an on-shell $W$ can be produced, the gauge coupling wins over the Yukawa one (the mass difference between $\tilde{\chi}_1^\pm$ and $\tilde{\chi}_1^0$ allows this to happen only in one parameter set $(M_1, M_2, \mu) = (100, 250, 250)$ GeV).
The decay of $\tilde{\chi}_2^0$ is mostly dominated by the slepton channel. For electroweak gaugino-like $\tilde{\chi}_2^0$, the branching ratio to each slepton flavour is 1/3. If $\tilde{\chi}_2^0$ has a higgsino component, the stau decay channel receives an additional contribution through the Yukawa couplings. Furthermore, in the case of a higgsino-like $\tilde{\chi}_2^0$, the

decay into $\tilde{\chi}_1^{\pm} W^{(*)}$ can become dominant, especially if aided by phase space (the latter occurs for high $M_1$ and roughly $M_2 < \mu$). In principle, the decay via a $Z^{0(*)}$ boson is also possible, but for most grid points highly suppressed due to a too small mass difference between the $\tilde{\chi}_2^0$ and $\tilde{\chi}_1^0$. (The decay via an on-shell $Z^0$ boson is kinematically allowed for only one parameter set, $(M_1, M_2, \mu) = (100, 250, 250)$ GeV.)

With respect to the studied tri-lepton final state, the production of heavier electroweak gauginos become relevant for some grid points. These heavier gauginos have similar decay modes as $\tilde{\chi}_1^{\pm}$ and $\tilde{\chi}_2^0$, but they have other bino/wino/higgsino compositions. However, due to their higher masses, the decays via on-shell $W/Z^0$ bosons dominate.

The bino/wino/higgsino composition of the neutralinos and charginos is mainly driven by the ratio of the parameters $M_2$ and $\mu$. If $|\mu| \gg M_2 \gg m_W$, where $m_W$ is the $W$ boson mass, the lightest chargino and the next-to-lightest neutralino are wino-like, while the lightest neutralino is bino-like. If $M_2 > |\mu| \gg m_W$, the lightest chargino and neutralino are mainly higgsino-like, while if $M_2 \approx |\mu|$ the mixing is non negligible. A mSUGRA-like case, where $\tilde{\chi}_1^0$ and $\tilde{\chi}_2^0$ are nearly bino and wino, respectively, is given for $(M_1, M_2, \mu) = (100, 250, 250)$ GeV.

**Monte Carlo Samples**

For each grid point, official ATLAS MC samples with 25000 events each are available. This number of events corresponds to integrated luminosities between approximately $3.8\,\text{fb}^{-1}$ and $320\,\text{fb}^{-1}$, depending on the grid point (see Appendix C). The mass spectra were produced with ISASUSY 7.80 [136]. The event generation was done with HERWIG++ [137] and a 2-lepton filter (electron, muon and tau with $p_T > 7\,\text{GeV}$) was applied at generator level. The detector was simulated by Atlfast-II [138], a fast simulation of the detector response to the passing particles. The Inner Detector and the muon spectrometer is fully simulated by GEANT 4 [139, 140], while the showers in the calorimeters are simulated by FastCaloSim [141], except for muons. The muons are fully simulated in the calorimeters. It has been shown that the fast detector simulation with Atlfast-II is in good agreement with the full detector simulation with GEANT 4 for different SUSY signal scenarios [142].

For 3 out of the 147 grid points the Atlfast-II simulated samples were not avail-

able, therefore these grid points[2] are not considered in the following.

### 6.4.2. Standard Model Background

Several SM processes can mimic a SUSY signal with three leptons and $E_T^{miss}$ in the final state. These processes can be classified into *irreducible* and *reducible* background. The former processes comprise events with three prompt and isolated leptons, referred to as "real leptons" and the latter processes comprise events with at least one non-prompt or at least one non-isolated lepton, referred to as "fake leptons". Among the irreducible backgrounds, $WZ/\gamma^*$ is the dominant one, but $ZZ/\gamma^*$ and $t\bar{t} + Z/W/WW$ also contribute considerably. Reducible backgrounds are $t\bar{t}$, $Wt$ single top, $Z/\gamma^*$, and $WW$ production (one fake lepton); $W$, $s$- and $t$-channel single top (two fake leptons); multi-jet production (three fake leptons). The reducible background is dominated by decays of top-quark pairs to leptons, which yield real $E_T^{miss}$ from neutrinos, two real leptons from top-decays and further leptons may be produced in leptonic bottom-quark decays, or may be faked by one of the numerous jets in the event. Despite the high production cross-sections, the multi-jet background is negligible due to the need for three fake leptons and fake $E_T^{miss}$. Similarly, the contribution of $W$ production in association with jets is small. Therefore, these two backgrounds are neglected in the following.

#### Monte Carlo Samples

The MC simulated samples utilised in this thesis to estimate the background are official ATLAS MC, which were produced using the ATLAS MC11c parameter tune [143] and a GEANT 4 based detector simulation. The derived SUSYD3PDs [144] with the processing tag p832 are used.

Fragmentation and hadronisation for MC@NLO [145] and ALPGEN [146] samples was performed with HERWIG [147] and the underlying event was simulated using JIMMY [148]. For the MADGRAPH [149] samples, PYTHIA [150] was utilised for the showering. The MC@NLO MC samples were generated using the next-to-leading order PDF set CTEQ6.6 [151], while the MADGRAPH and ALPGEN samples are generated using the PDF set CTEQ6L1. All other MC samples

[2]For the following grid points the Atlfast-II simulated samples were not available: $(M_1, M_2, \mu) = (100, 100, 100)$ GeV, $(250, 100, 100)$ GeV and $(250, 180, 250)$ GeV

were generated using the MRST2007LO* [152] modified leading-order PDFs. The used MC samples are similar to the samples used in [119]. In the following, the MC samples are described briefly. In Appendix D, for each MC sample the effective cross-section, consisting of the generator cross-section, k-factors for higher order corrections, branching ratios and filter efficiencies, and the resulting integrated luminosity is listed.

- The di-boson processes ($ZZ/\gamma^*$, $WZ/\gamma^*$ , $WW$) were generated with HERWIG and MADGRAPH. HERWIG was used for the $ZZ$, $WZ$, $WW$ samples, where on generator level a filter was applied to select events with masses of the off-shell $W^{\pm}$ and $Z^0$ bosons larger than 20 GeV, and at least one (three) lepton with $p_T > 10\,\text{GeV}$ and $|\eta| < 2.8$ for the $ZZ/WW$ ($WZ$) sample. Since the HERWIG $WW$ sample describes only opposite sign $WW$ production, additionally, a same sign $WW$ (+ 2 jets) sample is used, generated using the leading order (LO) MC generator MADGRAPH. In the following, the contribution of same sign and opposite sign $WW$ production is referred to as "$WW$". The $Z/W + \gamma^*$ samples were generated using the LO MADGRAPH generator, where on generator level a filter for leptonic $Z/W$ decays (lepton $p_T > 10\,\text{GeV}$ and $|\eta| < 2.5$) and at least one photon (photon $p_T > 7\,\text{GeV}$ and $|\eta| < 2.5$) was applied. These samples are denoted as "$V\gamma^*$" in the following.

- The production of top quarks ($t\bar{t}$, single top: $Wt$, $s$- and $t$-channel) was generated with MC@NLO, using a top quark mass of 172.5 GeV. In the following, the contributions from $s$-channel, $t$-channel and $Wt$ single top processes are referred to as "single top".

- The top-quark pair production in association with one or more weak bosons was generated using the LO MC generator MADGRAPH. The contribution of $t\bar{t} + Z/W/WW$(+jets) processes is denoted as "$t\bar{t}V$" in the following.

- The $Z/\gamma^*$ production in association with jets was produced with ALPGEN. Different samples for light-flavour (LF) jets and heavy-flavour (HF) jets were used, where HF jets refers to jets from $b$-quarks. The $Z/\gamma^*$+LF jets samples were generated with a di-lepton invariant mass range of $40\,\text{GeV} < M_{\ell\ell} < 2\,\text{TeV}$ and $10\,\text{GeV} < M_{\ell\ell} < 40\,\text{GeV}$ separately, where the latter is

referred to as "Drell-Yan" (DY) samples in the following. The $Z/\gamma^*$+HF jets samples have been generated with a di-lepton invariant mass range of $30\,\text{GeV} < M_{\ell\ell} < 2\,\text{TeV}$. Samples of $Z/\gamma^*$+HF jets to electrons or muons were filtered at generator level for three leptons ($e$, $\mu$, $\tau$) with $p_T > 5\,\text{GeV}$ and $|\eta| < 10$ from $Z$ and $b$-quark decays. The DY samples to taus were filtered for 2 leptons with $p_T > 15\,\text{GeV}$ ($p_T > 5\,\text{GeV}$) and $|\eta| < 5$ for the leading (sub-leading) lepton. The same filter was applied to the DY samples with electrons or muons and up to one additional jet in the final state. The addition of $Z$+LF jets, $Z$+HF jets and DY contributions is referred to as "$Z/\gamma^*$+jet" in the following. The overlap between LF and HF jets is taken into account [153].

### 6.4.3. Event Reconstruction and Preselection

The analysis presented in this chapter was performed using ATLAS software provided by the `ATHENA` framework (release 17.3.1). The event quality criteria and object definitions comply with the official recommendations from the ATLAS SUSY Working Group for this release [154] and are summarised in the following. Additionally, the applied corrections to the MC event weight are outlined.

#### Object Selection

- **Muons** are reconstructed using the STACO algorithm and the same object quality criteria as for the muon trigger efficiencies measurements in Section 4.3.4 are applied. In contrast to Section 4.3.4, besides combined muon candidates also segment-tagged muon candidates [113] are selected. Muons passing these selection criteria and with $p_T > 10\,\text{GeV}$ (shifted and smeared to reproduce the resolution in data [3], as recommended by the MCP Group) are called "baseline" muons and are subjected to an overlap removal scheme (described below). "Signal" muons are required to be isolated, defined as in Section 4.3.4.

- **Electrons** are reconstructed using the `egamma` [155] algorithm optimised

[3] The smearing procedure is carried out using the package `MuonMomentumCorrections-00-05-03`.

for high-$p_T$ electron (based on calorimeter cluster). The electron $\eta$ and $\phi$ are defined as either those of the track or the cluster, depending on the number of electron track hits: If the track contains at most three silicon hits, $\eta$ is taken from the cluster $\eta^{\text{cluster}}$, otherwise from the track $\eta^{\text{track}}$. The electron $E_T$ is defined as $E^{\text{cluster}}/\cosh(\eta)$. Additionally, the electron energy is smeared to reproduce the resolution in data [4]. The "baseline" electrons are required to satisfy $E_T > 10\,\text{GeV}$, $|\eta| < 2.47$ and "medium" [5] identification requirements. These electron candidates are subjected to the overlap removal scheme. "Signal" elections are additionally required to satisfy "tight" [6] identification requirements and to be isolated: the $p_T$ sum of tracks above 1 GeV within a cone of size $\Delta R < 0.2$ around the electron candidate (excluding the electron candidate itself) has to be less than 10% of the electron's $E_T$.

- **Jets** are reconstructed from topological clusters [157] using the anti-$k_t$ jet algorithm [158] with a distance parameter of $\Delta R = 0.4$. The energy measured by the calorimeter is determined at the electromagnetic energy scale and corrected for the non-compensating [7] nature of the calorimeter. "Baseline" jets are required to satisfy $E_T > 20\,\text{GeV}$ and $|\eta| < 4.5$. These jet candidates are subjected to the overlap removal scheme.
  In the analysis, events with $b$-tagged jets are vetoed to suppress background from SM processes. The jets are classified as $b$-jet candidates by the `JetFitterCombNN` algorithm [159] at the 60% operating point [8].

**Overlap Removal**

A particular particle (electron, muon or jet) may be reconstructed by several algorithms for different types of objects. In order to avoid this duplication the following overlap-removal scheme is applied (in the given order):

1. $\Delta R(e_1, e_2) < 0.1$: If the distance in terms of $\Delta R$ of any two baseline electrons ($e_1$ and $e_2$) is smaller than 0.1, the electron with the lower $E_T$ is

[4] The smearing procedure is carried out using the package `egammaAnalysisUtils-00-02-76` [156], as recommended by the ATLAS Egamma Combined Performance Group
[5] The "medium" electron identification criteria are mainly based on the lateral shower shape in the calorimeter.
[6] The "tight" electron identification criteria require additionally $E/p$ (where $E$ is the shower energy in the calorimeter and $p$ the track momentum measured in the ID) and TRT criteria.
[7] E.g. due to dead material and energy loss outside the defined cone.
[8] The 60% operating point corresponds to an average $b$-tagging efficiency of 60%.

discarded (removed from the baseline selection).

2. $\Delta R(e, j) < 0.2$: If the distance in terms of $\Delta R$ between any baseline jet ($j$) and any baseline electron ($e$) is smaller than 0.2, the jet is discarded.

3. $\Delta R(j, e) < 0.4$: If the distance in terms of $\Delta R$ between any baseline electron and any baseline jet is smaller than 0.4, the electron is discarded.

4. $\Delta R(j, \mu) < 0.4$: If the distance in terms of $\Delta R$ between any baseline muon ($\mu$) and any baseline jet is smaller than 0.4, the muon is discarded.

5. $\Delta R(e, \mu) < 0.1$: If the distance in terms of $\Delta R$ between any baseline muon and any baseline electron is smaller than 0.2, the electron and the muon are discarded.

Additionally, lepton pairs from the same generation and different charge (in the following referred to as same flavour opposite sign (SFOS) lepton pairs) with a invariant mass of $M_{\ell\ell} < 20\,\text{GeV}$ are discarded to suppress Drell-Yan and low-mass di-lepton resonances.

**Event Quality Criteria**

The events are required to satisfy a number of quality criteria:

- At least one primary vertex with more than four tracks.

- Events containing baseline muons before the overlap-removal with $\sigma_{q/p}/|q/p| \geq 0.2$ (where $p$ is the momentum of the muon and $q$ is its charge) are discarded to avoid potentially mis-measured muons.

- In order to reject background from cosmic radiation, events are discarded if there is a muon surviving the overlap-removal with a distance of closest approach to the vertex in longitudinal and transverse direction larger than 1.0 mm and 0.2 mm, respectively.

- Events with jets potentially originating from instrumental background effects are rejected. These jets are all "looser bad" jets, as defined in [160], with $E_T > 20\,\text{GeV}$ and any $\eta$, surviving the overlap removal.

- Events containing jets emerging in the "LAr hole" region [9] are discarded, if the estimated energy missed in the LAr hole contributes significantly to $E_T^{miss}$, following the recommendations of the ATLAS Jet and Etmiss Group [160, 161].

**Missing Transverse Momentum Definition**

The $E_T^{miss}$ is calculated from calibrated jets, electrons and muons, and the topological calorimeter clusters outside reconstructed objects. The definition used here is:

$$E_{(x,y)}^{miss} = E_{(x,y)}^{e} + E_{(x,y)}^{\mu} + E_{(x,y)}^{jets} + E_{(x,y)}^{cl} \tag{6.8}$$

and $E_T^{miss} = \sqrt{(E_x^{miss})^2 + (E_y^{miss})^2}$. The electron ($E_{(x,y)}^{e}$) and muon term ($E_{(x,y)}^{\mu}$) is calculated using electrons and muons passing the baseline selection (no isolation criteria applied and before the overlap-removal). For the jet term ($E_{(x,y)}^{jets}$) calculation, all jets calibrated to the electromagnetic-scale with jet-energy-scale corrections applied and $p_T > 20\,\text{GeV}$ are used. Any remaining topological calorimeter clusters not associated to pre-cited objects are used at the electromagnetic-scale to calculate the 'cell out' term ($E_{(x,y)}^{cl}$). The actual calculation is done using an official ATLAS software [10].

**Corrections to the MC event weight**

The MC simulation does not reproduce all aspects of the data correctly. Although the MC expectations are not compared to data, several corrections are applied to the MC event weight to account for the relevant known discrepancies.

- Lepton Identification Efficiency: To account for differences between data and simulation in the electron and muon reconstruction efficiency, a multiplicative weight for each signal muon and electron is applied. The product of these weights [11] is used to correct the MC event weight.

- *b*-Tagging Efficiency: Differences between data and simulation are observed

[9] The term "LAr hole" is used for the problem, which has been occurred since the beginning of period 2011E and affects part of the LAr ECal in the barrel. The region affected by the LAr hole is $[-0.1, 1.5] \times [-0.9, -0.5]$ in $\eta \times \phi$.

[10] The $E_T^{miss}$ is calculated with the MissingETUtility-00-02-13 package [162].

[11] The corrections for the electron and muon identification are calculated using the packages `egammaAnalysisUtils-00-02-76` and `MuonEfficiencyCorrections-00-05-03`, as recommended by the ATLAS Combined Performance Groups.

in the $b$-tagging efficiency and the light-jet mis-tag rate. Therefore, the MC event weight is corrected with a jet flavour ($b$, $c$, light), $E_T$, and $\eta$ dependent scale factor, following the recommendations of the Flavour Tagging Working Group [12].

- Pile-Up: The distribution of collision vertices in data and simulation differers. Therefore, the MC event weights are corrected so that the distribution observed in data is reproduced. Since the expectations from MC are not compared to data from a particular data-taking period, the MC is normalised to the full 2011 dataset recorded with the lowest unprescaled single muon triggers (EF_mu18 and EF_mu18_medium) following official ATLAS recommendations [13].

**Trigger Reweighting**

The trigger efficiencies are taken into account following the reweighting approach (cf. Section 4.3.5). The efficiencies for the studied muon triggers are determined on a MC $Z^0 \to \mu\mu$ sample [14]. Trigger efficiencies determined from MC are used, because the absolute efficiencies are not relevant for the presented studies and the expectations from MC are not compared to data. An additional reason for using trigger efficiencies determined on MC is that the measurement of the EF_mu6 trigger efficiencies, needed for the application of the EF_3mu6 trigger efficiencies, is not possible on data (Before the data-taking period 2011G, EF_mu6 was highly prescaled and not in the rerun mode, cf. Section 3.3.3)
The efficiencies of the different muon triggers are applied as follows:

- For the single muon triggers, each event is assigned a weight according to Equation 4.1, where all signal muons with sufficient $p_T$ to be in the trigger plateau of the studied trigger are taken into account. The trigger plateau is defined to start 2 GeV above the nominal $p_T$-threshold, as summarised in Appendix B. Note that for the virtual EF_mu16c22f and EF_mu22c16f, triggers the plateau is $\eta$ dependent.

- For the multi-muon triggers, the trigger efficiencies can be factorised into the single muon trigger efficiencies (discussed in detail in Section 5). The

[12] Scale factors as described in [163], but updated for the 2011 dataset, are applied.
[13] The `PileUpReweighting-00-02-02` [164] package is used.
[14] The same MC $Z^0 \to \mu\mu$ sample as in Section 5.3.2 is used, outlined in Appendix D.

di-muon trigger event weight is calculated according to Equation 5.4 and for the tri-muon trigger the weight is given by the probability that three signal muons issue the corresponding single muon trigger. For events with three signal muons this trigger probability is given by the product of the trigger efficiencies of each single muon and zero for events with less than three signal muons.

- For the combination of a single (si) and a di-muon trigger (di), the trigger efficiency is given by

$$\epsilon_{\text{si OR di}} = \epsilon(\text{si}) + \epsilon(\text{di}|!\text{si}), \tag{6.9}$$

where $\epsilon(\text{di}|!\text{si})$ is the conditional trigger efficiency that the di-muon trigger finds two muon candidates, while the single muon trigger finds none. The conditional di-muon trigger efficiencies are assumed to factorised into the conditional single muon trigger efficiencies. The latter are discussed in Section 4.3.6.

**Signal Event Reweighting**

Cross-sections of the SUSY signal processes were calculated by Prospino2.1 [165, 166] up to next-to-leading order (NLO), while the signal MC samples are produced with LO cross-sections. Therefore, each signal event is assigned an additional weight depending on the simulated subprocess, as recommended by the ATLAS SUSY Working Group [167].
For a few grid points, Prospino2.1 refuses to calculate the cross-sections for some of the subprocesses ($\tilde{\chi}_1^0\tilde{\chi}_1^0$, $\tilde{\chi}_1^0\tilde{\chi}_1^\pm$, $\tilde{\chi}_1^+\tilde{\chi}_1^-$), since the involved particles are too light. In these cases, an averaged k-factor for the NLO normalisation have been applied.

**Preselection**

The events passing the event quality criteria and containing at least one signal muon satisfy the "preselection". Note that events with no signal muon have zero weight anyway, since only muon triggers are considered for the trigger reweighting.

### 6.4.4. The Tri-Lepton Signal Region

The selection criteria for the signal region are designed to select events of chargino and neutralino pair production, where both electroweak gauginos decay leptonically, resulting in three leptons. In particular, the neutralinos can decay to leptons either via sleptons and off-shell $Z^0$ bosons or via on-shell $Z^0$ bosons (cf. Section 6.4.1). The latter leads to resonant final states, while the former does not. Since the decay via on-shell $Z^0$ bosons is highly suppressed for most of the assumed SUSY signals (cf. Appendix C), the considered signal region contains only the non resonant decays. The same selection criteria for the signal events as in [119] are chosen.

Signal events are required to contain exactly three signal leptons and at least one SFOS lepton pair (either from $Z^0$ bosons or intermediate sleptons). Additionally, the lightest neutralinos and neutrinos in the final state often result in a considerable amount of $E_T^{miss}$. It has been shown [119], that $E_T^{miss} > 50\,\text{GeV}$ is a reasonable choice to keep most of the signal events, while achieving a good suppression of SM background processes with no real $E_T^{miss}$, mainly $Z$+jets and $ZZ/\gamma^*$. To suppress SM background with real $Z^0$ bosons, SFOS pairs with a invariant mass consistent with nominal $Z$ mass (within 10 GeV) are vetoed. The remaining background from top quarks is reduced by applying a $b$-jet veto.

Figure 6.4 to 6.7 show the expected number of background events from various SM processes and the expected signal for a SUSY reference point at different stages of the event selection. The expectations are calculated for the reference trigger (EF_mu18) and are scaled to $0.5\,\text{fb}^{-1}$, such that sufficient statistics is available for all signal MC samples. The SUSY signal reference point is the parameter set $(M_1, M_2, \mu) = (100, 250, 110)$ GeV of the pMSSM grid (cf. Section 6.4.1). For this grid point, the $\tilde{\chi}_2^0$ decays dominantly via a slepton.

Additionally, in Figure 6.8 the number of jets and the $p_T$ distribution of the leading jet is presented for the events after the $Z$ veto before the $b$-jet veto is applied. A veto of $b$-jet candidates is more effective in suppressing the SM background from tops than either of these two variables (number of jets and the $p_T$ of the leading jet).

To summarise, the selection criteria for the signal region are:

- exactly 3 signal leptons (comprises signal muons and electrons, as defined in Section 6.4.3)

- at least one SFOS lepton pair
- $E_T^{miss} > 50\,\text{GeV}$
- $Z$ veto ($|M_{\text{SFOS}} - M_Z| > 10\,\text{GeV}$ for all SFOS lepton pairs)
- $b$-jet veto (`JetFitterCombNN` algorithm at the 60% operating point)

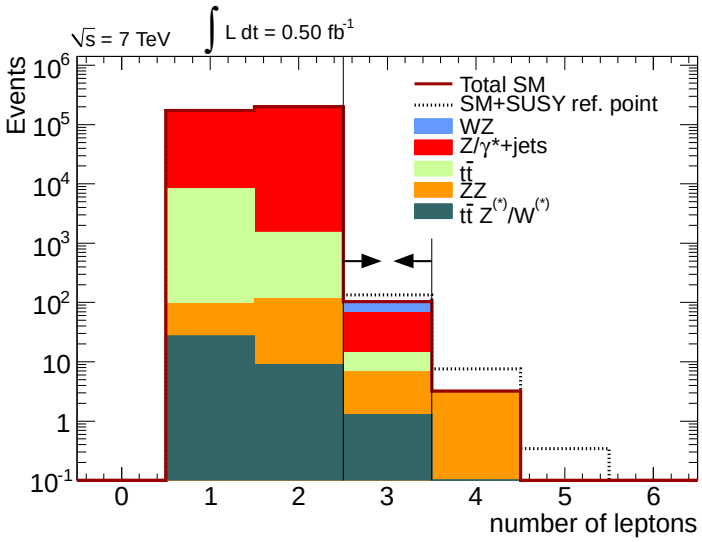


***Figure 6.4.:*** The expected number of signal leptons in events surviving the preselection for various SM processes and a SUSY reference point ($(M_1, M_2, \mu) = (100, 250, 110)$ GeV). The contributions from the different considered SM sources (cf. Section 6.4.2) are stacked. Additionally, the expectations from the SUSY reference point are stacked on top of the sum of all considered SM sources (dotted black line). The tri-lepton requirement is indicated by the arrows.

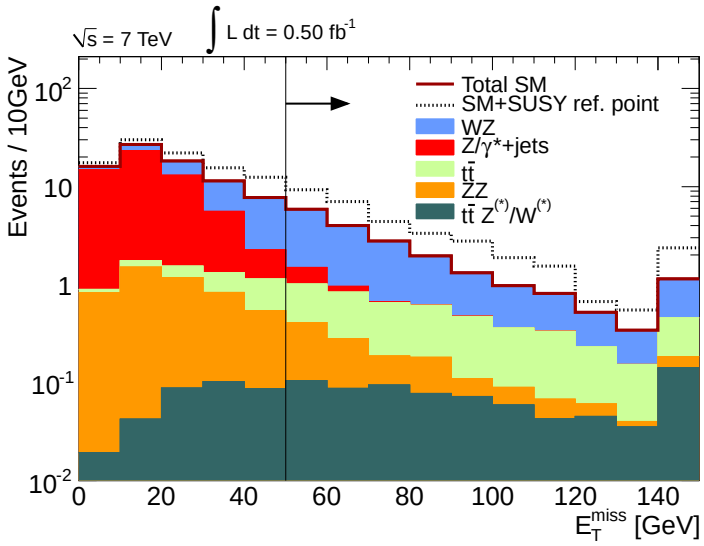


***Figure 6.5.:*** The $E_T^{miss}$ distribution in events with three signal leptons and at least one SFOS pair for various SM processes and a SUSY reference point ($(M_1, M_2, \mu) = (100, 250, 110)$ GeV). The contributions from the different considered SM sources (cf. Section 6.4.2) are stacked. Additionally, the expectations from the SUSY reference point are stacked on top of the sum of all considered SM sources (dotted black line). The last bin contains all expected events with $E_T^{miss} > 140\,\text{GeV}$. The cut on $E_T^{miss} > 50\,\text{GeV}$ is indicated by the arrow.

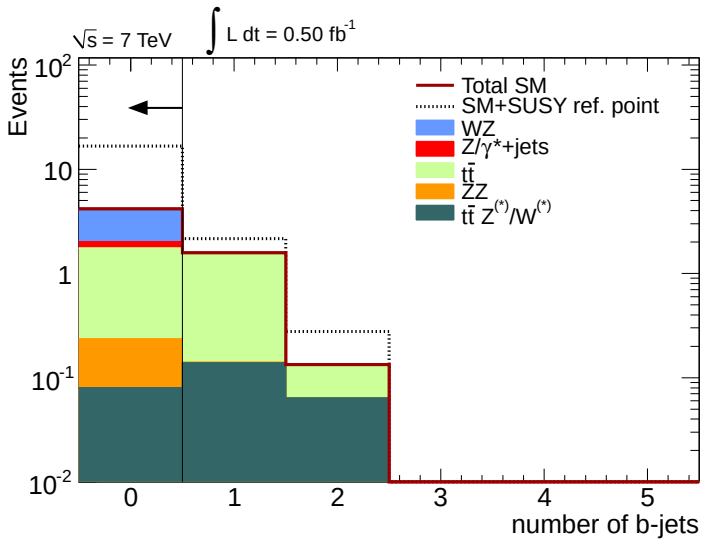


***Figure 6.7.:*** The number of $b$-tagged jets in events with three signal leptons, at least one SFOS pair, $E_T^{miss} > 50\,\text{GeV}$ and $|M_{\text{SFOS}} - M_Z| > 10\,\text{GeV}$ for various SM processes and a SUSY reference point ($(M_1, M_2, \mu) = (100, 250, 110)$ GeV). The contributions from the different considered SM sources (cf. Section 6.4.2) are stacked. Additionally, the expectations from the SUSY reference point are stacked on top of the sum of all considered SM sources (dotted black line). The $b$-jet veto is indicated by the arrow.

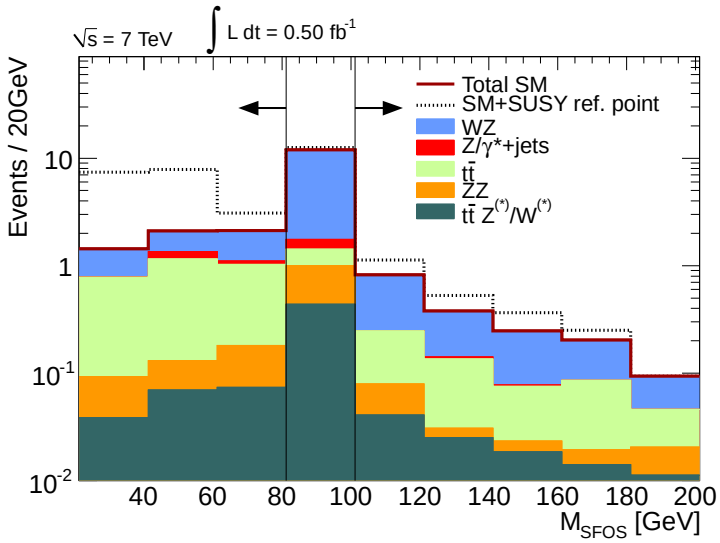


***Figure 6.6.:*** The $M_{\mathrm{SFOS}}$ distribution (SFOS lepton pairs with invariant mass closest to the $Z$ mass is shown) in events with three signal leptons, at least one SFOS pair and $E_T^{miss} > 50\,\mathrm{GeV}$ for various SM processes and a SUSY reference point ($(M_1, M_2, \mu) = (100, 250, 110)$ GeV). The contributions from the different considered SM sources (cf. Section 6.4.2) are stacked. Additionally, the expectations from the SUSY reference point are stacked on top of the sum of all considered SM sources (dotted black line). The last bin contains all expected events with $M_{\mathrm{SFOS}} > 180\,\mathrm{GeV}$. The $Z$ veto (within 10 GeV around the nominal $Z$ mass) is indicated by the arrows.

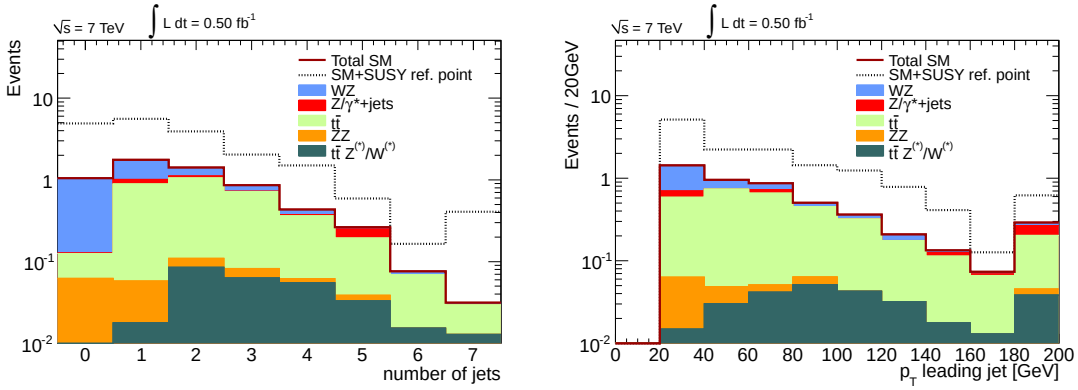


(a) number of jets

(b) jet $p_T$ of leading jet

***Figure 6.8.:*** The number of jets (a) and the $p_T$ distribution of the leading jet (b) in events with three signal leptons, at least one SFOS pair, $E_T^{miss} > 50\,\mathrm{GeV}$ and $|M_{\mathrm{SFOS}} - M_Z| > 10\,\mathrm{GeV}$ for various SM processes and a SUSY reference point ($(M_1, M_2, \mu) = (100, 250, 110)$ GeV). The contributions from the different considered SM sources (cf. Section 6.4.2) are stacked. Additionally, the expectations from the SUSY reference point are stacked on top of the sum of all considered SM sources (dotted black line). The last bins contain all expected events with more than 7 jets and jet $p_T > 180\,\mathrm{GeV}$, respectively.

### 6.4.5. Expected Significance for the Reference Trigger

The MC based estimation of the background can be used to determine the expected significance med$[Z_W]$ (cf. Section 6.3) of the search for various SUSY signals. The expected number of events in the analysis cutflow for the sum of all SM background processes and the SUSY reference point (cf. 6.4.4) is summarised in Table 6.2. A breakdown of the separate SM background processes can be found in Table 6.3. The expectations are calculated for the reference trigger and are scaled to $0.5\,\mathrm{fb}^{-1}$.

The expected number of signal events that satisfy all selection criteria from the signal region for the pMSSM signal grids are shown in Figure 6.9 (left). Additionally, the expected significance med$[Z_W]$ for every grid point is shown in Figure 6.9 (right).

| Cutflow Step | $\sum$ SM | | | SUSY ref. Point | | |
|---|---|---|---|---|---|---|
| | $n_{\mathrm{exp.}}$ | $\sigma_{\mathrm{stat.}}$ | $\epsilon_{\mathrm{cut}}$ | $n_{\mathrm{exp.}}$ | $\sigma_{\mathrm{stat.}}$ | $\epsilon_{\mathrm{cut}}$ |
| Preselection | 385714.70 | 141.25 | | 404.26 | 5.09 | |
| 3 lepton | 113.42 | 1.76 | 0.00 | 31.74 | 1.44 | 0.08 |
| SFOS pair | 110.49 | 1.75 | 0.97 | 31.42 | 1.43 | 0.99 |
| $E_T^{miss} > 50\,\mathrm{GeV}$ | 19.89 | 0.27 | 0.18 | 14.15 | 0.94 | 0.45 |
| $Z$ veto | 6.04 | 0.18 | 0.30 | 13.24 | 0.91 | 0.94 |
| **$b$-jet veto** | **4.53** | **0.17** | **0.75** | **12.60** | **0.89** | **0.95** |

***Table 6.2.:*** Event counts as they follow from the analysis cutflow for the sum of all SM background processes and a SUSY signal reference point ($(M_1, M_2, \mu) = (100, 250, 110)$ GeV). The expected event numbers $n_{\mathrm{exp.}}$ are calculated with respect to the reference trigger (EF_mu18) and normalized to $\int L\,\mathrm{d}t = 0.5\,\mathrm{fb}^{-1}$. $\sigma_{\mathrm{stat.}}$ is the statistical uncertainty on this number (from limited MC statistics), and $\epsilon_{\mathrm{cut}}$ is the efficiency of the applied cut with respect to the preceding cut. The highlighted row is the expected number of events in the signal region.

| Cutflow Step | $WW$ | | | $WZ$ | | | $ZZ$ | | | $V\gamma^{(*)}$ | | |
|---|---|---|---|---|---|---|---|---|---|---|---|---|
| | $n_{\text{exp.}}$ | $\sigma_{\text{stat.}}$ | $\epsilon_{\text{cut}}$ | $n_{\text{exp.}}$ | $\sigma_{\text{stat.}}$ | $\epsilon_{\text{cut}}$ | $n_{\text{exp.}}$ | $\sigma_{\text{stat.}}$ | $\epsilon_{\text{cut}}$ | $n_{\text{exp.}}$ | $\sigma_{\text{stat.}}$ | $\epsilon_{\text{cut}}$ |
| Preselection | 2431.69 | 2.66 | | 68.62 | 0.40 | | 182.71 | 0.66 | | 7809.86 | 34.97 | |
| 3 lepton | 0.09 | 0.02 | 0.00 | 35.30 | 0.29 | 0.51 | 5.45 | 0.12 | 0.03 | 10.13 | 0.96 | 0.00 |
| SFOS pair | 0.05 | 0.01 | 0.60 | 35.08 | 0.29 | 0.99 | 5.40 | 0.12 | 0.99 | 10.11 | 0.96 | 1.00 |
| $E_T^{miss} > 50\,\text{GeV}$ | 0.03 | 0.01 | 0.56 | 13.95 | 0.18 | 0.40 | 0.85 | 0.05 | 0.16 | 0.02 | 0.02 | 0.00 |
| $Z$ veto | 0.03 | 0.01 | 1.00 | 2.17 | 0.07 | 0.16 | 0.16 | 0.02 | 0.18 | 0.02 | 0.02 | 1.00 |
| **$b$-jet veto** | **0.03** | **0.01** | **1.00** | **2.15** | **0.07** | **0.99** | **0.15** | **0.02** | **0.98** | **0.02** | **0.02** | **1.00** |

| Cutflow Step | $t\bar{t}$ | | | $t\bar{t}V$ | | | singleT | | | $Z/\gamma^*$+jets | | |
|---|---|---|---|---|---|---|---|---|---|---|---|---|
| | $n_{\text{exp.}}$ | $\sigma_{\text{stat.}}$ | $\epsilon_{\text{cut}}$ | $n_{\text{exp.}}$ | $\sigma_{\text{stat.}}$ | $\epsilon_{\text{cut}}$ | $n_{\text{exp.}}$ | $\sigma_{\text{stat.}}$ | $\epsilon_{\text{cut}}$ | $n_{\text{exp.}}$ | $\sigma_{\text{stat.}}$ | $\epsilon_{\text{cut}}$ |
| Preselection | 9599.64 | 6.46 | | 37.55 | 0.15 | | 2998.98 | 8.01 | | 362585.65 | 136.44 | |
| 3 lepton | 7.45 | 0.18 | 0.00 | 1.28 | 0.03 | 0.03 | 0.41 | 0.07 | 0.00 | 53.33 | 1.43 | 0.00 |
| SFOS pair | 5.29 | 0.15 | 0.71 | 1.10 | 0.03 | 0.86 | 0.28 | 0.05 | 0.69 | 53.18 | 1.43 | 1.00 |
| $E_T^{miss} > 50\,\text{GeV}$ | 3.52 | 0.13 | 0.67 | 0.76 | 0.02 | 0.69 | 0.14 | 0.04 | 0.50 | 0.62 | 0.14 | 0.01 |
| $Z$ veto | 3.00 | 0.12 | 0.85 | 0.28 | 0.01 | 0.37 | 0.12 | 0.04 | 0.89 | 0.26 | 0.11 | 0.42 |
| **$b$-jet veto** | **1.71** | **0.09** | **0.57** | **0.09** | **0.01** | **0.33** | **0.12** | **0.04** | **0.94** | **0.26** | **0.11** | **0.99** |

***Table 6.3.:*** Breakdown of the event counts as they follow from the analysis cutflow for the SM background processes. The expected event numbers $n_{\text{exp.}}$ are calculated with respect to the reference trigger (EF_mu18) and normalized to $\int L\,\mathrm{d}t = 0.5\,\text{fb}^{-1}$. $\sigma_{\text{stat.}}$ is the statistical uncertainty on this number (from limited MC statistics), and $\epsilon_{\text{cut}}$ is the efficiency of the cut with respect to the preceding cut. The highlighted rows are the expected number of events in the signal regions.

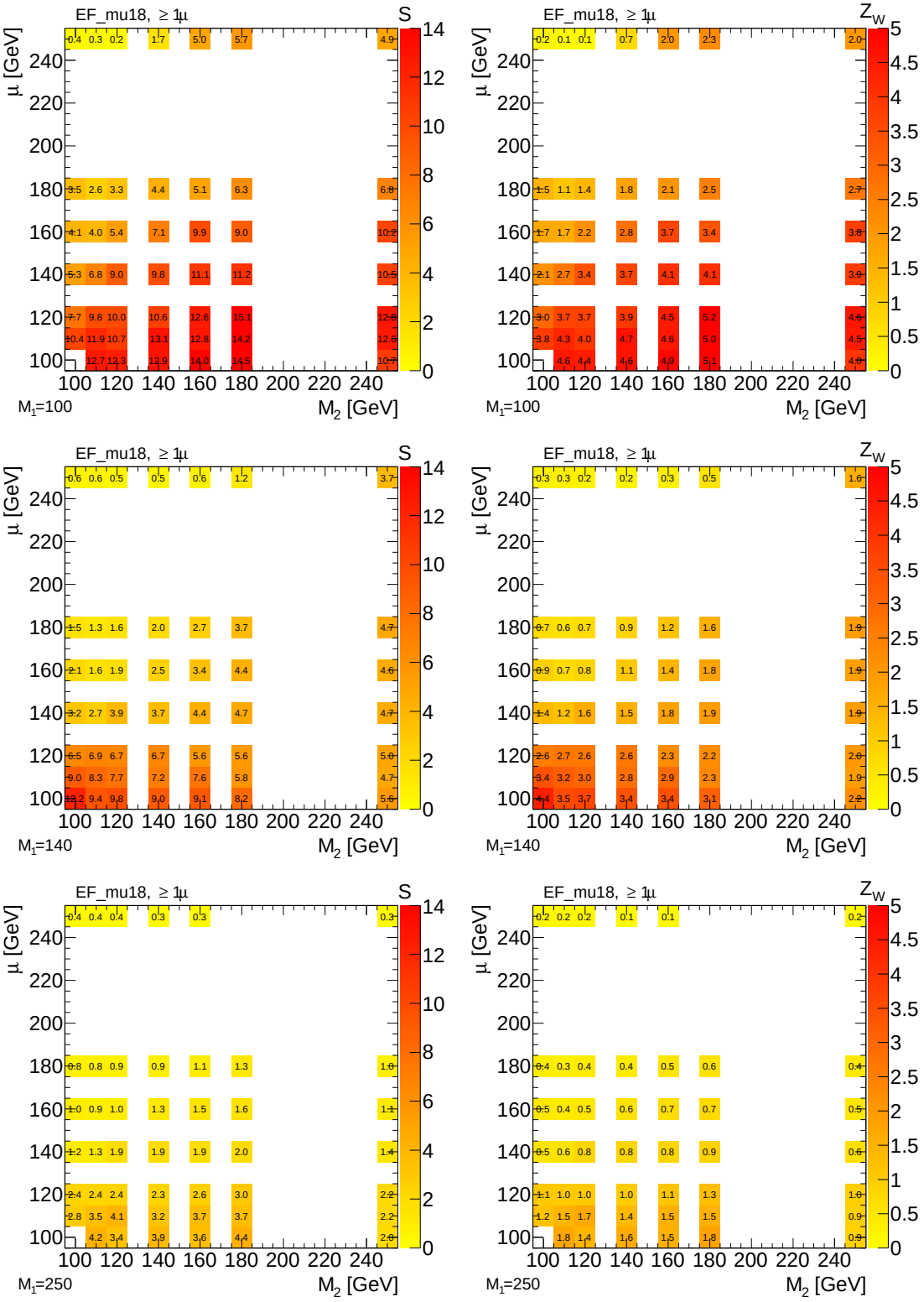


***Figure 6.9.:*** pMSSM signal grids: number of expected signal events $S$ (left) and expected significance med$[Z_W]$ (right) in the signal region. The expectations are calculated for the reference trigger (EF_mu18) and are scaled to 0.5 fb$^{-1}$.

### 6.4.6. Expected Significance for Studied Muon Triggers

To calculate the expected significance for the studied muon triggers, the number of background and signal events expected for the different muon triggers is calculated by reweighting the MC events according to the studied triggers. For each trigger, plots similar to Figure 6.9 for the reference trigger are obtained. The expected significance of the studied triggers is compared for each grid point with the expected significance of the reference trigger (EF_mu18), yielding in the factor $f^T$ (cf. Section 6.3). The factor $f^T$ describes how much more integrated luminosity is needed for a trigger $T$ to give the same expected significance as the reference trigger for a reference integrated luminosity. From the distribution of the $f^T$ factors over all pMSSM grid points (cf. Section 6.4.1), conclusions about the benefit of the trigger can be drawn.
The median $f^T$ of all studied grid points is summarised in Table 6.4 and illustrated in Figure 6.10. Additionally, the 0.05- and 0.95-quantiles are given as a measure of the spread of the distributions. The single muon triggers are compared to the reference trigger for all signal events with at least one signal muon ($\geq 1\mu$). For the comparison of the di- and tri-muon triggers with the reference trigger, only signal events with at least two ($\geq 2\mu$) and three signal muons ($= 3\mu$) are used, respectively, because the multi-muon triggers are only sensitive to these events. The combinations of single and di-muon triggers are compared for the $\geq 1\mu$ and the $\geq 2\mu$ channel separately. The raw (unweighted) numbers of signal events in the $1\mu$, $2\mu$ and $3\mu$ channel are shown in the Appendix C. For most of the grid points, roughly 50 signal events in each channel are available, but for some parameter sets, $(M_1, M_2, \mu) = (100, 100 - 140, 250)$ GeV, only a few signal events (less than 10) are available.
Note that the same signal events are used for the study of each muon trigger. Therefore, the signal yields are highly correlated [15] and the observed differences in the expected significance are due to different trigger efficiencies (applied in the trigger reweighting procedure).

[15] For triggers with the same $p_T$-threshold, the event yields are totally correlated. However, for events with signal muons which are in the plateau of only one of the triggers, the weights from the trigger reweighting procedure are not totally correlated.

| Trigger | $f^T$ $Q_{0.05}$ | $f^T$ median | $f^T$ $Q_{0.95}$ | Muon Multiplicity |
|---|---|---|---|---|
| EF_mu22 | 0.99 | 1.07 | 1.24 | $\geq 1$ $\mu$ |
| EF_mu18i* | 1.01 | 1.01 | 1.02 | $\geq 1$ $\mu$ |
| EF_mu15ps | 1.72 | 1.91 | 2.04 | $\geq 1$ $\mu$ |
| EF_mu16c22f* | 0.97 | 1.00 | 1.06 | $\geq 1$ $\mu$ |
| EF_mu22c16f* | 0.98 | 1.02 | 1.10 | $\geq 1$ $\mu$ |
| EF_mu22 OR EF_2mu10_loose | 0.95 | 1.03 | 1.08 | $\geq 1$ $\mu$ |
| EF_mu18i OR EF_2mu10_loose | 0.96 | 1.01 | 1.03 | $\geq 1$ $\mu$ |
| EF_2mu10_loose | 1.08 | 1.21 | 1.35 | $\geq 2$ $\mu$ |
| EF_mu22 OR EF_2mu10_loose | 0.94 | 1.01 | 1.04 | $\geq 2$ $\mu$ |
| EF_mu18i OR EF_2mu10_loose | 0.95 | 1.01 | 1.03 | $\geq 2$ $\mu$ |
| EF_3mu6 | 1.59 | 2.01 | 2.66 | $= 3$ $\mu$ |

***Table 6.4.:*** Median of the distribution of the $f^T$ factors (cf. Section 6.3) from all grid points for all studied muon triggers. These factors describe how much more integrated luminosity is needed for a trigger $T$ to give the same expected significance as the reference trigger (EF_mu18) for a reference integrated luminosity. Additionally, the 0.05- and 0.95-quantiles and the muon multiplicity in the events used for the $f^T$ factor calculation are given. Virtual triggers (cf. Section 6.1) are labeled by a star (*).

In the following, the results for each trigger are discussed briefly:

- EF_mu18i: For this trigger, exactly the same events as for the reference trigger are used for the calculation of the expected significance, because both triggers reach the trigger efficiency plateau (cf. Appendix B) at the same muon $p_T$. Since the measured trigger efficiencies for EF_mu18i are always slightly lower than for the reference trigger (where no isolation criterion is applied), $f^T$ factors between 1.01 and 1.02 are observed. The $f^T$ factors for each grid point are shown in Figure 6.11.

- EF_mu22: Due to the higher $p_T$-threshold, fewer signal muons than for the reference trigger are used for the calculation of the expected significance. In the plateau of both triggers, the trigger efficiencies are nearly the same, resulting in $f^T$ factors distributed around 1.07. Due to different $p_T$ distributions of the muons from SM background and signal processes, the $f^T$ factors can also be below 1. The $f^T$ factors for each grid

point are shown in Figure 6.12 (left). For grid points where the mass difference between $\tilde{\chi}_2^0$ and $\tilde{\chi}_1^0$ is smaller, higher $f^T$ factors are observed, e.g. for $(M_1, M_2, \mu) = (140, 100 - 180, 250)$ GeV the mass difference is smaller than for $(M_1, M_2, \mu) = (140, 100 - 130, 100 - 180)$ GeV (cf. Appendix C).

- EF_mu15: For most grid points, the gain in signal muons due to the low $p_T$-threshold is very small, such that the prescale factor of 2.01 leads to $f^T$ factors distributed around 1.91. The $f^T$ factors for each grid point are shown in Figure 6.12 (right).

- EF_mu16c22f and EF_mu22c16f: These triggers are very similar to the reference trigger. Thus, $f^T$ factors distributed around 1.00 (1.02) with a small spread are observed for the EF_mu16c22f (EF_mu22c16f). The trigger with the lower $p_T$-threshold in the barrel region (EF_mu16c22f) shows a slightly higher median expected significance than the trigger with the lower $p_T$-threshold in the endcap region. The $f^T$ factors for both triggers are shown in Figure 6.13.

- EF_2mu10_loose and EF_3mu6: These multi-muon triggers show $f^T$ factors above 1 (median 1.21 and 2.01, respectively) due to the lower trigger efficiencies. The spreads are wider than for the single muon triggers due to less statistics (only $\geq 2\mu$ and $= 3\mu$ channel, respectively). The $f^T$ factors for both triggers are shown in Figure 6.14. In contrast to the EF_mu22, for grid points where the mass difference between $\tilde{\chi}_2^0$ and $\tilde{\chi}_1^0$ is smaller, lower $f^T$ factors are observed. This effect is visible for the $M_2 = 250$ GeV grid, where in the lower right corner the mass difference is considerable smaller than in the upper left corner (cf. Appendix C), resulting in smaller $f^T$ factors in the lower right corner.

- "EF_mu22 OR EF_2mu10_loose" and "EF_mu18i OR EF_2mu10_loose": The combination of the single muon triggers with the di-muon trigger is an improvement with respect to the single muon triggers only. Especially, the EF_mu22 with the higher $p_T$-threshold benefits from the small $p_T$-thresholds of the di-muon trigger. The $f^T$ factors for the both combinations are shown separately for the $\geq 1\mu$ and $\geq 2\mu$ channel in Figure 6.15 and 6.16.

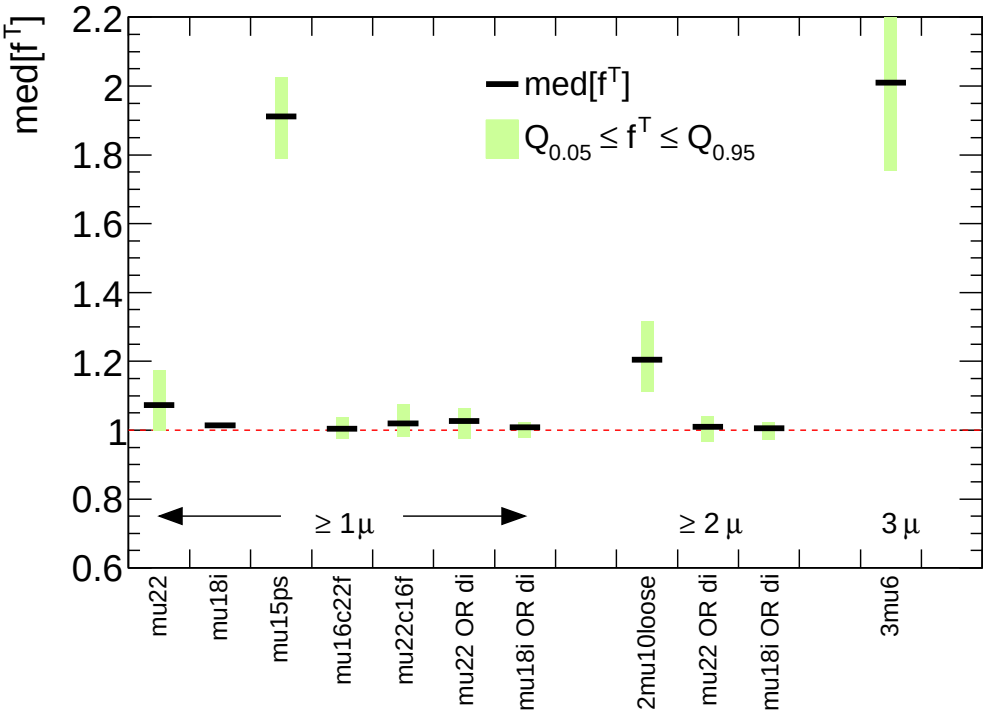


***Figure 6.10.:*** Median (black lines) of the distribution of the $f^T$ factors (cf. Section 6.3) over all grid points for all studied muon triggers. These factors describe how much more integrated luminosity is needed for a trigger $T$ to give the same expected significance as the reference trigger (EF_mu18) for a reference integrated luminosity. Additionally, the 0.05- and 0.95-quantiles are given (green bands). The prefix "EF_" before the name of the triggers has been omitted and the di-muon trigger EF_2mu10_loose is abbreviated with "di" in the single and di-muon trigger combinations for better readability.

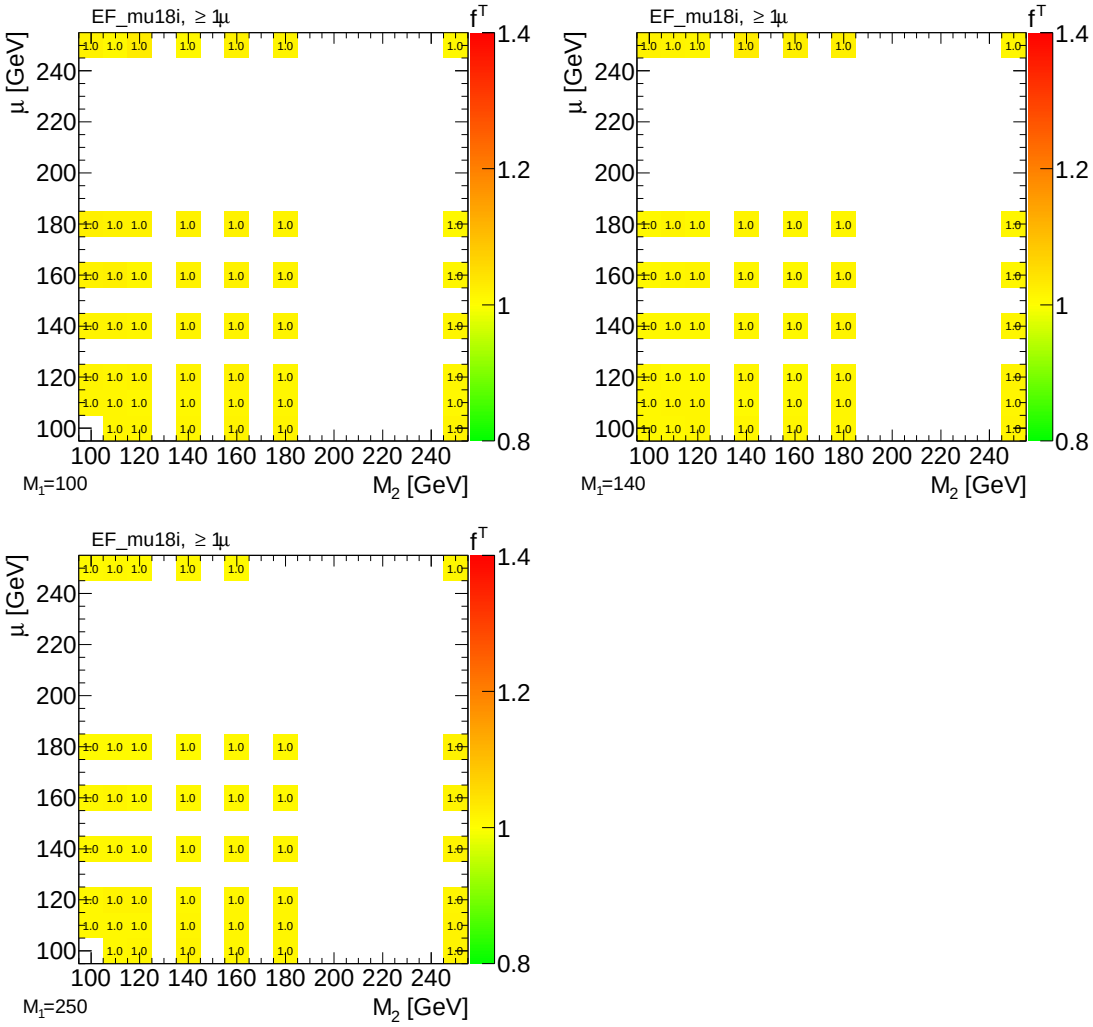


***Figure 6.11.:*** pMSSM signal grids: $f^T$ factors (cf. Section 6.3) for the EF_mu18i in events with at least one signal muons.

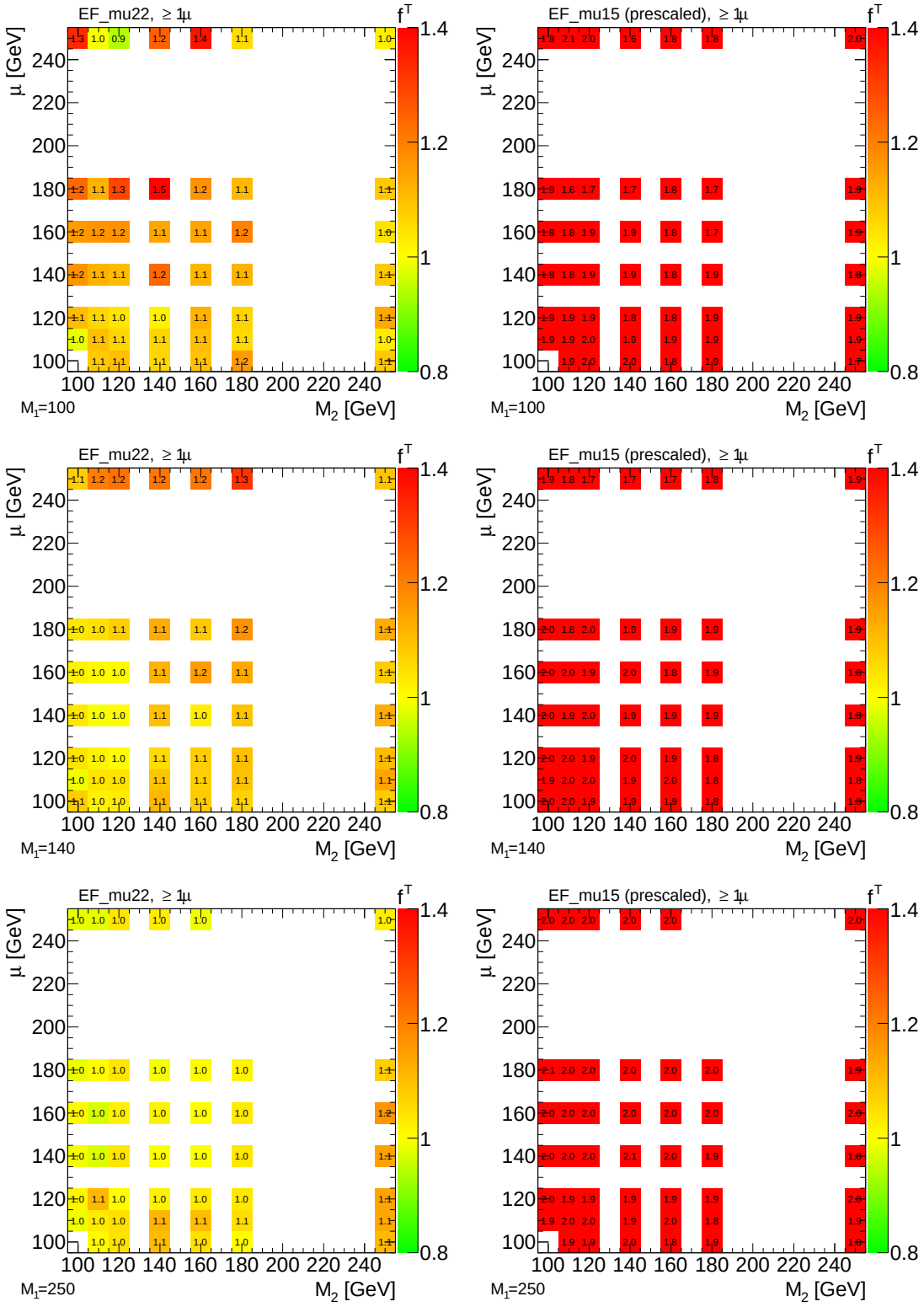


***Figure 6.12.:*** pMSSM signal grids: $f^T$ factors (cf. Section 6.3) for the EF_mu22 (left) and the prescaled EF_mu15 trigger (right) in events with at least one signal muons.

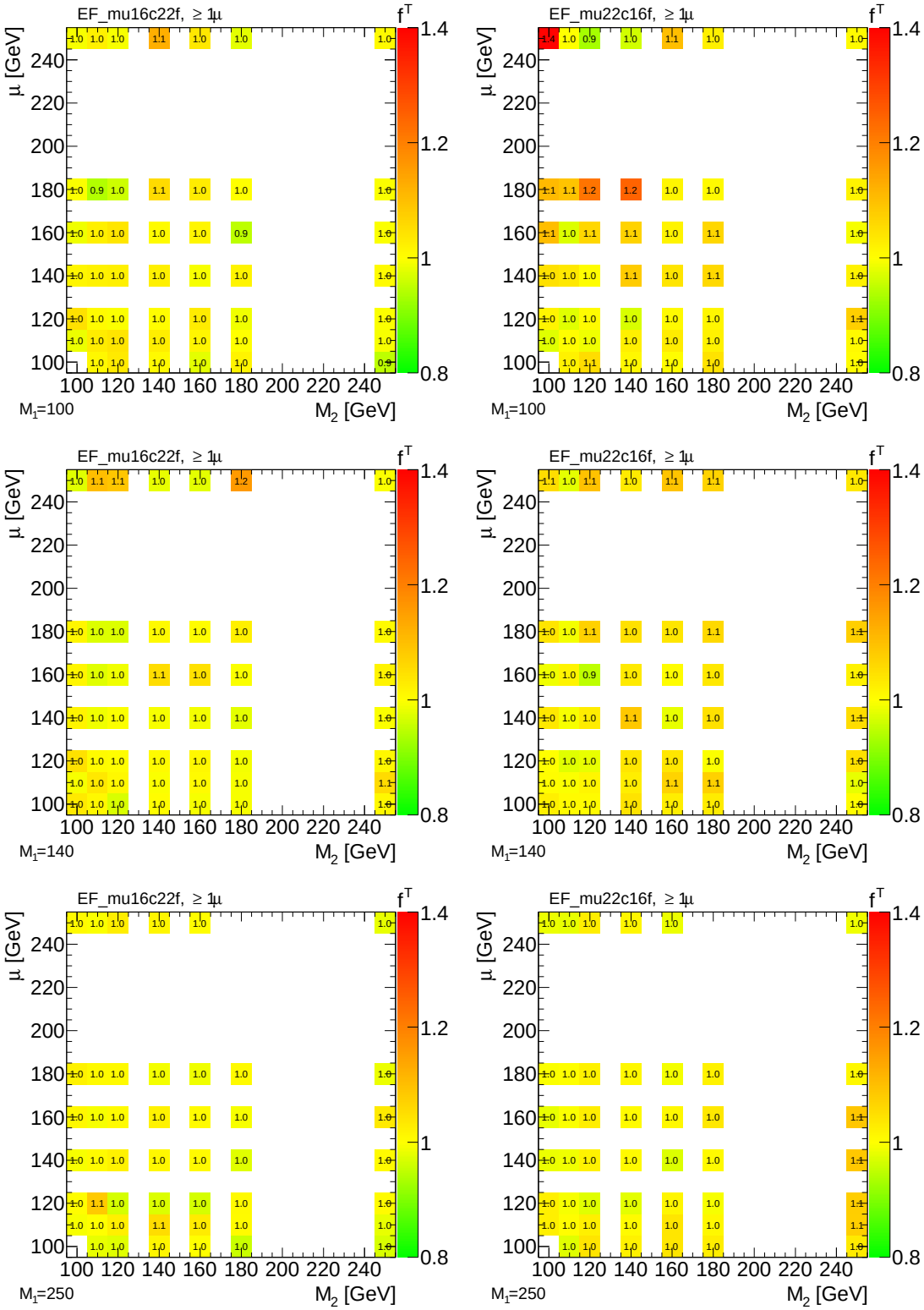


***Figure 6.13.:*** pMSSM signal grids: $f^T$ factors (cf. Section 6.3) for the EF_mu16c22f (left) and the EF_mu22c16f trigger (right) in events with at least one signal muons.

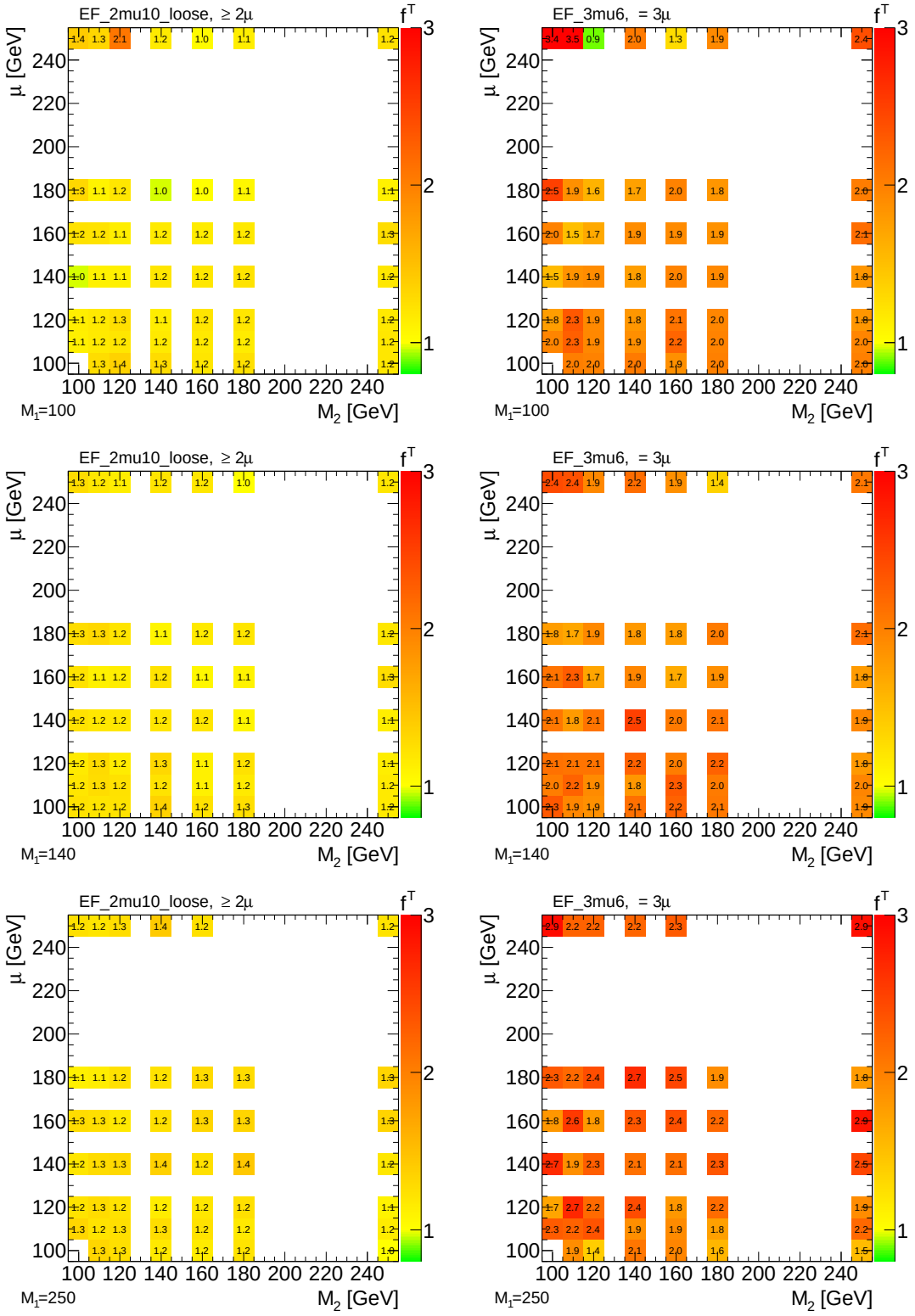


***Figure 6.14.:*** pMSSM signal grids: $f^T$ factors (cf. Section 6.3) for the EF_2mu10_loose (left) and the EF_3mu6 trigger (right) in events with at least one signal muons.

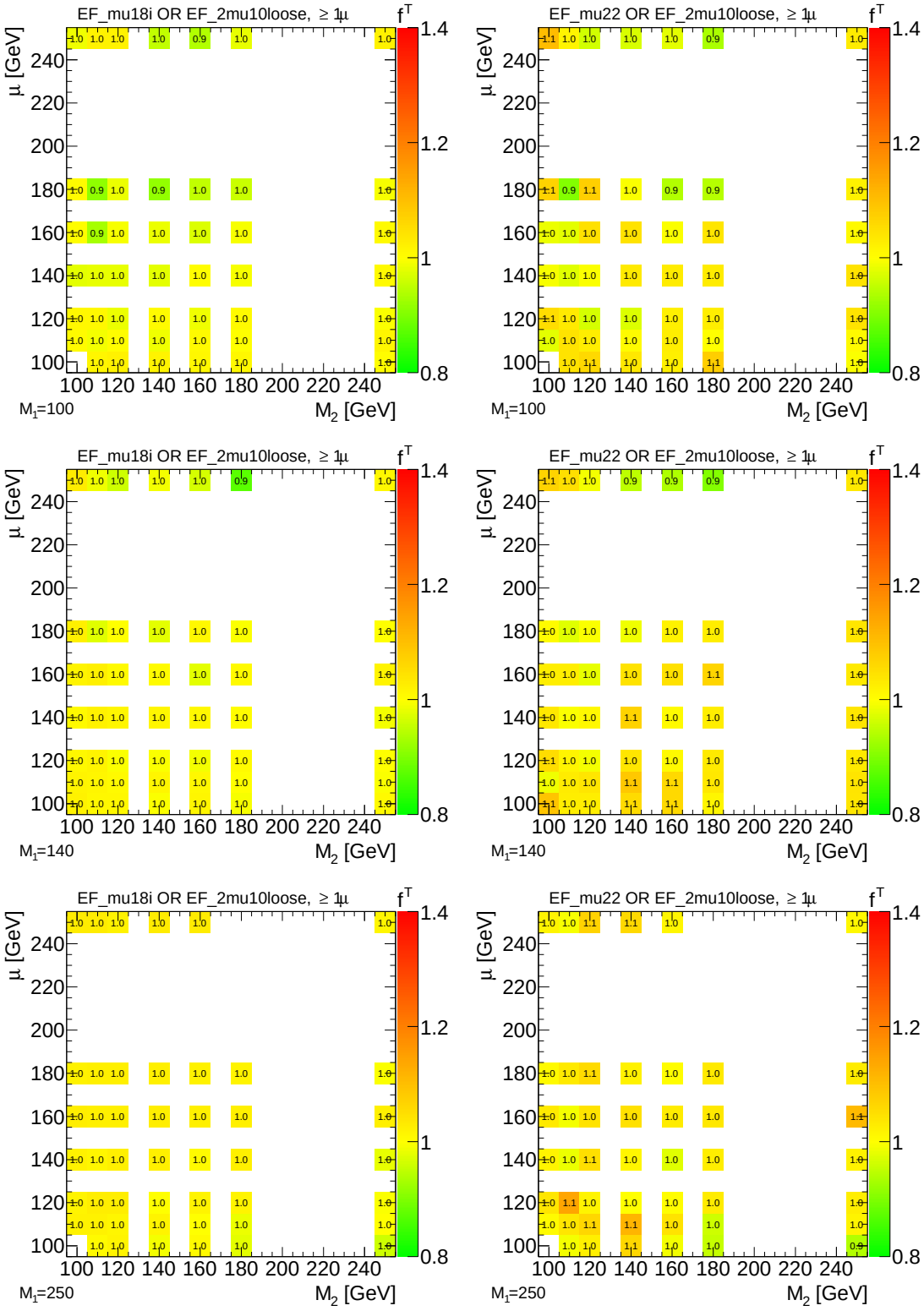


***Figure 6.15.:*** pMSSM signal grids: $f^T$ factors (cf. Section 6.3) for the EF_2mu10_loose (left) and the EF_mu22OR2mu10loose trigger (right) in events with at least one signal muons.

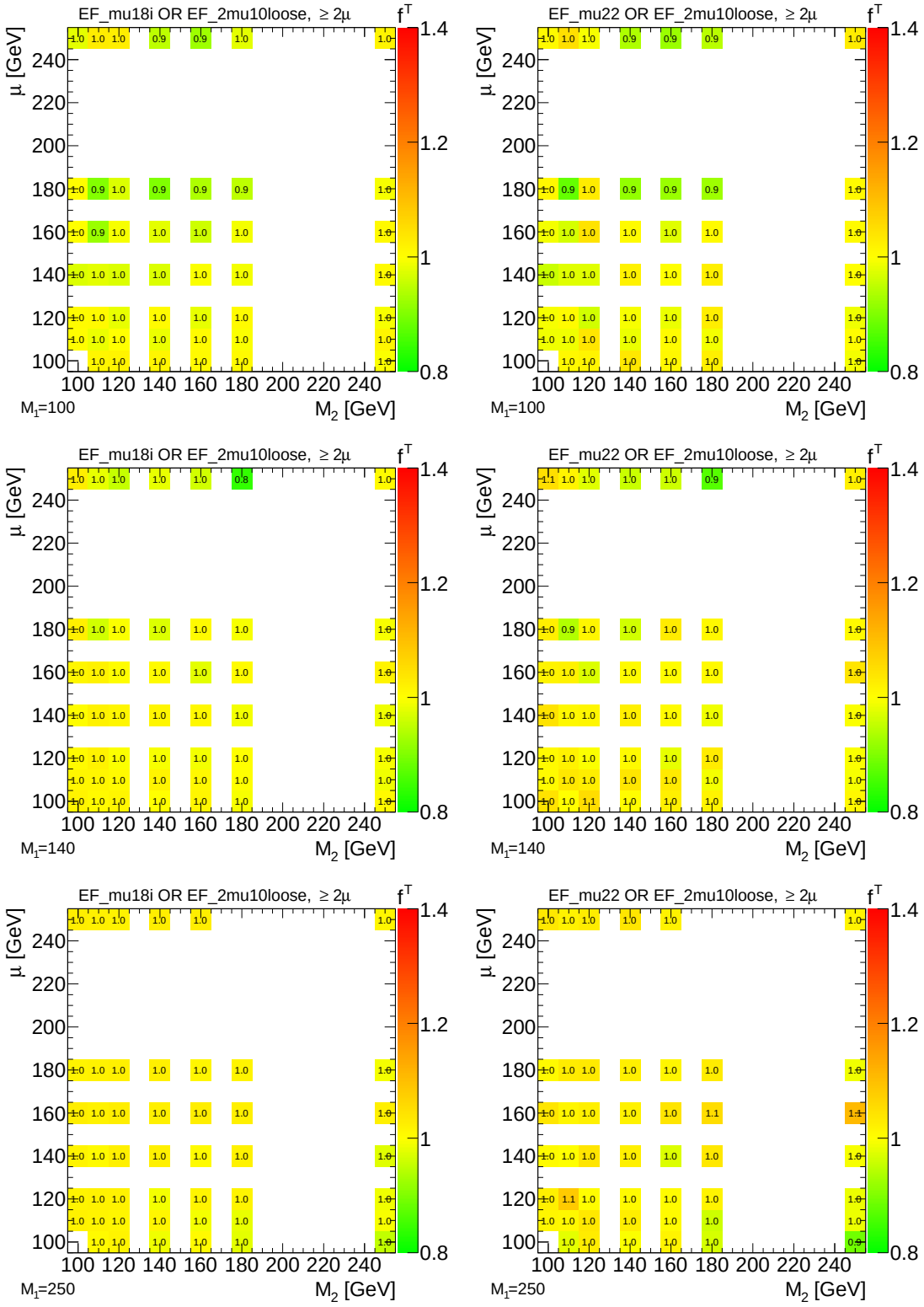


***Figure 6.16.:*** pMSSM signal grids: $f^T$ factors (cf. Section 6.3) for the EF_2mu10_loose (left) and the EF_mu22OR2mu10loose trigger (right) in events with at least two signal muons.

## 6.5. Discussion of the Output Rates and Expected Significances of Muon Triggers

The benefit of muon triggers is quantified in terms of their expected significance in a SUSY benchmark search and the costs are quantified in terms of their EF output rates. For this purpose, the factor $f^T$ (cf. Equation 6.7) and the ratio $r^T$ (cf. Equation 6.3) are introduced to put the costs and benefits of the studied triggers in relation to a reference trigger (EF_mu18). The factor $f^T$ describes how much more integrated luminosity is needed for a trigger $T$ to give the same expected significance as the reference trigger for a reference integrated luminosity and the ratio $r^T$ is the output rate of a trigger $T$ with respect to the output rate of the reference trigger. In general, the trigger output rates have to be below a certain limit (defined by the assigned bandwidth consumption). In this thesis, the maximum output rate is taken to be the output rate of the reference trigger, i.e. the ratio $r^T$ has to be smaller than one. Nevertheless, smaller values of $r^T$ are preferable in order to allow the running of the trigger for higher luminosities. The factor $f^T$ for the triggers should be as small as possible to allow for a discovery of the SUSY with a data set as small as possible. The results for both quantities for all studied triggers are summarised in Figure 6.17.
The benefit of a trigger, as it is defined in this thesis, depends by definition on the performed analysis (assumed signal model and analysis-specific criteria). Therefore, the results should not be interpreted to be universally applicable to all analyses and experimental conditions. The latter comprise, among others, the centre-of-mass energy and the instantaneous luminosities of the LHC.
For the chosen benchmark search for SUSY and the experimental conditions as in 2011 data-taking, the EF_mu18i trigger shows the best performance among the single muon triggers. Its expected significance is not significantly smaller than for the reference trigger, but the rate is considerably smaller. The EF_mu22 trigger shows the second best performance with a similar expected significance as the EF_mu18i, but a larger rate. The $\eta$-dependent single muon triggers, EF_mu16c22f and EF_m22c16f, show a similar performance as the reference trigger, with respect to rate (by construction) as well as expected significance. However, EF_mu16c22f seems to give slightly better expected significances than the EF_m22c16f. The prescaled EF_mu15 trigger shows the worst performance among all studied trig-

gers. It needs a factor of 1.91 (due to the prescale factor of 2.01) more integrated luminosity than the reference trigger to obtain the same expected significance, while it has the same output rate as the reference trigger. The multi-muon triggers have substantially smaller rates (more than one order of magnitude) and only a factor of 1.21 and 2.01, respectively, more integrated luminosity is needed to obtain the same expected significance as the reference single muon trigger in the channels (muon multiplicity) where the multi-muon triggers are sensitive to the signal. The combination of a single and the di-muon trigger improves the expected significance with respect to the single muon triggers only, while the rate increases only slightly. This makes the combination of "EF_mu18i OR EF_2mu10_loose" and "EF_mu22 OR EF_2mu10_loose" a good choice for the studied SUSY signal.

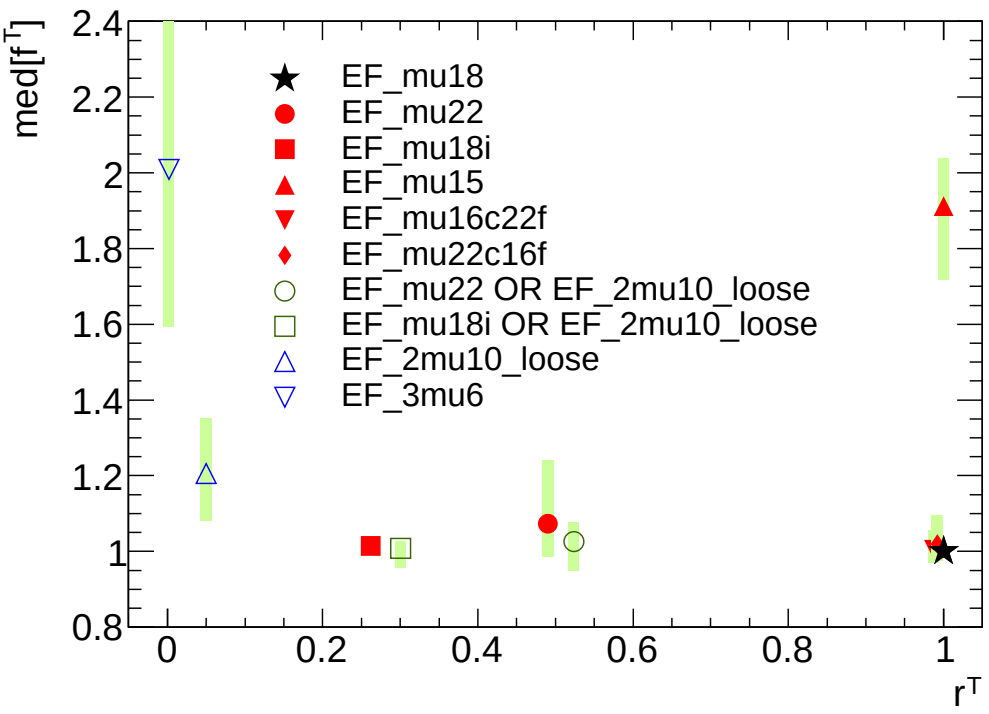


***Figure 6.17.:*** The performance of the studied muon triggers (and trigger combinations) in the $r^T$-$f^T$ plane. The factor $f^T$ (cf. Section 6.3) describes how much more integrated luminosity is needed to give the same expected significance as the reference trigger (EF_mu18, denoted by ★) for a reference integrated luminosity. The ratio $r^T$ (cf. Section 6.2) is the output rate with respect to the output rate of the reference trigger. The $r^T$ ratios and the $f^T$ factors are given separately in Table 6.1 and 6.4, respectively.

As indicated in Section 4.2, for single muon triggers, like EF_mu18, the output rate is directly proportional to the instantaneous luminosity for constant experimental conditions, in particular pile-up. However, for muon triggers which require isolation this is not the case. Due to pile-up, the output rate of muon triggers with isolation criteria saturates and can even decrease for very high instantaneous luminosities. The latter can occur if too much activity in the detector prevents the muons from being isolated (as "isolation" is defined at the moment, namely by the transverse momenta of the sum of all tracks in a cone around the track of the muon, cf. Section 4.3.4). The EF_mu15i trigger rate as a function of instantaneous luminosity is shown in Figure 6.18 (left) for the same run (run 184169) as in the previous chapters. Additionally, the trigger rates are fitted with a linear function through the origin in different intervals of instantaneous luminosity. For higher instantaneous luminosities, the slope of fits decreases significantly, showing the mentioned saturation effect. For comparison, Figure 6.18 (right) shows the EF_mu22 trigger rates fitted in the same intervals of instantaneous luminosity. The EF_mu22 trigger does not show a saturation effect as for the EF_mu15i trigger.

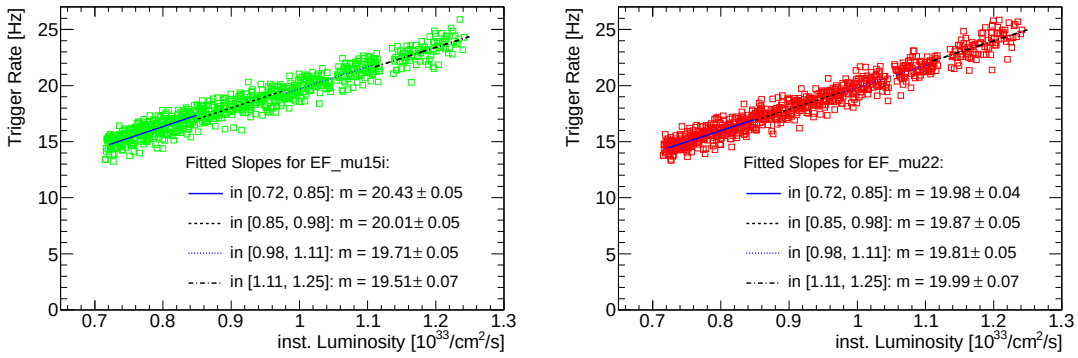


(a) EF_mu15i (b) EF_mu22

***Figure 6.18.:*** Output rate of the EF_mu15i (a) and EF_mu22 (b) trigger for run 184169 from period 2011H (same run as in the previous chapters) as a function of instantaneous luminosity. Additionally, the output rate is fitted with a linear function through the origin in different intervals of instantaneous luminosity. The slopes $m$ of these fits are shown in the plot.

For multi-muon triggers, a reversed behaviour is expected: an overproportional increase of the rate for higher instantaneous luminosities. This is not studied in

this thesis. However, this effect is expected to be rather small. An indication for this overproportional increase of the di-muon trigger rates would be a saturation of the single muon trigger rates, but this is not observed (cf. Figure 6.18, right). Under the assumption of trigger output rates increasing linearly with the instantaneous luminosity (discussed in Section 4.2), the triggers reach the output rate of the reference trigger at an instantaneous luminosity that is a factor $(r^T)^{-1}$ larger than the reference instantaneous luminosity (for which the output rate of the reference trigger is determined). The average instantaneous luminosity for which the trigger output rates shown in this chapter are determined is roughly $0.93 \cdot 10^{33}\,\mathrm{Hz/cm^2}$.

The triggers with additional isolation criteria show three disadvantages, which have not been discussed yet. Firstly, the trigger efficiency measurement introduces additional uncertainties due to the isolation criterion applied online by the trigger. In principle, the trigger efficiencies can depend on additional muon properties describing its isolation, which are not considered yet. To study these dependencies, additional studies have to be performed, which are beyond the scope of this thesis. Secondly, for many data-driven techniques for background (fake isolation) estimation, non-isolated muons are needed. These data-driven background estimations are discussed for instance in [68]. The third disadvantage concerns the expected event yield of the muon triggers. For higher instantaneous luminosities, the fraction of events which are expected to issue the muon trigger with isolation criterion decreases due to pile-up. The single muon triggers without these isolation criteria are expected to select a nearly [16] constant fraction of signal events. Nevertheless, for considerably higher instantaneous luminosities the "isolation" criterion applied in the analyses has to be reviewed to cope with the higher pile-up conditions.

Finally, the considered signal yield can be used to give a recommendation for the case that new physics, like SUSY, shows up in a certain discovery channel. In the following, the scenario that higher instantaneous luminosity than in the 2011 data-taking period are achieved, and that first signs of new physics became visible in events with high-$p_T$ muons, low-$p_T$ muons and more than one muon,

[16] The efficiencies for single muon triggers, like EF_mu18, is slightly lower for non-isolated muons. This is not discussed in this thesis.

are discussed.

- If processes not described by the SM yield high-$p_T$ muons, higher $p_T$-thresholds are an appropriate trigger strategy to keep most of the signal events, while complying with the bandwidth limitations. Most SUSY scenarios under study produce high-$p_T$ muons due to large mass differences between the predicted SUSY particles.

- If events with only one low-$p_T$ muon show the first signs of new physics, the studied muon triggers are not appropriate to achieve a high event yield. However, a combined trigger for a muon and "X" could be an adequate choice, where "X" depends on the signature of the signal events, e.g. $E_T^{\text{miss}}$ or jets.

- If a deviation from the SM is observed in events with more than one muon, multi-muon triggers are an appropriate trigger strategy, because they have a very low rate without prescaling. In SUSY scenarios where predominantly multi-muon events with low-$p_T$ muons are produced, the multi-muon triggers are the only applicable muon trigger strategy [17]. Of course, the combination with a single muon trigger can increase the signal yield.
  SUSY scenarios where predominantly multi-muon events with low-$p_T$ muons are produced are the ones, where the mass difference between the SUSY particles is relatively small such that high-$p_T$ muons are rare, e.g. in the upper left corner of the $M_1 = 100\,\text{GeV}$ or the lower right corner of the $M_1 = 250\,\text{GeV}$ pMSSM grids used in this thesis (cf. Appendix C). Other SUSY scenarios where predominantly staus are produced can also lead to such low-$p_T$ multi-muon events.

[17] A combined trigger of a muon and "X" could also be an adequate choice depending on how SUSY is realised in nature.

# 7. Conclusion and Outlook

In this thesis, the efficiencies and rates of single and di-muon triggers at the ATLAS detector at the Large Hadron Collider (LHC) have been studied. Additionally, various muon trigger strategies have been evaluated in the context of a benchmark search for Supersymmetry.

For every analysis performed on data which has been recorded based on a trigger selection, the precise knowledge of the trigger efficiency is crucial. Trigger efficiencies can be taken into account by following a reweighting approach. It has been shown that for the parametrisation of the muon trigger efficiencies, the transverse momentum $p_T$ and direction of the muon (described by $\eta$ and $\phi$) is sufficient. For the efficiencies of multi-muon triggers, possible correlations between the efficiencies of the individual muons have to be taken into account. Due to limited statistics, direct measurements of the multi-muon trigger efficiencies suffer from large statistical uncertainties. This precludes the application of directly measured multi-muon trigger efficiencies in the trigger reweighting approach.
For di-muon trigger efficiencies, it has been shown that they can be factorised into single muon trigger efficiencies, under the condition that the muons are separated by a sufficiently large angle. This factorisation makes the trigger reweighting approach applicable for di-muon triggers. The systematic uncertainties introduced by the factorisation are less than 1 %, while the statistical uncertainties are reduced considerably compared to the direct measurement of di-muon trigger efficiencies. A previous version of this study has been summarised in an ATLAS internal note [118].
Similar problems occur in the application of directly measured trigger efficiencies of other multi-object triggers, like di-electron or electron-muon triggers, following the trigger reweighting approach. The presented studies for the di-muon trigger

efficiencies suggest that the trigger efficiencies of multi-object triggers in general can be factorised into the corresponding single object trigger efficiencies. However, for other triggers than muon triggers additional studies have to be performed to examine under which conditions the factorisation ansatz is appropriate. For example, the trigger efficiencies of electrons with overlapping detector signatures have to be studied extensively (for instance [68]).

During data-taking in 2011, the muon trigger strategies worked well under the experimental conditions (instantaneous luminosity and centre-of-mass energy) of that time. For higher interaction rates, the current trigger strategies must be reviewed, in particular the bandwidth consumption of the different triggers. For this purpose, a cost-benefit analysis of various muon trigger strategies (single muon and multi-muon triggers with different $p_T$-thresholds, with and without isolation criteria) has been performed. The cost of the triggers has been quantified in terms of their rates at a reference instantaneous luminosity of roughly $0.9 \cdot 10^{33}\,\mathrm{Hz/cm^2}$ and for a centre-of-mass energy of 7 TeV. The benefit has been quantified in terms of the expected significance of a search for Supersymmetry with a tri-lepton final state. This signature favours multi-lepton triggers. The costs and benefits of the muon triggers have been evaluated with respect to a reference trigger (EF_mu18) and their applicability for interaction rates higher than for the reference instantaneous luminosity. The applicability for higher interaction rates has been assumed to be reflected by the instantaneous luminosity up to which the trigger can be run unprescaled because its rate does not exceed the rate of the reference trigger. For the performed analysis, the different muon triggers show very different behaviours with respect to rate and expected significance. Among the single muon triggers, the trigger (EF_mu22) with a higher $p_T$-threshold compared to the reference trigger and the muon trigger with an isolation criterion (EF_mu18i) show the best performance: similar expected significances as for the reference trigger are observed and a considerable rate suppression (factor 2 and 4, respectively) is achieved. However, as discussed, the isolation criteria have some drawbacks with respect to their signal yield for higher luminosities and data-driven techniques for background estimation. When prescaling a single muon trigger with a $p_T$-threshold lower than the reference trigger, a bad performance is observed, since a considerable fraction of signal events is discarded. The highest rate suppression

(more than an order of magnitude) is achieved by the multi-muon triggers. For the di-muon trigger (EF_2mu10_loose), only a factor of roughly 1.2 more data is needed to achieve the same expected significance as the reference trigger. A combination of one of the low-rate single muon trigger with the di-muon trigger improves the expected significance considerably with respect to the single muon trigger only, while the rate increases only slightly. In particular, the combination of a single muon trigger with a high $p_T$-threshold and a di-muon trigger with a low $p_T$-threshold extends the covered signal phase space.

Due to the chosen Supersymmetry discovery channel with a multi-lepton final state, the multi-muon triggers are favoured in this analysis. For other types of analyses, e.g. top quark measurements or other Supersymmetry scenarios, the benefits of the different triggers change. Nevertheless, the combination of different trigger signatures is a trigger strategy that can be pursued for many physics analysis strategies.

With an advanced understanding of the trigger system, more sophisticated modifications of the triggers can be implemented. Similar to the combination of different triggers in the analysis, specialised triggers combining different signatures are conceivable. Depending on the future plans of the ATLAS collaboration and whether indications of new physics like Supersymmetry are found at the LHC, several of these specially tailored triggers with small bandwidth consumption are possible.

# A. Statistical Uncertainties of Trigger Efficiencies

Trigger efficiency measurements always come with a statistical uncertainty as every measurement. Depending on the interpretation of probability different approaches to estimate this uncertainty are in use. In the following, a Frequentist and Bayesian approach to estimate the statistical uncertainty of a trigger efficiency measurement are described. Both approaches are used in this thesis.

## A.1. Frequentist Approach

The trigger decision can be interpreted as a Bernoulli process (two possible outcomes: triggered or not triggered). If the outcome of $n$ trigger decisions is $k$ triggered objects, the ratio $k/n$ tends for $n \to \infty$ to a limit, which is defined as the Frequentist probability $p(k)$ of $k$. Hence, from a Frequentist perspective the trigger efficiency $\varepsilon$ can be defined as:

$$\varepsilon = \frac{k}{n}. \tag{A.1}$$

For a given efficiency $\varepsilon$ the probability $p$ of having exactly $k$ triggered objects out of $n$ objects obeys a Binomial distribution:

$$p(k) = \binom{n}{k} \varepsilon^k (1-\varepsilon)^{n-k}. \tag{A.2}$$

The average of the Binomial distribution is given by its expectation value:

$$\langle p(k) \rangle = \sum_{k=0}^{n} k \binom{n}{k} \varepsilon^k (1-\varepsilon)^{n-k} = n\varepsilon \tag{A.3}$$

The variance of the Binomial distribution is a measure for its spread, i.e. its statistical uncertainty:

$$\sigma^2 = n\varepsilon(1-\varepsilon) \tag{A.4}$$

Thus, the Binomial uncertainty for a given efficiency $\varepsilon$ and number of trials $n$ is given by:

$$\sigma_n = \frac{\sigma}{n} = \sqrt{\frac{\varepsilon(1-\varepsilon)}{n}} \tag{A.5}$$

In practice, the uncertainty of a efficiency measurement is often approximated by a Gaussian uncertainties with a standard deviation equal to $\sigma_n$.
This model of the statistical uncertainties has two major deficiencies:

- The obtained uncertainty is symmetric and does not reflect the underlying Binomial distribution, which is asymmetric. This is in particular the case for low statistics and efficiencies close to zero or one. For different statistics the comparison between a Binomial distribution and the Gaussian approximation is shown in Figure A.1. For higher statistics the Binomial distribution is well approximated by a Gaussian.

- For certain cases, the obtained uncertainty are unrealistic. For efficiencies approaching zero or one, the resulting uncertainty vanishes. At the extreme cases of zero or $n$ out of $n$, the uncertainty is zero, independent of the available statistics. This is shown in Figure A.2.

## A.2. Bayesian Approach

To account for the asymmetry introduced by the Binomial distributed outcome of a trigger efficiency measurement and to solve the problem at the boundaries ($\varepsilon = 0$ and $\varepsilon = 1$) a Bayesian approach can be chosen. The Bayesian interpretation of probability is also known as subjective probability, because the probability is interpreted as subjective degree of belief. Bayesian inference uses Bayes' theorem [107] to update the probability of an event as additional evidence, that is meant to

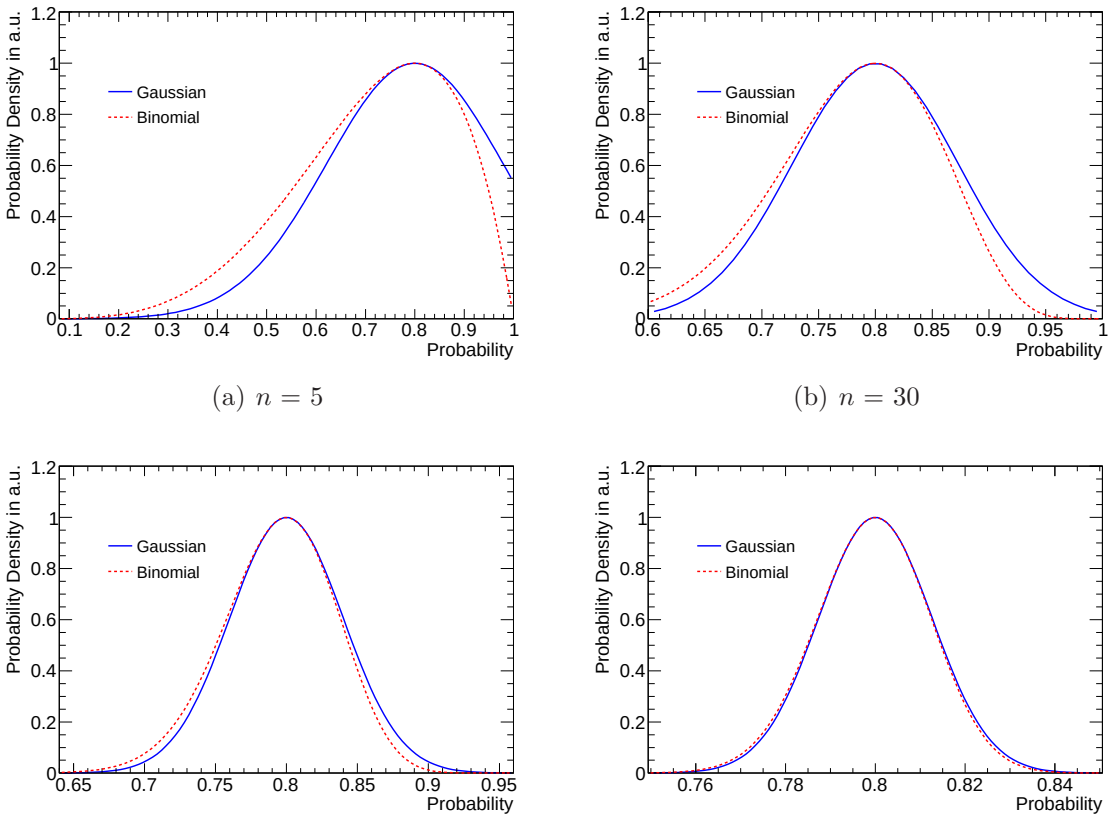


(a) $n = 5$ (b) $n = 30$

(c) $n = 100$ (d) $n = 1000$

***Figure A.1.:*** Comparison between a Binomial distribution and a Gaussian approximation with standard deviation equal $\sigma_n$ (cf. Equation A.5) for the same efficiency $\varepsilon$, but different statistics $n$. Note that the range of the x-axis changes. For higher statistics the Binomial distribution is well approximated by a Gaussian.

be consistent or inconsistent with a given hypothesis, is collected. Data analysis from a Bayesian perspective has been discussed in literature [168–170].
The Bayes' theorem gives the relationship between the probabilities of $x$ and $y$, $p(x)$ and $p(y)$, and the conditional probabilities of $x$ given $y$ and $y$ given $x$, $p(x|y)$ and $p(y|x)$:

$$p(x|y) = \frac{p(x,y)}{p(y)} = \frac{p(y|x)\,p(x)}{p(y)}. \tag{A.6}$$

For the particular case of efficiency $\varepsilon$, given $k$ and $n$, the Bayesian probability density is:

$$p(\varepsilon|k,n) = \frac{p(k,n|\varepsilon)\,p_0(\varepsilon)}{\int p(k,n|\varepsilon)\,\mathrm{d}\varepsilon}, \tag{A.7}$$

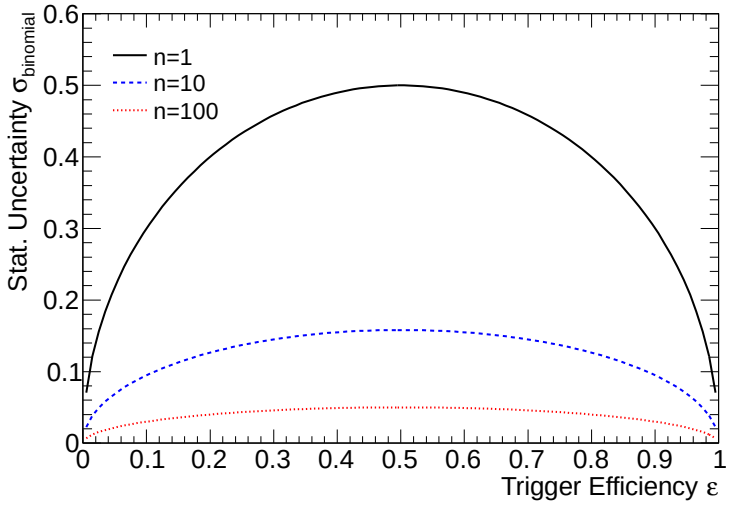


***Figure A.2.:*** Uncertainty of a Binomial distribution, defined as in Equation A.5, as a function of efficiency $\varepsilon$ for different statistics $n$. The uncertainties for efficiencies close to zero or one always approach zero, independent of the available statistics.

where $p(k, n|\varepsilon)$ is the probability density for $k$ and $n$ given $\varepsilon$ and $p_0(\varepsilon)$ the a priori probability to have the efficiency $\varepsilon$. The integration has to be performed over the whole allowed efficiency range $[0, 1]$ as a normalisation.
The probability density $p(k, n|\varepsilon)$ obeys a Binomial distribution (cf. Equation A.2). Considering a flat a priori probability density for $p_0(\varepsilon)$ yields in:

$$p(\varepsilon|k, n) = \frac{\varepsilon^k(1-\varepsilon)^{n-k}}{\int_0^1 \varepsilon^k(1-\varepsilon)^{n-k}\,\mathrm{d}\varepsilon}. \tag{A.8}$$

From this probability density an estimator for the absolute efficiency and asymmetric uncertainties can be derived:

$$\hat{\varepsilon} = \text{mode}\left(p\left(\varepsilon\right)\right), \tag{A.9}$$

$$\int_{\hat{\varepsilon}-\sigma^{\text{low}}}^{\hat{\varepsilon}+\sigma^{\text{high}}} p\left(\varepsilon\right) d\varepsilon = 0.6827 \text{ (equivalent to } 1\sigma \text{ region of a Gaussian)}, \tag{A.10}$$

where the sum $\sigma^{\text{high}} + \sigma^{\text{low}}$ is minimal, such that the smallest $\varepsilon$ region equivalent to the $1\sigma$ region (containing 68.27 %) of a Gaussian is chosen. This is shown in Figure A.3. Other quantiles can be defined similarly. In this thesis a similar procedure as described in [101] is used to extract these estimates numerically.
The estimator for the absolute efficiency as defined in Equation A.9 gives the

same result as the Frequentist approach (cf. Appendix A.1), which a posteriori justifies this estimator and in particular the choice of flat priors.

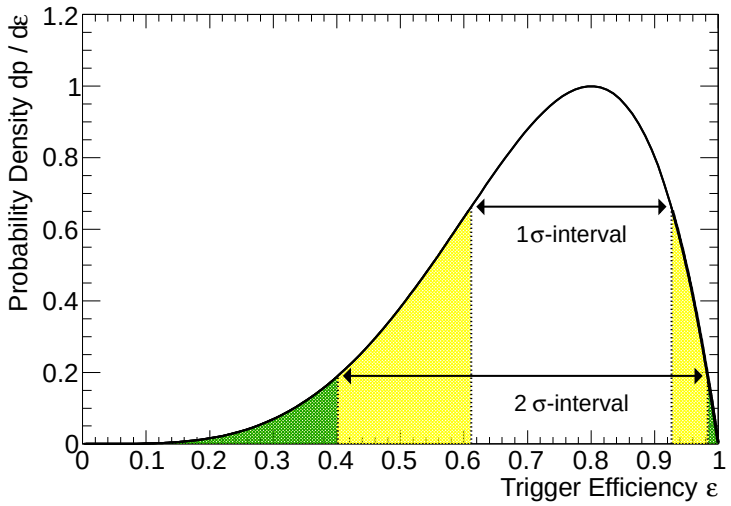


***Figure A.3.:*** Binomial distribution for $k = 4$ out of $n = 5$ with the $1\sigma$ and $2\sigma$ intervals as defined in Equation A.10. The mode of the distribution, and therefore also the estimator of the absolute efficiency, is equal to $k/n = 0.8$, which is also the Frequentist efficiency.

# B. Muon Trigger Configurations

| Trigger chain (Note) | EF trigger $p_T$-thresholds [GeV] ($\|\eta\|$ dependent): $\|\eta\| \in [0, 1.05, 1.5, 2, \infty]$ | L2 trigger | L1 trigger coincidence window [GeV] |
|---|---|---|---|
| EF_mu18 | EF_mu18 [17.53,17.39,17.34,17.28] | L2_mu18 [17.5,16.6,16.6,16.8] | L1_MU10 10 |
| EF_mu22 | EF_mu22 [21.40, 21.27,21.25,21.16] | L2_mu22 [21.4,20.3,20.3,20.1] | L1_MU10 10 |
| EF_mu15 | EF_mu15 [14.63,14.49,14.42,14.38] | L2_mu15 [14.5,14.0,14.0,14.5] | L1_MU10 10 |
| EF_mu15i (isolation) | EF_mu15i [14.63,14.49,14.42,14.38] | L2_mu15i [14.5,14.0,14.0,14.5] | L1_MU10 10 |
| EF_mu10_loose | EF_mu10_loose [9.77, 9.67, 9.62, 9.57] | L2_mu10_loose [9.8, 9.5, 9.6, 9.7] | L1_MU0* 0/4* |
| EF_mu6 | EF_mu6 [5.88, 5.81, 5.78, 5.76] | L2_mu6 [5.8, 5.8, 5.8, 5.6] | L1_MU6 6 |
| EF_2mu10_loose (2 muons) | EF_2mu10_loose [9.77, 9.67, 9.62, 9.57] | L2_2mu10_loose [9.8, 9.5, 9.6, 9.7] | L1_2MU0* $2 \times 0/4^*$ |
| EF_3mu6 (3 muons) | EF_3mu6 [5.88, 5.81, 5.78, 5.76] | L2_3mu6 [5.8, 5.8, 5.8, 5.6] | L1_3MU6 $3 \times 6$ |

***Table B.1.:*** Trigger configuration of the triggers used in this thesis: EF_mu18, EF_mu22, EF_mu15, EF_mu15i, EF_mu10_loose, EF_mu6, EF_2mu10_loose, EF_3mu6. * For EF_mu10_loose and EF_2mu10_loose the L1 $p_T$-threshold has changed from period 2011L onwards from 0 GeV (L1_MU0, L1_2MU0) to 4 GeV (L1_MU4, L1_2MU4).

| Trigger chain (Note) | EF trigger $p_T$-thresholds [GeV] ($\|\eta\|$ dependent): $\|\eta\| \in [0, 0.5, 1.05, 1.5, 2, \infty]$ | L1/L2 trigger |
|---|---|---|
| EF_mu18i (isolation) | EF_mu18i [17.53, 17.53, 17.39, 17.34, 17.28] | L1_MU10 L2_mu15i |
| EF_mu16c22f | EF_mu18i [15.63, 16.63, 19.39, 20.34, 21.16] | L1_MU10 L2_mu15 |
| EF_mu22c16f | EF_mu18i [21.40, 20.40, 16.49, 15.42, 15.38] | L1_MU10 L2_mu15 |

***Table B.2.:*** Trigger configuration of the virtual triggers used in this thesis: EF_mu18i, EF_mu16c22f, EF_mu22c16f.

| Trigger chain | Trigger Plateau $p_T$ [GeV] ($\|\eta\|$ dependent): $\|\eta\| \in [0 ,0.5 ,1.05 ,1.5 ,2 , \infty]$ | | | | |
|---|---|---|---|---|---|
| EF_mu6 | 8 | | | | |
| EF_mu10_loose | 12 | | | | |
| EF_mu15 | 17 | | | | |
| EF_mu18 | 20 | | | | |
| EF_mu22 | 24 | | | | |
| EF_mu15i | 17 | | | | |
| EF_mu18i | 20 | | | | |
| EF_mu16c22f | 18 | 18 | 22 | 23 | 24 |
| EF_mu22c16f | 22 | 21 | 19 | 18 | 18 |

***Table B.3.:*** Begin of the efficiency plateau of the triggers used in this thesis. The multi-muon trigger are assumed to start at the same muon $p_T$ value as the corresponding single muon triggers.

# C. pMSSM Grid

In this appendix, a number of plots are collected describing the phenomenology of the pMSSM signal grids used in this theses. Most of them are taken from [68], where also a detailed discussion of the plots can be found.
The integrated luminosity of each MC is shown in Figure C.1 and the relative contribution of the dominant decay channels is shown in Figure C.2, together with the relative fraction of a 0, 1, 2 and $> 3$ lepton final states. The number of signal events (unweighted) in the tri-lepton signal region, as defined in Section 6.4.4, are shown separately for the $1\mu$, $2\mu$ and $3\mu$ channel in Figure C.3 and C.4. Additionally, the bino/wino/higgsino composition of the neutralinos and charginos is shown in Figure C.7 and C.6, their masses are shown in Figure C.7-C.9 and the mass difference between $\tilde{\chi}_1^{\pm}$ and $\tilde{\chi}_1^0$ as well as between $\tilde{\chi}_2^0$ and $\tilde{\chi}_1^0$ is shown in Figure C.10. The relevant branching rations are shown in Figure C.11 and C.12. In the plots $M_2$ and $\mu$ are denoted as M2 and MU, and the neutralinos and charginos are denoted as $\tilde{N}_i$ and $\tilde{C}_i$. Most of the plots are so-called colour-ratio plots, where for a given bin the relative importance of a quantity is proportional to the amount of corresponding colour in this bin.
The effective cross-section (NLO cross-section from Prospino2.1 times filter efficiency) of each of the grid points can be inferred from their integrated luminosity and the fact that for each grid point 25000 events were generated. For a few grid points, Prospino2.1 refuses to calculate the cross-sections for some of the subprocesses ($\tilde{\chi}_1^0\tilde{\chi}_1^0$, $\tilde{\chi}_1^0\tilde{\chi}_1^{\pm}$, $\tilde{\chi}_1^+\tilde{\chi}_1^-$), since the involved particles are too light. In these cases, the LO cross-sections and an averaged k-factor for the NLO normalisation have been used.
The 147 datasets have the MC sample IDs 138421-138567.

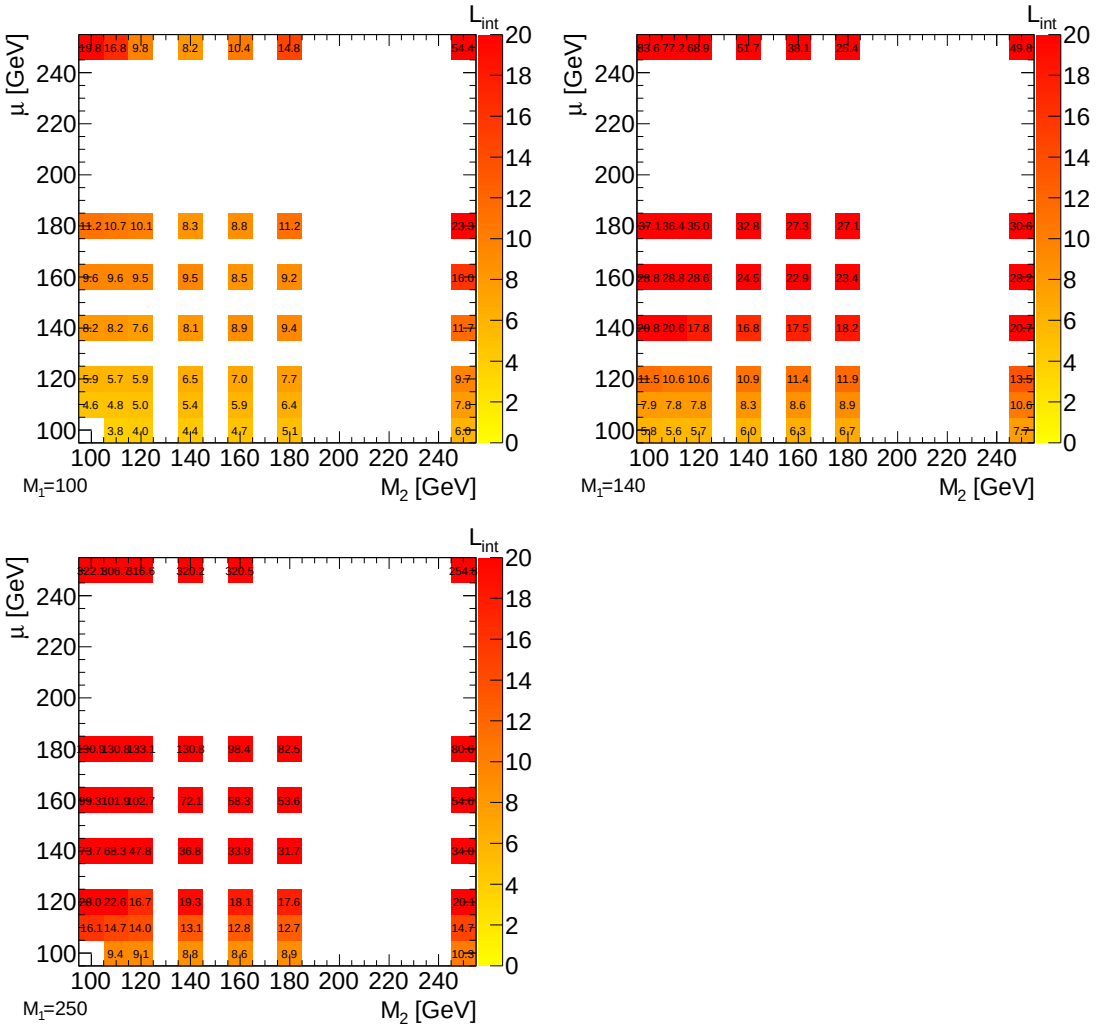


***Figure C.1.:*** pMSSM signal grids: integrated luminosities $L_{int}$, where the Prospino2.1 NLO cross-sections have been used, if applicable. For grid points where no integrated luminosity is stated, no MC sample is available.

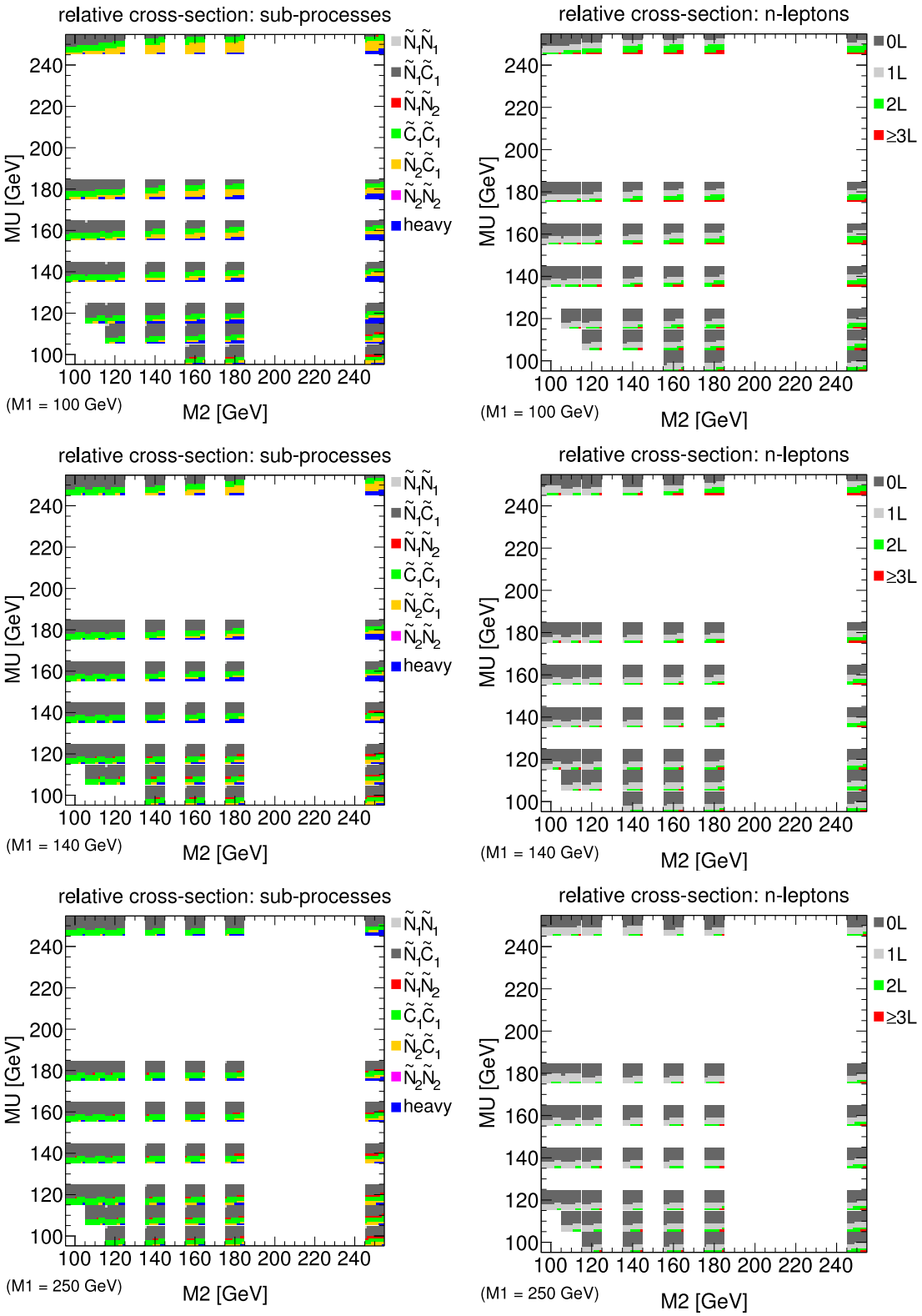


***Figure C.2.:*** pMSSM signal grids: relative contribution of the dominant decay channels (left) and the relative fraction the 0, 1, 2 and $> 3$ lepton final states (right). Taken from [68].

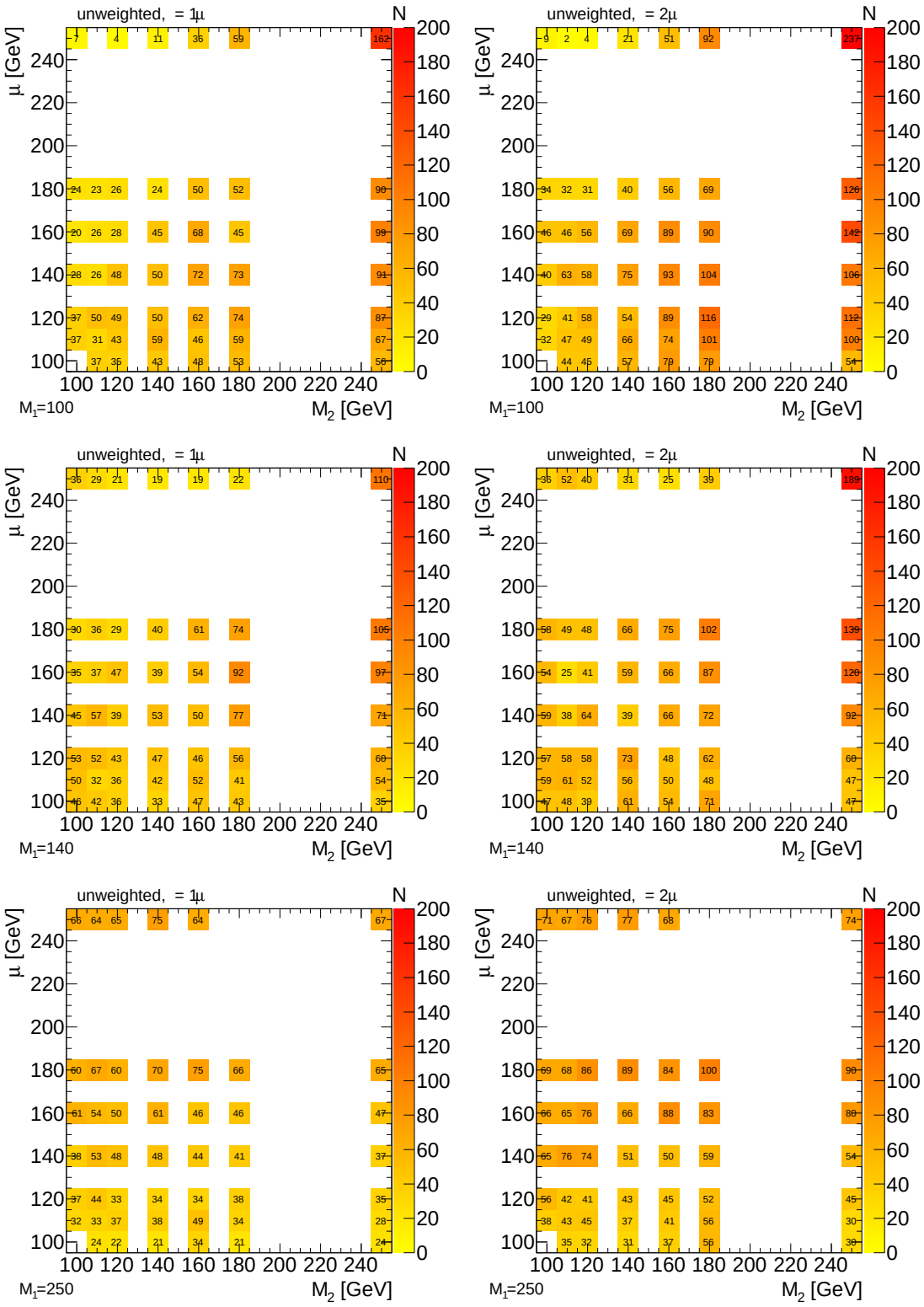


***Figure C.3.:*** pMSSM signal grids: unweighted number ($N$) of events in the signal region with exactly $1\mu$ (left) and $2\mu$ (right) signal muons.

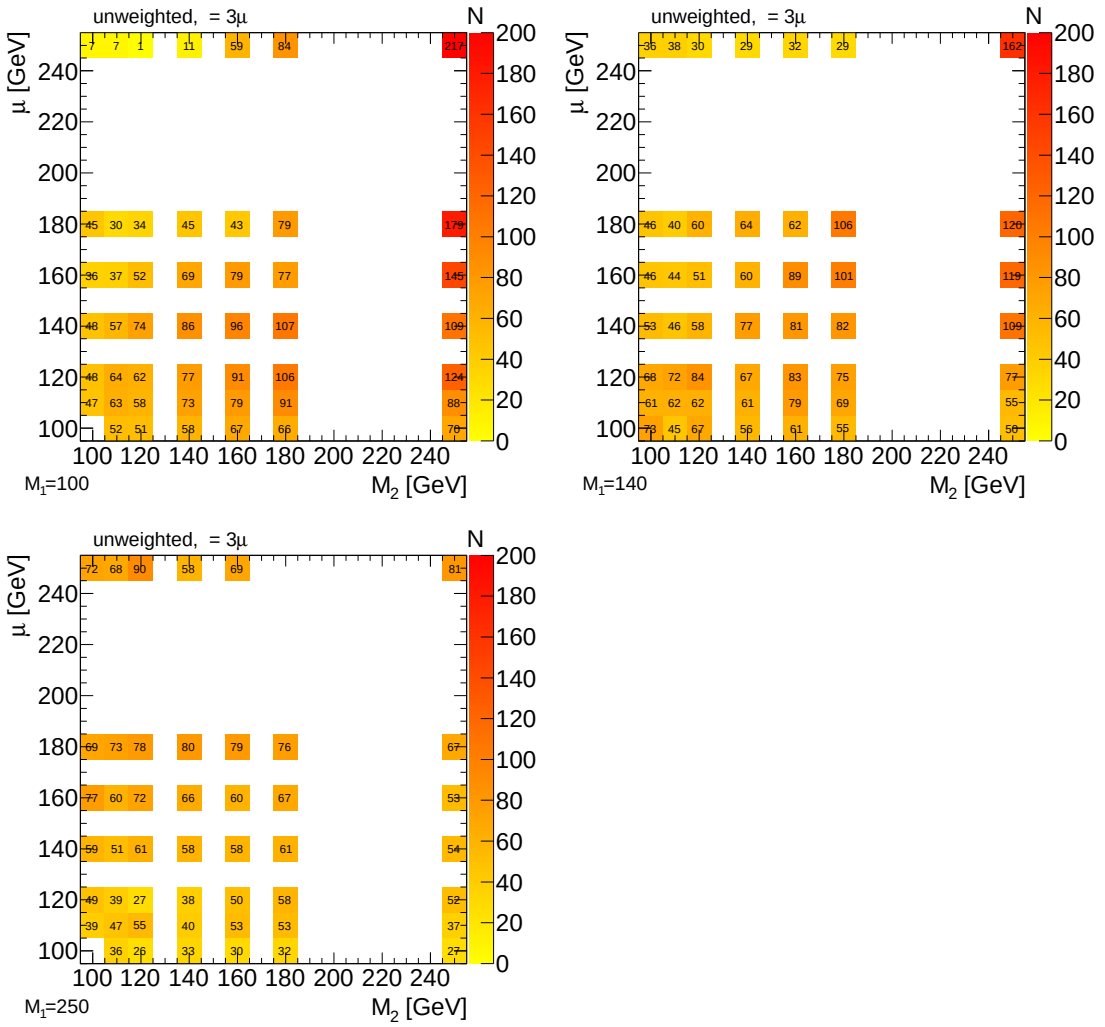


***Figure C.4.:*** pMSSM signal grids: unweighted number ($N$) of events in the signal region with exactly 3 signal muons.

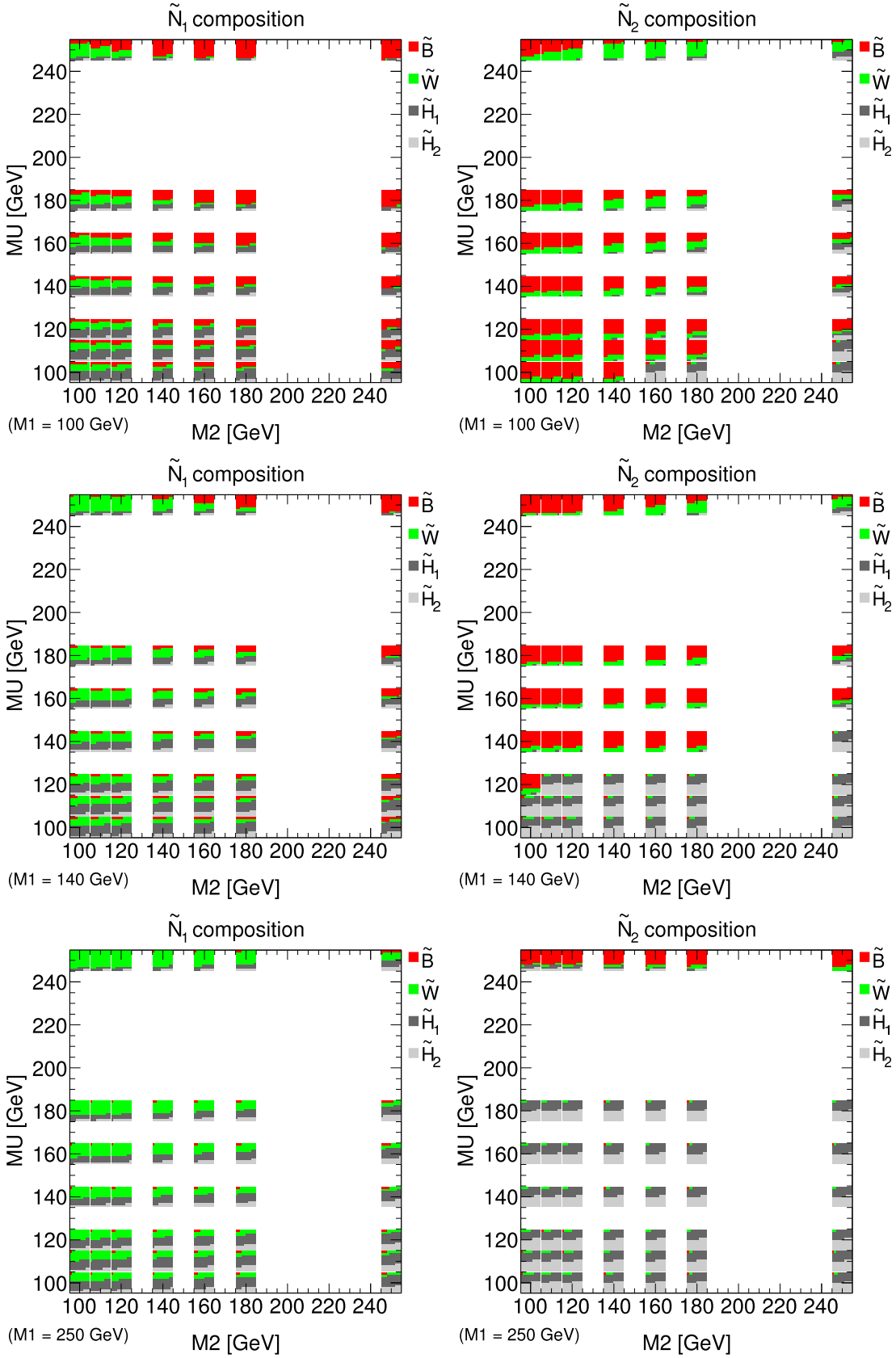


***Figure C.5.:*** pMSSM signal grids: composition of $\tilde{\chi}_1^0$ and $\tilde{\chi}_2^0$. Taken from [68].

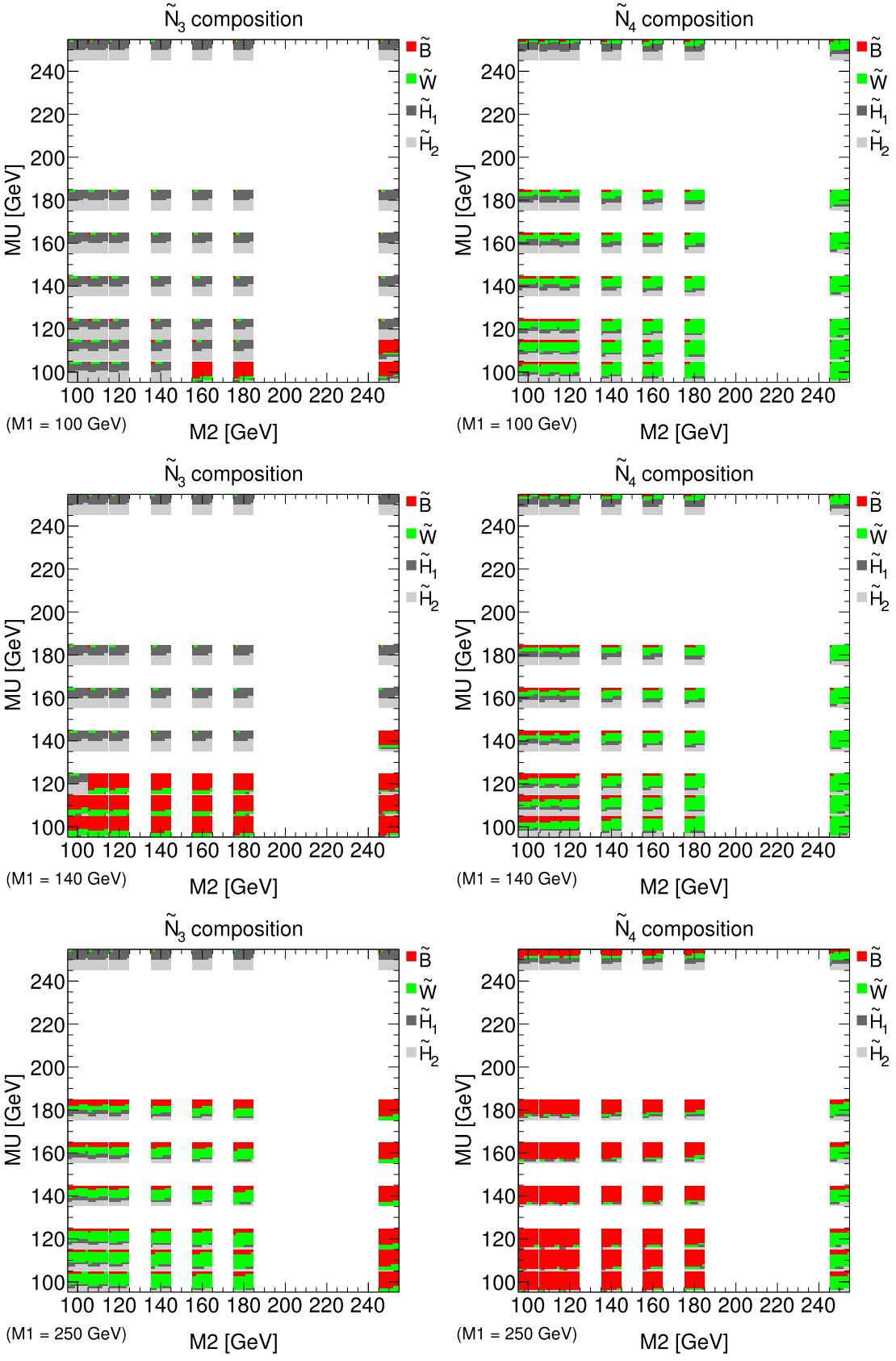


***Figure C.6.:*** pMSSM signal grids: composition of $\tilde{\chi}_3^0$ and $\tilde{\chi}_4^0$. Taken from [68].

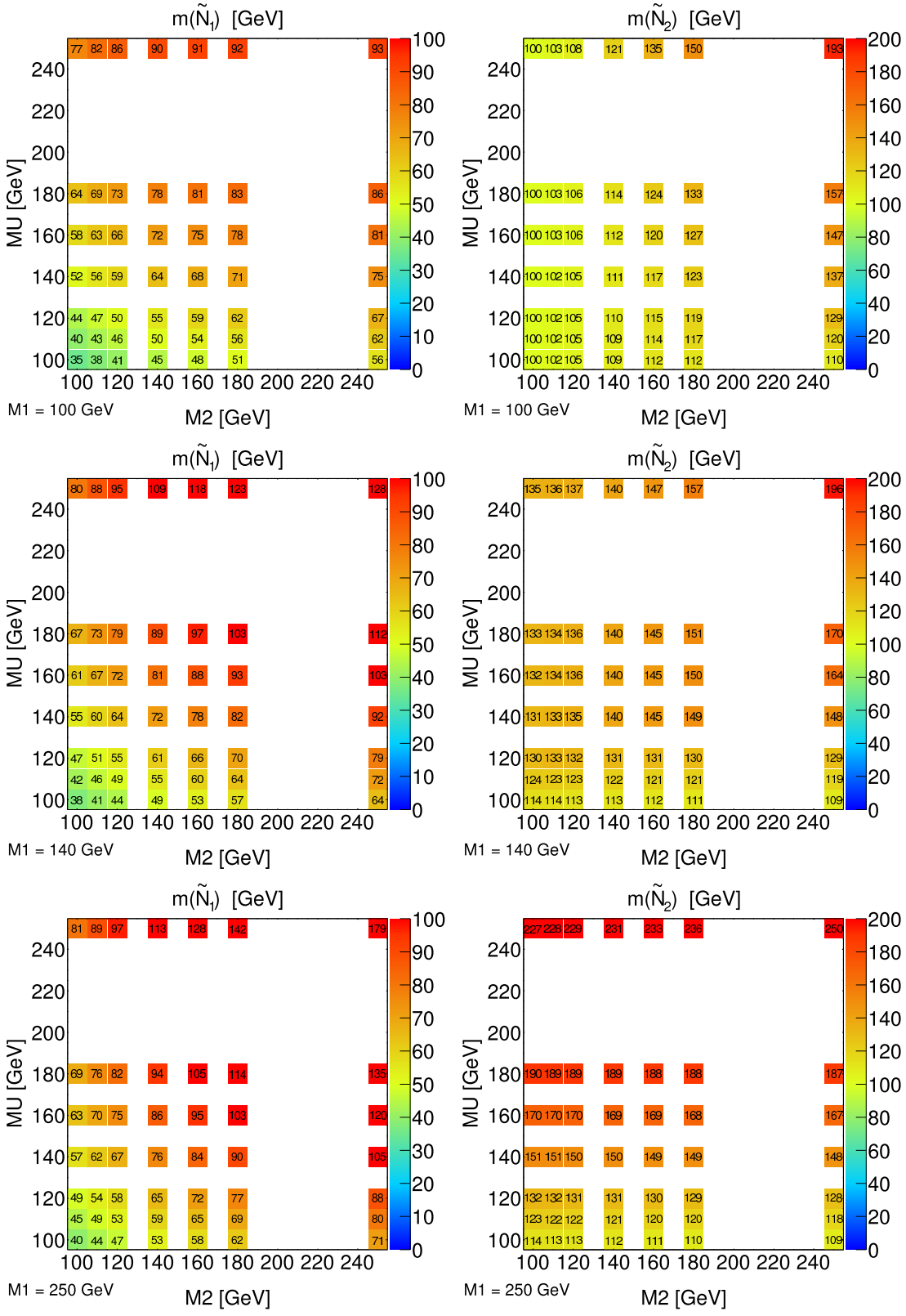


***Figure C.7.:*** pMSSM signal grids: masses of $\tilde{\chi}_1^0$ and $\tilde{\chi}_2^0$. Taken from [68].

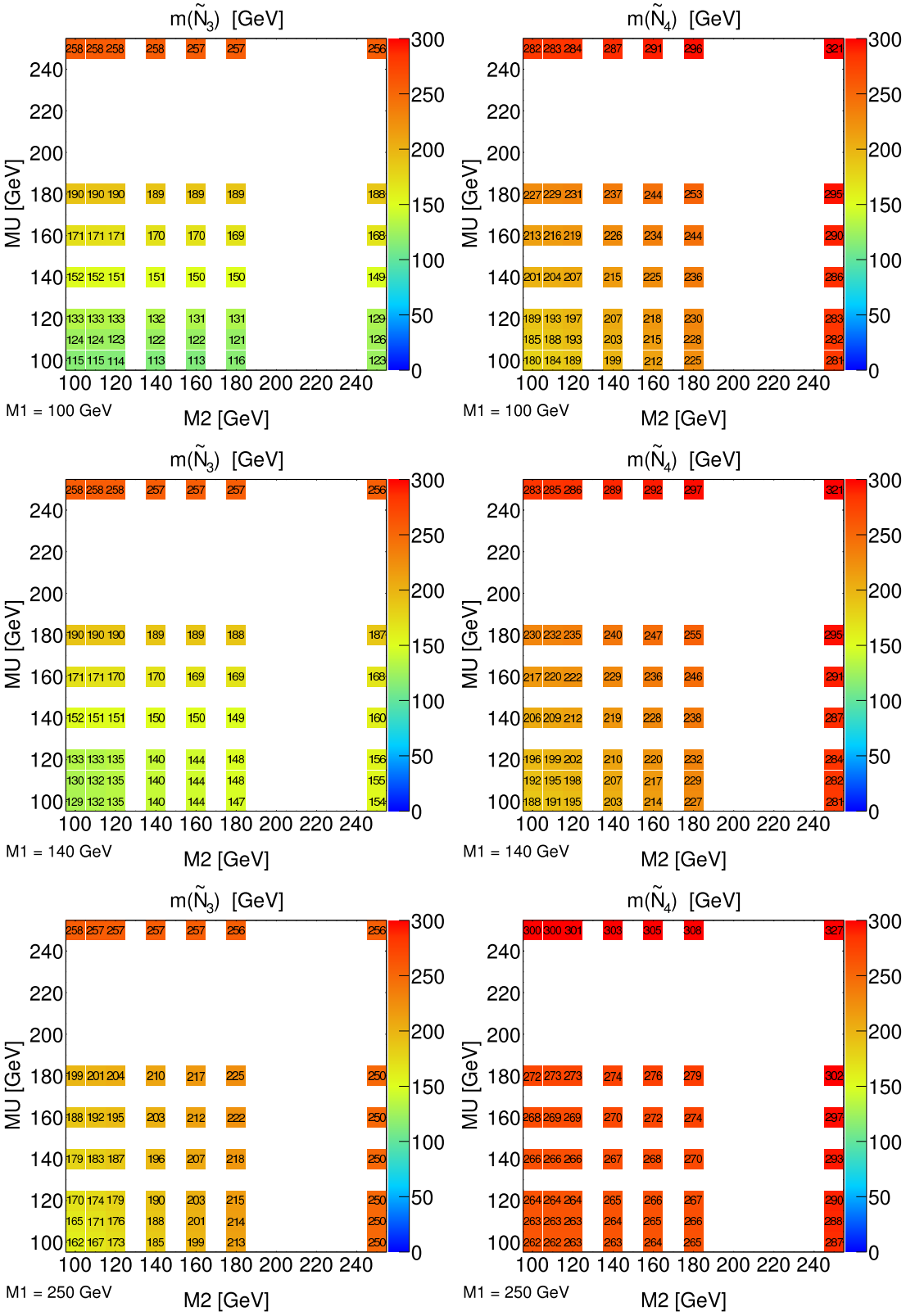


***Figure C.8.:*** pMSSM signal grids: masses of $\tilde{\chi}_3^0$ and $\tilde{\chi}_4^0$. Taken from [68].

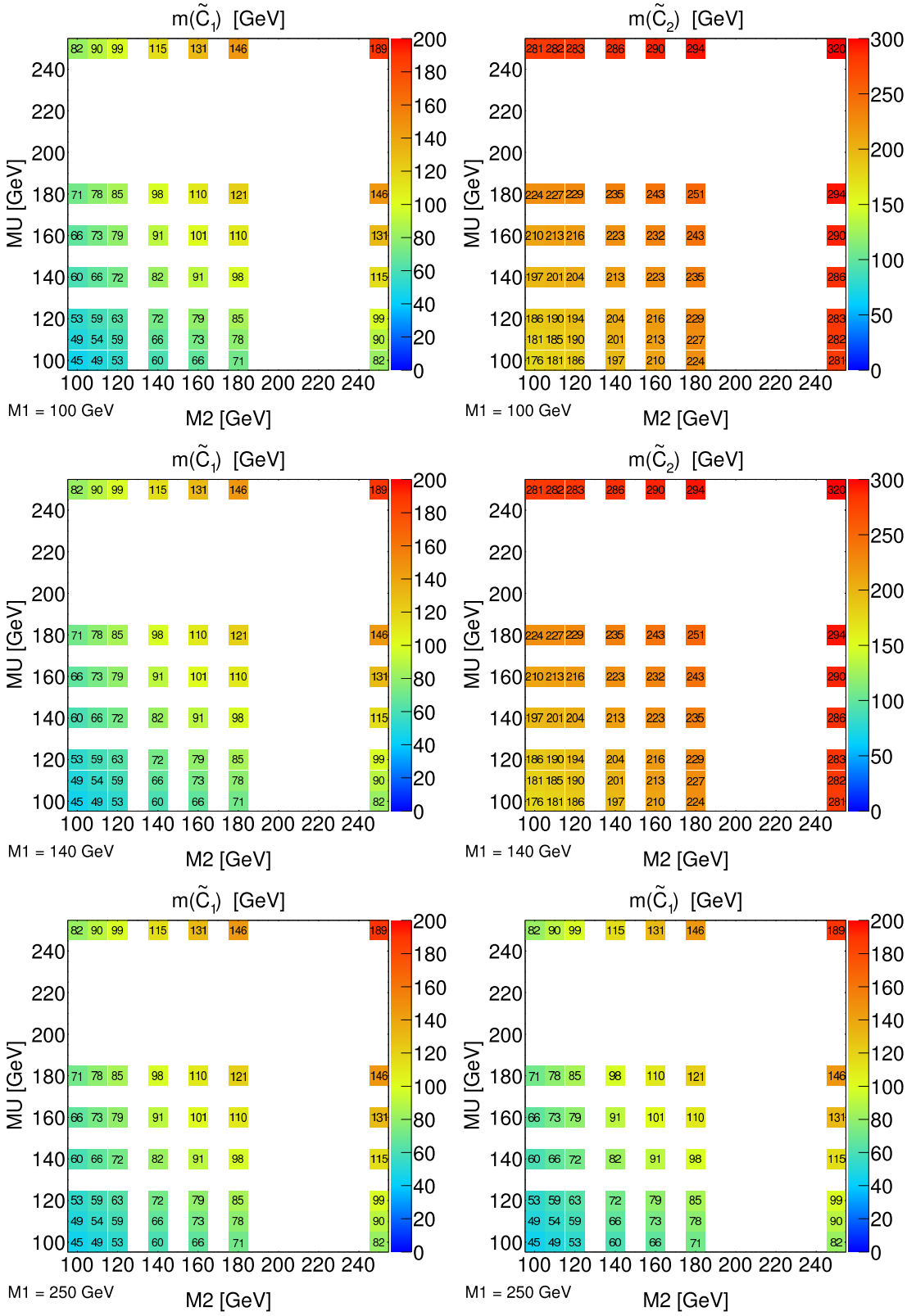


***Figure C.9.:*** pMSSM signal grids: masses of $\tilde{\chi}_1^{\pm}$ and $\tilde{\chi}_2^{\pm}$. Taken from [68].

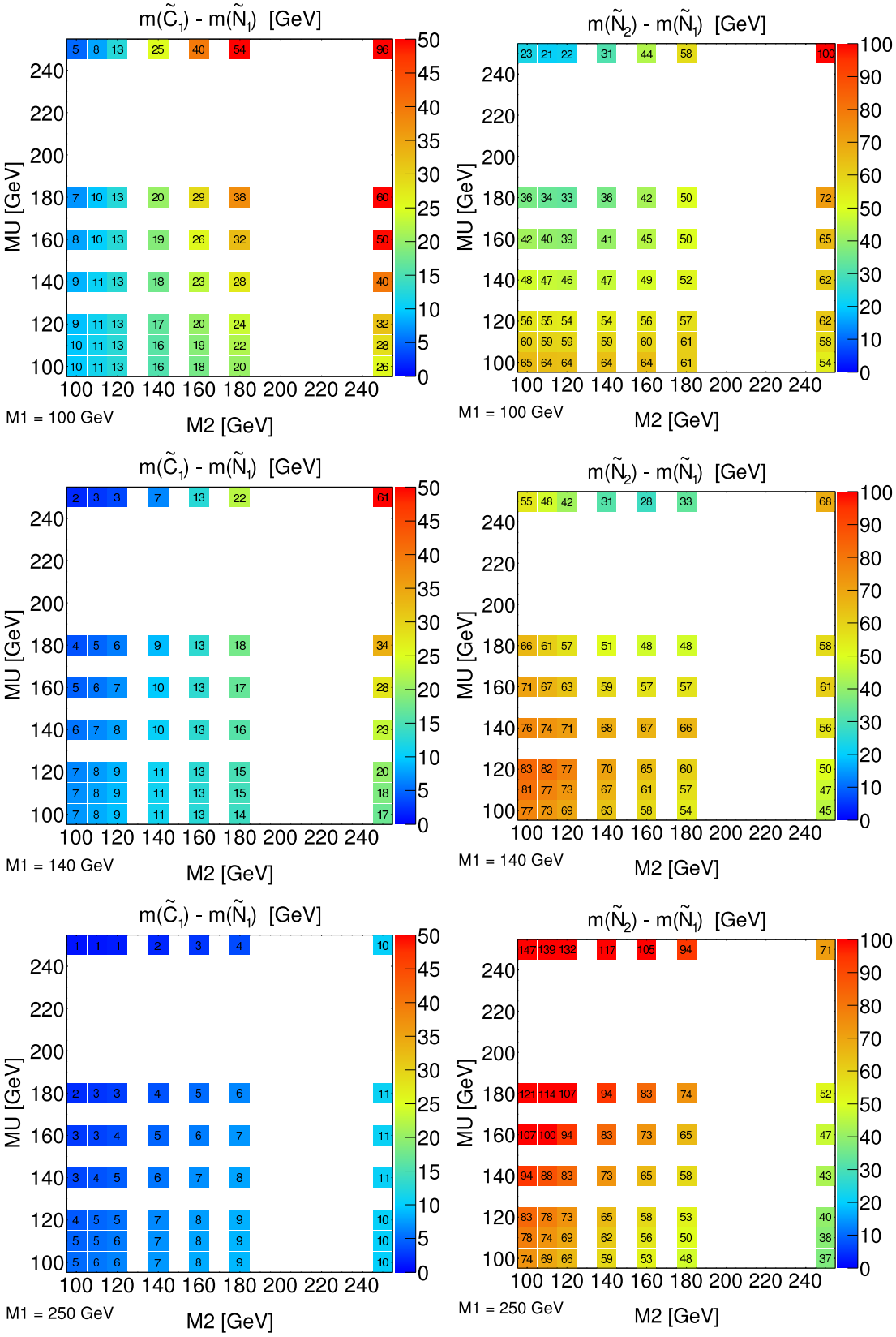


***Figure C.10.:*** pMSSM signal grids: mass differences between $\tilde{\chi}_1^{\pm}$ and $\tilde{\chi}_1^0$ as well as between $\tilde{\chi}_2^0$ and $\tilde{\chi}_1^0$. Taken from [68].

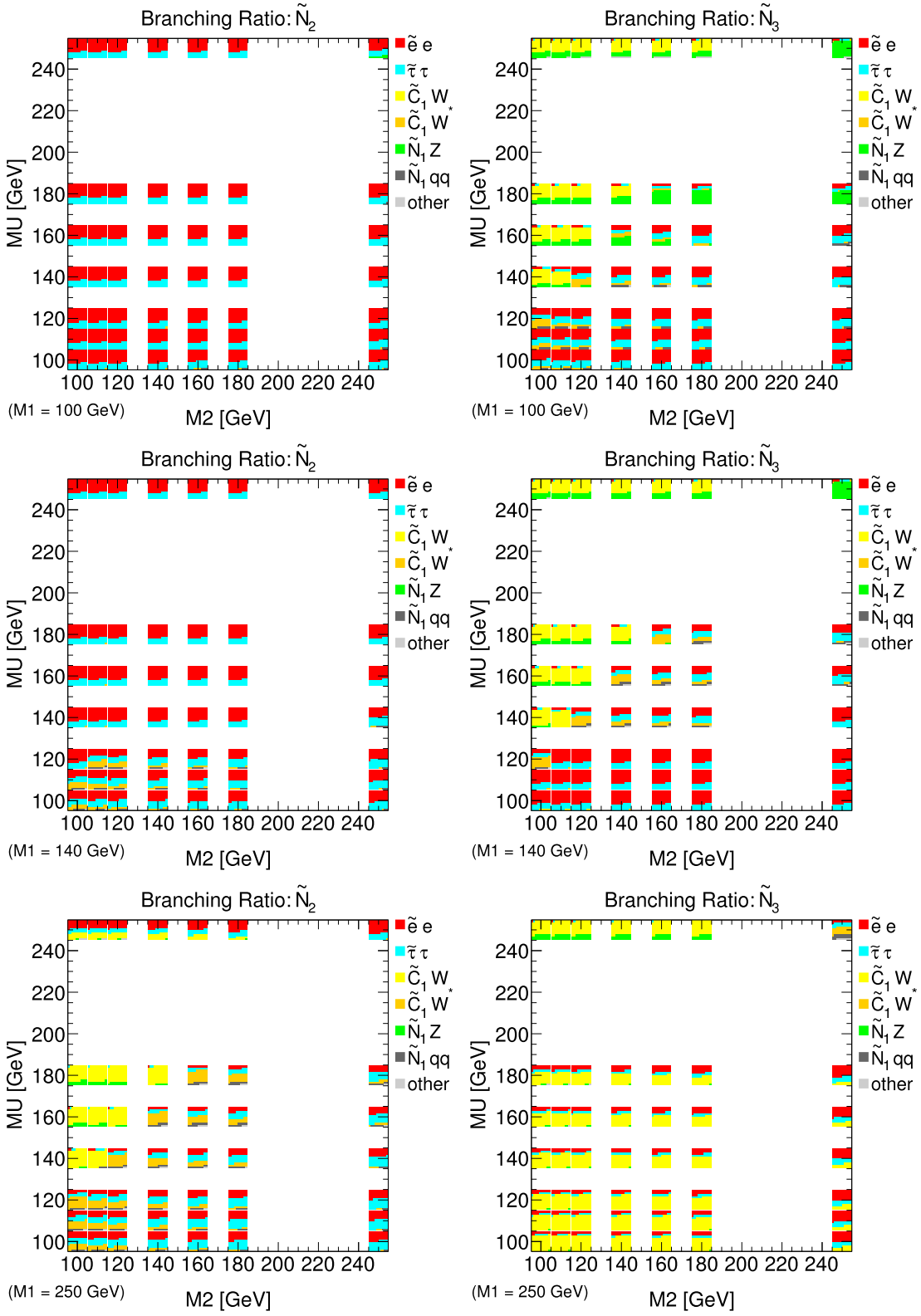


***Figure C.11.:*** pMSSM signal grids: branching rations of $\tilde{\chi}_2^0$ and $\tilde{\chi}_3^0$. Taken from [68].

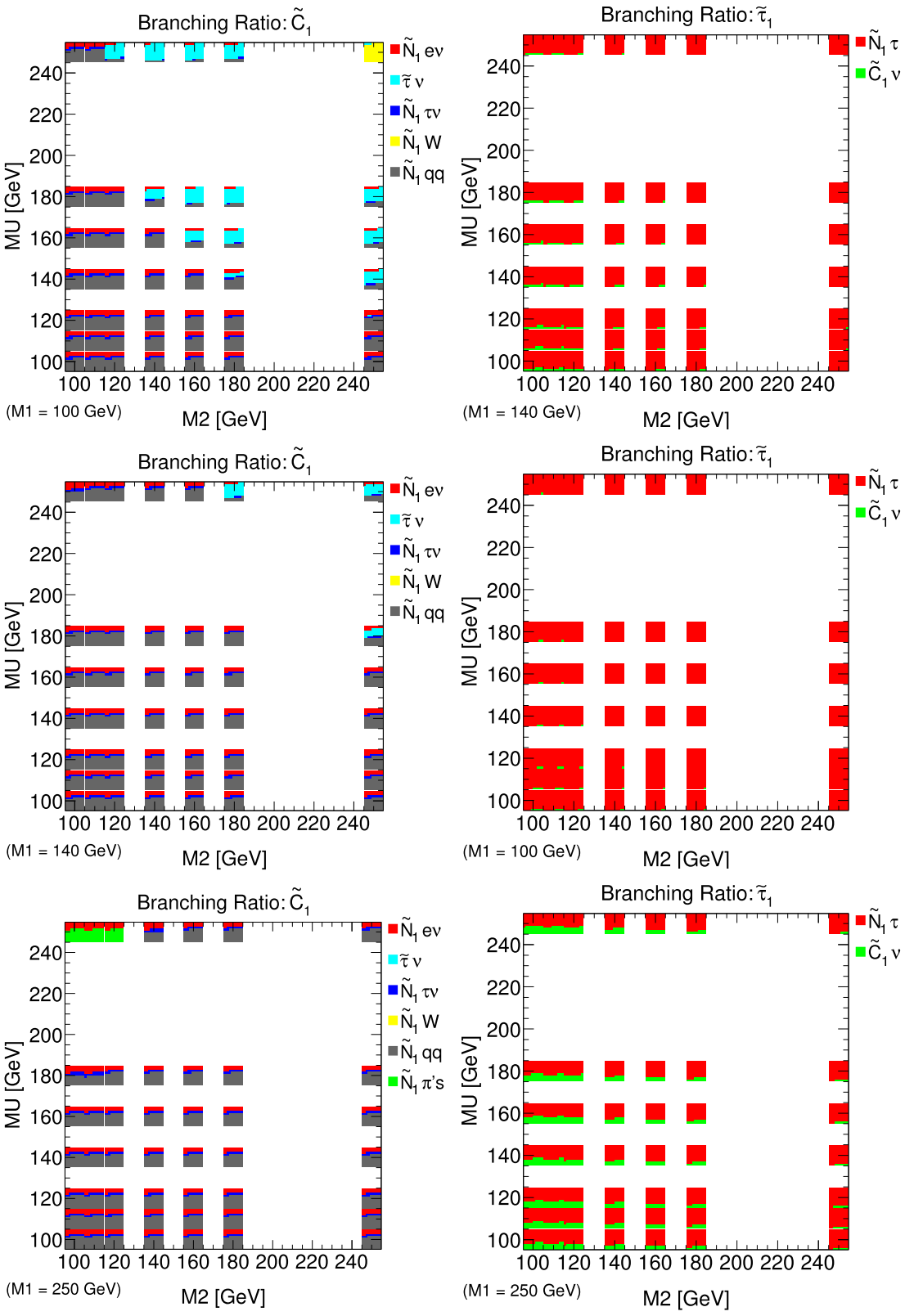


***Figure C.12.:*** pMSSM signal grids: branching rations of $\tilde{\chi}_1^{\pm}$ and $\tilde{\tau}$. Taken from [68].

# D. Information about Used Data and Monte Carlo Samples

In the following, the data and Monte Carlo (MC) samples used in this thesis are summarised. Furthermore, the applied GRL is given.

**GRL**
data11_7TeV.periodAllYear_DetStatus-v36-pro10_CoolRunQuery-00-04-08_Susy

**Data Samples Used For Trigger Efficiency and Rate Studies**
The data samples of the data-taking periods B, D-K are used. The SMWZD3PDs from the Muon, JetTauEtmiss and Egamma stream the with the processing tag p833 are used. The integrated luminosity of these periods is summarised in Table D.1.

**Monte Carlo Samples Used For Trigger Efficiency Measurements**
The MC samples used for the trigger efficiency measurements in this thesis summarised in Table D.2. The SMWZD3PDs of these samples with the reconstruction tag r3043_r2993 and the processing tag p833 are used.

**Monte Carlo Samples Used for the Search for Supersymmetry**
The MC samples used for the analysis presented in Section 6 are summarised in Tables D.3 to D.7. For every MC sample the effective cross-section, consisting of the generator cross-section, k-factors for higher order corrections and filter efficiencies, is listed.

| Period | Date range in 2011 | Run range | $\int L\,\mathrm{d}t$ [nb] |
|---|---|---|---|
| 2011B | 21 Mar - 24 Mar | 177986-178109 | 11.99 |
| 2011D | 14 Apr - 29 Apr | 179710-180481 | 175.53 |
| 2011E | 30 Mar - 3 May | 180614-180776 | 50.69 |
| 2011F | 15 May - 25 May | 182013-182519 | 130.92 |
| 2011G | 27 May - 14 Jun | 182726-183462 | 501.77 |
| 2011H | 16 Jun - 28 Jun | 183544-184169 | 256.39 |
| 2011I | 13 Jul - 29 Jul | 185353-186493 | 339.14 |
| 2011J | 30 Jul - 4 Aug | 186516-186755 | 227.44 |
| 2011K | 4 Aug - 22 Aug | 186873-187815 | 590.62 |

***Table D.1.:*** Integrated luminosity $\int L\,\mathrm{d}t$ of the data-taking periods in 2011 based on the used GRL (see above), calculated using `ILUMICALC` [171]. For period 2011B-2011I the EF_mu18 and for period 2011J-2011K the EF_mu18_medium trigger are used as reference.

| Process | sample ID | no. events |
|---|---|---|
| $Z^0 \to \mu\mu$ | 107660 | 6615230 |
| $WW$ | 105985 | 2489244 |
| $ZZ$ | 105986 | 249999 |
| $WZ$ | 105987 | 999896 |
| $t\bar{t}$ | 117200 | 9988454 |

***Table D.2.:*** MC samples used in this thesis for the trigger efficiency measurements. The number of events in samples is also given.

| Process | sample ID | $\sigma$ [pb] | $\int L\,\mathrm{d}t$ [fb$^{-1}$] |
|---|---|---|---|
| $t\bar{t}\,W$ | 119353 | 0.16 | 618.1 |
| $t\bar{t}\,W + jet$ | 119354 | 0.11 | 921.6 |
| $t\bar{t}\,Z$ | 119355 | 0.12 | 804.8 |
| $t\bar{t}\,Z + jet$ | 119356 | 0.11 | 942.7 |
| $t\bar{t}\,WW$ | 119583 | 0.001 | 61587.1 |

***Table D.3.:*** The $t\bar{t}V$ samples used for the analysis presented in Section 6. The cross-sections are normalised to NLO using k-factors [172]. Additionally, the integrated luminosities $\int L\,\mathrm{d}t$ corresponding to the total statistics in each sample are given.

| Process | sample ID | $\sigma$ [pb] | $\int L\,\mathrm{d}t$ [fb$^{-1}$] |
|---|---|---|---|
| $ZZ$ | 105986 | 1.32 | 189.9 |
| $ZW$ | 142604 | 0.25 | 197.1 |
| $W^+W^-$ | 105985 | 17.00 | 146.5 |
| $W^\pm W^\pm + jet$ | 119357 | 0.22 | 431.8 |
| $W^+\gamma$ $(e\nu)$ | 106001 | 27.97 | 1.8 |
| $W^+\gamma$ $(\mu\nu)$ | 106002 | 27.94 | 1.8 |
| $W^+\gamma$ $(\tau\nu)$ | 106003 | 25.42 | 11.6 |
| $W^-\gamma$ $(e\nu)$ | 108288 | 18.59 | 2.7 |
| $W^-\gamma$ $(\mu\nu)$ | 108289 | 18.59 | 2.7 |
| $W^-\gamma$ $(\tau\nu)$ | 108290 | 16.86 | 17.4 |
| $Z\gamma$ $(ee)$ | 108323 | 10.02 | 5.0 |
| $Z\gamma$ $(\mu\mu)$ | 108324 | 10.02 | 5.0 |
| $Z\gamma$ $(\tau\tau)$ | 108325 | 9.76 | 30.1 |

***Table D.4.:*** Di-boson samples used for the analysis presented in Section 6. The LO cross-sections are normalised to NLO [173] using k-factors (calculated as the ratio of the NLO MCFM[174] over the LO HERWIG cross-sections) and filter efficiencies are taken into account. Additionally, the integrated luminosities $\int L\,\mathrm{d}t$ corresponding to the total statistics in each sample are given.

| Process | sample ID | $\sigma$ [pb] | $\int L\,\mathrm{d}t$ [fb$^{-1}$] |
|---|---|---|---|
| $tt$ not all-hadronic | 105200 | 90.57 | 128.0 |
| $t$-channel $e\nu$ | 108340 | 6.97 | 25.4 |
| $t$-channel $\mu\nu$ | 108341 | 6.97 | 25.4 |
| $t$-channel $\tau\nu$ | 108342 | 7.10 | 25.3 |
| $s$-channel $e\nu$ | 108343 | 0.50 | 507.2 |
| $s$-channel $\mu\nu$ | 108344 | 0.50 | 506.8 |
| $s$-channel $\tau\nu$ | 108345 | 0.50 | 507.0 |
| $Wt$ | 108346 | 15.74 | 50.6 |

***Table D.5.:*** Top-quark samples used for the analysis presented in Section 6. The samples were generated with 0.108 $W \to \ell\nu$ branching ratio BR. The approximate NNLO cross-section $\sigma_{\mathrm{NNLO}}$ for the single top processes are taken from [175–177] and the $t\bar{t}$ cross-section is obtained from [178]. Additionally, the integrated luminosities $\int L\,\mathrm{d}t$ corresponding to the total statistics in each sample are given.

| Process | | sample ID | $\sigma$ [pb] | $\int L\,\mathrm{d}t$ [fb$^{-1}$] |
|---|---|---|---|---|
| $Z$+jets | ($ee$+Np0) | 107650 | 832.61 | 8.0 |
| | ($ee$+Np1) | 107651 | 167.31 | 7.9 |
| | ($ee$+Np2) | 107652 | 50.55 | 39.0 |
| | ($ee$+Np3) | 107653 | 14.00 | 38.2 |
| | ($ee$+Np4) | 107654 | 3.53 | 40.8 |
| | ($ee$+Np5) | 107655 | 0.95 | 50.0 |
| | ($\mu\mu$+Np0) | 107660 | 832.61 | 8.0 |
| | ($\mu\mu$+Np1) | 107661 | 167.31 | 7.9 |
| | ($\mu\mu$+Np2) | 107662 | 50.55 | 39.0 |
| | ($\mu\mu$+Np3) | 107663 | 14.00 | 38.2 |
| | ($\mu\mu$+Np4) | 107664 | 3.53 | 40.8 |
| | ($\mu\mu$+Np5) | 107665 | 0.95 | 50.0 |
| | ($\tau\tau$+Np0) | 107670 | 832.61 | 12.8 |
| | ($\tau\tau$+Np1) | 107671 | 167.31 | 19.8 |
| | ($\tau\tau$+Np2) | 107672 | 50.55 | 19.6 |
| | ($\tau\tau$+Np3) | 107673 | 14.00 | 35.4 |
| | ($\tau\tau$+Np4) | 107674 | 3.53 | 39.4 |
| | ($\tau\tau$+Np5) | 107675 | 0.95 | 45.1 |
| $Zbb$ | ($ee$+Np0) | 109380 | 0.73 | 274.4 |
| | ($ee$+Np1) | 109381 | 0.43 | 233.4 |
| | ($ee$+Np2) | 109382 | 0.18 | 193.3 |
| | ($ee$+Np3) | 109383 | 0.10 | 209.9 |
| $Zbb$ | ($\mu\mu$+Np0) | 109385 | 0.73 | 273.8 |
| | ($\mu\mu$+Np1) | 109386 | 0.43 | 232.5 |
| | ($\mu\mu$+Np2) | 109387 | 0.18 | 216.1 |
| | ($\mu\mu$+Np3) | 109388 | 0.10 | 210.2 |
| $Zbb$ | ($\tau\tau$+Np0) | 109310 | 8.17 | 17.9 |
| | ($\tau\tau$+Np1) | 109311 | 3.10 | 30.6 |
| | ($\tau\tau$+Np2) | 109312 | 1.11 | 25.7 |
| | ($\tau\tau$+Np3) | 109313 | 0.48 | 16.5 |

***Table D.6.:*** $Z$+jets samples used for the analysis presented in Section 6. Different samples are used for the contribution of $Z \to ee/\mu\mu/\tau\tau + NpX$ (LF jets) and the contribution of $Z + bb \to ee/\mu\mu/\tau\tau + NpX$ (HF jets), shown separately. The cross-section for each process is normalised to approximate NNLO using k-factors [173] (k-factors for $Z$+HF jets are assumed to be the same as for LF) and the filter efficiencies are taken into account. Note the different filters applied for different samples, as explained in Section 6.4.2. Additionally, the integrated luminosities $\int L\,\mathrm{d}t$ corresponding to the total statistics in each sample are given.

| Process | | sample ID | $\sigma$ [pb] | $\int L\,\mathrm{d}t$ [fb$^{-1}$] |
|---|---|---|---|---|
| Drell-Yan | ($ee$+Np0) | 116946 | 136.79 | 14.2 |
| | ($ee$+Np1) | 116947 | 50.13 | 20.0 |
| | ($ee$+Np2) | 116252 | 51.22 | 19.5 |
| | ($ee$+Np3) | 116253 | 10.37 | 14.4 |
| | ($ee$+Np4) | 116254 | 2.30 | 17.4 |
| | ($ee$+Np5) | 116255 | 0.57 | 17.5 |
| Drell-Yan | ($\mu\mu$+Np0) | 116948 | 140.59 | 13.8 |
| | ($\mu\mu$+Np1) | 116949 | 51.73 | 19.3 |
| | ($\mu\mu$+Np2) | 116262 | 51.22 | 19.5 |
| | ($\mu\mu$+Np3) | 116263 | 10.37 | 14.5 |
| | ($\mu\mu$+Np4) | 116264 | 2.33 | 17.2 |
| | ($\mu\mu$+Np5) | 116265 | 0.57 | 17.5 |
| Drell-Yan | ($\tau\tau$+Np0) | 116940 | 0.24 | 171.1 |
| | ($\tau\tau$+Np1) | 116941 | 0.39 | 204.0 |
| | ($\tau\tau$+Np2) | 116942 | 0.18 | 194.6 |
| | ($\tau\tau$+Np3) | 116943 | 0.07 | 230.1 |
| | ($\tau\tau$+Np4) | 116944 | 0.02 | 235.9 |
| | ($\tau\tau$+Np5) | 116945 | 0.01 | 291.2 |

***Table D.7.:*** Drell-Yan samples used for the analysis presented in Section 6. The cross-section for each process is normalised to approximate NNLO using k-factors [173] (k-factors for assumed to be the same as for on-shell $Z$ decays) and the filter efficiencies are taken into account. Note the different filters applied for different samples, as explained in Section 6.4.2. Additionally, the integrated luminosities $\int L\,\mathrm{d}t$ corresponding to the total statistics in each sample are given.

# E. List of Used Orthogonal Trigger

In the following all orthogonal triggers used in this thesis are summarised.

- **jet trigger:**
  EF_j10_a4tc_EFFS, EF_j15_a4tc_EFFS, EF_j20_a4tc_EFFS, EF_j30_a4tc_EFFS, EF_j40_a4tc_EFFS, EF_j55_a4tc_EFFS, EF_j75_a4tc_EFFS, EF_j100_a4tc_EFFS, EF_j135_a4tc_EFFS, EF_j180_a4tc_EFFS, EF_j240_a4tc_EFFS, EF_j320_a4tc_EFFS, EF_j240a10tc_EFFS, EF_j300a10tc_EFFS, EF_j320a10tc_EFFS, EF_j400a10tc_EFFS, EF_j425a10tc_EFFS, EF_fj10_a4tc_EFFS, EF_fj15_a4tc_EFFS, EF_fj20_a4tc_EFFS, EF_fj30_a4tc_EFFS, EF_fj55_a4tc_EFFS, EF_fj75_a4tc_EFFS, EF_fj100_a4tc_EFFS, EF_j30fj30_a4tc_EFFS, EF_j40_fj40_a4tc_EFFS, EF_j55_fj55_a4tc_EFFS, EF_j75_fj75_a4tc_EFFS, EF_3j30_a4tc_EFFS, EF_3j40_a4tc_EFFS, EF_3j45_a4tc_EFFS, EF_3j75_a4tc_EFFS, EF_3j100_a4tc_EFFS, EF_4j30_a4tc_EFFS, EF_3j100_a4tc_EFFS_L1J75, EF_4j40_a4tc_EFFS, EF_4j45_a4tc_EFFS, EF_4j55_a4tc_EFFS, EF_4j60_a4tc_EFFS, EF_5j30_a4tc_EFFS, EF_5j40_a4tc_EFFS, EF_5j45_a4tc_EFFS, EF_6j30_a4tc_EFFS, EF_6j30_a4tc_EFFS_L15J10, EF_7j30_a4tc_EFFS_L15J10, EF_L1J175_NoAlg, EF_L1J250_NoAlg, EF_L1FJ75_NoAlg, EF_j10_a4_EFFS, EF_j15_a4_EFFS, EF_j20_a4_EFFS, EF_j30_a4_EFFS, EF_j40_a4_EFFS, EF_j55_a4_EFFS, EF_j75_a4_EFFS, EF_j100_a4_EFFS, EF_j135_a4_EFFS, EF_j180_a4_EFFS, EF_j240_a4_EFFS, EF_fj30_a4_EFFS, EF_fj55_a4_EFFS, EF_fj75_a4_EFFS, EF_fj100_a4_EFFS, EF_j30_fj30_a4_EFFS, EF_j40fj40_a4_EFFS, EF_j55_fj55_a4_EFFS, EF_j75_fj75_a4_EFFS, EF_3j30_a4_EFFS,EF_4j30_a4_EFFS, EF_3j75_a4_EFFS, EF_5j30_a4_EFFS, EF_3j100_a4_EFFS_L1J75, EF_j120_j55_j40_a4_EFFS.
- **egamma trigger:**
  EF_e5_tight, EF_e10_medium, EF_e15_medium, EF_e15vh_medium, EF_e20_medium, EF_e20_medium1, EF_e20_medium2, EF_e22_medium, EF_e22_medium1, EF_e22_medium2, EF_e22vh_medium1, EF_e22vh_loose, EF_e33_medium, EF_e20_loose, EF_e20_loose1, EF_e60_loose, EF_2e10_medium EF_2e12_medium, EF_3e10_medium, EF_e15_medium_e12_medium,

EF_2e5_tight, EF_2e12T_medium, EF_2e15vh_medium, EF_2e12Tvh_medium, EF_g15_loose, EF_g20_loose, EF_g40_loose, EF_g60_loose, EF_g80_loose, EF_g40_tight, EF_2g15_loose, EF_g150_etcut, EF_g100_etcut_g50_etcut, EF_e11_etcut, EF_g11_etcut, EF_g20_etcut, EF_g40_tight_b10_medium.

- ***b*-jet and tau trigger:**
  EF_2b10_medium_L1JE140, EF_2b20_medium_3L1J20, EF_3b10_loose_4L1J10, EF_3b15_loose_4L1J15, EF_2b10_medium_L1JE100, EF_b10_tight_L1JE140, EF_2b15_medium_3L1J15, EF_b10_medium_4j30_a4tc_EFFS, EF_b10_medium_j45_3j30_a4tc_EFFS, EF_2b10_medium_4L1J10, EF_2b10_medium_j75_j30_a4tc_EFFS, EF_2b10_medium_4j30_a4tc_EFFS, EF_2b10_medium_L1_2J10J50, EF_b10_medium_j75_j55_2j30_a4tc_EFFS, EF_tau16_loose, EF_tau29_loose, EF_tau84_loose, EF_tau20_medium1, EF_tau20T_medium, EF_tau29_medium, EF_tau29_medium1, EF_tau100_medium, EF_tau125_medium, EF_tau125_medium1, EF_tauNoCut, EF_tauNoCut_L1TAU50, EF_2tau29_medium1, EF_tau50_medium, EF_tau16_loose_e15_tight, EF_tau16_loose_e15_medium, EF_b10_tight_4L1J10, EF_tau20_medium_e15_medium, EF_tau29T_medium1_tau20T_medium1, EF_tau20_medium_e15vh_medium, EF_tau29_medium1_tau20_medium1.

- **met trigger:**
  EF_xe_20_noMu, EF_xe_30_noMu, EF_xe_40_noMu, EF_xe_50_noMu, EF_xe_60_noMu, EF_xe_60tight_noMu, EF_xe60_verytight_noMu, EF_xe_70_noMu, EF_xe_80_noMu, EF_xe_90_noMu, EF_xe_100_noMu, EF_xe_110_noMu, EF_xs_30_noMu, EF_xs_45_noMu, EF_xs_60_noMu, EF_xs_70_noMu, EF_xs_75_noMu, EF_xs_70tight_noMu, EF_xs_90_noMu, EF_xs_100_noMu, EF_xs120_noMu.

- **met+X trigger:**
  EF_tau29_medium_xe35_noMu, EF_tau29_medium_xe40_loose_noMu, EF_tau29_loose_xs70_loose_noMu, EF_tau29_loose_xs80_loose_noMu, EF_tau29_loose1_xs45_loose_noMu_3L1J10, EF_e15_medium_xe30_noMu, EF_tau29T_medium1_xs45_loose_noMu_3L1J10, EF_j80_a4tc_EFFS_xe60_noMu, EF_tau29T_medium_xs45_noMu_3L1J10, EF_e15_medium_xe40_noMu, EF_tau29T_medium_xe35_noMu_3L1J10, EF_g20_etcut_xe30_noMu, EF_j75_a4tc_EFFS_xe55_loose_noMu, EF_j75_a4tc_EFFS_xe55_noMu, EF_j75_a4tc_EFFS_xe40_loose_noMu, EF_j75_a4tc_EFFS_xe45_loose_noMu, EF_e22vh_medium1_EFxe20_noMu, EF_g40_loose_xe45_medium_noMu, EF_tau29T_medium_xs75_loose_noMu, EF_e13_etcut_xs60_noMu, EF_tau29T_medium_xs75_noMu, EF_xs60_noMu_L1EM10XS45, EF_tau29T_medium1_xe35_noMu_3L1J10, EF_e15vh_medium_xe40_noMu, EF_b10_medium_EFxe25_noMu_L1JE140, EF_g40_loose_EFxe40_noMu.

# Bibliography


[1] E. Noether, "Invariante Variationsprobleme", Nachr. v. d. Ges. d. Wiss. zu Göttingen 1918, 235-257.

[2] S. Glashow, "Partial Symmetries of Weak Interactions", *Nucl.Phys.* **22** (1961) 579–588.

[3] A. Salam and J. C. Ward, "Electromagnetic and Weak Interactions", *Phys.Lett.* **13** (1964) 168–171.

[4] S. Weinberg, "A Model of Leptons", *Phys. Rev. Lett.* **19** (1967) 1264–1266.

[5] P. W. Higgs, "Broken Symmetries, Massless Particles and Gauge Fields", *Phys. Lett.* **12** (1964) 132–133.

[6] H. D. Politzer, "Reliable Perturbative Results for Strong Interactions", *Phys. Rev. Lett.* **30** (1973) 1346–1349.

[7] H. D. Politzer, "Asymptotic Freedom: An Approach to Strong Interactions", *Phys. Rept.* **14** (1974) 129.

[8] D. J. Gross and F. Wilczek, "Asymptotically Free Gauge Theories", *Phys. Rev. D* **8** (1973) 3633–3652.

[9] ALEPH Collaboration, CDF Collaboration, D0 Collaboration, DELPHI Collaboration, L3 Collaboration, OPAL Collaboration, SLD Collaboration, LEP Electroweak Working Group, Tevatron Electroweak Working Group, SLD Electroweak and Heavy Flavour Groups Collaboration, "Precision Electroweak Measurements and Constraints on the Standard Model", `arXiv:1012.2367`.

[10] M. Baak *et al.*, "Updated Status of the Global Electroweak Fit and Constraints on New Physics", `arXiv:1107.0975`.

[11] H. Flacher *et al.*, "Revisiting the Global Electroweak Fit of the Standard Model and Beyond with Gfitter", *Eur.Phys.J.* **C60** (2009) 543–583.

[12] F. Halzen and A. D. Martin, "Quarks and Leptons: An Introductory Course in Modern Particle Physics", Wiley, 1984.

[13] D. Griffiths, "Introduction to Elementary Particles", Wiley-VCH, 2nd ed., 2008.

[14] Particle Data Group Collaboration, K. Nakamura *et al.*, "Review of Particle Physics", *J.Phys.G* **G37** (2010) 075021.

[15] F. Englert and R. Brout, "Broken Symmetry and the Mass of Gauge Vector Mesons", *Phys. Rev. Lett.* **13** (1964) 321–322.

[16] G. S. Guralnik, C. R. Hagen, and T. W. B. Kibble, "Global Conservation Laws and Massless Particles", *Phys. Rev. Lett.* **13** (1964) 585–587.

[17] ATLAS Collaboration Collaboration, "Combined search for the Standard Model Higgs boson using up to 4.9 $fb^{-1}$ of pp collision data at sqrt(s) = 7 TeV with the ATLAS detector at the LHC", `arXiv:1202.1408`.

[18] CMS Collaboration Collaboration, "Combined results of searches for the standard model Higgs boson in pp collisions at sqrt(s) = 7 TeV", `arXiv:1202.1488`.

[19] TEVNPH (Tevatron New Phenomina and Higgs Working Group), CDF and D0 Collaboration Collaboration, "Combined CDF and D0 Search for Standard Model Higgs Boson Production with up to 10.0 $fb^{-1}$ of Data", `arXiv:1203.3774`.

[20] R. Stock, "Encyclopedia of Applied High Energy and Particle Physics", Wiley-VCH, 2009.

[21] R. M. Wald, "General Relativity", Chicago Univ. Pr. , 1984.

[22] S. P. Martin, "A Supersymmetry primer", `arXiv:hep-ph/9709356`.

[23] S. Weinberg, "Implications of Dynamical Symmetry Breaking", *Phys. Rev.* **D13** (1976) 974–996.

[24] E. Gildener, "Gauge Symmetry Hierarchies", *Phys. Rev.* **D14** (1976) 1667.

[25] S. Weinberg, "Implications of Dynamical Symmetry Breaking: An Addendum", *Phys. Rev.* **D19** (1979) 1277–1280.

[26] L. Susskind, "Dynamics of Spontaneous Symmetry Breaking in the Weinberg- Salam Theory", *Phys. Rev.* **D20** (1979) 2619–2625.

[27] J. C. Maxwell, "A dynamical theory of the electromagnetic field", *Phil. Trans. Roy. Soc. Lond.* **155** (1865) 459–512.

[28] H. Georgi and S. L. Glashow, "Unity of All Elementary Particle Forces", *Phys. Rev. Lett.* **32** (1974) 438–441.

[29] C. L. Bennett *et al.*, "Seven-Year Wilkinson Microwave Anisotropy Probe (WMAP) Observations: Sky Maps, Systematic Errors, and Basic Results", *Astrophys.J.Suppl.* **192** (2011) 14.

[30] H. Miyazawa, "Baryon Number Changing Currents", *Prog. Theor. Phys.* **36 (6)** (1966) 1266–1276.

[31] P. Ramond, "Dual Theory for Free Fermions", *Phys. Rev.* **D3** (1971) 2415–2418.

[32] Y. A. Golfand and E. P. Likhtman, "Extension of the Algebra of Poincare Group Generators and Violation of P Invariance", *JETP Lett.* **13** (1971) 323–326.

[33] A. Neveu and J. H. Schwarz, "Factorizable dual model of pions", *Nucl. Phys.* **B31** (1971) 86–112.

[34] A. Neveu and J. H. Schwarz, "Quark Model of Dual Pions", *Phys. Rev.* **D4** (1971) 1109–1111.

[35] J. Gervais and B. Sakita, "Field theory interpretation of supergauges in dual models", *Nucl. Phys.* **B34** (1971) 632–639.

[36] D. V. Volkov and V. P. Akulov, "Is the Neutrino a Goldstone Particle?", *Phys. Lett.* **B46** (1973) 109–110.

[37] J. Wess and B. Zumino, "A Lagrangian Model Invariant Under Supergauge Transformations", *Phys. Lett.* **B49** (1974) 52.

[38] J. Wess and B. Zumino, "Supergauge Transformations in Four-Dimensions", *Nucl. Phys.* **B70** (1974) 39–50.

[39] I. Aitchison, "Supersymmetry in Particle Physics. An Elementary Introduction", Cambridge Univ. Pr. , 2007.

[40] S. Weinberg, "The quantum theory of fields. Vol. 3: Supersymmetry", Cambridge Univ. Pr. , 2000.

[41] R. Haag, J. T. Lopuszanski, and M. Sohnius, "All Possible Generators of Supersymmetries of the s Matrix", *Nucl.Phys.* **B88** (1975) 257.

[42] S. R. Coleman and J. Mandula, "All Possible Symmetries of the S Matrix", *Phys.Rev.* **159** (1967) 1251–1256.

[43] P. Binetruy, "Supersymmetry: Theory, Experiment and Cosmology", Oxford Univ. Pr. ,2006.

[44] H. Goldberg, "Constraint on the Photino Mass from Cosmology", *Phys. Rev. Lett.* **50** (1983) 1419.

[45] J. Ellis *et al.*, "Supersymmetric Relics from the Big Bang", *Nucl. Phys.* **B238** (1984) 453–476.

[46] S. Dimopoulos and H. Georgi, "Softly Broken Supersymmetry and SU(5)", *Nucl. Phys.* **B193** (1981) 150.

[47] E. Witten, "Dynamical Breaking of Supersymmetry", *Nucl. Phys.* **B188** (1981) 513.

[48] M. Dine, W. Fischler, and M. Srednicki, "Supersymmetric Technicolor", *Nucl. Phys.* **B189** (1981) 575–593.

[49] S. Dimopoulos and S. Raby, "Supercolor", *Nucl. Phys.* **B192** (1981) 353.

[50] N. Sakai, "Naturalness in Supersymmetric Guts", *Zeit. Phys.* **C11** (1981) 153.

[51] R. Kaul and P. Majumdar, "Cancellation of quadratically divergent mass corrections in globally supersymmetric spontaneously broken gauge theories", *Nucl. Phys.* **B199** (1982) 36.

[52] C. Giunti, C. W. Kim, and U. Lee, "Running coupling constants and grand unification models", *Mod. Phys. Lett.* **A6** (1991) 1745–1755.

[53] J. Ellis, S. Kelley, and D. Nanopoulos, "Probing the desert using gauge coupling unification", *Phys. Lett.* **B260** (1991) 131–137.

[54] U. Amaldi, W. de Boer, and H. Furstenau, "Comparison of grand unified theories with electroweak and strong coupling constants measured at LEP", *Phys. Lett.* **B260** (1991) 447–455.

[55] P. Langacker and M.-X. Luo, "Implications of precision electroweak experiments for M(t), rho(0), sin**2-Theta(W) and grand unification", *Phys. Rev.* **D44** (1991) 817–822.

[56] H. Murayama, "Supersymmetry phenomenology", `arXiv:hep-ph/000p`.

[57] P. Fayet, "Supersymmetry and Weak, Electromagnetic and Strong Interactions", *Phys. Lett.* **B64** (1976) 159.

[58] P. Fayet, "Spontaneously Broken Supersymmetric Theories of Weak, Electromagnetic and Strong Interactions", *Phys. Lett.* **B69** (1977) 489.

[59] G. R. Farrar and P. Fayet, "Phenomenology of the Production, Decay, and Detection of New Hadronic States Associated with Supersymmetry", *Phys. Lett.* **B76** (1978) 575–579.

[60] P. Fayet, "Relations Between the Masses of the Superpartners of Leptons and Quarks, the Goldstino Couplings and the Neutral Currents", *Phys. Lett.* **B84** (1979) 416.

[61] N. Polonsky, "Supersymmetry: Structure and phenomena. Extensions of the standard model", *Lect. Notes Phys.* **M68** (2001) 1–169.

[62] L. J. Hall, J. D. Lykken, and S. Weinberg, "Supergravity as the Messenger of Supersymmetry Breaking", *Phys. Rev.* **D27** (1983) 2359–2378.

[63] C. F. Berger, J. S. Gainer, J. L. Hewett, and T. G. Rizzo, "Supersymmetry Without Prejudice", *JHEP* **0902** (2009) 023.

[64] J. A. Conley *et al.*, "Supersymmetry Without Prejudice at the 7 TeV LHC", `arXiv:1103.1697`.

[65] N. Cabibbo, "Unitary Symmetry and Leptonic Decays", *Phys. Rev. Lett.* **10** (1963) 531–533.

[66] M. Kobayashi and T. Maskawa, "CP Violation in the Renormalizable Theory of Weak Interaction", *Prog. Theor. Phys.* **49** (1973) 652–657.

[67] G. D'Ambrosio *et al.*, "Minimal flavor violation: an effective field theory approach", *Nucl.Phys.* **B645** (2002) 155–187.

[68] I. Santoyo Castillo *et al.*, "Searching for direct gaugino production and direct slepton production with two leptons and missing transverse momentum at $\sqrt{s} = 7$ tev (supporting INT note)", Tech. Rep. ATL-COM-PHYS-2011-1721.

[69] J. D. Bjorken and E. A. Paschos, "Inelastic Electron Proton and gamma Proton Scattering, and the Structure of the Nucleon", *Phys. Rev.* **185** (1969) 1975–1982.

[70] L. Evans and P. Bryant, "LHC Machine", *JINST* **3** (2008) S08001.

[71] O. S. Bruning *et al.*, "LHC design report. Vol. I: The LHC main ring", CERN-2004-003-V-1.

[72] O. S. Buning *et al.*, "LHC Design Report. 2. The LHC infrastructure and general services", CERN-2004-003-V-2.

[73] M. Benedikt *et al.*, "LHC Design Report. 3. The LHC injector chain", CERN-2004-003-V-3.

[74] O. S. Bruning and P. Collier, "Building a Behemoth", *Nature* **448** (2007) 285–289.

[75] "ATLAS: Detector and Physics Performance Technical Design Deport. Vol. 1", CERN-LHCC-99-14.

[76] CERN Press Office, "First beam in the LHC - accelerating science", Press release. `http://press.web.cern.ch/press/PressReleases/Releases2008/PR08.08E.html`. Retrieved 20.02.2012.

[77] CERN Press Office, "Incident in LHC sector 3-4", Press release. `http://press.web.cern.ch/press/PressReleases/Releases2008/PR09.08E.html`. Retrieved 20.02.2012.

[78] CERN Press Office, "The LHC is back", Press release. `http://press.web.cern.ch/press/PressReleases/Releases2009/PR16.09E.html`. Retrieved 20.02.2012.

[79] CERN Press Office, "Two circulating beams bring first collisions in the LHC", Press release. `http://press.web.cern.ch/press/PressReleases/Releases2009/PR17.09E.html`. Retrieved 20.02.2012.

[80] CERN Press Office, "LHC research programme gets underway", Press release. `http://press.web.cern.ch/press/PressReleases/Releases2010/PR07.10E.html`. Retrieved 20.02.2012.

[81] `https://atlas.web.cern.ch/Atlas/GROUPS/DATAPREPARATION/DataSummary/2011`. Retrieved 20.02.2012.

[82] CERN Press Office, "LHC to run at 4 tev per beam in 2012", Press release. `http://press.web.cern.ch/press/PressReleases/Releases2012/PR01.12E.html`. Retrieved 20.02.2012.

[83] CMS Collaboration, "The CMS experiment at the CERN LHC", *JINST* **3** (2008) S08004.

[84] ALICE Collaboration, "The ALICE experiment at the CERN LHC", *JINST* **3** (2008) S08002.

[85] LHCb Collaboration, "The LHCb Detector at the LHC", *JINST* **3** (2008) S08005.

[86] LHCf Collaboration, "The LHCf detector at the CERN Large Hadron Collider", *JINST* **3** (2008) S08006.

[87] MoEDAL Collaboration, "MoEDAL becomes the LHC's magnificent seventh", *CERN Cour.* **50N4** (2010) 19–20.

[88] TOTEM Collaboration, "The TOTEM experiment at the CERN Large Hadron Collider", *JINST* **3** (2008) S08007.

[89] ATLAS Collaboration, "The ATLAS Experiment at the CERN Large Hadron Collider", *JINST* **3** (2008) S08003.

[90] "ATLAS detector and Physics Performance. Technical Design Report. Vol. 2", CERN-LHCC-99-15.

[91] `http://atlas.ch`. Retrieved 20.02.2012.

[92] W. R. Leo, "Techniques for Nuclear and Particle Physics Experiments: A How-to Approach", Springer, 1987.

[93] R. L. Gluckstern, "Uncertainties in track momentum and direction, due to multiple scattering and measurement errors", *Nucl. Instrum. Meth.* **24** (1963) 381–389.

[94] "Muon Momentum Resolution in First Pass Reconstruction of pp Collision Data Recorded by ATLAS in 2010", Tech. Rep. ATLAS-CONF-2011-046.

[95] `http://silicondetector.org`. Retrieved 20.02.2012.

[96] ATLAS Collaboration, "ATLAS High-Level Trigger, Data Acquisition and Controls Technical Design Report", CERN-LHCC-2003-022.

[97] ATLAS Collaboration, "ATLAS computing: Technical design report", CERN-LHCC-2005-022.

[98] ATLAS Collaboration, "Performance of the ATLAS Trigger System in 2010", *Eur.Phys.J.* **C72** (2012) 1849.

[99] `http://atlas.web.cern.ch`. Retrieved 20.02.2012.

[100] M. Baak *et al.*, "Data Quality Status Flags and Good Run Lists for Physics Analysis in ATLAS", Tech. Rep. ATL-COM-GEN-2009-015.

[101] F. Kohn, "ATLAS High-Level Muon Trigger Studies: Development of a Method to Extract Trigger Efficiencies from Data", Diploma thesis, Universität Göttingen, 2008, II.Physik-UniGö-Dipl-2008/02.

[102] T. M. Hong, "TrigCostPython", `https://twiki.cern.ch/twiki/bin/viewauth/Atlas/TrigCostAnalysis`. Retrieved 16.11.2011.

[103] ATLAS SUSY Working Group, ATLAS TWiki: `https://twiki.cern.ch/twiki/bin/viewauth/AtlasProtected/SUSYWorkingGroup`. Retrieved 08.04.2012.

[104] A. Mann, "Calorimeter-Based Triggers at the ATLAS Detector for Searches for Supersymmetry in Zero-Lepton Final States", Dissertation, Universität Göttingen, 2012, II.Physik-UniGö-Diss-2012/01.

[105] The ATLAS Collaboration Collaboration, "Expected Performance of the ATLAS Experiment - Detector, Trigger and Physics", `arXiv:0901.0512`.

[106] A. C. Davison *et al.*, "Bootstrap methods and their application", Cambridge Univ. Pr, 1997.

[107] R. T. Bayes, "An Essay Toward Solving a Problem in the Doctrine of Chances", *Phil. Trans. Roy. Soc. Lond.* **53** (1764) 370–418.

[108] G. Barrand *et al.*, "GAUDI - A software architecture and framework for building HEP data processing applications", *Comput. Phys. Commun.* **140** (2001) 45–55.

[109] The ATLAS Computing Workbook, ATLAS TWiki: `https://twiki.cern.ch/twiki/bin/viewauth/Atlas/WorkBook`. Retrieved 07.03.2012.

[110] ATLAS Event Data Model, ATLAS TWiki: `https://twiki.cern.ch/twiki/bin/viewauth/Atlas/EventDataModel`. Retrieved 07.03.2012.

[111] TrigDecisionTool, ATLAS TWiki: `https://twiki.cern.ch/twiki/bin/viewauth/Atlas/TrigDecisionTool`. Retrieved 07.03.2012.

[112] S. Hassani *et al.*, "A muon identification and combined reconstruction procedure for the ATLAS detector at the LHC using the (MUONBOY, STACO, MuTag) reconstruction packages", *Nucl. Instrum. Meth.* **A572** (2007) 77–79.

[113] ATLAS Collaboration, B. Resende, "Muon identification algorithms in ATLAS", *PoS* **EPS-HEP2009** (2009) 431.

[114] ATLAS Muon Combined Performance Group, "Guidelines for Analyses of 2011 Data in Release 17", , ATLAS TWiki: `https://twiki.cern.ch/twiki/bin/viewauth/AtlasProtected/MCPAnalysisGuidelinesRel17MC11a`. Retrieved 05.03.2012.

[115] ATLAS Muon Combined Performance Group, "Quality of Staco Muon candidates documentation", , ATLAS TWiki: `https://twiki.cern.ch/twiki/bin/viewauth/AtlasProtected/QualityDefinitionStaco`. Retrieved 15.03.2012.

[116] ATLAS Collaboration Collaboration, "Searches for supersymmetry with the ATLAS detector using final states with two leptons and missing transverse momentum in sqrts = 7 TeV proton-proton collisions", *Phys.Lett.* **B709** (2012) 137–157.

[117] M. Hamer *et al.*, "Measurement of Trigger Efficiencies from Data and their Application in Physics Analyses", Tech. Rep. ATL-COM-DAQ-2011-083.

[118] C. Hensel, M. Hamer, and J. Hofestädt, "Trigger Efficiency Measurement for Di-Muon Triggers", Tech. Rep. ATL-COM-DAQ-2011-131.

[119] ATLAS SUSY Working Group, "SUSY Searches in the Final States with Three Leptons and Missing Transverse Momentum at ATLAS (Direct Gaugino support note for multileptons)", Tech. Rep. ATL-COM-PHYS-2011-1725. Draft Version 8.3, from 20.3.2012.

[120] A. Salvucci, "Measurement of muon momentum resolution of the atlas detector", Tech. Rep. ATL-PHYS-PROC-2012-013.

[121] "Muon momentum resolution in first pass reconstruction of pp collision data recorded by atlas in 2010", Tech. Rep. ATLAS-CONF-2011-046.

[122] R. J. Barlow, "A Guide to the Use of Statistical Methods in the Physical Sciences", Wiley-VCH, 1989.

[123] G. Cowan *et al.*, "Asymptotic formulae for likelihood-based tests of new physics", *Eur. Phys. J.* **C71** (2011) 1554, 1007.1727.

[124] S. S. Wilks, "The Large-Sample Distribution of the Likelihood Ratio for Testing Composite Hypotheses", *Ann. Math. Statist.* **9** (1938) 60–62.

[125] "Search for Charged Higgs bosons: Preliminary Combined Results Using LEP data Collected at Energies up to 209 GeV", Tech. Rep. hep-ex/0107031. LHWG-note-2001-05. DELPHI-2001-115-CONF-538. CERN-DELPHI-2001-115-CONF-538. L3-Notes-2689. OPAL-TN-696. ALEPH-2001-043. CERN-ALEPH-PHYSICS-2001-016.

[126] D0 Collaboration Collaboration, "Search for Supersymmetry via Associated Production of Charginos and Neutralinos in Final States with Three Leptons", *Phys.Rev.Lett.* **95** (2005) 151805.

[127] D0 Collaboration Collaboration, "Search for associated production of charginos and neutralinos in the trilepton final state using 2.3 $\text{fb}^{-1}$ of data", *Phys.Lett.* **B680** (2009) 34–43.

[128] CDF Collaboration Collaboration, "Search for chargino-neutralino production in $p\bar{p}$ collisions at $\sqrt{s} = 1.96$-TeV", *Phys.Rev.Lett.* **99** (2007) 191806.

[129] CDF Collaboration Collaboration, "Search for Supersymmetry in $p\bar{p}$ Collisions at $\sqrt{s} = 1.96$-TeV Using the Trilepton Signature of Chargino-Neutralino Production", *Phys.Rev.Lett.* **101** (2008) 251801.

[130] "SUSY Searches at ATLAS in Multilepton Final States with Jets and Missing Transverse Energy", Tech. Rep. ATLAS-CONF-2011-039.

[131] CMS Collaboration Collaboration, "Search for Physics Beyond the Standard Model Using Multilepton Signatures in pp Collisions at sqrt(s)=7 TeV", *Phys.Lett.* **B704** (2011) 411–433.

[132] CMS Collaboration Collaboration, "Multileptonic SUSY searches", CMS-PAS-SUS-11-013.

[133] LEP Collaboration Collaboration `http://lepsusy.web.cern.ch/lepsusy/`, LEPSUSYWG/01-03.1,LEPSUSYWG/02-04.1.

[134] "Search for supersymmetry in events with four or more leptons and missing transverse momentum in pp collisions at $\sqrt{s} = 7$ tev with the atlas detector", Tech. Rep. ATLAS-CONF-2012-001.

[135] ALEPH Collaboration, DELPHI Collaboration, L3 Collaboration, OPAL Collaborations, LEP Working Group for Higgs Boson Searches Collaboration, "Search for neutral MSSM Higgs bosons at LEP", *Eur.Phys.J.* **C47** (2006) 547–587.

[136] F. E. Paige *et al.*, "ISAJET 7.69: A Monte Carlo event generator for pp, anti-p p, and e+e- reactions", `arXiv:hep-ph/0312045`.

[137] M. Bahr *et al.*, "Herwig++ Physics and Manual", *Eur.Phys.J.* **C58** (2008) 639–707.

[138] E. Richter-Was, D. Froidevaux, and L. Poggioli, "ATLFAST 2.0 a fast simulation package for ATLAS", Tech. Rep. ATL-PHYS-98-131.

[139] GEANT4 Collaboration, "GEANT4: A simulation toolkit", *Nucl. Instrum. Meth.* **A506** (2003) 250–303.

[140] J. Allison *et al.*, "Geant4 developments and applications", *IEEE Trans. Nucl. Sci.* **53** (2006) 270.

[141] M. Beckingham *et al.*, "The simulation principle and performance of the ATLAS fast calorimeter simulation FastCaloSim", Tech. Rep. ATL-PHYS-PUB-2010-013.

[142] E. Torro Pastor, D. Cote, and X. Portell Bueso, "Validation of the ATLFAST-II package for the simulation of supersymmetry events", Tech. Rep. ATL-COM-PHYS-2011-1181.

[143] A. Buckley *et al.*, "ATLAS tunes of PYTHIA 6 and Pythia 8 for MC11", Tech. Rep. ATL-COM-PHYS-2011-744.

[144] ATLAS SUSY Working Group, ATLAS TWiki: `https://twiki.cern.ch/twiki/bin/viewauth/AtlasProtected/SUSYD3PDMaker`. Retrieved 09.04.2012.

[145] S. Frixione and B. R. Webber, "The MC@NLO 3.2 event generator", `arXiv:hep-ph/0601192`.

[146] M. L. Mangano *et al.*, "ALPGEN, a generator for hard multiparton processes in hadronic collisions", *JHEP* **0307** (2003) 001.

[147] G. Corcella *et al.*, "HERWIG 6.5: an event generator for Hadron Emission Reactions With Interfering Gluons (including supersymmetric processes)", *JHEP* **01** (2001) 010.

[148] J. Butterworth, J. R. Forshaw, and M. Seymour, "Multiparton interactions in photoproduction at HERA", *Z.Phys.* **C72** (1996) 637–646.

[149] J. Alwall, P. Demin, S. de Visscher, R. Frederix, M. Herquet, *et al.*, "MadGraph/MadEvent v4: The New Web Generation", *JHEP* **0709** (2007) 028.

[150] T. Sjostrand, S. Mrenna, and P. Z. Skands, "PYTHIA 6.4 Physics and Manual", *JHEP* **0605** (2006) 026.

[151] P. M. Nadolsky *et al.*, "Implications of CTEQ global analysis for collider observables", *Phys.Rev.* **D78** (2008) 013004.

[152] A. Sherstnev and R. Thorne, "Parton Distributions for LO Generators", *Eur.Phys.J.* **C55** (2008) 553–575.

[153] Heavy Flavor Overlap Removal Tool, ATLAS TWiki: `https://twiki.cern.ch/twiki/bin/viewauth/AtlasProtected/HforTool`. Retrieved 29.03.2012.

[154] ATLAS SUSY Working Group, ATLAS TWiki: `https://twiki.cern.ch/twiki/bin/viewauth/AtlasProtected/SusyObjectDefinitionsr17`. Retrieved 29.03.2012.

[155] "Expected electron performance in the ATLAS experiment", Tech. Rep. ATL-PHYS-PUB-2011-006.

[156] ATLAS Egamma Combined Performance Group, ATLAS TWiki: `https://twiki.cern.ch/twiki/bin/viewauth/AtlasProtected/EnergyRescaler`. Retrieved 09.04.2012.

[157] W. Lampl *et al.*, "Calorimeter Clustering Algorithms: Description and Performance", Tech. Rep. ATL-LARG-PUB-2008-002. ATL-COM-LARG-2008-003.

[158] M. Cacciari, G. P. Salam, and G. Soyez, "The Anti-k(t) jet clustering algorithm", *JHEP* **0804** (2008) 063.

[159] G. Piacquadio and C. Weiser, "A new inclusive secondary vertex algorithm for b-jet tagging in ATLAS", *J. Phys. Conf. Ser.* **119** (2008) 032032.

[160] ATLAS Jet and Missing Et Group , ATLAS TWiki: `https://twiki.cern.ch/twiki/bin/viewauth/AtlasProtected/HowToCleanJets2011`. Retrieved 29.03.2012.

[161] ATLAS Jet and Missing Et Group , ATLAS TWiki: `https://twiki.cern.ch/twiki/bin/viewauth/AtlasProtected/FakeMetEstimator`. Retrieved 29.03.2012.

[162] ATLAS Jet and Missing Et Group , ATLAS TWiki: `https://twiki.cern.ch/twiki/bin/viewauth/AtlasProtected/MissingETUtility`. Retrieved 29.03.2012.

[163] "Calibrating the b-Tag Efficiency and Mistag Rate in $35pb^{-1}$ of Data with the ATLAS Detector", Tech. Rep. ATLAS-CONF-2011-089.

[164] ATLAS Physics Analysis Tools Group, ATLAS TWiki: `https://twiki.cern.ch/twiki/bin/viewauth/AtlasProtected/ExtendedPileupReweighting`. Retrieved 09.04.2012.

[165] W. Beenakker, R. Hopker, and M. Spira, "PROSPINO: A Program for the production of supersymmetric particles in next-to-leading order QCD", `arXiv:hep-ph/9611232`.

[166] W. Beenakker *et al.*, "The Production of charginos / neutralinos and sleptons at hadron colliders", *Phys.Rev.Lett.* **83** (1999) 3780–3783.

[167] ATLAS SUSY Working Group, ATLAS TWiki: `https://twiki.cern.ch/twiki/bin/viewauth/AtlasProtected/SUSYSignalUncertainties`. Retrieved 29.03.2012.

[168] G. D'Agostini, "Bayesian reasoning in data analysis: A critical introduction", World Scientific, 2003.

[169] F. James, "Statistical methods in experimental physics", World Scientific, 2006.

[170] D. S. Sivia and J. Skilling, "Data Analysis: A Bayesian Tutorial", Oxford Univ. Pr., 2006.

[171] ATLAS Luminosity Working Group, "ATLAS Luminosity Calculator", Online tool, `https://atlas-lumicalc.cern.ch`. Retrieved 27.02.2012.

[172] A. Lazopoulos *et al.*, "Next-to-leading order QCD corrections to $t\bar{t}Z$ production at the LHC", *Phys.Lett.* **B666** (2008) 62–65.

[173] J. Butterworth *et al.*, "Single Boson and Diboson Production Cross Sections in pp Collisions at sqrts=7 TeV", Tech. Rep. ATL-COM-PHYS-2010-695.

[174] J. M. Campbell *et al.*, "An Update on vector boson pair production at hadron colliders", *Phys.Rev.* **D60** (1999) 113006.

[175] N. Kidonakis, "Two-loop soft anomalous dimensions for single top quark associated production with a W- or H-", *Phys.Rev.* **D82** (2010) 054018.

[176] N. Kidonakis, "NNLL resummation for s-channel single top quark production", *Phys.Rev.* **D81** (2010) 054028.

[177] N. Kidonakis, "Next-to-next-to-leading-order collinear and soft gluon corrections for t-channel single top quark production", *Phys.Rev.* **D83** (2011) 091503.

[178] M. Aliev *et al.*, "HATHOR: HAdronic Top and Heavy quarks crOss section calculatoR", *Comput.Phys.Commun.* **182** (2011) 1034–1046.

# Acknowledgement/Danksagung

Writing this thesis would not have been possible without the support of a lot of people.
First of all, I would like to thank my referees, A. Quadt and C. Hensel, for giving me the opportunity to work on this projects for my Master's thesis.
Many thanks to my immediate advisors, C. Hensel and M. Hamer, who were always open for questions and advice. Furthermore, I would like to thank A. Mann and M. Hamer for helping me to settle in the ATLAS software. Thanks for working with me and answering a lot (!) of questions.
This whole work could not have been done without the support of the ATLAS community, especially the SUSY-Etmiss-Multilepton group, and the other members of the II. Physikalisches Institut of the University of Göttingen. Unfortunately, too many to name all of them.
Thanks to A. Ancu and L. Marti from LHEP at the University of Bern, for working together on a common cutflow code for the Multilepton group.
Danke an Alex, Matthias und insbesondere Henrike für das fleißige Korrekturlesen, die Formulierungstipps und viele hilfreiche Anmerkungen.
Desweiteren möchte ich meinen Freunden und Eltern danken für die Unterstützung in weniger guten Zeiten. Ohne eure Aufmunterungen wäre die Arbeit nicht möglich gewesen. Besonderen Dank an meine Liebe, Tracy!
Und zu guter Letzt möchte ich meinen Eltern für die finanzielle Unterstützung während des gesamten Physikstudiums danken.

**Erklärung** nach §18(8) der Prüfungsordnung für den Bachelor-Studiengang Physik und den Master-Studiengang Physik an der Universität Göttingen:

Hiermit erkläre ich, dass ich diese Abschlussarbeit selbstständig verfasst habe, keine anderen als die angegebenen Quellen und Hilfsmittel benutzt habe und alle Stellen, die wörtlich oder sinngemäß aus veröffentlichten Schriften entnommen wurden, als solche kenntlich gemacht habe.
Darüberhinaus erkläre ich, dass diese Abschlussarbeit nicht, auch nicht auszugsweise, im Rahmen einer nichtbestandenen Prüfung an dieser oder einer anderen Hochschule eingereicht wurde.

Göttingen, den April 14, 2012

(Jannik Hofestädt)